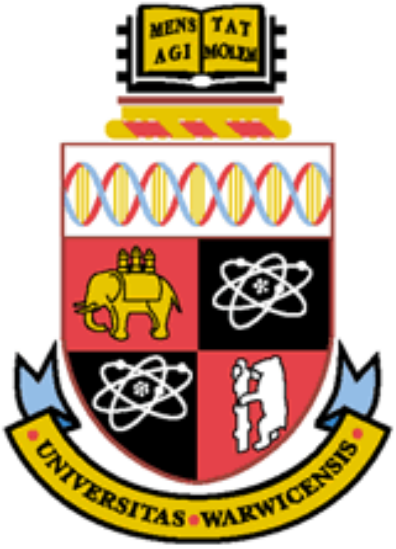

Uses of Polycrystalline Boron-Doped Diamond in Electroanalysis

Laura Anne Hutton

A thesis submitted for the degree of Doctor of Philosophy

THE UNIVERSITY OF WARWICK

Department of Chemistry

April 2011

To my parents

TABLE OF CONTENTS

ACKNOWLEDGMENTS

Firstly I would like to thank my supervisor, Prof. Julie Macpherson, for all her invaluable help and support over the years. I have found your enthusiasm and love for science both inspiring and contagious. Thank you for motivating me on the slow days and on the more emotional ones, calming me down. Many thanks to Dr. Mark Newton and Prof. Pat Unwin, I can only hope I have picked up a small part of your immense amount of knowledge in the fields of diamond and electrochemistry. Thank you to BAE Systems and Element Six for providing this opportunity and insight into industry.

Thank you to all the members of the Electrochemistry and Interfaces group, past and present. I have enjoyed our scientific and non-scientific discussions. It has been a great experience working with you all.

Hollie Patten, you are a star. Thank you for all the great times we spent together, whether it was in the lab, fancy dress parties at ours or nights in gossiping.

A massive thank you to Michael Mbogoro for your love, understanding and support. What little sanity I have left, I owe to you.

Finally, thank you to my family for all your support. A special thanks to my mum and dad for all the opportunities and encouragement you have given me. I could never have done this without you.

LIST OF FIGURES

LIST OF TABLES

DECLARATION

The work contained within this thesis is entirely original and my own work, except where acknowledged. I confirm that this thesis has not been submitted for a degree at another university. The electrochemical experiments in Chapter 5 were carried out in conjunction with Marcio Vidotti, who also aided in the experimental set-up of the TFRE. The DBE was lapped by Chris Kelly.

Parts of this thesis have been published as detailed below:

L. Hutton, M. E. Newton, P. R. Unwin and J. V. Macpherson, *Amperometric Oxygen Sensor Based on a Platinum Nanoparticle-Modified Polycrystalline Boron Doped Diamond Disc Electrode, Anal. Chem.*, **2009**, *81*(3), 1023-1032.

L. A. Hutton, M. Vidotti, A. N. Patel, M. E. Newton, P. R. Unwin & J. V. Macpherson, *Electrodeposition of Nickel Hydroxide Nanoparticles on Boron-Doped Diamond Electrodes for Oxidative Electrocatalysis, J. Phys. Chem. C.*, **2011**, 115 (5), 1649-1658.

L. A. Hutton, M. E. Newton, P. R. Unwin and J. V. Macpherson, *Factors Controlling Stripping Voltammetry of Lead at Polycrystalline Boron Doped Diamond Electrodes: New Insights from High-Resolution Microscopy, Anal. Chem.*, **2011**, 83 (3), 735-745.

L. A. Hutton, M. Vidotti, J. Iacobini, M. E. Newton, P. R. Unwin and J. V. Macpherson, *Fabrication and Characterization of an All Diamond Tubular Flow Microelectrode for Electroanalysis*, Submitted to *Anal. Chem.*

ABSTRACT

Interest and utilisation of polycrystalline boron-doped diamond (pBDD) as an electrode material has rapidly grown over the last decade, due to its unique properties and advantages over other available electrode materials. The possibility of lower detection limits and an increased range of detectable analytes has seen pBDD flourish in electroanalysis. Due to its stability at high temperatures, pressures and acidity, pBDD also has the potential to perform electrochemistry in extreme conditions. These unique properties, however, make the material difficult to manipulate in order to produce well defined and reproducible electrodes. Deviations in electrical and electrochemical responses can also arise from sample to sample, due to differing synthesis conditions and experimental set-ups.

This thesis aims to characterise pBDD available from a commercial source and through fabrication of electrodes of various designs, best utilise the material in the electroanalysis of several species. Characterisation is performed using high resolution microscopic and spectroscopic techniques which show a heterogeneous material with negligible levels of non-diamond like carbon and boron concentrations of at least 1 x 10^{20} atoms cm^{-3} throughout. Disc electrodes, fabricated using laser machining, are electrochemically characterised showing low background currents, wide solvent windows and close to reversible behaviour for $Ru(NH_3)_6^{3+/2+}$, $IrCl_6^{2-/3-}$ and $Fe(CN)_6^{3-/4}$. Functionalisation of these pBDD disc electrodes with nanoparticles enables the detection of dissolved oxygen and glucose to detection limits of ~ ppb. Furthermore, the fabricated electrodes are used in the study of Pb deposition and stripping behaviour at a pBDD surface, as well as Pb^{2+} detection. The last chapter in this thesis details the next step in diamond electrode development; the fabrication of all-diamond electrodes, where the pBDD is insulated with intrinsic diamond. Two electrode geometries are described, the first being a tubular flow ring electrode which has well-defined hydrodynamics and is used in the detection of dopamine. The second all-diamond geometry is a dual band electrode which it utilised as a solution conductivity sensor.

ABBREVIATIONS

AFM	atomic force microscopy
ASTeX	applied science and technology, Inc
ASV	anodic stripping voltammetry
BDD	boron-doped diamond
C-AFM	conducting atomic force microscopy
CNTs	carbon nanotubes
CV	cyclic voltammetry or cyclic voltammograms
CVD	chemical vapour deposition
DBE	dual band electrode
DP-ASV	differential pulse anodic stripping voltammetry
DPV	differential pulse voltammetry
ECL	electrogenerated chemiluminescence
FE-SEM	field emission scanning electron microscopy
FIA	flow injection analysis
FWHM	full width half maximum
HFCVD	hot filament chemical vapour deposition
HOPG	highly orientated pyroltic graphite
HPHT	high-pressure high-temperature
LSV	linear sweep voltammetry
MWCVD	microwave plasma chemical vapour deposition
NPs	nanoparticles
pBDD	polycrystalline boron-doped diamond
scBDD	single crystal boron-doped diamond
SECM	scanning electrochemical microscopy
SEM	scanning electron microscopy
SG-TC	substrate generation-tip collection
SIMS	secondary ion mass spectrometry
SWASV	square wave anodic stripping voltammtry
SWV	square wave voltammetry
TFRE	tubular flow ring electrode

UMEs	ultramicroelectrodes
WLI	white light interferometry
XPS	x-ray photoelectron spectroscopy

GLOSSARY OF SYMBOLS

$2h$	height of the channel
A	area of the electrode
a	diameter of the circular nozzle
C	capacitance between the electrodes
c^*	bulk concentration of redox species
C_0	initial concentration
C_w	capacitance per unit width of the planar electrodes
d	perpendicular distance between the electrodes
D	diffusion coefficient of the redox species
E_A	acceptor level
E_C	conduction band
E_F	potential of the fermi level
E_{fb}	flat band potential
$\mathcal{E}_o$	permittivity of free space
E^o	standard redox potential
$\mathcal{E}_r$	relative dielectric constant
E_V	valence band potential
F	Faraday constant
i	current
$\bar{i}$	experimental current density
i_{lim}	magnitude of the limiting current
i_p	magnitude of the peak current
iR	ohmic drop
i_{ss}	magnitude of the steady-state current
j_0	flux
k	cell constant
k^o_{app}	apparent heterogeneous electron transfer rate constant
k_r	electron transfer rate
K_{sp}	solubility product
k_t	mass transport coefficient

l	separation between the electrode surface and a parallel boundary
l_{chan}	channel length
M	molar mass
m	number of points used in the numerical simulation
n	apparent number of electrons transferred
N_{d}	number density of NPs
Q_{AFM}	charge determined via AFM
Q_{ox}	charge associated with oxidation
Q_{red}	charge associated with reduction
R	gas constant
r	radius of a spherical NP
R	radius of the electrode
R_s	resistance of solution
r_t	radius of the tube
s	electrode separation
S	relative saturation ratio
T	temperature
t	time
υ	the viscosity of the solution
$\bar{U}$	linear velocity
V	voltage
V_f	volume flow rate
w	width of the electrode exposed to solution
w_{chan}	channel width
X	length of the electrode
x	distance from electrode
Z	impedance
Γ	effective surface concentration
δ	diffusion layer thickness
ΔE_p	peak to peak separation
ρ	density or solution resistivity
υ	potential scan rate
ω	frequency of the ac

CHAPTER 1

Introduction

1.1. INTRODUCTION TO BORON-DOPED DIAMOND

Over the centuries, mankind has had a long and complex relationship with diamond, not only due to the attraction of diamond as a gemstone, but also in recognition of diamond's remarkable physical and chemical properties. A list of these properties can be found in several reviews[1] and include the hardest (most compressible) known material (ca. 90 GPa) and highest thermal conductivity at room temperature (2×10^3 W m^{-1} K^{-1}). Diamond is transparent over a wide range of wavelengths (deep ultraviolet to far infrared) and resistant to chemical corrosion. Due to the scarcity and value attributed to diamond, it is unsurprising that many attempts have been made to synthesise this allotrope of carbon. While several methods are now used to grow diamond, the advances made in chemical vapour deposition (CVD) have enabled the utilisation of diamond in a wide range of fields from high-powered lasers[2] to radiation detectors.[3] In recent years, CVD has produced high quality material with tuneable and relatively consistent characteristics, of which a prime example is conducting diamond via boron doping. Furthermore, this material is now commercially available in wafers tens of centimetres across, as shown in Figure 1.1, and at reasonably low cost.[4]

Figure 1.1: Commercially grown wafer of chemical vapour deposition polycrystalline boron-doped diamond.[4]

The application of boron-doped diamond (BDD) in the electrochemical arena has seen increased interest over the last decade.[5] Early studies showed that conductive diamond has a wide potential window in aqueous solvents,[6,7] along with low capacitive currents[8,9] and resistance to fouling,[10-12] thus showing promise as an excellent material for electroanalysis.[13] However, electrochemical results have been seen to differ greatly depending on the quality of the diamond employed, as well as the experimental set-up. This introduction will briefly discuss the synthesis of diamond and how the structural and electronic properties can affect the electrochemical behaviour of BDD. Characterisation and development of these electrodes will be summarised, as well as their use in electroanalysis, focusing on topics relevant to the work performed in this thesis.

1.1.1 **Synthesis of Diamond**

The first industrialised technique for the synthesis of diamond was the high-pressure high-temperature (HPHT) method, which mimics nature in that thermodynamically stable conditions are used for growth.[14] Graphite is compressed to tens of thousands

of atmospheres (~ 5 GPa) and heated to over 1800 K, in the presence of a metal solvent.[15] This process has been used to synthesise single crystal industrial grade diamond for decades; however, the diamonds produced are often small, in the micron to millimetre range and are typically used for grinding and abrasive tools. Exceptional process control is required to produce large (> 1 carat) single crystal HPHT diamond relatively free from impurities.[16]

The second technique, CVD will be the focus of this chapter as the work outlined in this thesis was performed solely on diamond synthesised using this process. CVD produces diamond under metastable conditions, where carbon atoms are added one-by-one to a template forming a tetrahedrally bonded network.[17] Initial work in this area began with Eversole[18] and Deryaguin *et al.*[19] who grew a combination of diamond and graphitic carbon on a natural diamond surface at low growth rates. Angus *et al.* later found that the presence of atomic hydrogen lead to less graphitic carbon deposition and higher growth rates.[20] Since these early discoveries, significant investigation has been carried-out across the world into the diamond CVD process,[21] with work in Russia showing growth on non-diamond substrates[22] and Japanese research building the first hot filament[23] and microwave reactors.[24] Several reviews summarise the work towards improved CVD diamond quality and growth rates.[25-27]

There are various types of diamond CVD processes, the majority of which involve a carbon-containing gas phase of a few per cent (typically 0.5 to 5%) in background hydrogen with peak gas temperatures in excess of 2000 K. For the growth of BDD, a source of boron is also necessary which is usually in the form of B_2H_6 gas.

Heating or activation of the gas phase can be achieved through several methods including hot filament or microwave plasma. Figure 1.2 shows schematics of (a) hot filament CVD (HFCVD) and (b) Applied Science and Technology, Inc (ASTeX) commercialized[28] microwave plasma CVD (MWCVD) reactors. In HFCVD a metal filament (tungsten or tantalum) is heated to temperatures greater than 2450 K for chemical activation, whilst the substrate is heated to 950-1170 K. The pressure inside the chamber is maintained at ca. 20-30 Torr, while gases are flowed in. HFCVD can deposit relatively good quality diamond on temperature sensitive substrates,[29] in a planar and 3D format, at low cost.[30] However, there are major drawbacks to this process including metal contamination from the filament and only a limited number of gas combinations can be used.

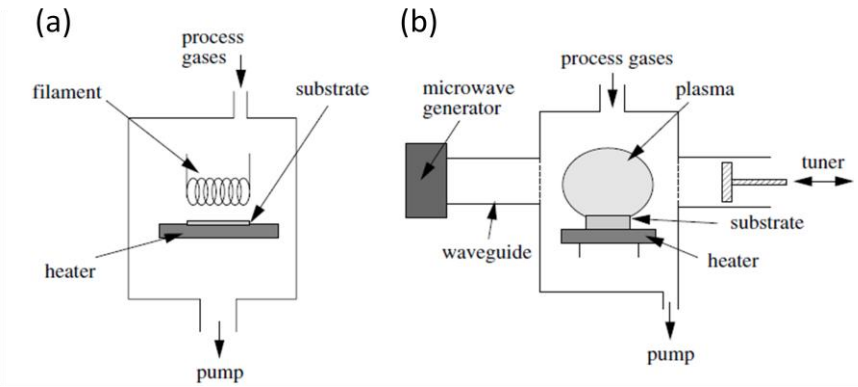

Figure 1.2: Schematics for (a) hot filament CVD reactor and (b) 'ASTeX-type' microwave plasma CVD reactor.[1]

MWCVD is currently one of the most commonly used methods of diamond synthesis. Microwaves create a discharge which couples energy into the gas phase electrons, which in turn pass energy to the surrounding gas molecules. There are several forms of MWCVD reactors including the ASTeX-type reactor shown in Figure 1.2 (b).[31] High microwave powers (up to 5 kW) and high growth rates (> 10 μm h^{-1}) can be achieved with this process, where a variety of gas mixtures can also

be used. Potential biasing of the substrate is also possible giving increased nucleation rates and greater growth control. Another advantage of MWCVD over the HFCVD system is a much lower level of contamination, producing very high quality diamond. The substrate material itself has been shown to be an important factor in diamond synthesis, where it's melting point, thermal expansion coefficient, ability to form carbide, as well as it's orientation and pretreatment all influence diamond growth rates and quality.[1] Using the methods described above, diamond has been successfully deposited on a number of substrates such as Si, Mo, W, Ti and diamond.

The chemistry of diamond CVD growth is very complex and has been the subject of intense investigation,[32] from which several important principals have come to light.[32-35] First, the activation of the gas phase has two main functions. Energy is provided to the carbon and boron-containing gaseous species causing the molecules to fragment into reactive radicals, ions and electrons. These continue to mix and react until striking the substrate surface were they can absorb and react with the surface. Diffusion across the surface can also take place until a suitable reaction site is found. If not, the atoms/molecules simply desorb back into the gas phase. The second role of activation is to break down the hydrogen gas into atomic hydrogen which is crucial for several reasons:

(1) Hydrogen atoms react with the source hydrocarbon species to create reactive radicals e.g. $CH_3^{\cdot}$ which react with the surface. Atomic hydrogen also creates reactive sites on the diamond surface by removing hydrogen from CH sites aiding carbon incorporation into the lattice.

(2) Even though diamond is sp^3 hybridised, there is a 'dangling bond' at the surface which needs to be terminated in order to avoid cross-linking and reconstruction to graphite. H atoms stabilise the diamond lattice by bonding to the surface carbons where they can be abstracted and replaced by carbon-containing species during the diamond growth.

(3) Atomic hydrogen etches sp and sp^2 carbon at a much faster rate than sp^3 carbon, thus helping remove any graphitic clusters, while leaving behind diamond.[20]

Interestingly, with the hugely complex chemistry occurring within the chamber it has been found that the CVD process is highly insensitive to the type of carbon source gas chosen, i.e. using CH_4 or C_2H_2 gives similar results.[36] This is because these gases breakdown into the key radical for diamond growth, $CH_3^{\bullet}$.

1.1.2 **Electrical Properties: Diamond Structure and Doping**

Formed from one of the most abundant elements in the world, diamond is a cubic polymorph of carbon.[37] As shown in Figure 1.3 (a), tetrahedrally bonded carbon atoms form a face centred cubic lattice. The single σ bonds binding the carbons together in this structure are responsible for the fundamental properties of diamond. Intrinsic (undoped) diamond is a wide bandgap semiconductor with a gap of 5.47 eV at T=300 K,[38] making it electrically insulating, though surface processes can induce conductivity at the diamond surface, as discussed in section 1.1.3.

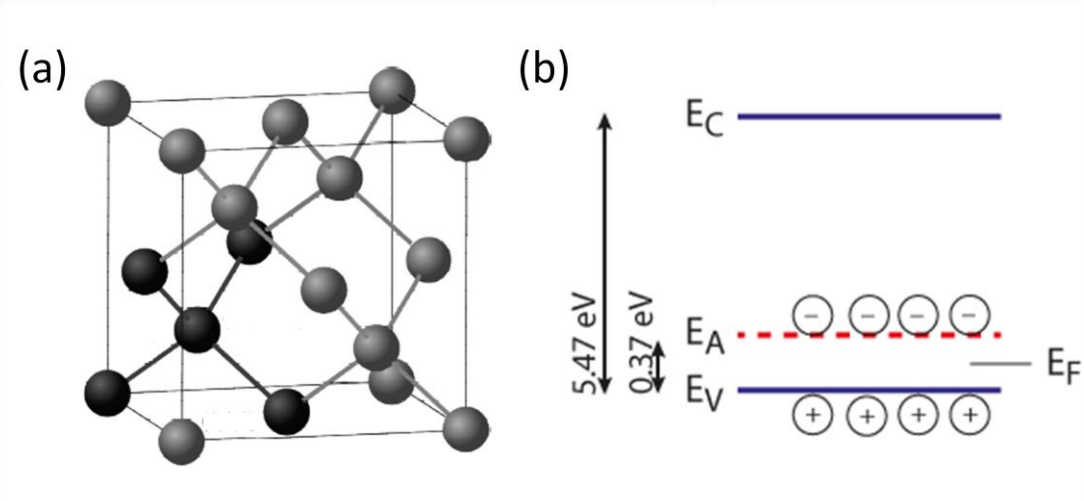

Figure 1.3: (a) The structure of diamond with tethrahedrally coordinated carbon atoms (b). Band structure for p-type semiconducting BDD, where E_V is the valence band potential, E_A is the acceptor level, E_C is the conduction band and E_F is the potential of the fermi level.

Diamond can also be made conducting via doping. N-type and p-type doping are most often achieved with nitrogen and boron respectively. Being similar in size to carbon, they are readily incorporated into the dense crystal lattice. For p-type conductivity, boron doping introduces an acceptor level 0.37 eV above the valence band (Figure 1.3 (b)).[39] While BDD can be found in nature, they are usually very lowly doped (ca. 1 to 5 ppm atoms cm^{-3}) and extremely rare.[40]

BDD can now be routinely grown by the addition of a boron containing source during CVD. There are two main classes of diamond grown, single crystal and polycrystalline. Single crystal diamond is produced mainly by homoepitaxial growth, where the substrate is single crystal diamond itself.[41] Heteroepitaxy has been achieved on an iridium substrate.[42] Polycrystalline diamond is produced when a non-diamond substrate is used. Individual diamond crystals nucleate on the surface, where up to 10^{12} cm^{-2} nucleation sites can exist. All sites proceed to grow in three dimensions, but certain grains with preferential facets and orientations grow at

a faster rate in comparison to their neighbours. Eventually the crystals coalesce forming a film and growth continues upwards.[21] As the film thickness increases, the grain size increases (Figure 1.4 (a)), this results in a decreasing number of grain boundaries at the top surface. Polycrystalline boron-doped diamond (pBDD) can be grown with a range of grain sizes, including microcrystalline, nanocrystalline and ultrananocrystalline, as depicted in Figure 1.4 (b - d). The work carried out in this thesis is performed on microcrystalline BDD and as such shall be the focus of the remainder of the introduction.

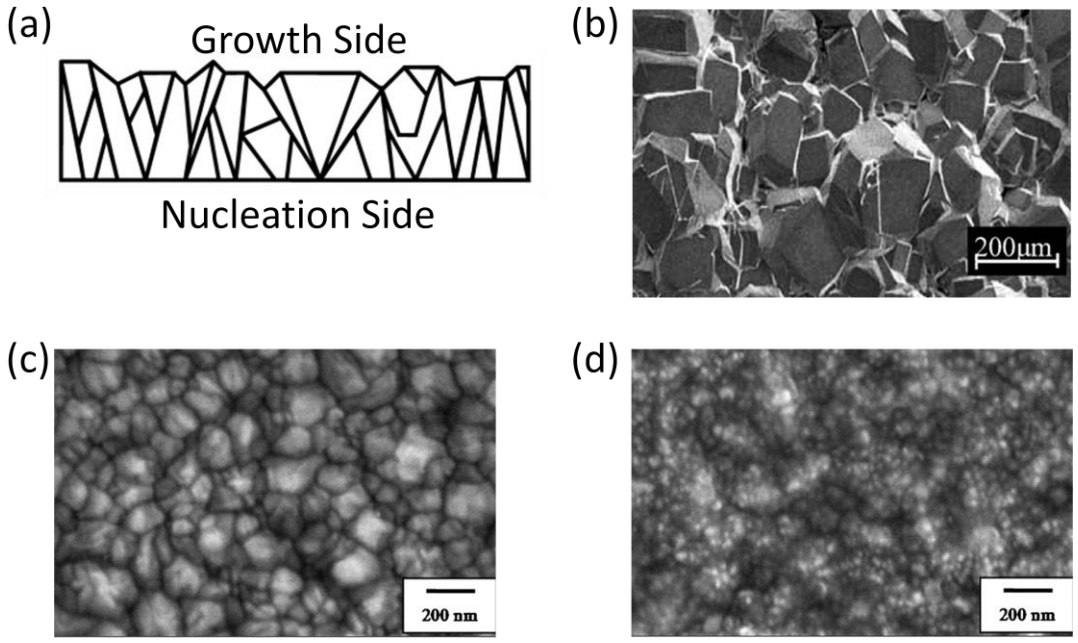

Figure 1.4: (a) Schematic showing grain structure of thick pBDD film;[43] scanning electron microscope images showing the growth side surface of (b) microcrystalline BDD;[44] (c) nanocrystalline BDD and (d) ultrananocrystalline BDD.[45]

The electrical properties and conductivity of pBDD has been the subject of much investigation. While boron doping can produce conducting diamond due to the acceptor level 0.37 eV above the valence band, this shallow doping still has a relatively high activation energy compared to boron in silicon. Thus the probability of excitation of valence band electrons into the acceptor level is only 4-5 % at 500

K.[46] This means in order to get reasonable conductivity at room temperature, doping concentrations in excess of 10^{17} boron atoms cm^{-3} are necessary. Secondary ion mass spectrometry (SIMS) is often used to determine the boron concentration in CVD grown BDD. It is important to note that in the case of polycrystalline diamond, the given value is an average over the different crystallites present.

It has been observed that the nature of the boron acceptor level and the diamond resistivity are related to the amount of boron in the lattice as shown in Figure 1.5.[46] The majority of research in this area has utilised single crystal BDD (scBDD), although the knowledge gained is largely applicable to pBDD. In lightly doped diamond with levels of less than 10^{17} atoms cm^{-3}, boron creates an acceptor level and conductivity activation energy of 0.368 eV. As the boron concentration is increased to ca. 3×10^{18} atoms cm^{-3}, the average distance between boron atoms in the lattice decreases. Hopping conduction is possible as the boron-boron distance decreases further. The wavefunctions on neighbouring boron atoms start to overlap giving rise to an impurity band, correlating with a reduction in the activation energy.[47,48] This is termed moderate doping and produces diamond resistivities of ca. 2×10^{3} Ω cm. Highly doped samples are generally considered to have a boron content between 1.5×10^{19} and 3×10^{20} atoms cm^{-3}. At this doping level hopping type conductivity in the impurity band is thought to occur between ionized and unionized neighbouring boron atoms.[46] At ca. 3×10^{20} boron atoms cm^{-3} the activation energy falls to zero and the transition to metallic conductivity occurs.[41] At dopant densities greater than this, diamond is considered a semi-metal and is termed heavily doped with resisitivites ≤ 0.1 Ω cm. Precise details of the physics underpinning the electrical conductivity is currently under investigation.[49-51]

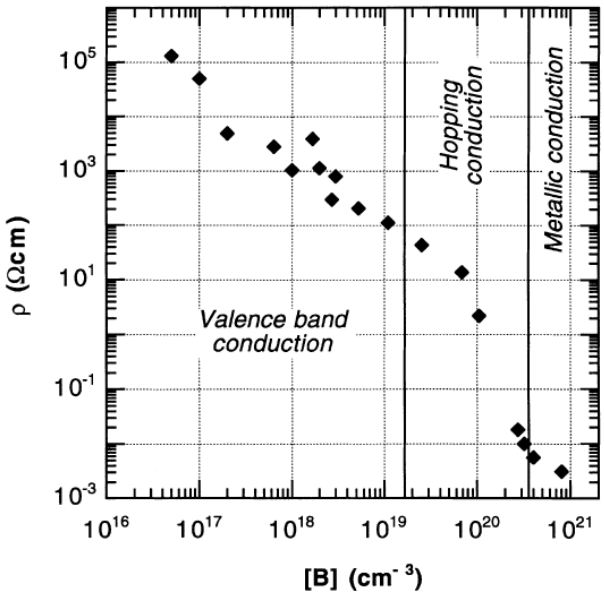

Figure 1.5: Room temperature resistivity as a function of boron concentration for scBDD.[46]

Carrier concentrations and hole mobilities have also been calculated for scBDD and pBDD from Hall measurements. It was found that for pBDD with an average boron concentration of 6 x 10^{19} atoms cm^{-3}, there was 5 % activation of the boron at room temperature, giving a carrier concentration of 3 x 10^{18} carriers cm^{-3}. However, at higher doping levels complete activation of boron was observed.[52] For polycrystalline diamond, grain boundary effects must also be considered as they may scatter carriers, reducing mobility.[53] Hole mobilities can range from 3800 to 1 cm^2 V^{-1} s^{-1},[42,54-56] for intrinsic to doped diamond, where pBDD hole mobilities are generally 10 to 50 times smaller than in their equivalent single crystal counterparts.[37] However, it has been shown that with heavily doped diamond there is little difference between scBDD and pBDD hole mobilities (0.5 and 0.28 respectively).[52] At these doping levels the effects from the impurity band are greater than those of the grain boundaries.[57]

Several factors influence how boron is incorporated into the lattice, including boron gas concentration, crystal orientation, substrate temperature, the nature of the substrate and the type of CVD process employed.[58,59] The relationship between the amount of boron in the diamond and the boron gas concentration during the growth process has shown inconsistent results from group to group.[60] However, several trends have been noted. Firstly, the boron concentration in the diamond increases approximately linearly with boron in the source gas.[61-64] Secondly, boron is incorporated by an order of magnitude more into the (111) crystal surface when compared to (100).[22,65] As polycrystalline diamond consists of different crystal orientations, this difference in boron uptake gives rise to sectors of differing conductivity and thus a heterogeneous sample. This electrical heterogeneity has been studied by several groups using techniques including micro-Raman, field emission scanning electron microscopy (FE-SEM) and conducting atomic force microscopy (C-AFM).[43,66]

Figure 1.6, shows C-AFM and FE-SEM images of a lapped heavily doped oxygen-terminated pBDD surface. In Figure 1.6 (a) the white sections are the regions of higher conductivity and thus higher boron concentration. These correlate well with the grain morphology shown in the FE-SEM image in Figure 1.6 (b) taken at 1 kV with an In-lens detector. Here the darker areas correspond to higher conductivity. Looking closely at the C-AFM image, variations in conductivity within growth sectors can also be seen. This is most probably due to defects that can also influence boron incorporation. Variations in boron content may also occur within single crystal samples, due primarily to the presence of growth defects and changes in growth conditions.[67,68]

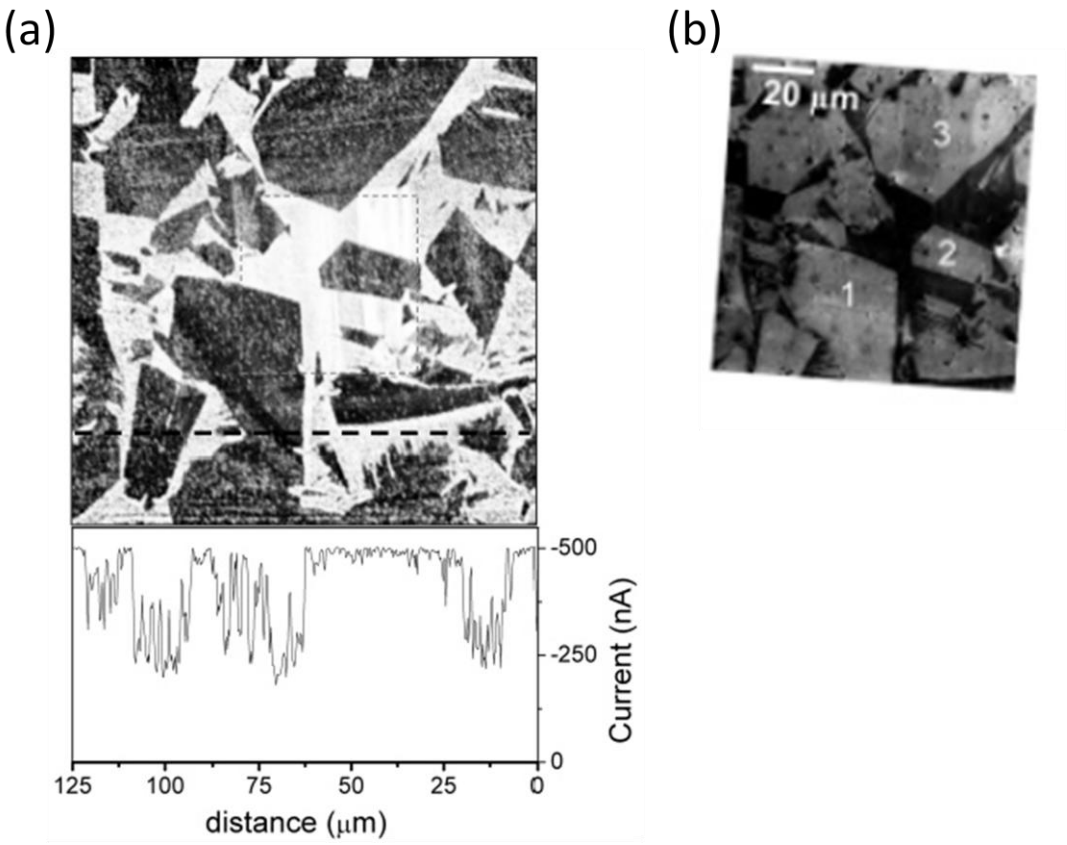

Figure 1.6: (a) C-AFM image in air with a -5 V tip potential and a 10 MΩ resistor in series, (b) FE-SEM image taken with an In-lens detector at 1 kV of lapped pBDD surface.[43]

1.1.3 **Electrical Properties: Surface Structure and Diamond Quality**

After boron concentration, the next most influential factor on the electrical properties of diamond is surface termination. When diamond is grown via CVD, the surface is hydrogen-terminated. While hydrogen-termination has been found to be stable over months in air, there is evidence of gradual oxidation.[69,70] A much faster oxidation process has also been observed to occur when the material is anodically biased in solution.[7] Interest in oxygen-terminated surfaces has increased from an electrochemical view point due to the more stable nature of the surface, in air and under potential control. Also the hydrophilic nature of the oxygenated surface is likely to be preferred for electron transfer processes in aqueous solutions. There are

several methods for oxygen-termination including boiling in acid,[71,72] exposure to oxygen plasma,[45] photochemical oxidation,[73] anodic polarisation[74] or reactions with oxygen at high temperatures.[75]

Contact angles on the diamond surface, as in Figure 1.7 (a), show that hydrogen termination produces a hydrophobic surface; for water, contact angles of ca. 90^{o} are obtained.[73,75] Oxygen-terminated hydrophilic diamond results in contact angles (water) ranging from 0.6^{o} to 65^{o} depending on the method of termination, surface roughness etc.[76,77] X-ray photoelectron spectroscopy (XPS) has been used to investigate the functional groups formed on the diamond surface, as shown in Figure 1.7 (b).[78] Oxygen-terminated pBDD shows a range of oxygen containing functional groups on the surface including hydroxyl groups C-OH, ether groups C-O-C, and carbonyl groups >C=O.[78,79] Studies at single crystal diamond show that C-OH groups are most abundant on the (111) diamond surface, while C-O-C and >C=O groups are dominant on the (100) face.[80,81] In particular, highly doped (ca. 10^{19} to 10^{20} boron atoms cm^{-3}) pBDD anodic, UV and oxygen plasma treatments are reported to result in a low number of >C=O groups (with a O1s/C1s ratio of ca. 3 to 5 %), with UV treatments producing larger amounts of C-OH groups (ca. 29 %) compared to the other two oxidation processes.[82] Interestingly, it has also been shown that increasing the amount of charge passed during anodic polarisation i.e. > 10 mC cm^{-2}, increases the number of C-O containing groups on the surface while maintaining the number of >C=O groups.[83] This indicates that the oxygen-containing functional groups produced on a pBDD surface relate to both the growth sectors present and the method of oxygen termination.

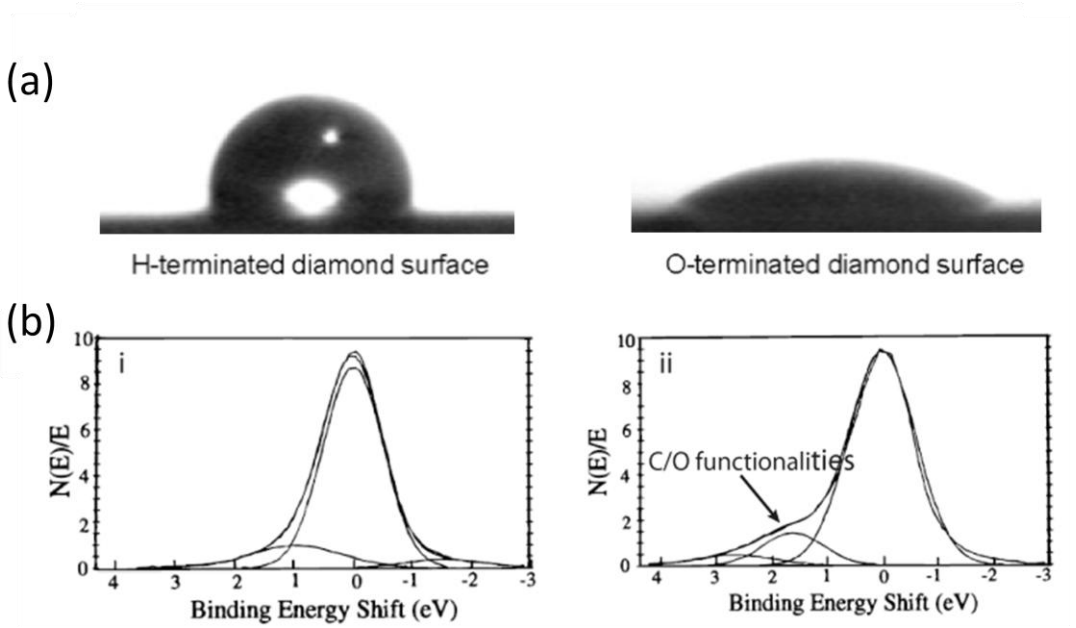

Figure 1.7: (a) Contact angles for hydrogen and oxygen-terminated pBDD[84] (b) XPS C 1s spectra of semiconducting hydrogen-plasma treated pBDD i) before and ii) after electrochemical oxidation at 1.5 V for 10 mins in 0.1 M KH_2PO_4.[78]

The surface electronic properties of intrinsic and BDD can be changed as a result of surface terminations. In fact, since 1989 it has been known that intrinsic hydrogen-terminated diamond possesses surface conductivity,[85,86] with p-type carriers present in an accumulation layer at the diamond surface.[87,88] Initially this was attributed to doping via sub-surface hydrogen.[89] It wasn't until 2000 that it was discovered that atmospheric adsorbates were also required for surface conductivity through a process called surface transfer doping.[90] A wetting layer of solvated hydronium ions and corresponding anions is expected on any surface in atmosphere, due to the dissociation of CO_2 to H_3O^+ and HCO_3^- in a humid environment. It is proposed that the chemisorbed hydrogen lowers the ionisation potential of the diamond surface, whilst the hydronium/hydrogen adsorbate couple present supplies a potential driving force for electron transfer from the diamond,[91,92] thus leaving an accumulation of holes at the diamond surface. Lightly doped hydrogen-terminated pBDD surfaces have been shown by impedance spectroscopy and scanning probe microscopy *i-V*

curves to result in increased surface conductivity compared to oxygen-terminated pBDD.[72]

The dipoles of different surface terminations can also have an impact on the surface electrical properties. Carbon is more electronegative than hydrogen, but less electronegative than oxygen, therefore localised dipoles can arise at the terminated interface and change the electron affinity of the diamond surface.[91] Hydrogen-termination has a lowering effect on the electron affinity of the diamond surface to such an extent that negative electron affinity occurs, whereas oxygen-termination increases the electron affinity.[93,94] Furthermore, the type of surface termination can also cause a change in the surface band structure.[81] Charge carrier transfer can occur between the bulk diamond and states at the surface causing band bending and a space charge layer which stretches hundreds of nanometres into the bulk. The method of surface termination most often changes the surface states, hence the band structure. The flat band potential (E_{fb}) of hydrogen-terminated semiconducting pBDD has been reported to fall in the range 0 to 0.75 V vs SCE,[78,95] whilst that for oxygen-terminated pBDD has been experimentally determined between 1 to 4 V vs SCE.[78,83,96] There is also evidence that the method of oxidation i.e. the relative amounts of different carbon-oxygen functional groups, influences E_{fb}.[83] For both hydrogen-terminated and oxygen-terminated pBDD the E_{fb} shows some dependence on pH.[78]

The quality of bulk CVD diamond can be assessed by studying the amount of parasitic phases, crystallographic defects and impurities present, all of which are influenced by the deposition technique and parameters. For example non-diamond

carbon, hydrogen and metal impurities are all detrimental to the overall quality of diamond and affect its electrical properties. The crystalline quality of individual grains in polycrystalline diamond has been shown to improve with increasing film thickness and hence increasing grain size, so that crystallites on the order of 100 μm approach the crystalline quality of homoepitaxial films.[97] Raman spectroscopy is often used to determine the material quality and concentration of foreign phases. The intensity, frequency and full width half maximum (FWHM) of the diamond zone-centre peak optical phonon line at 1332 cm^{-1} give an indication of the amount of defects present. The FWHM has been observed to decrease with increasing boron concentration up to metallic conductivity which has been ascribed to a decrease in the number of defects.[52,98] This can be seen in the Raman spectra (632.8 nm laser) in Figure 1.8 (a) for various pBDD films of varying boron concentrations. Non-diamond carbon has also been observed to decrease with increasing boron concentration.[98,99] These effects were predicted by Bernholc *et al.* due to the increased vacancy mobility allowing increased surface diffusion of carbon.[100] Above the metallic threshold, a distortion of the 1332 cm^{-1} peak is seen due to a Fano effect which increases with increasing boron concentration, shown in Figure 1.8 (b).[101,102] Furthermore, the peak at ca. 500 cm^{-1} can be used to determine boron concentration at these high levels.[102] The diamond phase can exist in pBDD up to dopant concentrations of at least 8×10^{21} boron atoms cm^{-3}.[103]

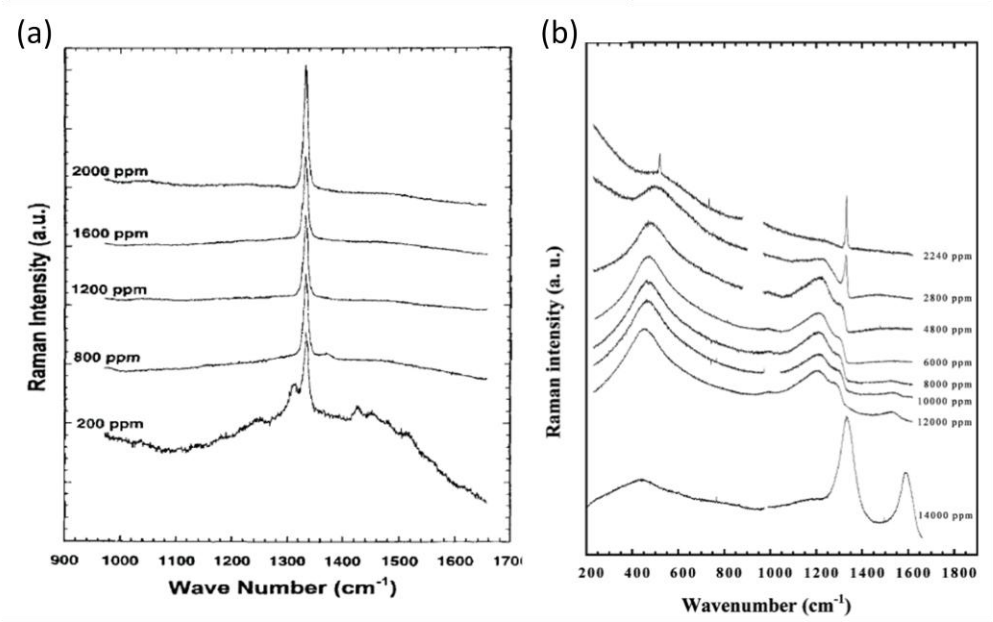

Figure 1.8: (a) Raman spectra of semiconducting pBDD[104] (b) Raman spectra of semiconducting to metallic pBDD.[102]

For pBDD grown via MWCVD with a boron concentration of > 10^{21} boron atoms cm^{-3}, an additional graphitic phase can occur (Figure 1.8 (b)).[105] Other Raman signals (not shown) at ca. 1580 cm^{-1} and a pair at ca. 1350 – 1580 cm^{-1} are known to originate from graphite and nanocrystallites of graphite respectively,[106] whereas signals at 1550 cm^{-1} and 1500 cm^{-1} are due to amorphous carbon.[107] If present in the film, these parasitic phases are thought to be found primarily at grain boundaries for polycrystalline diamond. Moving from microcrystalline to nanocrystalline diamond can increase the amount of non-diamond carbon present at grain boundaries, this is most likely due to the deposition parameters necessary for nanocrystalline growth.[108,109] Early C-AFM images on semiconducting pBDD were interpreted as showing enhanced conductivity at grain boundaries due to inclusion of graphitic carbon.[110] However, it is now generally accepted that for high quality pBDD, grain boundaries do not show regions of enhanced conductivity i.e. non-diamond carbon is

negligible as seen in Figure 1.6 and boron concentration and surface terminations are the major contributing factors to bulk and surface conduction.[43,111]

1.2. ELECTROCHEMISTRY AT BORON-DOPED DIAMOND ELECTRODES

1.2.1 **Initial Electrochemical Studies of BDD**

In 1983, Iwaki *et al*. first reported the use of diamond as an electrode material. Solution electrochemistry performed with zinc ion- implanted natural diamond was shown to give wider potential windows and lower background currents in comparison to glassy carbon electrodes.[112] However, it wasn't until 1987 that more extensive studies of diamond as an electrode material were performed by Pleskov *et al*.[113] Here, semiconducting CVD grown polycrystalline diamond was used for photoelectrochemical studies in 1 M KCl at sub-bandgap wavelengths. In the early nineties, Fujishima and co-workers also reported the photoresponse of diamond electrodes[114] and in 1993 Fujishima *et al.* demonstrated the use of pBDD for the reduction of nitrate to ammonia.[115] Over a series of papers from 1993 to 1995, Swain and co-workers detailed the low capacitance and featureless background of high quality thin film pBDD and its suitability for electroanalysis.[95,116,117] Further work on diamond continued with investigations by Angus and colleagues into water stability at pBDD electrodes, the electrochemical response with respect to several different redox mediators and applications in the anodic destruction of organic waste, as well as electroanalysis.[7]

1.2.2 **Fundamental Electrochemistry of pBDD**

It is well documented that the electrochemical behaviour of pBDD is influenced by several factors, the first among these being boron concentration. As discussed in section 1.1.2, the effect of boron content on the electrical properties of pBDD can be dramatic which strongly affects the electrochemical behaviour. The quality or purity of diamond is also important, increasing sp^2 content in the material can result in differing electro-activity compared to pure sp^3 diamond. As electrochemistry is an interfacial science, the electrochemical performance of pBDD is also observed to change with surface termination. As mentioned previously, the most common surface terminations are hydrogen and oxygen, where different surface preparations and functional groups can affect the diamond surface properties. The rest of this section will discuss the electrochemical characteristics of pBDD and how the above factors have an impact on the behaviour observed.

One of the first electrochemical characteristics noted on pBDD was a wide potential window in water in comparison to traditional electrodes e.g. platinum.[118] Figure 1.9 shows oxygen and hydrogen evolution at high and low quality pBDD in 0.5 M H_2SO_4.[7] A wide potential range (approx. -1.25 to 2.3 vs. SHE) was observed, as shown in Figure 1.9 (a) for high quality hydrogen-terminated pBDD with a boron content of ca. 10^{21} atoms cm^{-3}.[7] The overpotentials for oxygen and hydrogen evolution indicate that water electrolysis is inhibited on pBDD suggesting high molecular adsorption energies for these reactions.[119] Initially, these slow kinetics for hydrogen evolution were attributed to a lack of adsorption sites on the hydrogen-terminated surface, however several studies have shown that oxygen-terminated pBDD surfaces also show a large potential window.[9] It should be noted that for

pBDD with low dopant levels there is an increased surface resistance at the oxygen-terminated surface compared to hydrogen-terminated and decrease in the number of electronic states as mentioned above. [72,120] Similar to that on Hg, weak adsorption of atomic hydrogen at the diamond surface has also been used to explain high the overpotentials for hydrogen evolution. It is known that the electrode-H bond is inversely proportional to atomic hydrogen adsorption, with the C-H bond being relatively strong at ca. 81 kcal.[7]

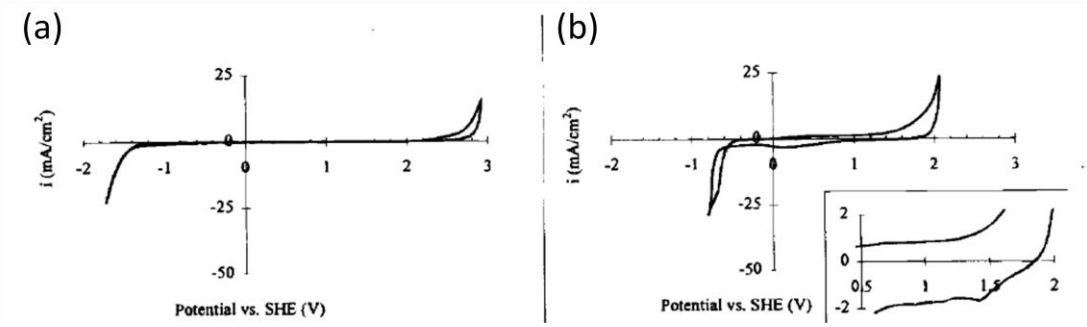

Figure 1.9: CVs in 0.5 M H_2SO_2 at a scan rate of 200 mV s^{-1} at as grown (a) high quality pBDD and (b) low quality pBDD.[7]

Much narrower potential windows are observed on lower quality diamond as shown in Figure 1.9 (b), due to the increased sp^2 carbon content, water discharges at lower overpotentials on sp^2 carbon, and were found to be similar to that of glassy carbon and highly orientated pyrolytic graphite (HOPG) electrodes.[121] By varying the carbon/hydrogen ratio during growth, Bennett *et al.* also showed the detrimental effect of increasing sp^2 content on the width of the hydrogen-terminated pBDD potential window.[122] Moving from semiconducting pBDD electrodes to metallic-like pBDD also gives a slight narrowing of the potential window, however much larger charge densities result for the reduction and oxidation of water.[123] This is thought to be due to the percolation of levels across the space charge region through the boron impurity band, thus allowing easier electron transfer. While the origins of

the extended diamond potential window are still not fully understood, it allows for a greater range of electroactive species to be detected, compared to the more traditional electrodes, as well as the generation of species with an oxidation potential greater than molecular oxygen.[124]

Low background currents, are another property of pBDD resulting in improved current sensitivity in electroanalysis.[10] Typically background currents an order of magnitude lower (per geometric area) than those of glassy carbon can be achieved with pBDD allowing for improved signal-to-noise ratios and therefore lower limits of detection. These reduced currents stem from two properties of pBDD, the first being low double layer capacitance.[117] For semiconducting diamond there is a low density of electronic states at the Fermi level, with a space-charge region existing near the surface through which charge can be distributed. While this is responsible for low capacitance at lightly doped diamond, it is unclear to what extent it can be applied to heavily doped pBDD, though the density of states is still lower than in a metal. The second reason for the low background currents is the stability of the sp^3 diamond surface. The diamond surface itself cannot be oxidised or reduced unlike that of a metal, where metal oxides are routinely formed and reduced. Although hydrogen-terminated pBDD can be oxygen-terminated at high anodic potentials, once this transition occurs pBDD is extremely chemically stable. Very little surface processes occur during electrochemistry in comparison to metal electrodes, thus producing low current density *i-V* responses within the solvent window. In fact, there seems to be very little effect of surface-termination on the background currents in traditional electrolytes for highly doped pBDD.[104] However, increasing the sp^2

content of the BDD material results in an increase in background currents, due to increased capacitance as well as surface redox processes as shown in Figure 1.9 (b).

The reduction of oxygen has been found to be inhibited at the diamond surface, thus aiding in a wide potential window and low background interferences. Heavily doped (ca. x 10^{21} boron atoms cm^{-3}) pBDD was found to reduce oxygen at -1.2 V and -0.6 V vs. Ag/AgCl in alkaline and acidic conditions respectively, however this was found to be due to non-diamond sp^2 carbon impurities.[9,121] Once these were deactivated by potential cycling, the pBDD was very insensitive to oxygen. Another advantage of using pBDD electrodes is their resistance to deactivation by fouling.[125] Passivation of an electrode is particularly a problem where electrochemical detection produces an insoluble electrode coating or in *in-vivo* and *in-vitro* biosensing, where biological matrices can adsorb to the surface.[126] Initial studies attributed the antifouling properties of pBDD to the lack of adsorption at the hydrogen-terminated surface,[10,127] however oxygen-terminated pBDD has also shown resistance to fouling.[12,128]

There have been many studies on the voltammetry of standard electrochemical reactions at pBDD electrodes. Several redox mediators (both inner- and outer-sphere) have been investigated using diamond of varying dopant densities, quality and surface terminations. Due to the variation possible in pBDD material, a wide range of electrochemical responses to given redox mediators has been reported. However, several trends can be drawn from literature; (i) for a given reaction (either inner- or outer-sphere) a more reversible behaviour is observed on heavily doped (metallic) pBDD than on moderately doped (semiconductor) diamond;[60,129] (ii) due

to the additional surface conductivity, more reversible behaviour for outer-sphere species is also seen at hydrogen-terminated electrodes.; (iii) outer-sphere electroactive species with a positive standard redox potential, E^o, are more reversible than those with a more negative E^o.[130] These last two trends are more pronounced with lower doping concentrations. There are several redox couples which are commonly employed to characterise pBDD which include, $Ru(NH_3)_6^{3+/2+}$, $Fe(CN)_6^{3-/4-}$, $IrCl_6^{3+/2+}$, dopamine, hydroquinone/quinone and benzoquinone. The first two are discussed in more detail below.

$Ru(NH_3)_6^{3+/2+}$ is an outer-sphere redox couple and is therefore fairly insensitive to the physiochemical nature of the pBDD surface. The E^o for $Ru(NH_3)_6^{3+/2+}$ is less positive than the experimentally measured flatband potential, E_{fb}, for p-type semiconducting BDD.[131,132] Consequently, for $Ru(NH_3)_6^{3+/2+}$ reduction at a semiconducting BDD electrode, electron transfer occurs with BDD in the depletion region. Hence $Ru(NH_3)_6^{3+/2+}$ electrolysis is sensitive to the electronic properties of the BDD.

Figure 1.10 shows how the reversibility of $Ru(NH_3)_6^{3+/2+}$ varies with boron concentration and surface termination. ΔE_p has been reported to range from 70, 99 to 140 mV on hydrogen-terminated highly (ca. 10^{19} to 10^{20} boron atoms cm^{-3}), moderately and lightly (ca. 10^{17} boron atoms cm^{-3}) doped diamond.[95,111,133,134] As the dopant concentration increases, a decrease in ΔE_p is observed, which reflects the increase in the density and mobility of midgap electronic states i.e. moving from neighbouring boron atom impurity band conduction to hopping ionised – unionised boron conduction, and thus increasingly more facile electron transfer.[123,130,134] For

highly doped samples, peak current is proportional to the square root of scan rate indicating a linear diffusion controlled reaction. It is important to note that increasing scan rate and/or analyte concentration, both of which increase the current being passed, can result in the increase of ΔE_p.[43,135] This is likely to be due to solution resistance becoming important with the higher currents passed and the fact that BDD has a limited number of charge carriers compared to a typical metal. This can become rate limiting when the surface is challenged with a high flux of electroactive species.

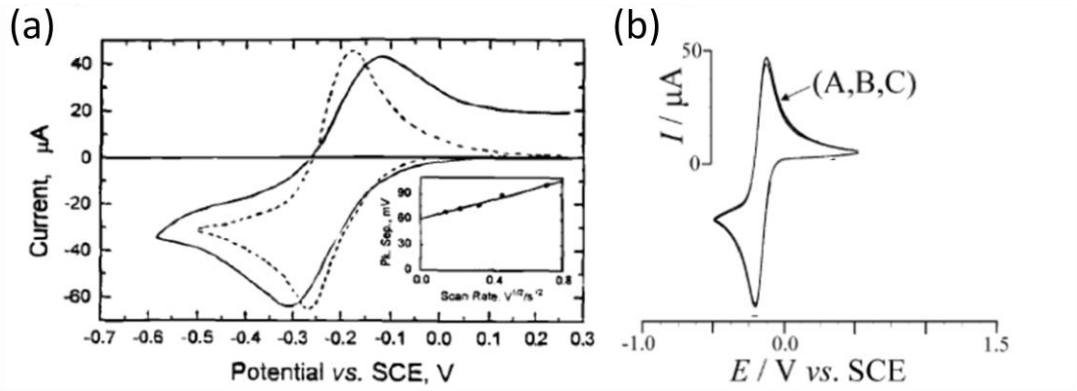

Figure 1.10: CVs for the reduction of 1 mM $Ru(NH_3)_6^{3+/2+}$ in 1 M KCl at (a) highly, ca. 10^{20} boron atoms cm^{-3}, (dashed line) and moderately ca. 10^{18} boron atoms cm^{-3}, (solid line) doped pBDD electrodes at a scan rate of 200 mV s^{-1};[130] (b) highly doped, ca. 10^{20} boron atoms cm^{-3}, pBDD electrodes at a scan rate of 100 mV s^{-1} (A) after polishing with alumina, (B) after anodic pretreatment and (C) after cathodic pretreatment.[133]

At highly doped (ca. 10^{20} boron atoms cm^{-3}) pBDD, there seems to be little effect of surface termination for $Ru(NH_3)_6^{3+/2+}$ electrolysis.[111] This is shown in Figure 1.10 (b), where similar CVs are observed for the reduction of $Ru(NH_3)_6^{3+/2+}$ at as-grown alumina polished (hydrogen-terminated), HNO_3 anodically cycled (oxygen-terminated) and HNO_3 cathodically cycled (hydrogen-terminated) pBDD.[133] This is most likely because the number of charge carriers in the highly doped material is sufficient to enable electron transfer. The additional surface conductivity arising

from the hydrogen-termination layer thus does not appear to affect the *i-V* response. The apparent heterogeneous electron transfer rate constant, k^o_{app}, has been calculated to be in the range 0.01 to 0.1 cm s^{-1} for hydrogen-terminated heavily doped diamond.[134]

The electrochemistry of $Fe(CN)_6^{3-/4-}$ is more complex than that of $Ru(NH_3)_6^{3+/2+}$ and has been studied extensively on many different materials, for example, on glassy carbon and HOPG sp^2 carbon electrodes. Several factors have been shown to influence the electron transfer kinetics such as the amount of edge plane carbon exposed, adsorbed monolayers, as well as the electrolyte composition.[136,137] These results indicate that $Fe(CN)_6^{3-/4-}$ electrolysis is most likely inner-sphere and therefore sensitive to the chemical nature of the electrode surface. Given the complexities involved in $Fe(CN)_6^{3-/4-}$ electrolysis, it is perhaps surprising that this mediator is used so widely to characterise the electrochemical properties of electrode materials; as is the case with pBDD.[111]

For hydrogen-terminated pBDD, the effect of boron concentration on $Fe(CN)_6^{3-/4-}$ reversibility was found to be similar to that for $Ru(NH_3)_6^{3+/2+}$ where ΔE_p values were found to range from 70 to 245 mV for heavily (ca 10^{20} boron atoms cm^{-3}) to moderately doped (ca. 10^{18} boron atoms cm^{-3}) hydrogen-terminated pBDD respectively.[111,138,139] Attention must be paid to the anions present, as well as the pH as these are shown to have an influence on the $Fe(CN)_6^{3-/4-}$ response.[140] Again, an increase in ΔE_p can be seen with increasing analyte concentration.[141] While quasi-reversible behaviour is observed for moderately to highly doped hydrogen-terminated semiconducting pBDD, this is not the case for oxygen-terminated

semiconducting pBDD. Figure 1.11 (a) shows the electrolysis of $Fe(CN)_6^{3-/4-}$ at moderately doped (ca. 10^{18} boron atoms cm^{-3}) (i) hydrogen-terminated pBDD, (ii) oxygen-termianted pBDD and (iii) highly doped (ca. 10^{20} boron atoms cm^{-3}) oxygen-terminated pBDD.[132] At moderate doping, the change from quasi-reversible to irreversible upon oxygen-termination is attributed to a decrease in the density of electronic states at the diamond surface. This suggests that the boron doping itself is not enough for electron transfer, especially at more negative potentials where the pBDD maybe in a depletion region, and that the hydrogen-termination (section 1.1.3) is benefical.[129] It must also be remembered that oxygen-termination may lower the energy of the pBDD valence band at the surface (section 1.1.3), which may also have an effect on electron transfer.[72,142] Figure 1.11 (aiii) shows that highly doped pBDD provides enough density of states through boron doping alone, to achieve quasi-reversible electron transfer.

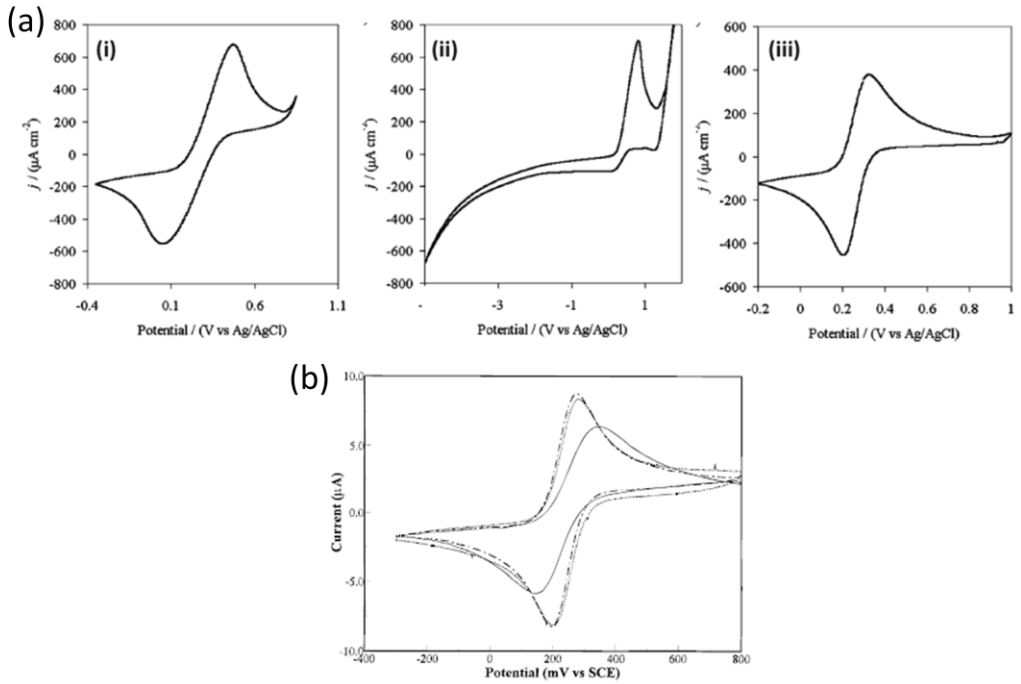

Figure 1.11: CVs for the oxidation of (a) 0.1 mM $Fe(CN)_6^{3-/4-}$ in 0.1 M KCl at a (i) moderately doped hydrogen-terminated, (ii)moderately doped oxygen-terminated and (iii) highly doped oxygen-terminated pBDD electrode with a scan rate of 20 mV s^{-1}.[132] (b) 10 mM $Fe(CN)_6^{3-/4-}$ in 1 M KCl plus 0.5 M phosphate buffer at a highly

doped as-grown hydrogen-terminated (dashed line) and anodically oxygen-terminated (solid line) pBDD electrode at a scan rate of 100 mV s^{-1}.[111]

It has been reported by several groups that $Fe(CN)_6^{3-/4-}$ is relatively sensitive to pBDD surface termination,[73,96,111,133] as shown in Figure 1.11 (b) where pBDD on the edge of metallic conductivity (ca. x 10^{20} boron atoms cm^{-3}) gives more reversible voltammograms when hydrogen-terminated in comparison to anodically oxygen-terminated.[111] In this work the reversibility of $IrCl_6^{2-/3-}$ (ΔE_p = 60 mV) and $Ru(NH_3)_6^{3+/2+}$ (ΔE_p = 70 mV) is largely unchanged by the surface-termination of the electrode, therefore the difference in behaviour of $Fe(CN)_6^{3-/4-}$ can be interpreted as a chemical effect of the terminations and not due to surface conductivity from hydrogen-terminated surface. The increased ΔE_p and decrease in the peak currents indicate much slower electron transfer kinetics at oxygen-terminated diamond.[140] As mentioned previously, carbon-oxygen functionalities are formed upon anodic polarisation, which may cause site blocking or electrostatic interferences. Arguments for an electrostatic effect have focused on pH dependent behaviour,[76] however alternate highly charged anions i.e. $IrCl_6^{2-/3-}$ show no surface-termination dependence.[111] Instead it is suggested the $Fe(CN)_6^{3-/4-}$ is an inner-sphere mediator which benefits from specific hydrogen-terminated surface interactions for electron transfer. Further evidence for this argument is that the reversibility of other inner-sphere redox couples such as $Fe^{3+/2+}$ is improved upon oxygen-termination due to the catalytic effect of carbonyl groups.[139]

Doping concentration has been shown to have a major influence on the electrochemical behaviour of pBDD, especially the transition between semiconducting and metallic-like conductivity. Hydrogen-terminated semiconducting pBDD can display metallic-like qualities due to additional surface

conductivity, even for redox species with E^o within the band gap. However, this unstable surface conductivity can be removed via oxygen-termination of the diamond, which then exhibits semiconductor electrochemical behaviour. This oxidation process may also lower the energy of the semiconducting diamond valence band at the surface, making electron transfer with redox species even more energetically unfavourable. Caution must be taken when investigating surface termination effects with semiconducting pBDD, as a combination of both chemical and electronic effects may be observed. On the other hand, the electrochemical properties of metallic-like degenerately doped pBDD seem to be largely unaffected by the surface termination, unless the species is influenced by the chemical nature of the termination itself. Mediators with E^o at both positive and negative potentials have quasi/reversible behaviour, where the density of states required for fast electron transfer is provided by the high doping concentration. It is however, important to note that this density of states is still not as high as for a true metal and can therefore be challenged with high redox concentrations.

1.2.3 **Heterogeneity and Grain Boundaries**

The electrochemical properties of pBDD described above have been elucidated by carrying out measurements on a macroscale, employing CV and large electrodes with a typical area of 0.2 cm^2, which averages over the whole surface. However, as pBDD is a heterogeneous material, this is clearly not ideal for understanding the fundamental properties. Thus, there has been work, albeit limited, undertaken at the microscopic level to aid in a more detailed understanding of the behaviour of pBDD. Polycrystallinity means that different crystal orientations are present, which uptake boron at different rates during growth, producing grains of varying conductivity.[22,66]

Independent of conductivity, it is also thought that the crystal orientation itself may affect electrochemical behaviour.[104]

Electron transfer rate constants have been determined for several redox species at pBDD, however these have most often employed CV resulting in rate constants which are an average for the whole surface. The influence of grain boundaries on the electrochemical response has also been investigated. If sp^2 carbon is present, it was thought that it accumulated in grain boundaries resulting in highly conducting regions on the surface, responsible for the observed electrochemistry. Several groups have addressed these issues using high spatial resolution techniques such as electrogenerated chemiluminescence (ECL) and scanning electrochemical microscopy (SECM).[43,110,143,144]

Figure 1.12 (a) shows the ECL image of heavily doped (ca. 1.5×10^{21} boron atoms cm^{-3}) hydrogen-terminated pBDD at 1.2 V for the reaction of 300 µM $Ru(bpy)_3^{2+}$ and 0.1 M tripropylamine in 0.2 M phosphate buffer.[144] The intensities for (100) square faced growth sectors were found to be 50 % of those at the (111) triangular sectors. While the intensities of the (111) grains remained constant, independent of the applied potential, the (100) sector intensities increased linearly with applied potential, thus showing that a larger overpotential is needed to drive the reaction at this crystallographic orientation. Furthermore, SECM in substrate generation-tip collection (SG-TC) mode for the substrate production of $Ru(NH_3)_6^{2+}$ from $Ru(NH_3)_6^{3+}$ at a heavily doped (ca. 5×10^{20} boron atoms cm^{-3}) oxygen-terminated pBDD surface (Figure 1.12 (b)) showed heterogeneities, with some area presenting metallic-like behaviour.[43] The trench lines shown in red were due to laser

patterning. These were thought to represent the most heavily doped regions of the surface which are associated with grains of a certain crystallographic orientations e.g (111) and (100). The lower doped regions of the surface were also active towards $Ru(NH_3)_6^{3+}$ reduction, albeit at a reduced rate.

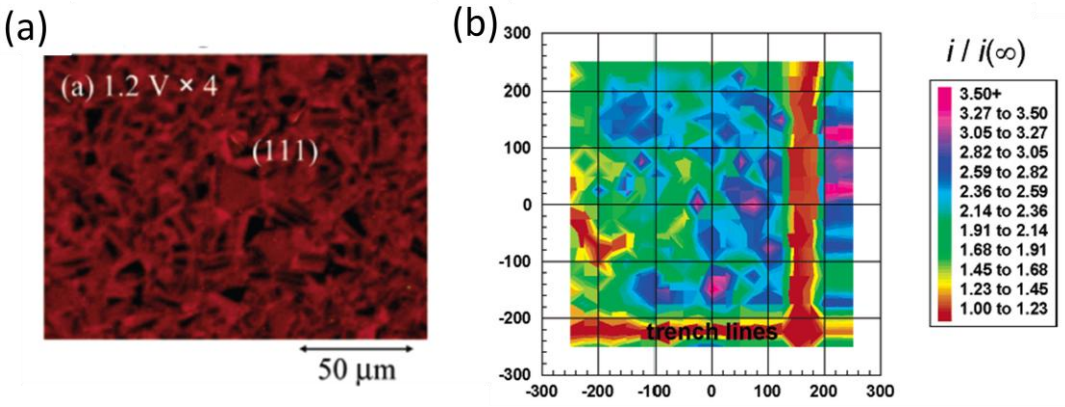

Figure 1.12: (a) ECL image of heavily doped pBDD centred on a (111) growth sector at 1.2 V in 0.2 M phosphate buffer containing 300 µM $Ru(bpy)_3^{2+}$ and 0.1 M TprA;[144] (b) 500 µm x 500 µm SECM tip collection scan for heavily doped pBDD held at -0.3 V in 5 mM $Ru(NH_3)_6^{3+/2+}$ in 0.1 M KCl.[43]

1.3. Electroanalytical Applications of pBDD

1.3.1 **pBDD Electrochemical Cells and Electrode Geometries**

In order to achieve high enough conductivity for reliable electrochemistry, the majority of diamond used in electroanalysis is typically highly doped with a dopant density > 10^{19} boron atoms cm^{-3} and polycrystalline in nature, unless otherwise stated. The electrochemical properties of pBDD have generated much interest especially in electroanalysis. Low background currents,[8,9] wide potential window,[6,7] stability in extreme conditions and aggressive media and resistance to fouling have resulted in an increasing number of analytical applications. [10-12] With this growing field, has come an increasing array of fabricated pBDD electrode geometries.

Initial electrochemical studies with pBDD were carried out on unpolished planar thin-films (ca. 5 μm thick) of diamond deposited on various substrates such as Si, Mo and W and were mainly concerned with the voltammetric characterisation of the pBDD itself.[116,145] Figure 1.13 (a) shows a typical electrochemical cell where the unpolished H-terminated thin-film diamond, as shown in the SEM image labelled b, is clamped to the bottom of a glass cell using an o-ring, giving a working electrode area of ca. 0.2 cm^2.[134] Electrical connection was made either through the bottom of the Si substrate or to the top of the diamond film using Ag paste. Electroanalysis of a wide range of eletroactive species has also been performed at pBDD electrodes. For example, voltammetric detection of L-cysteine in the micromolar concentration range was reported. The oxidation mechanism for L-cysteine was found to differ on pBDD compared to that on glassy carbon, resulting in a comparatively superior performance.[146] Anodic voltammetry has also been used to detect xanthine and its derivatives.[147] In order to improve upon the already low detection limits achievable with pBDD, the electrodes have also been used in conjunction with flow injection analysis (FIA) for amperometric detection of various chemicals.[148] Figure 1.13 (b) shows the design of a thin-layer flow cell FIA system where solution is flown from right to left over the pBDD electrode.[148] Inorganic molecules such as azide anions,[149] nitrite[150] and iodide[151] have been determined at pBDD via FIA with nanomolar detection limits. In addition electroactive organic molecules including catecholamines, chlorpromazine, polyamines,[152,153] histamine and serotonine[125], ascorbic acid and oxalic acid,[154] have also been detected using FIA with amperometric detection at pBDD.

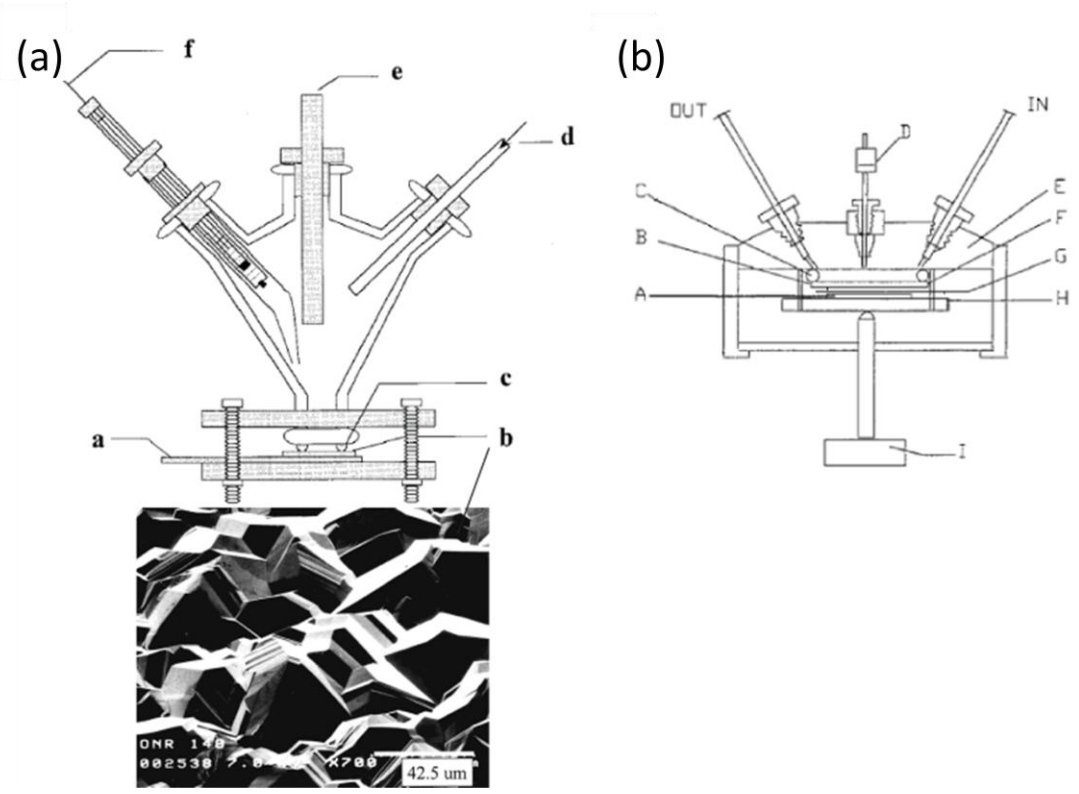

Figure 1.13: (a) Diagram of a single-compartment, glass electrochemical cell where a)is the metal current collecting plate, b) is the diamond film electrode, c) is the O-ring seal, d)is for nitrogen input, e) is the counter electrode, and f) reference electrode;[134] (b) diagram of the flow injection analysis system with thin-layer flow cell comprised of B) the pBDD electrode, C) neoprene rubber gasket, D) reference electrode, F) metal backing for contact and H) screw clamp for pressing the two pieces of the body together.[148]

More recently, free standing thick (ca. 500 µm thick) planar pBDD has become more common-place as an electrode material allowing more complicated electrochemical set-ups to be employed, due to easier manipulation of the diamond. For example, hydrogen-terminated pBDD has been used in a hydrodynamic flow-cell for the detection of chlorophenols.[155] Linear detection up to 20 µM was achieved due to the anti-fouling effect of pBDD, where organic molecules tend not to adsorb to the sp^3 carbon surface. Other forms of hydrodynamic electrodes have also been fabricated, such as a pBDD rotating ring-disc, where the anti-fouling and oxygen evolution overpotential of diamond were utilised to study the oxidation of methoxyphenol.[156] Similar results were also observed for phenols and naphthols. pBDD rotating discs

were also used in the detection of sulphates and peroxodisulfate.[157] An alternative method for increasing mass transport to the electrode surface and thus improving the analytical signal, has been the use of ultrasound.[158] This has been coupled successfully with pBDD electrodes as the surface remains undamaged even after subject to the harsh cavitation events in a sonoelectrochemistry experiment.

Ultramicroelectrodes (UMEs), where at least one dimension is in the range 0.1 to 100 µm, have been used extensively in electroanalytical chemistry in recent years due to their high diffusional flux, low interfacial capacitance and ability to be employed *in-vivo*. Considering the advantages of pBDD described previously, it is not surprising that several groups have investigated routes of production of pBDD UMEs. Most pBDD UMEs are fabricated via thin-film deposition on a sharpened metal wire as shown in Figure 1.14. Those shown in Figure 1.14 (a) were used directly with no insulation, however, using this method, the size and geometry of the diamond growth and hence the UME was difficult to control.[159] Microfiber electrodes have been prepared from etched tungsten wires, where pBDD deposition and subsequent sealing with glass or epoxy yielded electrode diameters of 10-75 µm.[160,161]

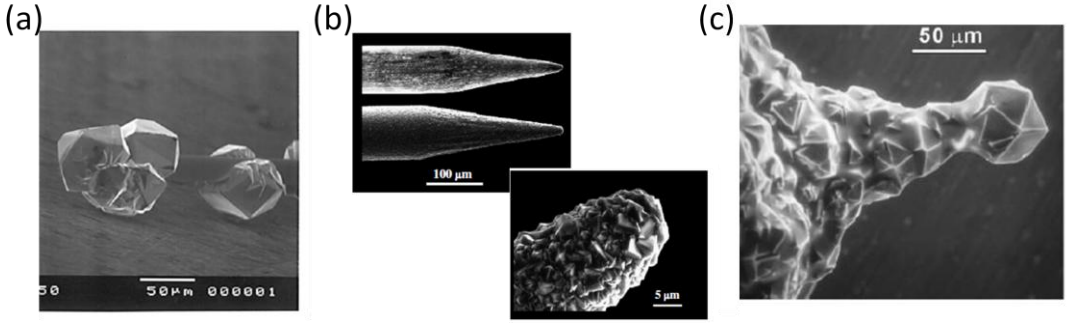

Figure 1.14: SEM images of (a) highly (ca. 10^{20} boron atoms cm^{-3}) BDD deposited onto etched tungsten wire giving a diameter of ca. 50 µm;[159] (b) highly (ca. 10^{19} to 10^{20} boron atoms cm^{-3}) BDD deposited onto sharpened platinum wire with a tip of 76 µm,[162] (c) BDD UME insulated with a thin layer of electrophoretic paint.[163]

Deposition of pBDD has also been carried-out on sharpened platinum wires, as shown in Figure 1.14 (bi) and at higher resolution in Figure 1.14 (bii).[162] Various forms of insulation have been tested, where coating with nail varnish or sealing with polypropylene produced mixed cylinder - cone geometries ca. 80 μm in diameter.[164] However, these insulating techniques gave inadequate reproducibility of the exposed electrode area, with polyimide coatings reducing the potential window of the electrode. Insulation to expose the tip only has been a problem due to the rough nature of the microcrystalline diamond.[165] Figure 1.14 (c) shows a FE-SEM image of a BDD electrode insulated with a layer of electrophoretic paint which has receded and exposed the sharp diamond edges.[163]

pBDD microelectrodes have been used in combination with capillary electrophoresis to analyse napthol,[164] chlorinated phenol solutions,[166] dopamine[167] and norepinephrine.[162] As well as *in-vivo* measurements of dopamine,[168] *in-vitro* detection has also been performed for serotonin,[169] adenosine[170] and norepinephrine[171], where pBDD sensitivity has been shown to have improvements over other carbon electrodes. Increased sensitivity by employing smaller UMEs i.e. < 25 μm has been explored, although again, there has been difficulty in reproducibly fabricating electrodes of these dimensions. While nanocrystalline boron-doped diamond deposition on sharpened wires has been shown to produce smaller electrode diameters, the higher sp^2 content of the nanocrystalline films means the electrodes have narrower potential windows and higher background currents than microcrystalline electrodes.[165,172]

Although microelectrodes give improved performance over macroelectrodes, for the reasons stated above, the current signal detected is significantly smaller. In order to increase the analytical signal, arrays of UMEs are typically used. Several groups have fabricated pBDD micro-arrays of various structures usually using different types of lithographic processing. Tsunozaki *et al*. fabricated an array of 30 µm diameter disc pBDD electrodes spaced 250 µm apart.[173] Photoresist patterning and etching of a silicon substrate enabled structured diamond deposition which was then insulated with a polyimide layer to form the disc electrodes. Similar microfabrication methods were used by Soh *et al*. to produce UME arrays of ca. 10 µm x 10 µm recessed squares with various spacings from 20 µm to 100 µm.[174] The same group also produced 2 µm x 80 µm UME-band arrays (Figure 1.15 (a)) for use as a dopamine sensor.[175,176]

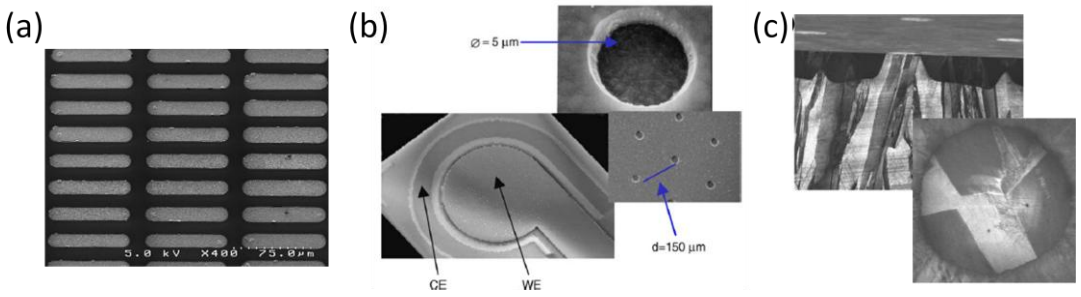

Figure 1.15: SEM images of (a) SiO_2 insulated pBDD micro-band array;[176] (b) Si_3N_4 insulated pBDD micro-disc array;[157] (c) all diamond micro-disc array.[177]

UME arrays have also been fabricated by the deposition of pBDD films and subsequent pattering of a Si_3N_4 top layer to reveal 5 µm diameter recessed discs, separated by 150 µm (Figure 1.15 (b)).[157] These were integrated with a diamond counter electrode and used in the detection of sulphate and peroxodisulfate. The ultimate BDD array structure is that which is coplanar and all-diamond as shown in Figure 1.15 (c).[177] Here, thick pBDD films were grown and column structures were cut into the film using laser micromachining techniques. Intrinsic (insulating)

diamond was then overgrown and polished back to reveal 50 μm diameter co-planar disc electrodes.[178] These all-diamond arrays have been used for the detection of 4-nitrophenol, manganese and sulphide in the low micromolar range.[179]

1.3.2 **Heavy Metal Detection**

Detection and monitoring of heavy metals is of great importance around the world, due to their toxicity and harmful effects. The most common electrochemical technique for the detection of metals is anodic stripping voltammetry (ASV), where metal ions are reduced onto the electrode surface and then stripped off with an oxidising potential sweep. Different forms of this technique are often used to enhance the current signal including square wave and differential pulse voltammetries.[180] Traditionally ASV has been performed with mercury electrodes, however increasing concern over the hazardous properties of mercury itself has prompted a move away from this electrode material. pBDD has been touted as a viable replacement, with several qualities making it ideal for trace metal analysis.[181] These include a large overpotential for hydrogen evolution, a large over potential for oxygen reduction, no known metal complexes and stability at extreme potentials. As such there are a large number of reports on the electrochemical stripping response of metals on pBDD. As shown in Figure 1.16 (a), the differential pulse - ASV (DP-ASV) response for Pb^{2+}, Zn^{2+}, Cd^{2+}, Cu^{2+}, Ag^{+} on pBDD has been reported with detection limits of 5 ppb, 50 ppb, 1 ppb, 10 ppb and 1 ppb respectively.[181,182] Methods of increasing mass transport to the electrode during the accumulation step have also been investigated, such as optimised insonation which decreased the detection limit of cadmium by an order of magnitude to 1 nM (Figure 1.16 (b)).[183] Microwave enhanced square wave anodic stripping voltammtry (SWASV) has been

used to detect lead in digested river sediment finding good agreement with other analytical techniques.[184] The effect of temperature on the deposition of lead at pBDD surfaces has also been investigated.[185] Increased temperature was reported to aid in the reduction of Pb^{2+} at the surface with larger nuclei being initially formed, thus allowing lower limits of detection. The influences of diamond grain size and electrolyte composition have also been explored.[186] [187] [188]

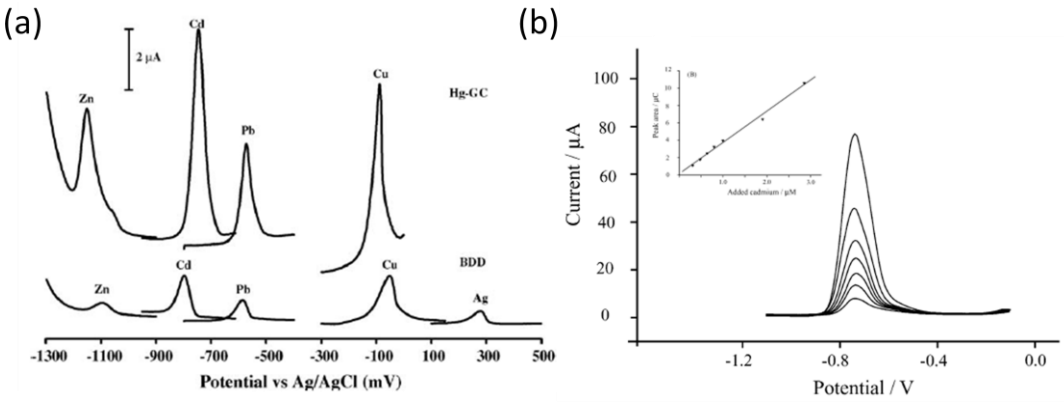

Figure 1.16: (a) Overlaid individual stripping voltammetric curves for 100 ppb solutions of each metal in 0.1 M acetate buffer at Hg-GC and pBDD electrodes;[181] (b) square wave anodic stripping voltammetric curves for increasing additions of cadmium in 0.5 M acetate buffer at an insonated pBDD electrode, with the insert showing the resulting calibration plot.[183]

The above studies show that pBDD can detect trace amounts of single metal species in solution, however for real world applications the simultaneous detection of several metals is necessary. Investigations have thus focused on how the metal-metal interactions on the pBDD surface effect deposition and stripping behaviour of individual species. Prado *et al.* highlighted the difficulties of independent quantification in mixed solutions by showing that copper increases the relative amount of lead deposited by aiding nucleation, whereas lead hinders the deposition of copper, both effecting the current response.[189] Assisted nucleation has also been seen for silver deposition at lead pre-treated pBDD electrodes, most probably due to the lowering of the initial nucleation energy barrier.[190] Complications also arise

during stripping, such as that reported by Manivannan *et al.* where cadmium deposited on lead is removed at lead oxidising potentials.[191] Foord and co-workers report the broadening of stripping peaks due to metal-metal interactions and stressed the effect on current magnitude that co-deposition can have, an effect which is dependent on the metal combinations present.[190,192]

1.3.3 **Functionalisation of pBDD Electrodes**

As a conducting material with low background currents, pBDD is an ideal support substrate for catalytic materials,[193] thus extending its ability to detect a wider range of species. Functionalisation of diamond has been carried-out through various methods including electrochemical deposition,[193-197] ion implantation,[198-200] chemical modification[201,202] and physical patterning.[203] As a result of their small size, leading to enhanced flux and increased catalytic activity, metal nanoparticles are commonly used to decorate electrode surfaces in order to catalyse reactions.[204] Using electrochemical deposition, the number density and size of nanoparticles can be optimised by varying the deposition potential, time, metal concentration and electrolyte. Obviously for a heterogeneous surface, such as pBDD, the varying conductivity of different grains needs to also be taken into account. Electrochemical deposition and plating of a variety of metals has been performed on pBDD including copper,[205] palladium (Figure 1.17 (a)),[206] platinum,[207] silver and gold.[208] These have been used to detect nitrate, hydrazine, dissolved oxygen, hydrogen peroxide and arsenic respectively. However, due to the heterogeneous electrochemical nature of the pBDD surface, deposition of the particles on the diamond surface is not always homogeneous. Different metal deposition behaviour at different growth sectors has been reported, as shown in Figure 1.17 (b).[178,209] An alternate method of pBDD

modification with metal is by ion implantation, as in the case of Ni^{2+} and Cu^{2+} for the oxidation of glucose.[198,210] Platinum implantation into pBDD was also employed for stable hydrogen peroxide sensing, with a detection limit of 30 nM.[199]

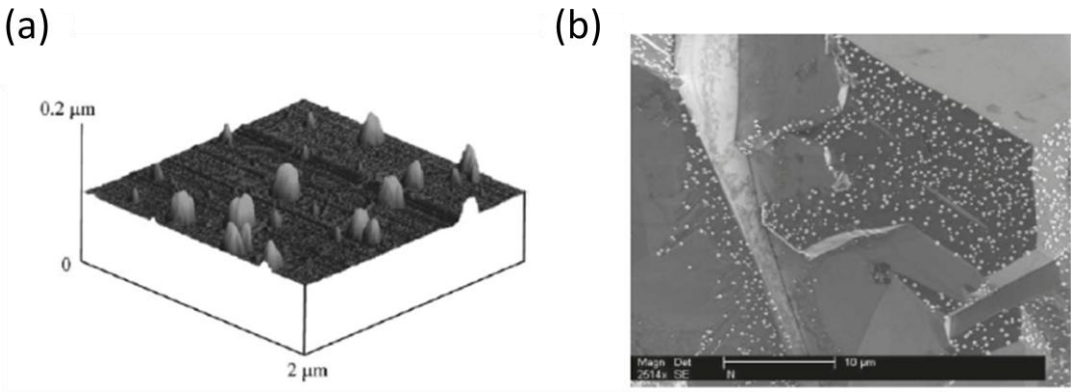

Figure 1.17: (a) AFM image of palladium particles electrochemically deposited onto pBDD electrode;[206] (b) SEM image of facet selective electrochemical deposition of platinum particles onto pBDD.[211]

The chlorination and amination of the initially hydrogen-terminated diamond surface via photochemistry has been shown on nanocrystalline diamond.[212,213] Chemical modification of the diamond surface has been attempted with a variety of groups containing a terminal amine e.g. 3-aminopropyltriethoxysilane and 4-nitrobenzenediazonium tetrafluoroborate.[201] Typically the surface is coated with a view to immobilising biological molecules such as enzymes and DNA onto the surface for biosensor applications with low detection limits.[214] Adsorbed molecules can also be immobilised on the diamond surface, such as glucose oxidase, which was used in combination with platinum nanoparticles to detect glucose.[215] Electropolymerized thin films including tyramine and pyrrole-1-propionic acid, have also been used in biosensing in order to screen out electroactive interferences.[216]

1.4. AIMS AND OBJECTIVES

The electrical and electrochemical characterisation of BDD discussed above, highlights the difference in behaviour that can be observed for different samples of CVD grown BDD depending on the doping concentration, surface termination and quality. Understanding the impact of these factors is of great importance when interpretating data. Furthermore, the effect of electrode fabrication and electrochemical set-up on the results observed should be taken into account and made negligible wherever possible. Furthermore, more robust BDD electrode architectures are needed for ease and reliability. Chapter 3 thus details the fabrication of user-friendly 1 mm diameter disc pBDD electrodes. The heavily doped (ca. 5 x 10^{20} boron atoms cm^{-3}) oxygen-terminated pBDD is extensively characterised using Raman spectroscopy, FE-SEM and AFM. Voltammetric measurements are also used to characterise the electrode.

In Chapter 4 the fabricated pBDD electrodes are used as a conducting support for the controlled electrodeposition of catalytic platinum nanoparticles, for application in dissolved oxygen sensing. The platinum electrodeposition procedure was optimised in order to provide the most sensitive electrochemical response towards O_2 reduction, in aqueous solutions of varying pH. In Chapter 5 the pBDD electrode is again used as a conducting support, but in this case for the electrodeposition of nickel hydroxide nanoparticles. The relationship between nanoparticles size and catalytic activity towards glucose oxidation and methanol/ethanol oxidation was investigated. In Chapter 6, the low background currents and wide potential window of the fabricated pBDD electrodes are utilised for the detection of sub ppb levels of lead via differential pulse anodic stripping voltammetry. The deposition and

stripping behaviour of lead at the diamond surface was studied using AFM and FE-SEM in order to understand and correctly interpret the electrochemical responses observed and optimise the performance of the electrode in real world analysis. Chapter 7, focuses on the use of laser micromachining technology to fabricate all-diamond electrode devices. All-diamond ring electrodes are characterised and used in conjunction with tubular flow for voltammetric experiments. All-diamond dual band electrodes are also presented and employed for conductivity measurements. Finally Chapter 8 discusses further work and conclusions.

1.5. REFERENCES

(1) May, P. W. *Philos. Trans. R. Soc. London, A* **2000**, *358*, 473.
(2) Godfried, H. P.; Coe, S. E.; Hall, C. E.; Pickles, C. S. J.; Sussmann, R. S.; Tang, X.; van der Voorden, W. K. L. In *Use of CVD diamond in high-power CO2 lasers and laser diode arrays*; SPIE, Bellingham: 2000.
(3) Wallny, R. S.; Cindro, V.; Dolenc, I.; Frais-Kolbl, H.; Mikuz, M.; Niegl, M.; Pernegger, H.; Trischuk, W.; Weilhammer, P.; Zavrtanik, M.; Mathes, M.; Barbero; Huegging, F.; Kagan, H.; Meuser, S.; Velthuis, J.; Wermes, N.; Dong, P.; Eusebi, R.; Schrupp, C.; Sfyrla, A.; Tesarek, R. J.; Wallny, R.; Bell, A.; Deboer, W.; Fugeri, A.; Gray, R.; Gamatsch, A.; Hall-Wilton, R.; Macpherson, A.; Marlow, D.; Ryjof, V.; Rodrigues, N.; Stickland, D.; Stone, R.; Schnetzer, S. *Nucl. Instrum. Methods Phys. Res., Sect. A* **2007**, *582*, 824.
(4) www.e6.com.
(5) Kraft, A. *Int. J. Electrochem. Sci.* **2007**, *2*, 355.
(6) Panizza, M.; Cerisola, G. *Electrochim. Acta* **2005**, *51*, 191.
(7) Martin, H. B.; Argoitia, A.; Landau, U.; Anderson, A. B.; Angus, J. C. *J. Electrochem. Soc.* **1996**, *143*, L133.
(8) Pleskov, Y. V. *Russ. J. Electrochem.* **2002**, *38*, 1275.
(9) Yano, T.; Tryk, D. A.; Hashimoto, K.; Fujishima, A. *J. Electrochem. Soc.* **1998**, *145*, 1870.
(10) Xu, J. S.; Granger, M. C.; Chen, Q. Y.; Strojek, J. W.; Lister, T. E.; Swain, G. M. *Anal. Chem.* **1997**, *69*, A591.
(11) Sarada, B. V.; Rao, T. N.; Tryk, D. A.; Fujishima, A. *Chem. Lett.* **1999**, 1213.
(12) Guell, A. G.; Meadows, K. E.; Unwin, P. R.; Macpherson, J. V. *Phys. Chem. Chem. Phys.* **2010**, *12*, 10108.
(13) Compton, R. G.; Foord, J. S.; Marken, F. *Electroanalysis* **2003**, *15*, 1349.
(14) Bundy, F. P.; Hall, H. T.; Strong, H. M.; Wentorf, R. H. *Nature* **1955**, *176*, 51.
(15) Bundy, F. P. *J. Chem. Phys.* **1963**, *38*, 631.
(16) Martineau, P. M.; Gaukroger, M. P.; Guy, K. B.; Lawson, S. C.; Twitchen, D. J.; Friel, I.; Hansen, J. O.; Summerton, G. C.; Addison, T. P. G.; Burns, R. *J. Phys.: Condens. Matter* **2009**, *21*, 1.
(17) Angus, J. C.; Hayman, C. C. *Science* **1988**, *241*, 913.
(18) Eversole, W. G.; Kenmore, N. Y. 1958; Vol. US Patent 3030187.
(19) Derjaguin, B. V.; Fedoseev, D. V.; Lukyanovich, V. M.; Spitzin, B. V.; Ryabov, V. A.; Lavrentyev, A. V. *J. Cryst. Growth* **1968**, *2*, 380.
(20) Angus, J. C.; Will, H. A.; Stanko, W. S. *J. Appl. Phys.* **1968**, *39*, 2915.
(21) Yarbrough, W. A.; Messier, R. *Science* **1990**, *247*, 688.
(22) Spitsyn, B. V.; Bouilov, L. L.; Derjaguin, B. V. *J. Cryst. Growth* **1981**, *52*, 219.
(23) Matsumoto, S.; Sato, Y.; Tsutsumi, M.; Setaka, N. *J. Mater. Sci.* **1982**, *17*, 3106.
(24) Kamo, M.; Sato, Y.; Matsumoto, S.; Setaka, N. *J. Cryst. Growth* **1983**, *62*, 642.
(25) Celii, F. G.; Butler, J. E. *Annu. Rev. Phys. Chem.* **1991**, *42*, 643.
(26) Varnin, V. P.; Laptev, V. A.; Ralchenko, V. G. *Inorganic Materials* **2006**, *42*, S1.
(27) Das, D. S., R. N *Int. Mater. Rev.* **2007**, *52*, 29.
(28) http://www.sekicvdsolutions.com/.
(29) Piazza, F.; Gonzalez, J. A.; Velazquez, R.; De Jesus, J.; Rosario, S. A.; Morell, G. *Diamond Relat. Mater.* **2006**, *15*, 109.
(30) Herlinger, J. *Thin Solid Films* **2006**, *501*, 65.
(31) Sevillano, E.; Williams, B. *Diamond Film Technol.* **1998**, *8*, 73.
(32) Ashfold, M. N. R.; May, P. W.; Petherbridge, J. R.; Rosser, K. N.; Smith, J. A.; Mankelevich, Y. A.; Suetin, N. V. *Phys. Chem. Chem. Phys.* **2001**, *3*, 3471.
(33) Butler, J. E.; Woodin, R. L.; Brown, L. M.; Fallon, P. *Philos. Trans. R. Soc. London, A* **1993**, *342*, 209.

(34) Angus, J. C.; Argoitia, A.; Gat, R.; Li, Z.; Sunkara, M.; Wang, L.; Wang, Y. *Philos. Trans. R. Soc. London, A* **1993**, *342*, 195.
(35) Ma, J.; Richley, J. C.; Davies, D. R. W.; Ashfold, M. N. R.; Mankelevich, Y. A. *J. Phys. Chem. A* **2010**, *114*, 10076.
(36) Ma, J.; Richley, J. C.; Ashfold, M. N. R.; Mankelevich, Y. A. *J. Appl. Phys.* **2008**, *104*, 103305.
(37) Nebel, C. E.; Ristein, J. *Thin-Film Diamond I*; Elsevier Academic Press, 2003; Vol. 76.
(38) Sze, S. M. *Proceedings of the IEEE* **1981**, *69*, 1121.
(39) Collins, A. T.; Williams, A. W. *J. Phys. C.* **1971**, *4*, 1789.
(40) Chrenko, R. M. *Phys. Rev. B* **1973**, *7*, 4560.
(41) Shiomi, H.; Nishibayashi, Y.; Fujimori, N. *Jpn. J. Appl. Phys., Part 1* **1991**, *30*, 1363.
(42) Stoner, B. R.; Kao, C. T.; Malta, D. M.; Glass, R. C. *Appl. Phys. Lett.* **1993**, *62*, 2347.
(43) Wilson, N. R.; Clewes, S. L.; Newton, M. E.; Unwin, P. R.; Macpherson, J. V. *J. Phys. Chem. B* **2006**, *110*, 5639.
(44) Luong, J. H. T.; Male, K. B.; Glennon, J. D. *Analyst* **2010**, *135*, 3008.
(45) Wang, S.; Swope, V. M.; Bulter, J. E.; Feygelson, T.; Swain, G. M. *Diamond Relat. Mater.* **2009**, *18*, 669.
(46) Lagrange, J. P.; Deneuville, A.; Gheeraert, E. *Diamond Relat. Mater.* **1998**, *7*, 1390.
(47) Gheeraert, E.; Deneuville, A.; Mambou, J. *Diamond Relat. Mater.* **1998**, *7*, 1509.
(48) Inushima, T.; Matsushita, T.; Ohya, S.; Shiomi, H. *Diamond Relat. Mater.* **2000**, *9*, 1066.
(49) Williams, A. W.; Lightowl.Ec; Collins, A. T. *J. Phys. C.* **1970**, *3*, 1727.
(50) Boeri, L.; Kortus, J.; Andersen, O. K. *Phys. Rev. Lett.* **2004**, *93*.
(51) Deneuville, A.; Baron, C.; Ghodbane, S.; Agnès, C. *Diamond Relat. Mater.* **2007**, *16*, 915.
(52) Nishimura, K.; Das, K.; Glass, J. T. *J. Appl. Phys.* **1991**, *69*, 3142.
(53) Orton, J. W.; Powell, M. J. *Rep. Prog. Phys.* **1980**, *43*, 1263.
(54) Huang, J. T.; Guo, W. H.; Hwang, J.; Chang, H. *Appl. Phys. Lett.* **1996**, *68*, 3784.
(55) Masood, A.; Aslam, M.; Tamor, M. A.; Potter, T. J. *Appl. Phys. Lett.* **1992**, *61*, 1832.
(56) Isberg, J.; Hammersberg, J.; Johansson, E.; Wikström, T.; Twitchen, D. J.; Whitehead, A. J.; Coe, S. E.; Scarsbrook, G. A. *Science* **2002**, *297*, 1670.
(57) Zhang, R. J.; Lee, S. T.; Lam, Y. W. *Diamond Relat. Mater.* **1996**, *5*, 1288.
(58) Silva, F.; Achard, J.; Bonnin, X.; Brinza, O.; Michau, A.; Secroun, A.; De Corte, K.; Felton, S.; Newton, M.; Gicquel, A. *Diamond Relat. Mater.* **2008**, *17*, 1067.
(59) Barbosa, D. C.; Almeida, F. A.; Silva, R. F.; Ferreira, N. G.; Trava-Airoldi, V. J.; Corat, E. J. *Diamond Relat. Mater.* **2009**, *18*, 1283.
(60) Angus, J. C.; Martin, H. B.; Landau, U.; Evstefeeva, Y. E.; Miller, B.; Vinokur, N. *New Diamond Front. Carbon Technol.* **1999**, *9*, 175.
(61) Lee, B. J.; Ahn, B. T.; Baik, Y. J. *Diamond Relat. Mater.* **1999**, *8*, 251.
(62) Spicka, H.; Griesser, M.; Hutter, H.; Grasserbauer, M.; Bohr, S.; Haubner, R.; Lux, B. *Diamond Relat. Mater.* **1996**, *5*, 383.
(63) Gheeraert, E.; Deneuville, A.; Mambou, J. *Carbon* **1999**, *37*, 107.
(64) Locher, R.; Wagner, J.; Fuchs, F.; Wild, C.; Hiesinger, P.; Gonon, P.; Koidl, P. *Mater. Sci. Eng., B* **1995**, *29*, 211.
(65) Ushizawa, K.; Watanabe, K.; Ando, T.; Sakaguchi, I.; Nishitani-Gamo, M.; Sato, Y.; Kanda, H. *Diamond Relat. Mater.* **1998**, *7*, 1719.
(66) Levy-Clement, C.; Ndao, N. A.; Katty, A.; Bernard, M.; Deneuville, A.; Comninellis, C.; Fujishima, A. *Diamond Relat. Mater.* **2003**, *12*, 606.
(67) Malta, D. M.; Vonwindheim, J. A.; Wynands, H. A.; Fox, B. A. *J. Appl. Phys.* **1995**, *77*, 1536.

(68) Barbu, B. *Electrical and Electrochemical Characterisation of Single Crystal Diamond* (PhD Thesis, **2010**).
(69) Salazar-Banda, G. R.; Andrade, L. S.; Nascente, P. A. P.; Pizani, P. S.; Rocha, R. C.; Avaca, L. A. *Electrochim. Acta* **2006**, *51*, 4612.
(70) Ghodbane, S.; Ballutaud, D.; Omnes, F.; Agnes, C. *Diamond Relat. Mater.* **2010**, *19*, 630.
(71) Pehrsson, P. E.; Long, J. P.; Marchywka, M. J.; Butler, J. E. *Appl. Phys. Lett.* **1995**, *67*, 3414.
(72) Liu, F. B.; Wang, J. D.; Liu, B.; Li, X. M.; Chen, D. R. *Diamond Relat. Mater.* **2007**, *16*, 454.
(73) Boukherroub, R.; Wallart, X.; Szunerits, S.; Marcus, B.; Bouvier, P.; Mermoux, M. *Electrochem. Commun.* **2005**, *7*, 937.
(74) Girard, H. A.; Simon, N.; Ballutaud, D.; de La Rochefoucauld, E.; Etcheberry, A. *Diamond Relat. Mater.* **2007**, *16*, 888.
(75) Ostrovskaya, L.; Perevertailo, V.; Ralchenko, V.; Dementjev, A.; Loginova, O. *Diamond Relat. Mater.* **2002**, *11*, 845.
(76) Yagi, I.; Notsu, H.; Kondo, T.; Tryk, D. A.; Fujishima, A. *J. Electroanal. Chem.* **1999**, *473*, 173.
(77) Kaibara, Y.; Sugata, K.; Tachiki, M.; Umezawa, H.; Kawarada, H. *Diamond Relat. Mater.* **2003**, *12*, 560.
(78) Rao, T. N.; Tryk, D. A.; Hashimoto, K.; Fujishima, A. *J. Electrochem. Soc.* **1999**, *146*, 680.
(79) Shirafuji, J.; Sakamoto, Y.; Furukawa, A.; Shigeta, H.; Sugino, T. *Diamond Relat. Mater.* **1995**, *4*, 984.
(80) Thomas, R. E.; Rudder, R. A.; Markunas, R. J. *J. Vac. Sci. Technol., A* **1992**, *10*, 2451.
(81) Nebel, C. E.; Ristein, J. *Thin-Film Diamond II*; Elsevier Academic Press, 2004; Vol. 77.
(82) Wang, M.; Simon, N.; Decorse-Pascanut, C.; Bouttemy, M.; Etcheberry, A.; Li, M. S.; Boukherroub, R.; Szunerits, S. *Electrochim. Acta* **2009**, *54*, 5818.
(83) Girard, H. A.; Simon, N.; Ballutaud, D.; Etcheberry, A. *C. R. Chim.* **2008**, *11*, 1010.
(84) Hoffmann, R.; Kriele, A.; Obloh, H.; Hees, J.; Wolfer, M.; Smirnov, W.; Yang, N.; Nebel, C. E. *Appl. Phys. Lett.* **2010**, *97*, 052103.
(85) Landstrass, M. I.; Ravi, K. V. *Appl. Phys. Lett.* **1989**, *55*, 975.
(86) Landstrass, M. I.; Ravi, K. V. *Appl. Phys. Lett.* **1989**, *55*, 1391.
(87) Kawarada, H. *Surf. Sci. Rep.* **1996**, *26*, 205.
(88) Denisenko, A.; Aleksov, A.; Pribil, A.; Gluche, P.; Ebert, W.; Kohn, E. *Diamond Relat. Mater.* **2000**, *9*, 1138.
(89) Hayashi, K.; Yamanaka, S.; Watanabe, H.; Sekiguchi, T.; Okushi, H.; Kajimura, K. *J. Appl. Phys.* **1997**, *81*, 744.
(90) Maier, F.; Riedel, M.; Mantel, B.; Ristein, J.; Ley, L. *Phys. Rev. Lett.* **2000**, *85*, 3472.
(91) Ristein, J. *Appl. Phys. A: Mater. Sci. Process.* **2006**, *82*, 377.
(92) Garrido, J. A.; Nebel, C. E.; Stutzmann, M.; Snidero, E.; Bergonzo, P. *Appl. Phys. Lett.* **2002**, *81*, 637.
(93) Himpsel, F. J.; Knapp, J. A.; Vanvechten, J. A.; Eastman, D. E. *Phys. Rev. B* **1979**, *20*, 624.
(94) Maier, F.; Ristein, J.; Ley, L. *Phys. Rev. B* **2001**, *64*, art. no.
(95) Alehashem, S.; Chambers, F.; Strojek, J. W.; Swain, G. M.; Ramesham, R. *Anal. Chem.* **1995**, *67*, 2812.
(96) Actis, P.; Denoyelle, A.; Boukherroub, R.; Szunerits, S. *Electrochem. Commun.* **2008**, *10*, 402.
(97) Coe, S. E.; Sussmann, R. S. *Diamond Relat. Mater.* **2000**, *9*, 1726.
(98) Deneuville, A.; Gheeraert, E. In *Eurodiamond '96*; Editrice Compositori: Bologna, 1996.

(99) Wang, J.; Swain, G. M.; Mermoux, M.; Lucazeau, G.; Zak, J.; Strojek, J. W. *New Diamond Front. Carbon Technol.* **1999**, *9*, 317.
(100) Bernholc, J.; Antonelli, A.; Delsole, T. M.; Baryam, Y.; Pantelides, S. T. *Phys. Rev. Lett.* **1988**, *61*, 2689.
(101) Pruvost, F.; Bustarret, E.; Deneuville, A. *Diamond Relat. Mater.* **2000**, *9*, 295.
(102) Bernard, M. *Diamond Relat. Mater.* **2004**, *13*, 282.
(103) Werner, M.; Job, R.; Zaitzev, A.; Fahrner, W. R.; Seifert, W.; Johnston, C.; Chalker, P. R. *Phys. Status Solidi A* **1996**, *154*, 385.
(104) Fujishima, A.; Einaga, Y.; Rao, T. N.; Tryk, D. A. *Diamond Electrochemistry*; Elsevier, Amsterdam and BKC INC., Tokyo, 2005.
(105) Kobashi, K.; Nishimura, K.; Kawate, Y.; Horiuchi, T. *Phys. Rev. B* **1988**, *38*, 4067.
(106) Knight, D. S.; White, W. B. *J. Mater. Res.* **1989**, *4*, 385.
(107) Bachmann, P. K.; Leers, D.; Lydtin, H. *Diamond Relat. Mater.* **1991**, *1*, 1.
(108) Gruen, D. M. *Annu. Rev. Mater. Sci.* **1999**, *29*, 211.
(109) Hian, L. C.; Grehan, K. J.; Compton, R. G.; Foord, J. S.; Marken, F. *J. Electrochem. Soc.* **2003**, *150*, E59.
(110) Holt, K. B.; Bard, A. J.; Show, Y.; Swain, G. M. *J. Phys. Chem. B* **2004**, *108*, 15117.
(111) Granger, M. C.; Swain, G. M. *J. Electrochem. Soc.* **1999**, *146*, 4551.
(112) Iwaki, M.; Sato, S.; Takahashi, K.; Sakairi, H. *Nucl. Instrum. Methods Phys. Res., Sect. A* **1983**, *209*, 1129.
(113) Pleskov, Y. V.; Sakharova, A. Y.; Krotova, M. D.; Bouilov, L. L.; Spitsyn, B. V. *J. Electroanal. Chem.* **1987**, *228*, 19.
(114) Patel, K.; Hashimoto, K.; Fujishima, A. *Denki Kagaku* **1992**, *60*, 659.
(115) Tenne, R.; Patel, K.; Hashimoto, K.; Fujishima, A. *J. Electroanal. Chem.* **1993**, *347*, 409.
(116) Swain, G. M.; Ramesham, R. *Anal. Chem.* **1993**, *65*, 345.
(117) Swain, G. M. *Adv. Mater. (Weinheim, Ger.)* **1994**, *6*, 388.
(118) Argoitia, A.; Martin, H. B.; Rozak, E. J.; Landau, U.; Angus, J. C. *Electrochemical studies of boron-doped diamond electrodes*; Materials Research Soc: Pittsburgh, 1996.
(119) Suffredini, H. B.; Machado, S. A. S.; Avaca, L. A. *J. Braz. Chem. Soc.* **2004**, *15*, 16.
(120) Tryk, D. A.; Tsunozaki, K.; Rao, T. N.; Fujishima, A. *Diamond Relat. Mater.* **2001**, *10*, 1804.
(121) Yano, T.; Popa, E.; Tryk, D. A.; Hashimoto, K.; Fujishima, A. *J. Electrochem. Soc.* **1999**, *146*, 1081.
(122) Bennett, J. A.; Wang, J. A.; Show, Y.; Swain, G. M. *J. Electrochem. Soc.* **2004**, *151*, E306.
(123) Levy-Clement, C.; Zenia, F.; Ndao, N. A.; Deneuville, A. *New Diamond Front. Carbon Technol.* **1999**, *9*, 189.
(124) Michaud, P. A.; Mahe, E.; Haenni, W.; Perret, A.; Comninellis, C. *Electrochem. Solid-State Lett.* **2000**, *3*, 77.
(125) Sarada, B. V.; Rao, T. N.; Tryk, D. A.; Fujishima, A. *Anal. Chem.* **2000**, *72*, 1632.
(126) Trouillon, R.; O'Hare, D. *Electrochim. Acta* **2010**, *55*, 6586.
(127) Shin, D.; Tryk, D. A.; Fujishima, A.; Merkoci, A.; Wang, J. *Electroanalysis* **2005**, *17*, 305.
(128) Rao, T. N.; Yagi, I.; Miwa, T.; Tryk, D. A.; Fujishima, A. *Anal. Chem.* **1999**, *71*, 2506.
(129) Modestov, A. D.; Evstefeeva, Y. E.; Pleskov, Y. V.; Mazin, V. M.; Varnin, V. P.; Teremetskaya, I. G. *J. Electroanal. Chem.* **1997**, *431*, 211.
(130) Vinokur, N.; Miller, B.; Avyigal, Y.; Kalish, R. *J. Electrochem. Soc.* **1996**, *143*, L238.
(131) Pleskov, Y. V.; Mazin, V. M.; Evstefeeva, Y. E.; Varnin, V. P.; Teremetskaya, I. G.; Laptev, V. A. *Electrochem. Solid-State Lett.* **2000**, *3*, 141.
(132) Latto, M. N.; Pastor-Moreno, G.; Riley, D. J. *Electroanalysis* **2004**, *16*, 434.

(133) Marken, F.; Paddon, C. A.; Asogan, D. *Electrochem. Commun.* **2002**, *4*, 62.
(134) Granger, M. C.; Witek, M.; Xu, J. S.; Wang, J.; Hupert, M.; Hanks, A.; Koppang, M. D.; Butler, J. E.; Lucazeau, G.; Mermoux, M.; Strojek, J. W.; Swain, G. M. *Anal. Chem.* **2000**, *72*, 3793.
(135) Goeting, C. H.; Foord, J. S.; Marken, F.; Compton, R. G. *Diamond Relat. Mater.* **1999**, *8*, 824.
(136) Chen, P. H.; Fryling, M. A.; McCreery, R. L. *Anal. Chem.* **1995**, *67*, 3115.
(137) Ranganathan, S.; Kuo, T. C.; McCreery, R. L. *Anal. Chem.* **1999**, *71*, 3574.
(138) Becker, D.; Juttner, K. *J. Appl. Electrochem.* **2003**, *33*, 959.
(139) Fischer, A. E.; Show, Y.; Swain, G. M. *Anal. Chem.* **2004**, *76*, 2553.
(140) Ferro, S.; De Battisti, A. *Electrochim. Acta* **2002**, *47*, 1641.
(141) Ramesham, R.; Rose, M. F. *Diamond Relat. Mater.* **1997**, *6*, 17.
(142) Simon, N.; Girard, H.; Ballutaud, D.; Ghodbane, S.; Deneuville, A.; Herlem, M.; Etcheberry, A. *Diamond Relat. Mater.* **2005**, *14*, 1179.
(143) Neufeld, A. K.; O'Mullane, A. P. *J. Solid State Electrochem.* **2006**, *10*, 808.
(144) Honda, K.; Noda, T.; Yoshimura, A.; Nakagawa, K.; Fujishima, A. *J. Phys. Chem. B* **2004**, *108*, 16117.
(145) Ramesham, R.; Roppel, T.; Ellis, C.; Loo, B. H. *J. Electrochem. Soc.* **1991**, *138*, 2981.
(146) Spataru, N.; Sarada, B. V.; Popa, E.; Tryk, D. A.; Fujishima, A. *Anal. Chem.* **2001**, *73*, 514.
(147) Spataru, N.; Sarada, B. V.; Tryk, D. A.; Fujishima, A. *Electroanalysis* **2002**, *14*, 721.
(148) Jolley, S.; Koppang, M.; Jackson, T.; Swain, G. M. *Anal. Chem.* **1997**, *69*, 4099.
(149) Xu, J. Z.; Swain, G. M. *Anal. Chem.* **1998**, *70*, 1502.
(150) Granger, M. C.; Xu, J. S.; Strojek, J. W.; Swain, G. M. *Anal. Chim. Acta* **1999**, *397*, 145.
(151) Chailapakul, O.; Amatatongchai, M.; Wilairat, P.; Grudpan, K.; Nacapricha, D. *Talanta* **2004**, *64*, 1253.
(152) Koppang, M. D.; Witek, M.; Blau, J.; Swain, G. M. *Anal. Chem.* **1999**, *71*, 1188.
(153) Witek, M. A.; Swain, G. M. *Anal. Chim. Acta* **2001**, *440*, 119.
(154) Ivandini, T. A.; Rao, T. N.; Fujishima, A.; Einaga, Y. *Anal. Chem.* **2006**, *78*, 3467.
(155) Prado, C.; Murcott, G. G.; Marken, F.; Foord, J. S.; Compton, R. G. *Electroanalysis* **2002**, *14*, 975.
(156) Sopchak, D.; Miller, B.; Avyigal, Y.; Kalish, R. *J. Electroanal. Chem.* **2002**, *538*, 39.
(157) Provent, C.; Haenni, W.; Santoli, E.; Rychen, P. *Electrochim. Acta* **2004**, *49*, 3737.
(158) Saterlay, A. J.; Foord, J. S.; Compton, R. G. *Electroanalysis* **2001**, *13*, 1065.
(159) Sarada, B. V.; Rao, T. N.; Tryk, D. A.; Fujishima, A. *J. Electrochem. Soc.* **1999**, *146*, 1469.
(160) Cooper, J. B.; Pang, S.; Albin, S.; Zheng, J. L.; Johnson, R. M. *Anal. Chem.* **1998**, *70*, 464.
(161) Olivia, H.; Sarada, B. V.; Shin, D.; Rao, T. N.; Fujishima, A. *Analyst* **2002**, *127*, 1572.
(162) Park, J.; Quaiserova-Mocko, V.; Peckova, K.; Galligan, J. J.; Fink, G. D.; Swain, G. M. *Diamond Relat. Mater.* **2006**, *15*, 761.
(163) Hu, J. P.; Holt, K. B.; Foord, J. S. *Anal. Chem.* **2009**, *81*, 5663.
(164) Cvacka, J.; Quaiserova, V.; Park, J.; Show, Y.; Muck, A.; Swain, G. M. *Anal. Chem.* **2003**, *75*, 2678.
(165) Hu, J.; Foord, J. S.; Holt, K. B. *Phys. Chem. Chem. Phys.* **2007**, *9*, 5469.
(166) Muna, G. W.; Quaiserova-Mocko, V.; Swain, G. M. *Electroanalysis* **2005**, *17*, 1160.
(167) Shin, D. C.; Sarada, B. V.; Tryk, D. A.; Fujishima, A. *Anal. Chem.* **2003**, *75*, 530.
(168) Suzuki, A.; Ivandini, T. A.; Yoshimi, K.; Fujishima, A.; Oyama, G.; Nakazato, T.; Hattori, N.; Kitazawa, S.; Einaga, Y. *Anal. Chem.* **2007**, *79*, 8608.

(169) Halpern, J. M.; Xie, S. T.; Sutton, G. P.; Higashikubo, B. T.; Chestek, C. A.; Lu, H.; Chiel, H. J.; Martin, H. B. *Diamond Relat. Mater.* **2006**, *15*, 183.
(170) Xie, S. T.; Shafer, G.; Wilson, C. G.; Martin, H. B. *Diamond Relat. Mater.* **2006**, *15*, 225.
(171) Park, J.; Galligan, J. J.; Fink, G. D.; Swain, G. M. *Anal. Chem.* **2006**, *78*, 6756.
(172) Holt, K. B.; Hu, J. P.; Foord, J. S. *Anal. Chem.* **2007**, *79*, 2556.
(173) Tsunozaki, K.; Einaga, Y.; Rao, T. N.; Fujishima, A. *Chem. Lett.* **2002**, 502.
(174) Soh, K. L.; Kang, W. P.; Davidson, J. L.; Basu, S.; Wong, Y. M.; Cliffel, D. E.; Bonds, A. B.; Swain, G. M. *Diamond Relat. Mater.* **2004**, *13*, 2009.
(175) Soh, K.; Kang, W.; Davidson, J.; Wong, Y.; Cliffel, D.; Swain, G. *Diamond Relat. Mater.* **2008**, *17*, 240.
(176) Soh, K. L.; Kang, W. P.; Davidson, J. L.; Wong, Y. M.; Cliffel, D. E.; Swain, G. M. *Diamond Relat. Mater.* **2008**, *17*, 900.
(177) Pagels, M.; Hall, C. E.; Lawrence, N. S.; Meredith, A.; Jones, T. G. J.; Godfried, H. P.; Pickles, C. S. J.; Wilman, J.; Banks, C. E.; Compton, R. G.; Jiang, L. *Anal. Chem.* **2005**, *77*, 3705.
(178) Colley, A. L.; Williams, C. G.; Johansson, U. D.; Newton, M. E.; Unwin, P. R.; Wilson, N. R.; Macpherson, J. V. *Anal. Chem.* **2006**, *78*, 2539.
(179) Lawrence, N.; Pagels, M.; Meredith, A.; Jones, T.; Hall, C.; Pickles, C.; Godfried, H.; Banks, C.; Compton, R.; Jiang, L. *Talanta* **2006**, *69*, 829.
(180) Jones, S. E. W.; Compton, R. G. *Curr. Anal. Chem.* **2008**, *4*, 170.
(181) McGaw, E. A.; Swain, G. M. *Anal. Chim. Acta* **2006**, *575*, 180.
(182) Manivannan, A.; Tryk, D. A.; Fujishima, A. *Electrochem. Solid-State Lett.* **1999**, *2*, 455.
(183) Banks, C. E.; Hyde, M. E.; Tomcik, P.; Jacobs, R.; Compton, R. G. *Talanta* **2004**, *62*, 279.
(184) Tsai, Y. C.; Coles, B. A.; Holt, K.; Foord, J. S.; Marken, F.; Compton, R. G. *Electroanalysis* **2001**, *13*, 831.
(185) Prado, C.; Wilkins, S. J.; Grundler, P.; Marken, F.; Compton, R. G. *Electroanalysis* **2003**, *15*, 1011.
(186) Sonthalia, P.; McGaw, E.; Show, Y.; Swain, G. M. *Anal. Chim. Acta* **2004**, *522*, 35.
(187) El Tall, O.; Jaffrezic-Renault, N.; Sigaud, M.; Vittori, O. *Electroanalysis* **2007**, *19*, 1152.
(188) Babyak, C.; Smart, R. R. *Electroanalysis* **2004**, *16*, 175.
(189) Prado, C.; Wilkins, S. J.; Marken, F.; Compton, R. G. *Electroanalysis* **2002**, *14*, 262.
(190) Foord, J. S.; Eaton, K.; Hao, W.; Crossley, A. *Phys. Chem. Chem. Phys.* **2005**, *7*, 2787.
(191) Manivannan, A.; Kawasaki, R.; Tryk, D. A.; Fujishima, A. *Electrochim. Acta* **2004**, *49*, 3313.
(192) Foord, J. S.; Hao, W.; Eaton, K. *Phys. Status Solidi A* **2005**, *202*, 2116.
(193) Sine, G.; Duo, I.; El Roustom, B.; Foti, G.; Comninellis, C. *J. Appl. Electrochem.* **2006**, *36*, 847.
(194) Hyde, M. E.; Jacobs, R.; Compton, R. G. *J. Phys. Chem. B* **2002**, *106*, 11075.
(195) Toghill, K. E.; Wildgoose, G. G.; Moshar, A.; Mulcahy, C.; Compton, R. G. *Electroanalysis* **2008**, *20*, 1731.
(196) Bennett, J. A.; Show, Y.; Wang, S. H.; Swain, G. M. *J. Electrochem. Soc.* **2005**, *152*, E184.
(197) Bonne, M. J.; Helton, M.; Edler, K.; Marken, F. *Electrochem. Commun.* **2007**, *9*, 42.
(198) Ivandini, T.; Sato, R.; Makide, Y.; Fujishima, A.; Einaga, Y. *Diamond Relat. Mater.* **2004**, *13*, 2003.
(199) Ivandini, T. A.; Sato, R.; Makide, Y.; Fujishima, A.; Einaga, Y. *Diamond Relat. Mater.* **2005**, *14*, 2133.
(200) Treetepvijit, S.; Preechaworapun, A.; Praphairaksit, N.; Chuanuwatanakul, U.; Einaga, Y.; Chailapakul, O. *Talanta* **2006**, *68*, 1329.

(201) Kondo, T.; Honda, K.; Tryk, D. A.; Fujishimad, A. *J. Electrochem. Soc.* **2005**, *152*, E18.
(202) Sarapuu, A.; Helstein, K.; Schiffrin, D. J.; Tammeveski, K. *Electrochem. Solid-State Lett.* **2005**, *8*, E30.
(203) Sine, G.; Foti, G.; Comninellis, C. *J. Electroanal. Chem.* **2006**, *595*, 115.
(204) Toghill, K. E.; Compton, R. G. *Electroanalysis* **2010**, *22*, 1947.
(205) Welch, C. M.; Hyde, M. E.; Banks, C. E.; Compton, R. G. *Anal. Sci.* **2005**, *21*, 1421.
(206) Batchelor-McAuley, C.; Banks, C. E.; Simm, A. O.; Jones, T. G. J.; Compton, R. G. *Analyst* **2006**, *131*, 106.
(207) Hutton, L.; Newton, M. E.; Unwin, P. R.; Macpherson, J. V. *Anal. Chem.* **2009**, *81*, 1023.
(208) Simm, A. O.; Banks, C. E.; Ward-Jones, S.; Davies, T. J.; Lawrence, N. S.; Jones, T. G. J.; Jiang, L.; Compton, R. G. *Analyst* **2005**, *130*, 1303.
(209) Stradiotto, N. R.; Toghill, K. E.; Xiao, L.; Moshar, A.; Compton, R. G. *Electroanalysis* **2009**, *21*, 2627.
(210) Ohnishi, K.; Einaga, Y.; Notsu, H.; Terashima, C.; Rao, T. N.; Park, S. G.; Fujishima, A. *Electrochem. Solid-State Lett.* **2002**, *5*, D1.
(211) Gonzalez-Gonzalez, I.; Fachini, E. R.; Scibioh, A. A.; Tryk, D. A.; Tague, M.; Abruna, H. D.; Cabrera, C. R. *Langmuir* **2009**, *25*, 10329.
(212) Wang, J.; Firestone, M. A.; Auciello, O.; Carlisle, J. A. *Langmuir* **2004**, *20*, 11450.
(213) Zhang, G.-J.; Song, K.-S.; Nakamura, Y.; Ueno, T.; Funatsu, T.; Ohdomari, I.; Kawarada, H. *Langmuir* **2006**, *22*, 3728.
(214) Zhou, Y.; Zhi, J. *Electrochem. Commun.* **2006**, *8*, 1811.
(215) Song, M. J.; Kim, J. H.; Lee, S. K.; Lee, J. H.; Lim, D. S.; Hwang, S. W.; Whang, D. *Microchim. Acta* **2010**, *171*, 249.
(216) Shang, F. J.; Liu, Y. L.; Hrapovic, S.; Glennon, J. D.; Luong, J. H. T. *Analyst* **2009**, *134*, 519.

CHAPTER 2

Experimental

This section details the instrumentation, methodologies, reagents and apparatus used in the experiments described within this thesis.

2.1. MATERIALS AND CHEMICALS

2.1.1 **Polycrystalline Diamond Samples**

The pBDD samples used in Chapters 3, 4, 5 and 6 were prepared by Element Six Ltd., Ascot, UK, using a commercial microwave plasma CVD process described in Chapter 1, developed in-house. The average boron doping level of this material is ca. 5 x 10^{20} atoms cm^{-3}, as determined by secondary ion mass spectroscopy (SIMS).[1] The pBDD samples were polished by Element Six Ltd. to give a 500 μm thick sample with a surface roughness of ca. 1-3 nm, as measured by AFM. The layered diamond structures for the tubular flow ring electrode (TFRE) and the intrinsic polycrystalline diamond samples were grown via MWCVD by Element Six Limited. The pBDD for the conducting band structures was grown by Ken Haenen at the University of Hasselt via MWCVD. Further details and the characterisation of these diamond structures are in Chapter 7.

2.1.2 **Chemicals**

All solutions were prepared from Milli-Q water (Millipore Corp.), resistivity 18.2 MΩ cm at 25 ^{o}C. The chemicals were weighed using a four figure analytical balance (Sartorius A2008) and the pH of the solutions was taken with a pH meter (PHM201 Portable pH meter, Radiometer, Copenhagen). The chemicals used in this thesis are listed in Table 2.1.

Chemicals	Details	Supplier
Ruthenium (III) Hexaamine, $Ru(NH_3)_6^{3+}$	99%	Strem Chemicals Ltd., U.K.
Ferrocenylmethyltrimethylammonium Hexafluorophosphate, $FcTMA.PF_6$		Made in-house
Potassium Ferrocyanide, $K_4Fe(CN)_6.3H_2O$	≥99.99% trace metals basis	Sigma-Aldrich Co.
Tris(bipyridine)ruthenium(II) Chloride, $Ru(bpy)_3.Cl_2$		Sigma-Aldrich Co.
2-chlorophenol	99%	Sigma-Aldrich Co.
Ferrocene	98%	Sigma-Aldrich Co.
Potassium Hexachloroplatinate(IV), K_2PtCl_6	≥99.99% trace metals basis	Sigma-Aldrich Co.
Lead Nitrate, $Pb(NO_3)_2$	≥99.99% trace metals basis	Sigma-Aldrich Co.
Nickel Nitrate, $Ni(NO_3)_2$	99.999% trace metals basis	Sigma-Aldrich Co.
Glucose		Sigma-Aldrich Co.
Dopamine Hydrochloride	98%	Sigma-Aldrich Co.
Potassium Hydroxide, KOH	85%	Fisher Scientific
Potassium Nitrate, KNO_3	99.999% trace metals basis	Sigma-Aldrich Co.
Potassium Nitrate, KNO_3	99%	Sigma-Aldrich Co.
Potassium Chloride, KCl	99%	Sigma-Aldrich Co.
Tetrabytylammonium Perchlorate, TBAP		Lancaster synthesis
Methanol	99.99%	Fisher Scientific

Ethanol	99.99%	Fisher Scientific
Hydrochloric Acid, HCl	*Trace*SELECT® Ultra, ≥30.0%	Sigma-Aldrich Co. (Fluka)
Sulphuric Acid, H_2SO_4	*Trace*SELECT®, , ≥95%	Sigma-Aldrich Co. (Fluka)
Acetonitrile	99%	Fisher Scientific

Table 2.1: Chemicals used during the thesis including purity and supplier.

2.2. DIAMOND ELECTRODE FABRICATION

2.2.1 **Ohmic Contacts**

In order to study the electrical and electrochemical properties of pBDD, it is necessary to form an ohmic contact to the pBDD. Metal ohmic contacts can be formed in a variety of ways using metal layer deposition e.g. Ti/Au/Pt or Mo/Au, with subsequent annealing in air, nitrogen or argon at temperatures of at least 400 ^{o}C.[2,3] This process forms a carbide layer at the diamond/Ti or diamond/Mo interface, which allows ease of carrier tunnelling due to electronic defect states in the carbide layer.[3] The Au acts as an antioxidant layer over the Ti, while the Pt is used as a diffusion blocking film. Other forms of ohmic contact to diamond have also been investigated including ion-implanation,[4] laser graphitisation[5] and Si-C contacts.[6] While Au only contacts can be made to the surface of hydrogen-terminated diamond due to its surface conductivity,[7] carbide based contacts are necessary for oxygen-terminated pBDD. In order to utilise the conducting diamond as an electrode, in this work a reliable ohmic connection was made to the back of the pBDD by sputtering (Edwards E606 sputter/evaporator) a layer of Ti (20 nm), followed by Au (1 μm). The samples were then annealed in a tube furnace (MTF 12/25/400, Carbolite, UK) at 475 ^{o}C for 4 h in air.

2.2.2 **Electrode Fabrication Procedures**

The fabrication procedure for 1 mm diameter disc pBDD electrodes is discussed in Chapter 3. However for AFM analysis, it was necessary to prepare the electrode in a slightly different way to that described, to allow subsequent imaging of the surface. The Au/Ti back-contacted pBDD columns were annealed on a flat quartz disk, which had also been sputtered with Ti/Au. A conducting wire was then adhered to the Au contact on the quartz, using silver electrodag (Agar scientific, UK). Finally, epoxy resin (Araldite, Bostik Findley, UK) was used to seal around the edges of the pBDD column and the quartz, so that only the pBDD disk was left exposed to electrolyte solution as shown in Figure 2.1.

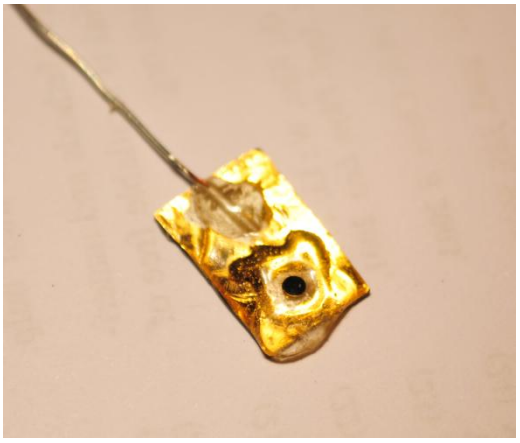

Figure 2.1: Photograph of a 1 mm disc electrode fabricated for AFM characterisation.

Chapter 7 contains the fabrication process for all-diamond electrodes in both the TFRE and dual band electrode formats. In all three cases, laser micromachining technology was employed to create the desired electrode geometry. A laser micromachiner E-355H-3-ATHI- O system, Oxford Lasers Ltd., UK, was used with a nanosecond pulsed laser at 20 kHz frequency giving a power of ca. 6 W.

2.3. CHARACTERISATION

This section will discuss the techniques used in the characterisation of the diamond samples employed to make electrodes. Several of these techniques were also used to investigate the deposition of a number of materials on the diamond surface.

2.3.1 **Micro-Raman Spectroscopy**

The Raman effect is a form of inelastic scattering of monochromated light by molecules in a sample.[8] Laser wavelengths from visible to near ultraviolet, can be used to probe a variety of compounds. Excitation photons interact with the rotational and vibrational modes of a sample molecule, exciting it from the ground state to a virtual energy state. The molecule then relaxes to an energy state, different to the original, and emits a photon. The shift in frequency of the emitted and excitation photons is related to the energy difference in the molecular states. This shift can be to a lower frequency (Stokes shift) or to a higher frequency (Anti-stokes shift). The advantages of micro-Raman are that it is a non-destructive technique which can give qualitative and quantitative analysis on very small samples.

Raman spectroscopy is an important tool for the characterisation of diamond films. It is sensitive to both non-diamond sp^2 carbon and crystalline sp^3 diamond. As such, it has been used extensively to investigate the quality of CVD grown diamond films and when appropriate, determine boron content (section 1.2.3). In this thesis, Raman spectra were taken to assess diamond quality and to verify if the boron concentration was high enough for metallic-like behaviour. Micro-Raman was performed at room temperature with a Renishaw inVia Raman microscope. An excitation wavelength

of 514.5 nm was employed using an Ar^+ laser with a power of 10 mW. A spot size of ca. 3 µm was used to examine the diamond surface and detection was carried out with a CCD detector (visible to near IR).

2.3.2 **Field-Emission Scanning Electron Microscopy (FE-SEM)**

FE-SEM is used to study surface features and can produce highly informative images. Under high vacuum, the field emission electron source produces a beam of electrons which can be accelerated through a column by applying voltages between 0.1 and 30 kV. Electromagnetic lenses and apertures are used to condense and refine the electron beam in order to achieve high resolution imaging. The beam can be 1 to 10 nm in diameter once focused on the specimen surface. When the electrons hit the sample, several types of interactions can occur as represented in Figure 2.2.[9] In this work, the most important are secondary and backscattered electron processes.

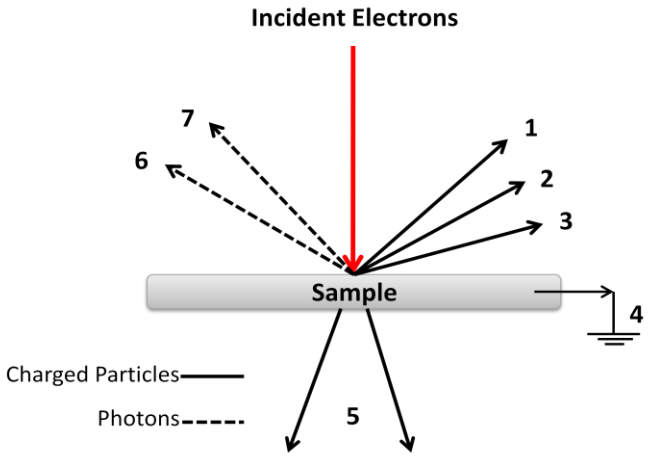

Figure 2.2: Schematic showing photon and charged particle emission from a surface following electron beam intereaction. 1 = secondary electrons, 2 = backscattered electrons, 3 = Auger electrons, 4 = absorbed current, 5 = transmitted electrons, 6 = X-rays, and 7 = cathodoluminescence.

In thick samples, inelastic scattering events occur where energy from the incident beam is transferred to the atoms in the specimen. This results in low energy secondary electron emission from the sample which is a function of the surface topography. This type of detection is used to study surface morphology, uniformity and particle size and can give very high resolution when using the In-lens detector.[10] Elastic events can also occur when the electron beam collides with the surface, where the electrons are reflected by the sample atoms. These backscattered electrons have high energy and can provide information about the composition of the sample.

Studies of pBDD with scanning electron microscopy (SEM) include investigations into grain boundaries, grain morphology and the distribution of incorporated boron.[11] Figure 2.3 shows the secondary electron emission image and a backscattered image of the same area of a polished pBDD surface.[11] The features observed in Figure 2.3 (a) are individual grains of different growth facets. The contrast is due to the differing boron concentrations in these facets producing varying conductivity (as mentioned in section 1.2.2), where higher levels of boron enhance secondary electron emission (brighter areas).[12] The features seen in Figure 2.3 (b) are grain clusters with identical growth directions, made-up of the individual grains seen in Figure 2.3 (a).The contrast results from the intensity of the backscattered electrons being dependent on the crystal lattice planes with respect to the incident electron beam.[13]

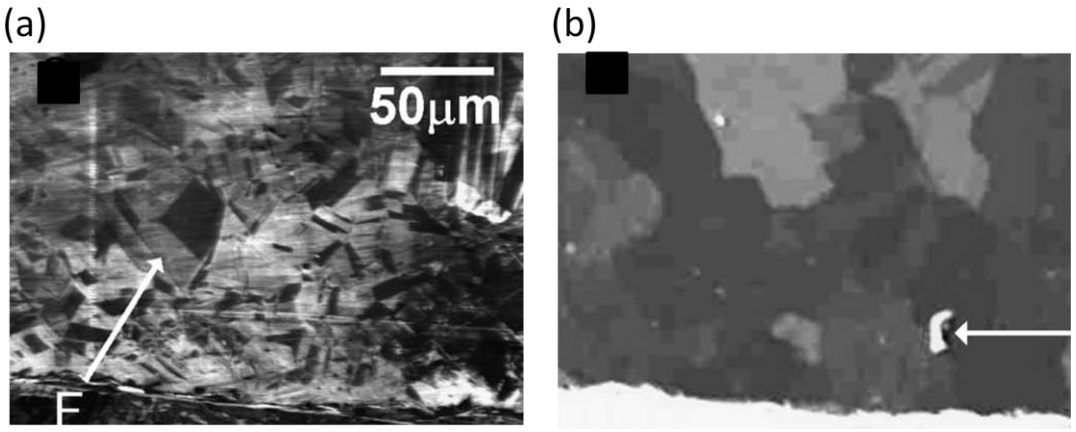

Figure 2.3: Comparison of SEM techniques of a polished hydrogen-terminated pBDD. The images are of the same area. (a) Low voltage (1 keV) secondary electron image and (b) high voltage (15 keV) backscattered image.

For the work detailed in this thesis FE-SEM images were recorded using a high resolution Zeiss Supra 55 VP. As surfaces can be imaged over a large area, this allowed characterisation of the uniformity of the diamond surface, as well as the homogeneity of any subsequent electrodepositions described in Chapters 4, 5 and 6. In order to clearly visualize the pBDD grain structure, an In-lens detector was used at accelerating voltages between 2 and 15 kV with a working distance of 4 mm. A secondary electron detector at 2 kV with a working distance of 5 mm was used to image metal deposits on the diamond surface.

2.3.3 **Atomic Force Microscopy (AFM)**

AFM is another surface imaging technique designed for nanometer resolution.[14,15] Topographical information is obtained by scanning a sharp tip over the surface of the sample, as shown in the schematic Figure 2.4. The tip is connected to a force sensitive cantilever, which is deflected by attractive or repulsive forces felt between the tip and the sample. A laser is shone onto the back of the cantilever where it is reflected onto a photodiode. Any movement in the cantilever is detected on the

photodiode and a feedback mechanism is set-up where the sample is moved in order to maintain a constant force between the tip and the sample. Lateral resolution is dependent upon the radius of the curvature of the tip apex. AFM can be operated in contact or tapping mode. The latter is of relevance here, where the tip is oscillated close to its resonant frequency as it is scanned, gently tapping along the surface.

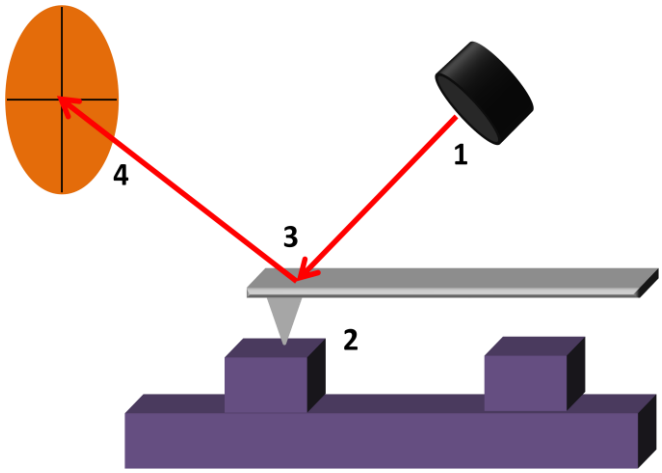

Figure 2.4; Schematic of an AFM system. A laser beam (1) is shone onto the cantilever as the tip (2) scans across the surface of the sample. The laser reflects off the back of the cantilever (3) into a photodiode detector (4).

AFM was carried out in order to characterise the topography of the diamond surface, but also to study the number density and morphology of metal electrodeposits on the surface of the pBDD electrodes in Chapters 4, 5 and 6. While AFM is limited to smaller *x* and *y* scan dimensions than FE-SEM e.g. scan ca. 100 µm, it enables highly accurate measurements in the *z* direction i.e. < nm. All AFM was performed using a Veeco EnviroScope AFM with NanoScope IV controller. Tapping mode was used in order to minimise distortion and avoid features on the surface such as electrodeposited nanoparticles being disturbed. AFM in solution was also performed in order to directly compare the morphology of the electrode surface before and after

electrodeposition in the same area. In air, RFESP (Veeco) tips were used, whereas NP-type probes (Veeco) were used in solution.

2.3.4 **X-ray Photoelectron Spectroscopy (XPS)**

XPS uses monochromated x-rays, which lie in the range 200 to 2000 eV, to probe the elemental composition of the surface of a sample.[16] Incident photons hit the sample surface and are absorbed by the atoms, which emit electrons from core atomic orbitals and become ionised. The kinetic energy of the emitted electrons is determined by the energy of the incident photon and the binding energy of the atom i.e. the difference in energy of the neutral and ionised atom. The kinetic energy distribution of the emitted electrons is detected in an analyser. For each element there is a specific binding energy for each of the core atomic orbitals, therefore quantitative analysis of chemical composition can occur. XPS is capable of parts per million detection limits[17] and has often been used to study the surface of natural and CVD grown diamond, as discussed in section 1.1.3.[18,19]

The XPS chemical analysis in this thesis was performed with a Scienta ESCA300 spectrometer at the National Centre for Electron Spectroscopy and Surface analysis, Daresbury Laboratory, UK. The samples were probed using a monochromated rotating anode Al $K\alpha$ x-ray source and analysed by a 300 mm radius hemispherical analyzer with a slit width of 0.8 mm at a pass energy of 150 eV.

2.3.5 **White Light Interferometry (WLI)**

White Light Interferometry, WLI is an optical method for investigating surface topography.[20] In contrast to AFM, WLI can image an area of 500 µm x 500 µm in ca. 20 s, measuring features in the range of tens of nanometers to hundreds of microns. In this technique white light from a source is passed through a collimator before being split in two. One half is reflected from a reference mirror and the other half from the sample. The beams recombine and interfere causing fringes on sections of the sample as the lens is scanned towards the sample and are detected by the camera. The instrument used in this work was a WYKO Systems WLI: WYKO NT-2000 surface profiler.

2.4. ELECTROCHEMICAL MEASUREMENTS

2.4.1 **Dynamic Electrochemistry**

Dynamic electrochemistry studies the processes occurring at the electrode/solution interface under non-equilibrium conditions and the factors that affect them. Two types of processes occur at the interface, faradaic and non-faradaic. The latter type can occur when there is a change in the electrode/solution interface causing a current to flow even though there is no charge transfer across the interface itself. Capacitance due to the electrode and the electrical double layer are examples of non-faradaic processes and must be taken into account when analysing the more commonly investigated faradaic reactions. Faradaic processes are those which involve an exchange of electrons across the interface resulting in the oxidation or reduction of the chemical species in solution. The overall rate of these reactions, and therefore the current magnitude, is governed by several parameters including applied

potential, electron kinetics and mass transport.[21] Figure 2.5 is a schematic of the different steps that can occur during a faradic electrochemical reaction.

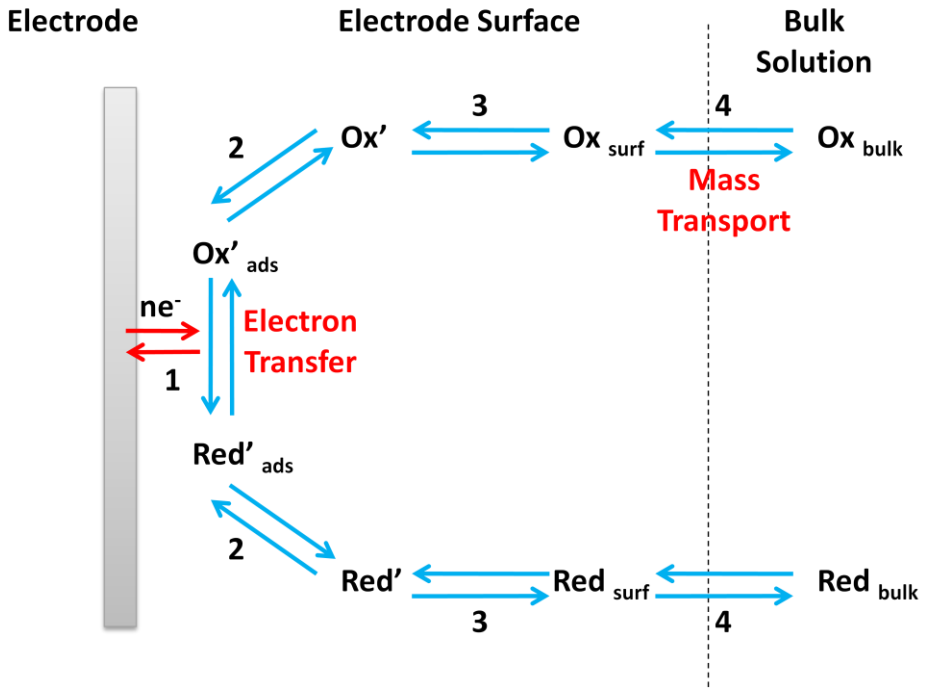

Figure 2.5: Schematic of the processes that can occur at the electrode surface. (1) electron transfer across the interface; (2) surface reactions such as adsorption/desorption; (3) chemical reactions before/after electron transfer and (4) mass transport of the electroactive species from bulk solution to/from the electrode surface.[21]

Chemical reactions before or after the electron transfer, any adsorption or desorption at the electrode surface and the electron transfer itself, all have associated overpotentials necessary to provide energy for the step to take place. For simple electrochemical reactions electron transfer kinetics and mass transport are the most important factors, where the rate of mass transport is most often the slowest and therefore rate determining step.[22] Migration, diffusion and convection are the three types of mass transport that can cause the movement of chemical species towards the electrode surface and are described mathematically in the Nernst-Planck equation. Migration is the movement of ions in solution due to the presence of an electric field. This is made negligible by the addition of an excess of chemically inert ions known

as supporting electrolyte. Under static conditions natural convection due to thermal or vibrational effects is very small on a typical voltammetric experiment time scale. Thus diffusion, the movement of species down a concentration gradient, is the most influential mass transport regime and often controls the rate of reaction in a mass transport limited system. However, convection can be deliberately applied to a system via stirring, heating or pumping, causing an increase in mass transport. Forced convection can be introduced using well defined hydrodynamic conditions and can therefore be utilised to control reaction rates.[23] In fact, if the rate of mass transport is increased enough to be comparable with or greater than the rate of electron transfer kinetics, the system becomes kinetically controlled, enabling the elucidation of electron transfer kinetics.

2.4.2 **Cyclic Voltammetry (CV) – Static and Hydrodynamic Conditions**

CV is one of the simplest and most common of the electrochemical techniques. Consider the reversible reaction given by the equation,

$$R \leftrightharpoons O + e^- \qquad (2.1)$$

where O is the oxidized form of the electroactive species and R is the reduced form. The potential of the working electrode is swept linearly from a potential where no reaction occurs to one where electron transfer takes place. The direction of the sweep is then reversed and is scanned back to the starting potential. This wave form is shown in Figure 2.6 (a). Figure 2.6 (b) shows the resulting CV for a macroelectrode. At the starting potential no oxidation occurs and so the current is zero. As the potential increases, the rate of oxidative electron tranfer increases, and so the current increases approximately exponentially with increasing potential, as predicted by the Butler-Volmer equation.[24] A maximum current value is observed as

a peak in the voltammogram. The magnitude of the peak current is determined by several factors including species concentration and whether the process is kinetic or diffusion controlled. For a diffusion limited process, as the overpotential is further increased past the peak current, the rate of mass transfer is not sufficient to replace redox species at the electrode surface at the same rate they are removed. Thus a fall in current is seen. As the potential is reversed, the reaction proceeds in the opposite direction giving a similar voltammogram in a negative direction, with the peak shifted by 59/*n* mV in comparison to the oxidation peak, as dictated by the Nernst equation (at 298 K).

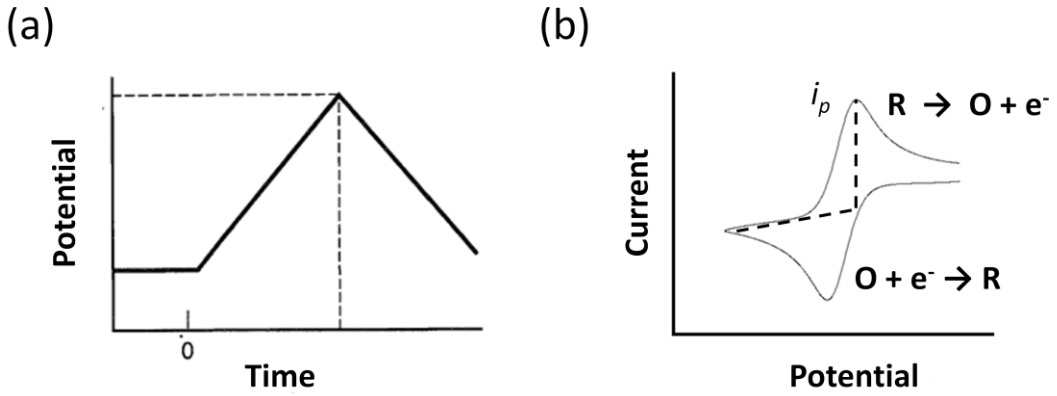

Figure 2.6: (a) The wave form for a CV and (b) a typical CV for a simple reversible electrochemical system at a macroelectrode.(Adjusted from ref [21])

The peak current for diffusion controlled conditions with planar diffusion , i_p is given by the equation,[21]

$$i_p = 0.4463 \left(\frac{F^3}{RT}\right)^{1/2} n^{3/2} A D^{1/2} c^* \upsilon^{1/2} \qquad (2.2)$$

where n is the apparent number of electrons transferred, A is the area of the electrode in cm^2, D is the diffusion coefficient of the electroactive species in $cm^2\ s^{-1}$, c^* is the bulk concentration of the species in mol cm^{-3} and υ is the potential scan rate in $V\ s^{-1}$. CVs can be used to study the influence of the electrode material on the electrode/solution interfacial process as well as to extract electron transfer rate

constants. However, a CV averages over the whole surface so it can be complicated to analyse for a heterogeneous electrode surface. Furthermore, if all other constants are known, the concentration of the electroactive species can be determined.

Under well defined hydrodynamic conditions, such as solution laminar flow, there is an increase in the mass transport of the species to the electrode surface, resulting in an increase in the current that flows and a change in shape of the CV produced. Figure 2.7 shows a CV of the redox process in equation 2.1 under convective flow conditions. A sigmoidal shape is now observed as the increased mass transport arising from forced convection is able to compete with the rate at which redox species are removed, resulting in a steady-state limiting current. The magnitude of the limiting current, i_{lim} is dependent upon the type of hydrodynamic technique employed with the electrode of interest, for example a rotating disc,[25] tubular flow,[26] channel flow,[27] etc.

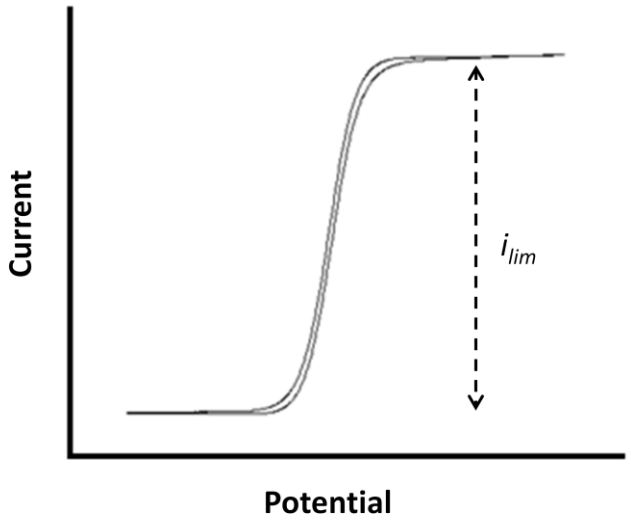

Figure 2.7: A typical CV for a simple reversible redox process at a macroelectrode under hydrodynamic control.

All electrochemical measurements using the 1 mm diameter disc pBDD electrodes were made in a three-electrode mode using a potentiostat (CHI730A, CH Instruments Inc. TX) connected to a laptop computer. Either a silver-silver chloride electrode (Ag/AgCl: chloridized Ag wire) or a saturated calomel electrode (SCE) was used as a reference electrode with a Pt gauze serving as a counter electrode. A 3 mm Pt diameter disc electrode (CHI102, CH Instruments Inc) was used to compare pBDD with Pt.

For experiments on oxygen detection, the dissolved oxygen concentration in the solution was controlled using oxygen and nitrogen gas mixtures to gasify the solution. Different ratios of oxygen to nitrogen, flowed into the solution for ca. 30 mins, were controlled accurately using mass flow controllers (MKS Instruments) linked to a four channel power supply and display. The total gas flow rate was kept constant at 35 standard cubic centimetres, while the ratio of oxygen to nitrogen was varied. The laboratory was air conditioned to 21 ± 1 ^{o}C for all measurements

Hydrodynamic conditions were used for the electrochemical characteristics of the all-diamond TFRE. CVs were performed in a 2-electrode configuration using a Ag/AgCl reference electrode where syringe pumps (KD Scientific) were used to flow solution through the set-up at various volume flow rates. This is described in more detail in Chapter 7.

2.4.3 **pBDD Functionalisation via Electrodeposition**

For the detection of dissolved oxygen the pBDD electrode was functionalized with Pt nanoparticles (NPs) by applying a potential of -1.0 V vs. SCE in a solution of 1

mM K_2PtCl_6 and 0.1 M HCl, for various time periods in the range 1 ms to 30 s. The electrode was then rinsed with ultrapure water.

For the detection of glucose and primary alcohols, nickel hydroxide NPs were synthesized *in-situ* on the pBDD surface from a 10 mM nickel nitrate solution (pH = 6), by applying a potential of – 1.1 V vs. Ag/AgCl for different times in order to increase the amount of material on the surface.

2.4.4 **Heavy Metal Detection**

ASV is employed for the effective electrochemical sensing of heavy metals. The technique involves a deposition stage, where a reducing potential is applied to the electrode for a given amount of time, depositing metal solid onto the electrode surface. The potential of the electrode is then swept through oxidising potentials, removing the metal from the surface, known as the stripping step. The resulting voltammograms can be analysed in terms of peak current and area and correlated back to the metal concentration in solution. In order to improve the detection limits of this method, it can be coupled with hydrodynamic systems to increase the mass transport at the deposition stage. In this work an impinging wall-jet set-up was employed as shown schematically in Figure 2.8. Typically, during deposition, solution was flowed onto the electrode from a co-axial[28,29] of inner diameter 50 µm, placed 500 µm from the pBDD surface, at a flow rate of 0.1 ml s^{-1}. During deposition, the pBDD electrode was held at -1.5 V vs. SCE to drive the electroreduction process.

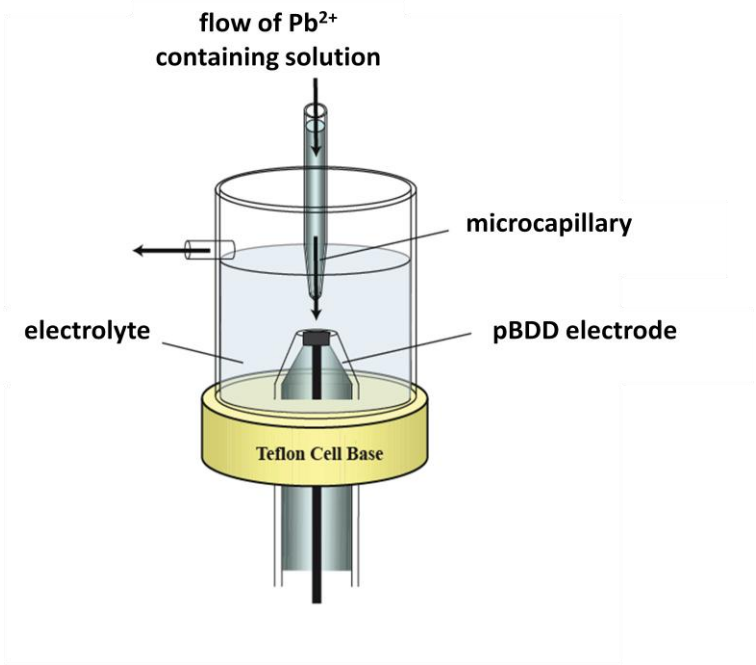

Figure 2.8: Schematic of the impinging jet arrangement for hydrodynamic delivery of solution to a macrodisc pBDD electrode.

In order to improve the electrochemical response, DPV was used in the stripping stage. DPV is a pulse voltammetric method, the wave form and resulting voltammograms of which are shown in Figure 2.9. DPV was performed under quiescent conditions in 2 mV steps, with a pulse width and amplitude of 50 ms and 50 mV, respectively.

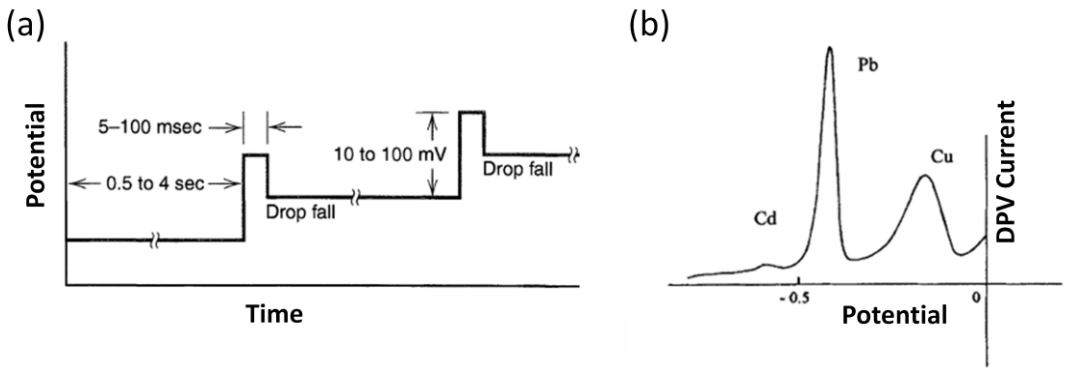

Figure 2.9: (a) The wave form for a DPV and (b) a typical DPV for heavy metal stripping analysis.(Adjusted from ref [21])

2.4.5 **Solution Conductivity Measurements**

The all-diamond dual bands were used for solution conductivity measurements. These were performed by applying an ac current of 5 μA at 10 kHz between the two bands while in solution and measuring the potential. This was carried-out with an ac power supply and voltmeter built in-house.

2.5. REFERENCES

(1) Wilson, N. R.; Clewes, S. L.; Newton, M. E.; Unwin, P. R.; Macpherson, J. V. *J. Phys. Chem. B* **2006**, *110*, 5639.
(2) Moazed, K. L.; Zeidler, J. R.; Taylor, M. J. *J. Appl. Phys.* **1990**, *68*, 2246.
(3) Tachibana, T.; Williams, B. E.; Glass, J. T. *Phys. Rev. B* **1992**, *45*, 11975.
(4) Chen, Y. G.; Hasegawa, M.; Okushi, H.; Koizumi, S.; Yoshida, H.; Sakai, T.; Kobayashi, N. *Diamond Relat. Mater.* **2002**, *11*, 451.
(5) Geis, M. W.; Rothschild, M.; Kunz, R. R.; Aggarwal, R. L.; Wall, K. F.; Parker, C. D.; McIntosh, K. A.; Efremow, N. N.; Zayhowski, J. J.; Ehrlich, D. J.; Butler, J. E. *Appl. Phys. Lett.* **1989**, *55*, 2295.
(6) Vescan, A.; Daumiller, I.; Gluche, P.; Ebert, W.; Kohn, E. *Diamond Relat. Mater.* **1998**, *7*, 581.
(7) Kawarada, H. *Surf. Sci. Rep.* **1996**, *26*, 205.
(8) Long, D. A. *Raman spectroscopy*; McGraw-Hill, New York, 1977.
(9) Watt, I. M. *The Principles and Practice of Electron Microscopy, 2nd ed.* ; Cambridge University Press: Cambridge, 1997.
(10) Thornton, P. R. *Scanning electron microscopy: applications to materials and device science* Chapman & Hall, London, 1968.
(11) Steeds, J. W.; Mora, A. E.; Charles, S. J.; Evans, D. J. F.; Butler, J. E. *Mater. Chem. Phys.* **2003**, *81*, 281.
(12) Miller, J. B.; Brandes, G. R. *J. Appl. Phys.* **1997**, *82*, 4538.
(13) Schulson, E. *J. Mater. Sci.* **1977**, *12*, 1071.
(14) Binnig, G.; Quate, C. F.; Gerber, C. *Phys. Rev. Lett.* **1986**, *56*, 930.
(15) Quate, C. F. *Surf. Sci.* **1994**, *299*, 980.
(16) Briggs, D.; Seah, M. P. *Practical surface analysis : by auger and x-ray photoelectron spectroscopy* Wiley, New York 1983.
(17) Hüfner, S. *Very high resolution photoelectron spectroscopy*; Springer, New York, 2007.
(18) Goeting, C. H.; Marken, F.; Gutierrez-Sosa, A.; Compton, R. G.; Foord, J. S. *Diamond Relat. Mater.* **2000**, *9*, 390.
(19) Wang, M.; Simon, N.; Decorse-Pascanut, C.; Bouttemy, M.; Etcheberry, A.; Li, M. S.; Boukherroub, R.; Szunerits, S. *Electrochim. Acta* **2009**, *54*, 5818.
(20) Mücklich, F. *Handbook of Microscopy:Applications in Materials Science, Solid-State Physics and Chemistry*; VCH, Weinheim 1997.
(21) Bard, A. J.; Faulkner, L. R. *Electrochemical methods: Fundamentals and Applications*; John Wiley & Sons, INC., 2001.
(22) Fisher, A. C. *Electrode Dynamics*; Oxford University Press: Oxford, 2003.
(23) Rees, N.; Compton, R. *Russ. J. Electrochem.* **2008**, *44*, 368.
(24) Brett, C. M. A.; Brett, A. M. O. *Electrochemistry: Principles, Methods and Applications*; Oxford University Press: Oxford, 2000.
(25) Sopchak, D.; Miller, B.; Avyigal, Y.; Kalish, R. *J. Electroanal. Chem.* **2002**, *538*, 39.
(26) Blaedel, W. J.; Klatt, L. N. *Anal. Chem.* **1966**, *38*, 879.
(27) Snowden, M. E.; King, P. H.; Covington, J. A.; Macpherson, J. V.; Unwin, P. R. *Anal. Chem.* **2010**, *82*, 3124.
(28) Macpherson, J. V.; Marcar, S.; Unwin, P. R. *Anal. Chem.* **1994**, *66*, 2175.
(29) Macpherson, J. V.; Beeston, M. A.; Unwin, P. R. *J. Chem. Soc., Faraday Trans.* **1995**, *91*, 899.

CHAPTER 3

pBDD Electrodes: Fabrication, Characterisation and Electrochemical Properties

In this chapter, the pBDD material was extensively characterised using AFM, FE-SEM, micro-Raman and XPS. The lapped pBDD surface was found to have grain sizes ranging from 2 – 20 µm for the 500 µm thick samples employed, with topographical features no larger than tens of nm. Correlated AFM and FE-SEM images showed that the larger, less conducting grains were generally higher in topography than the more conducting grains. Micro-Raman showed that all areas of the pBDD surface were expected to be within at least the hopping conduction regime, with the higher doped regions in the metallic conduction region. XPS performed on the surface of the pBDD indicated an oxygen-terminated surface with a range of oxygen containing functional groups present, including carbonyls, hydroxides and ethers.

1 mm diameter pBDD disc electrodes were fabricated using laser machining and glass sealing techniques. An extended solvent window with low background currents was observed in comparison with a commercially available Pt electrode. The current-voltage response of these electrodes were shown to give close to reversible behaviour for $Ru(NH_3)_6^{3+/2+}$, $IrCl_6^{2-/3-}$ and $Fe(CN)_6^{3-/4}$ with a slight increase in ΔE_p when increasing the concentration from 1 mM to 10 mM. The electrochemical response of the pBDD was also shown to be stable even after applying relatively harsh cleaning conditions i.e. -4 V vs. SCE for 3 min to aid in the oxidation of 2-chlorophenol.

3.1. INTRODUCTION

pBDD is presently the subject of considerable interest as an electrode material, as discussed in Chapter 1. The very wide potential window in aqueous solution, low background currents and resistance to fouling,[1-3] make it particularly attractive for use in electroanalysis. pBDD is resistant to corrosion under both acidic and alkaline conditions, as well as at extreme positive and negative applied potentials,[4] and is stable at high temperatures and pressures.[3]

While recent review articles have focused on the many applications of pBDD electrodes,[3,5-7] early papers summarised research into an understanding of the basic electrochemical properties of pBDD.[4,8-12] The results were found to differ greatly depending on the diamond sample used, as well as the experimental set-up.[13] It has now been shown that several factors, both inherent and external to the material, can influence the electrochemical properties, such as boron dopant density. Here electrical conductivity measurements show that at boron dopant levels of ca. > 3 x 10^{20} atoms cm^{-3} the material undergoes a transition to semi-metallic.[14,15] The surface termination of the pBDD has also been found to affect the electrochemical response, with investigations focusing on the behaviour of as-grown, hydrogen-termination and various forms of oxygen-terminated pBDD. Several papers have reported slower electron transfer kinetic rate constants at oxygen-terminated surfaces compared to hydrogen-terminated pBDD, for similar boron dopant concentrations, for mediators with complex (inner-sphere) electron transfer mechanisms such as $Fe(CN)_6^{3-/4-}$ and $Fe^{2+/3+}$.[10,12,16,17] In contrast, no difference was seen for the electrolysis of simple outer sphere redox species such as $Ru(NH_3)_6^{3+/2+}$ and $IrCl_6^{3-/4-}$.

The surface termination itself can differ from sample to sample based on crystal orientation, non-diamond like carbon content and termination method.[18] The influence that surface termination has on the electrochemical response also seems to be largely dependant on the boron concentration of the diamond. In particular, it is more pronounced for diamond containing lower dopant densities i.e. in the semiconducting/hopping regimes < 10^{20} atoms cm^{-3}.[10,19] It is important to note that for initially hydrogen-terminated samples, cycling to positive potentials can oxygen-terminate the surface and has been reported as a necessary step to stabilise the electrode response.[20] The amount of non-diamond like carbon incorporated into the diamond during the growth process, most likely at grain boundaries and defects,[21] can also change the overall electrochemical response of the pBDD electrode.[22] It is therefore important to thoroughly characterise the material properties of the pBDD before use as an electrode, in order to interpret any electrochemical response correctly.

Improvements in understanding of pBDD electrochemistry appears to have gone hand in hand with improvements in both the quality of CVD grown BDD and characterisation techniques. Free-standing high quality, heavily doped CVD grown pBDD is now readily available.[23] However, in order to take advantage of the unique attributes of pBDD as an electrode material, it is beneficial to design and deploy an electrode format which lends itself to both unlimited and quantifiable measurements.

In this chapter we demonstrate the wide range applications of oxygen-terminated pBDD with an average dopant density ca. 5 x 10^{20} B atoms cm^{-3}. At this dopant density the material can be considered metal like, furthermore by employing an

oxygen-terminated surface, issues concerning the stability of the terminated surface, subject to a wide potential range, as with hydrogen,[24] are removed. The pBDD is mechanically polished by Element Six (lapped) to give a surface roughness of ca. 4 nm, as measured by AFM. Using a laser micromachining technique, cylinders 1 mm in diameter, can be machined, electrically connected using a Ti-carbide ohmic contact and then sealed in glass to provide a standard macrodisc electrode format, as described below.

3.2. POLYCRYSTALLINE BORON-DOPED DIAMOND CHARACTERISATION

Prior to use, it is of great importance to characterise the material properties of the pBDD. As such, AFM and FE-SEM were carried out to fully assess the roughness and grain morphology of the polished diamond surface, whilst micro-Raman spectroscopy was used to verify the quality of the pBDD produced, via observation of the D (sp^3) and G (sp^2) peaks in the resulting spectrum. SIMS (Cameca ims 4f) measurements we taken at Loughborough Surface Analysis Centre, gave an average boron dopant concentration of ca. 5×10^{20} atoms cm^{-3}.[25] The pBDD samples were lapped by Element Six to give a ca. 500 μm thick sample with typical grain sizes, as measured by FE-SEM (Figure 3.1 (a)), of between 2-20 μm. Lapping involves a polishing process in which the pBDD is rotated and translated while in contact with a spinning polishing wheel.[26] Since diamond has highly anistropic hardness/wear rates and the pBDD is made up from differently orientated grains, this approach is necessary to achieve a low roughness surface. Typical AFM and FE-SEM images of the pBDD used in this study, recorded in the same area, are shown in Figure 3.1.

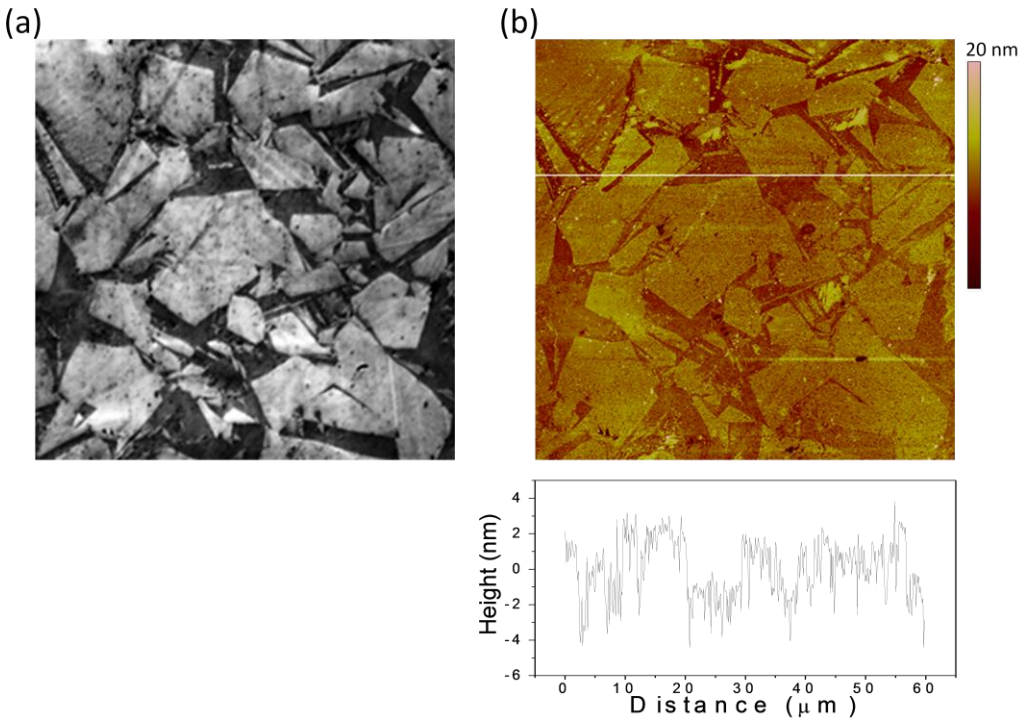

Figure 3.1: (a) Typical 60 μm x 60 μm in-lens FE-SEM image and (b) AFM height image with cross-sectional data recorded below in the same area of a pBDD surface.

SEM studies of pBDD have shown that secondary electron emission yields from BDD reach a maximum at boron concentrations of 10^{19}-10^{20} atoms cm^{-3}.[27] Previous work has shown that for pBDD material grown via the same growth receipe, the dark regions in the FE-SEM images correlated with the more highly boron doped regions, as confirmed by cathodluminescence and C-AFM maps recorded in the same area.[25] The change in dopant levels across the surface is likely to be associated with grain-dependant boron uptake, as it is well known that boron is more readily incorporated, by a factor of approximately 10, into (111) growth sectors than (100) sectors.[28] Interestingly, in Figure 3.1 it can also be seen that the darker, more highly doped regions in the FE-SEM image also correlate with the lower lying regions in the AFM image. For example, the cross section below Figure 3.1 (b) shows a height difference of, ca. 6 nm, associated with moving across one grain to the next, which the FE-SEM

image indicates is a transition from a less doped grain to one which is more doped. The change in height between differently doped regions could be a result of differently orientated crystal grains, or grains with different boron dopant levels polishing at slightly different rates,[29] this is currently under further investigation. On the surface of a grain, AFM reveals a surface roughness of ca. 1-2 nm. Thus, from FE-SEM images and AFM height images, it is possible to qualitatively infer how boron uptake across the surface of pBDD varies. This is important when elucidating whether differently doped grains show different electrochemical characteristics e.g. for electrodeposition, as discussed further in Chapter 4.

Micro-Raman was also used to investigate the grain dependent boron uptake. Figure 3.2 shows typical micro-Raman spectra taken at a wavelength of 514.5 nm at a (a) bright grain and (b) centred on a darker grain as seen in FE-SEM. Due to the laser spot size under these conditions of ca. 10 μm diameter, it was possible to probe the larger bright grains individually, however, when focused on the smaller dark grains a small incorporation of grain boundaries was unavoidable, as shown in the optical microscope images in Figures 3.2 (a) and (b). The diamond zone centre optical phonon peak at ca. 1332 cm^{-1} is immediately obvious in both spectra, however overall the spectra appear very different. A slight asymmetric deformation of the sp^3 diamond peak can be seen in Figure 3.2 (a). This feature is attributed to a Fano-type interference between the discrete zone centre phonon and a continuum of electronic excitations, indicating that the grain is has a dopant density $\geq 1 \times 10^{20}$ atoms cm^{-3}.[30] Peaks at ca. 1220 cm^{-1} and ca. 500 cm^{-1} have previously been recorded at BDD and were found to correlate with boron concentration in heavily doped samples.[31,32]

Peaks of weak intensity can be observed in the bright grains at 1220 cm^{-1} and 600 cm^{-1} also indicating a doping level just below 3 x 10^{20} atoms cm^{-3}.[33]

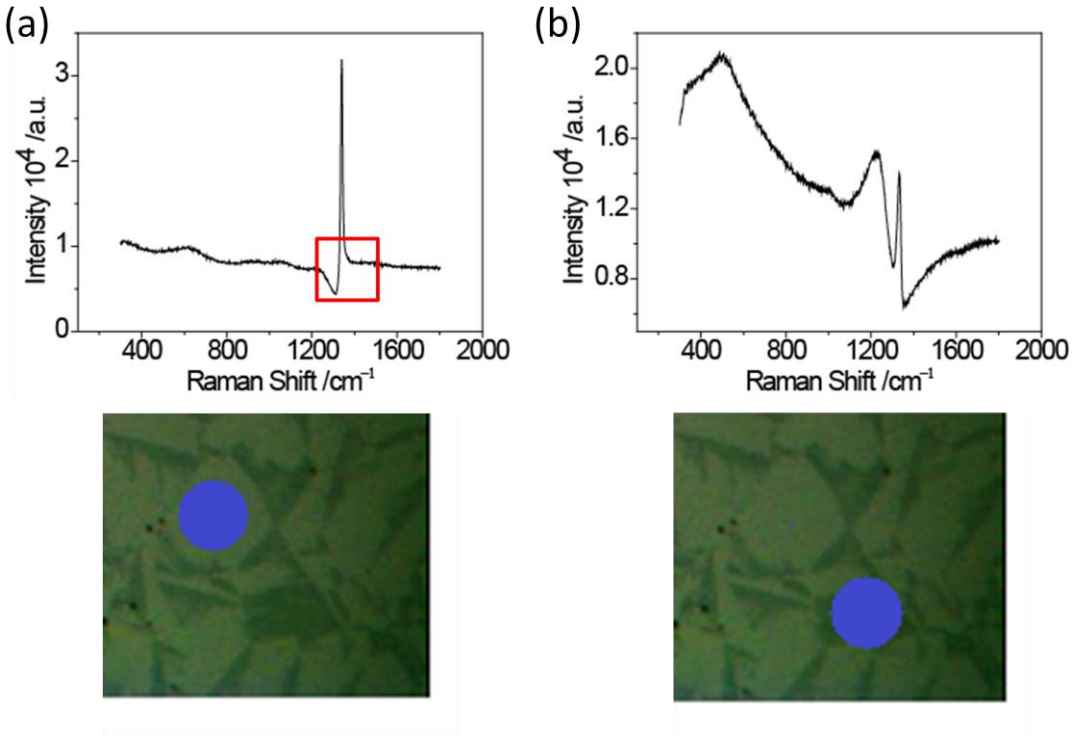

Figure 3.2: Typical micro-Raman taken at room temperature with a 514.5 nm laser at (a) a bright grain and (b) a dark grain and grain boundaries for pBDD. The optical microscope images show the corresponding type of grain being investigated and its size in relation to the laser spot size (the blue spot).

The Raman spectra taken of a darker grain, Figure 3.2 (b), shows a greatly attenuated diamond peak, which has been shifted to 1327 cm^{-1} and has become broader demonstrating a larger Fano effect.[30] The 1220 cm^{-1} peak has a much greater intensity and the peak centred at 550 cm^{-1} in the bright grain has shifted to a lower wavenumber of 460 cm^{-1} indicating a higher boron concentration than that associated with the grain in Figure 3.2 (a). These spectra coincide with the FE-SEM showing that the darker grains have a higher boron concentration than the brighter grains. Importantly the presence of the Fano interference in both light and dark regions of the pBDD sample indicate that even in the lighter doped regions, the boron concentration is $\geq$ 1 x 10^{20} atoms cm^{-3} indicating that the regions are not

semiconducting.[34] Both spectra show an absence of peaks at ca. 1350 cm^{-1} – 1580 cm^{-1} suggesting a negligible amount of non-diamond sp^2 carbon present at the diamond surface, this is true even in spectra 3.2 (b) where the laser spot crossed over a grain boundary.

The surface of diamond can be ideally simplified in terms of 'dangling bonds' where each surface carbon atom has a singly-occupied outwardly-directed sp^3 hybrid orbital. In reality however, CVD diamond at room temperature and pressure is terminated with hydrogen and oxygen containing functional groups. The functional groups present are determined by the history of the diamond i.e. the termination process and treatments and also the crystal orientation. Figure 3.3 shows schematics for oxygen-terminated diamond for (a) the (100) surface and (b) the (111) surface.

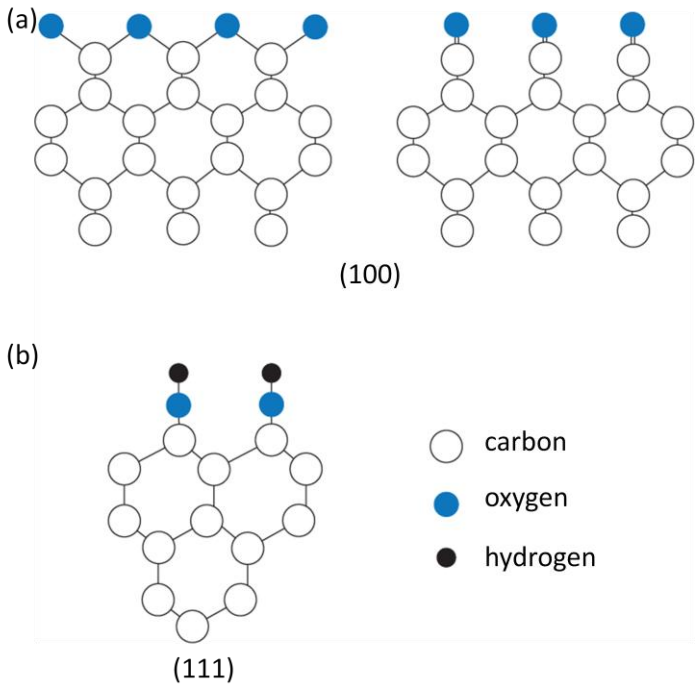

Figure 3.3: Schematic of the possible termination structures of oxygen-terminated (a) (100) and (b) (111) diamond surface.

Low energy electron diffraction,[35] XPS analysis[36] and electrochemical experiments[37,38] have shown that carbonyl, >C=O and ether, >C-O-C< groups are dominant on the diamond (100) surface, whereas hydroxyl groups, C-OH, are generated at the (111) surface. Investigations into the oxygen-termination of pBDD have shown that O/C ratios can been seen to range from 10 to 20 for mild and severe electrochemical anodic oxidation,[18,39] as well as for UV and oxygen plasma treatments, for HFCVD and MWCVD grown diamond.[18,36]

XPS was carried-out on the pBDD used in this work in order to investigate the surface termination. Figure 3.4 (a) shows the XPS survey spectra and (b) C 1s spectra of the oxygen-terminated pBDD after acid treatment and electrode fabrication. From the survey spectra a clear O 1s peak is observed at ca. 530 eV, indicating oxygen-terminated pBDD. The O/C 1s ratio is determined as 10 %, which is comparable to ratios found at severely anodised terminated pBDD.[36,40] The high resolution C 1s peak in Figure 3.4 (b) has been fitted to analyse the different carbon containing species present. The most intense peak centred at 284.4 eV (i) can be attributed to the bulk diamond component.[41] The peak shifted by + 0.7 eV (ii) with respect to peak (i), centred at 285.1 eV, can be attributed to hydrogenated diamond with CH_x species absorbed on the surface and contributes 18 % of the total C 1s peak area.[36] The peak centred at 286.2 eV (iii) can be assigned to either hydroxyl or ether groups and contributes 8.5 % of the C 1s peak.[40] The last peak at 287.4 eV (iv) can be attributed to more oxidised functional groups such as carboxyl, carbonyl and ester groups. The peak has a low contribution of 1.5 %.

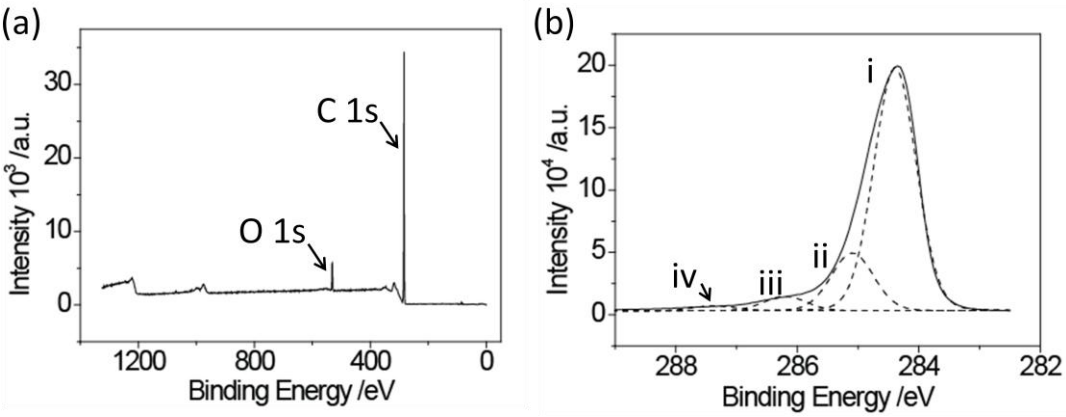

Figure 3.4: (a) Survey and (b) high resolution C 1s spectra for the acid oxidised lapped pBDD.

3.3. pBDD Electrode Fabrication

In order to fabricate pBDD disc electrodes with well-defined dimensions, a laser micromachiner (E-355H-3-ATHI-O system, Oxford Lasers) was used to cut 1 mm diameter pBDD columns (ca. 500 μm thick) from the samples provided. Given that the typical material removal depth is approximately 60 μm per pass, cutting through the thick diamond sample required several passes using the laser at 20 kHz with a power of ca. 6.6 W at a scan rate of 1 mm s^{-1}. In principle, this can make the attainment of a smooth and precise cut difficult as the laser may reflect or absorb onto the walls of the recess, producing a poorly cut geometry. Laser kerfing, shown schematically in Figure 3.5 (a), was therefore incorporated into the laser cutting program in order to minimise these effects. This is a technique in which (i) a series of cuts of a certain depth either side of an axis are used to remove a section of diamond. (ii) The laser is then refocused onto the lower depth and used to kerf again, this time removing a smaller section of diamond, (iii) eventually producing a V shaped cut. Figure 3.5 (b) shows a lasered pBDD column (i) top surface that will be exposed to solution and (ii) the side of the column.

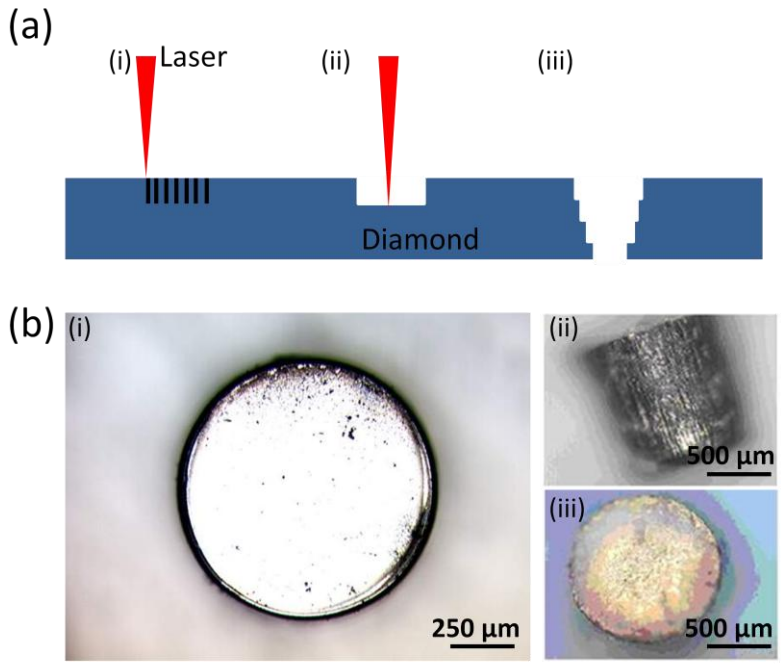

Figure 3.5: (a) Schematic of laser kerfing and (b) photographs of lasered pBDD column, (i) top surface, (ii) column side and (iii) Au/Ti sputtered back surface.

Prior to further preparation, the pBDD columns were acid cleaned in boiling concentrated H_2SO_4 (98%), supersaturated with KNO_3. The solution was heated until it was just boiling and the KNO_3 had been exhausted (fumes given off turned from brown to white). Once the solution had cooled, the samples were removed, rinsed repeatedly in water and allowed to dry in air. This process removed any non diamond like carbon that could have been generated during the laser micromachining[42] and also oxygen-terminated the pBDD surface.[43]

In order to utilise the conducting diamond as an electrode, a reliable ohmic connection[44] was made to the back of the BDD columns by sputtering (Edwards E606 sputter/evaporator) a layer of Ti (20 nm), followed by Au (1 µm), as shown in Figure 3.5 (biii). The samples were then annealed in a tube oven in air for 4 h at 450 ^{o}C. Upon annealing the Ti forms a carbide-based tunneling contact between the

diamond and TiC through which carriers can tunnel, lowering the contact resistivity to less than 1 Ω cm. The Au top contact serves as a highly conductive antioxidation layer. A similar method to the standard procedures for sealing metal wires in glass, for the production of metal microelectrodes,[45] was adopted in order to insulate the pBDD columns so that only the top (disc) surface was exposed. After sealing the diamond disc in a pulled glass capillary (o.d. 2 mm, i.d. 1.16 mm, Harvard Apparatus Ltd, Kent, UK), the pBDD surface was exposed by polishing with carbimet grit paper discs (Buehler, Germany). Electrical contact was made to the pBDD|Au surface using silver epoxy (RS Components Ltd, Northants, UK) and a tinned copper wire used to form an external electrical contact. Finally, epoxy resin (Araldite, Bostik Findley, UK) was placed around the top of the capillary to stabilize the copper wire. Figure 3.6 shows a schematic and photograph of a final pBDD 1 mm diameter disc macroelectrode.

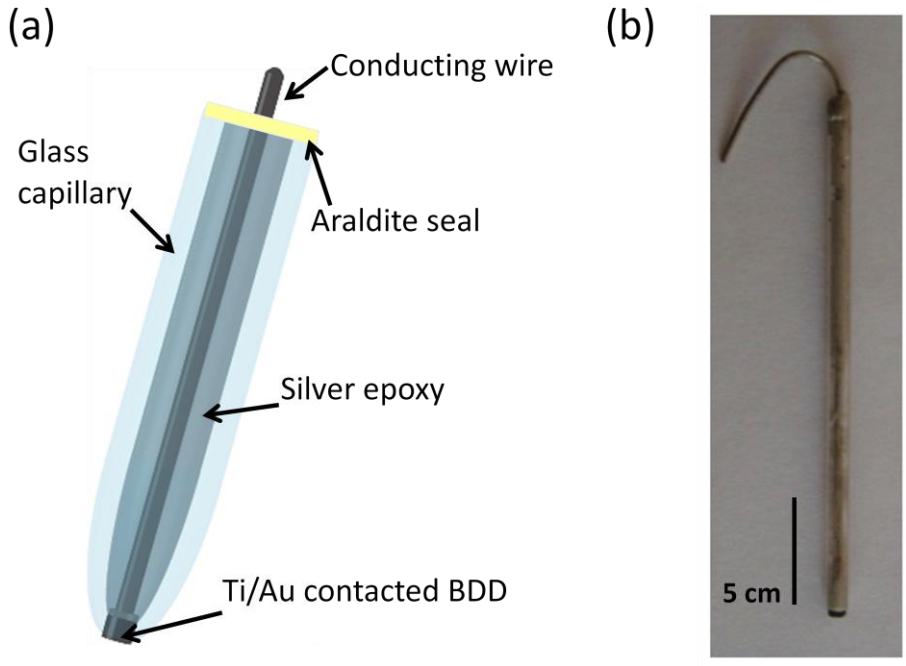

Figure 3.6: (a) Schematic and (b) photograph of fabricated 1 mm disc pBDD electrode.

3.4. ELECTROCHEMICAL CHARACTERISATION OF PBDD ELECTRODE

In order to verify that the fabrication process had no detrimental effect on the pBDD material and that a good insulating glass-pBDD seal had been formed, solvent windows were recorded in various supporting electrolytes. An example is shown in Figure 3.7 (a) where CVs were performed in 0.1 M KNO_3 at a scan rate of 50 mV s^{-1} using the fabricated pBDD 1 mm diameter disc electrode and commercially available Pt 2 mm diameter and glassy carbon 1.5 mm diameter disc electrodes. No preconditioning of the pBDD electrode was required in order to obtain reproducible voltammograms. The extended potential window of the pBDD electrode is clearly visible especially in the cathodic region where the current density does not reach 20 mA cm^{-2} until -2.4 V. The electrochemical process of water decomposition defines the range of the solvent window, where hydrogen and oxygen evolution occur at cathodic and anodic extremes respectively. Both of these reactions are known to occur via complex mechanisms involving adsorbed intermediates on the electrode surface.[46,47] In these cases, the activity of the electrode is a function of its surface structure and outer electron configuration e.g. on platinum the intermediates of water electrolysis can chemisorb via partially filled d-orbitals enabling efficient electrolysis. However, as Figure 3.7 (a) shows for the pBDD electrode, water decomposition occurs at high overpotentials, indicating these reactions are likely to be inhibited at the pBDD surface. As discussed in section 3.2, the surface of the diamond is oxygen-terminated with a variety of functional groups containing strong C-O (358 kJ mol^{-1}) and C=O bonds (805 kJ mol^{-1}). Rearrangement or breaking of these bonds in order to form intermediates is a likely factor in hindering the hydrogen and oxygen evolution reactions.

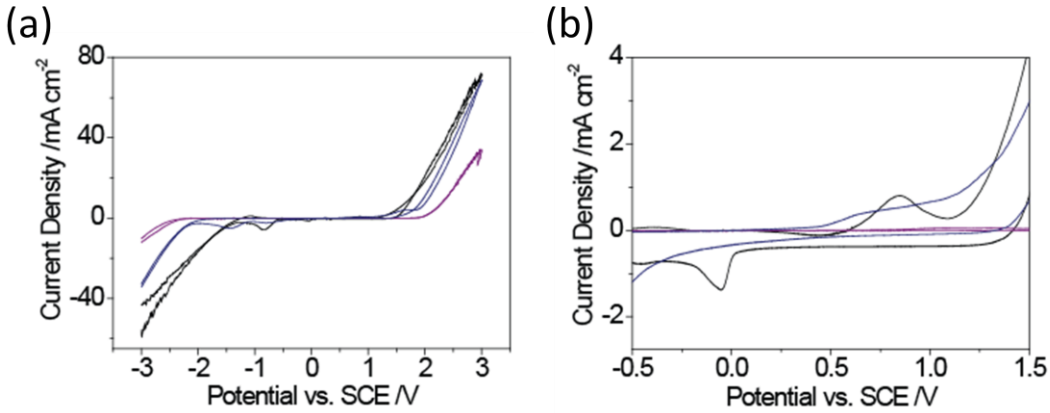

Figure 3.7: CVs in (a) aerated 0.1 M KNO_3 in the potential region of (a) -3 to 3 V and (b) -0.5 to 1.5 V for (purple) pBDD, (blue) glassy carbon and (black) Pt electrodes at a scan rate of 50 mV s^{-1}.

On a similar basis, oxygen reduction is absent on the CV for the pBDD electrode, but can be clearly observed on the Pt electrode at -0.05 V vs. SCE in Figure 3.7 (b). Again, oxygen reduction occurs through a mechanism were dioxygen molecules bind to the electrode surface. For Pt and glassy carbon electrodes, oxygen adsoprtion is facilitated by d-orbitals and quinone groups respectively.[48,49] However, at the oxygen-terminated pBDD electrode the surface is already saturated with stable oxygen functionalities, strongly hindering oxygen adsorption and resulting in an absent oxygen reduction signal.

Another feature of the diamond surface is the lack of easily ionisable surface groups, which consequently produces featureless voltammograms between -1.6 and +1.5 V with current densities of 0.1 mA cm^{-2} and no significant background processes apart from a capacitative contribution, as seen in Figure 3.7 (b). A capacitance value of ca. 4 µF cm^{-2} was calculated for the pBDD electrode at 0 V vs. SCE, approximately an order of magnitude smaller than that for Pt which was found to be 35 µF cm^{-2}. This low value is likely to be due to the lower density of states at the diamond

surface in comparison to a true metal and the lack of easily ionisable groups. The wide solvent window also indicates that there is no residual non-diamond like carbon or other contaminants on the diamond surface from the fabrication of the electrode.

The electrochemical response of the fabricated pBDD and commercial Pt electrodes were also compared using the electroactive species 10 mM $Ru(bpy)_3^{2+/3+}$ in 0.1 M KNO_3 Figure 3.8 (a) shows a near reversible single electron oxidation peak at 1.06 V vs. SCE for pBDD associated with $Ru^{2+/3+}$, with a ΔE_p of 67 mV and an i_p of 1.5 mA cm^{-2}. This peak appears at a less positive potential of 1.00 V vs. SCE at the Pt electrode with a ΔE_p of 110 mV and an i_p of 1.6 mA cm^{-2}. The larger ΔE_p could be due to Pt oxide formation on the electrode at these positive potentials effecting the rate of electron transfer. The signal from the pBDD electrode is much clearer due to the low background currents, especially in the aerated solution.

The reduction of the first bipyridine ligand π^* system to $[Ru^{II}(bpy)\ (bpy)\ (bpy^{-})]$ can also be seen at -1.5 V vs. SCE on the pBDD electrode. For most other electrode materials, the electrolysis of water does not allow the study of this process in aqueous solutions. This is exemplified by the response on the Pt electrode, where the reduction of water masks any other signal. The electrolysis of the bipyridine ligand on pBDD is similar to the redox potentials usually observed in acetonitrile, which is employed as a means of extending the solvent window of metal and glassy carbon electrodes.[50]

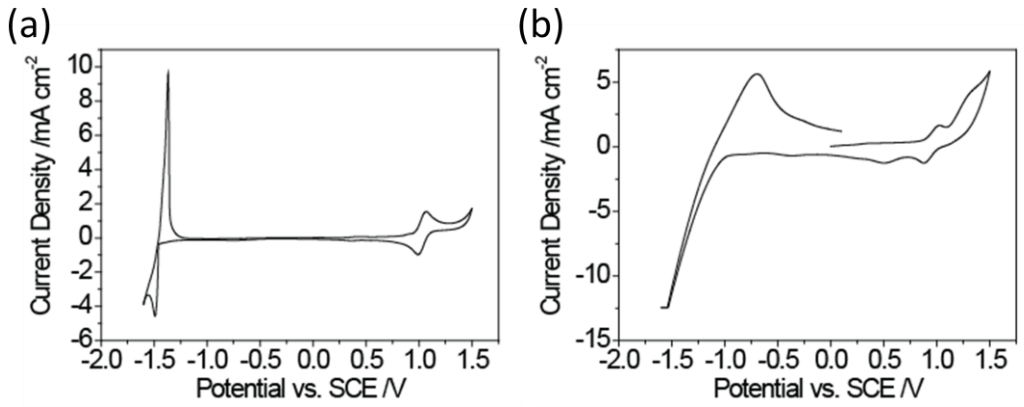

Figure 3.8: CVs in aerated 10 mM $Ru(bpy)_3^{2+/3+}$ in 0.1 M KNO_3 *for (a) pBDD and (b) Pt electrodes at a scan rate of 50 mV* s^{-1}.

The electrochemical response of the pBDD electrode was further characterised using various redox active species including $Ru(NH_3)_6^{3+/2+}$, $IrCl_6^{2-/3-}$, $Fe(CN)_6^{3-/4-}$ and $Fe^{2+/3+}$ as shown in Figures 3.9 and 3.10. The voltammetric data for scan rate dependance for $Ru(NH_3)_6^{3+/2+}$, $IrCl_6^{2-/3-}$ and $Fe(CN)_6^{3-/4-}$ is summarised in Table 3.1.

	0.1 mM $Ru(NH_3)_6^{3-/4-}$			10 mM $Ru(NH_3)_6^{3-/4-}$			0.1 mM $IrCl_6^{2-/3-}$			10 mM $IrCl_6^{2-/3-}$			0.1 mM $Fe(CN)^{3-/4-}$		
Scan Rate ($mV\ s^{-1}$)	ip^{red} (μA)	ip^{ox} (μA)	ΔEp (mV)	ip^{red} (μA)	ip^{ox} (μA)	ΔEp (mV)	ip^{ox} (μA)	ip^{red} (μA)	ΔEp (mV)	ip^{ox} (μA)	ip^{red} (μA)	ΔEp (mV)	ip^{ox} (μA)	ip^{red} (μA)	ΔEp (mV)
500	-0.41	0.34	67	-41.50	37.30	103	0.35	-0.32	61	32.00	-27.04	82	0.39	-0.39	77
300	-0.33	0.27	67	-33.30	30.10	91	0.28	-0.24	65	25.00	-20.96	80	0.31	-0.31	70
200	-0.28	0.23	66	-27.70	25.50	90	0.22	-0.19	65	19.00	-16.96	80	0.23	-0.23	66
100	-0.19	0.17	66	-19.30	18.30	80	0.15	-0.14	64	13.00	-12.13	78	0.19	-0.18	66
50	-0.14	0.12	71	-14.60	13.80	79	0.01	-0.10	65	9.00	-8.61	78	0.13	-0.13	69
20	-0.09	0.07	79	-8.96	8.36	77	0.07	-0.07	67	5.00	-4.97	77	0.09	-0.07	66
10	-0.07	0.06	83	-6.86	6.28	78	0.05	-0.05	71	3.00	-2.64	78	0.07	-0.07	68

Table 3.1: Analysis of CVs for $Ru(NH_3)_6^{3+/2+}$, $IrCl_6^{2-/3-}$ *and* $Fe(CN)_6^{3-/4-}$ *for various scan rates.*

The reversible nature of electron transfer for each species was analysed by comparing the experimental i_p to the theoretical i_p as defined in equation 3.1 and experimental and theoretical ΔE_p defined in equation 3.2. Due to precision laser micromachining and the lapped nature of the diamond surface, shown in Figure 3.5

(b), the electrode has a well-defined and reproducible surface area. Therefore it was possible to calculate the expected i_p and ΔE_p using equations 3.1 and 3.2,[51]

$$i_p = 0.4463 \left(\frac{F^3}{RT}\right)^{1/2} n^{3/2} A D^{1/2} c^* \upsilon^{1/2} \quad (3.1)$$

$$\Delta E_p = 2.3RT/nF \quad (3.2)$$

where R and F are the gas and Faraday constants and T is the temperature (23 ^oC). Using D = 8.8 x 10^{-6} cm^2 s^{-1},[52] 6.8 x 10^{-6} cm^2 s^{-1} [13] and 6.3 x 10^{-6} cm^2 s^{-1} [53,54] for $Ru(NH_3)_6^{3+/2+}$, $IrCl_6^{2-/3-}$ and $Fe(CN)_6^{3-/4}$ respectively, the experimental i_p was found to correspond well with theory and also demonstrated a linear dependence of oxidation i_p with $\upsilon^{1/2}$ (exemplified in the inset in Figure 3.9 (a) where r^2 of the linear fit is > 0.998) demonstrating semi-infinite linear diffusion of the reactant to the electrode surface.

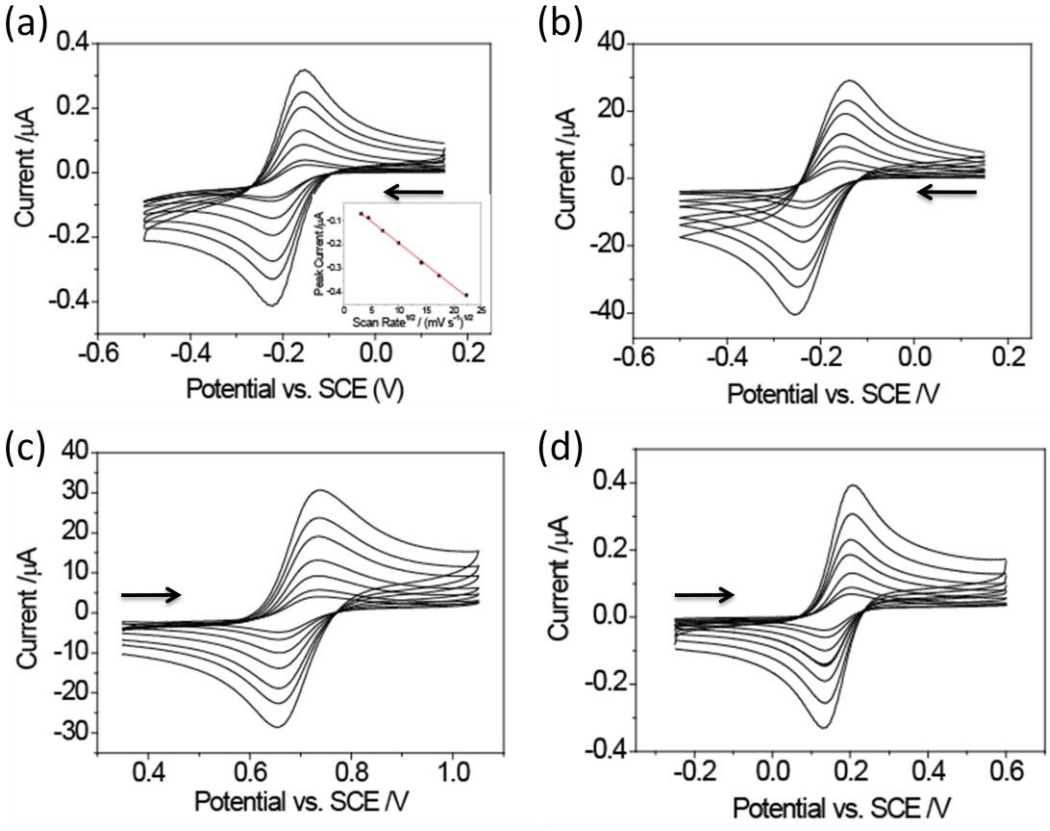

Figure 3.9: Background corrected CVs of (a) 0.1 mM (b) 10 mM $Ru(NH_3)_6^{3+/2+}$ (c) 10 mM $IrCl_6^{2-/3-}$ and (d) 0.1 mM $Fe(CN)_6^{3-/4-}$ in 0.1 M KNO_3 at various scan rates from 10 mV s^{-1} (smallest peak current to 500 mV s^{-1} (highest peak current).

From equation 3.2, for a reversible reaction a ΔE_p of 59 mV would be expected. For redox concentrations of 0.1 mM, as shown in Table 3.1, all three species exhibited close to reversible ΔE_p behaviour, e.g. for υ of 100 mV s^{-1} separations of 66 mV, 64 mV and 66 mV were recorded for $Ru(NH_3)_6^{3+/2+}$, $IrCl_6^{2-/3-}$ and $Fe(CN)_6^{3-/4}$ respectively.

$Ru(NH_3)_6^{3+/2+}$ is regarded as an outer-sphere redox mediator and therefore by definition expected to be unaffected by the chemical identity of the conducting surface. For the species used in these investigations, the E^o of $Ru(NH_3)_6^{3+/2+}$ is the most negative from the flatband potential (ca. 1 to 4 V vs. SCE for oxygen-terminated samples)[16,39,55] of p-type semiconducting pBDD. Therefore for semiconducting pBDD the electrolysis of $Ru(NH_3)_6^{3+/2+}$ is expected to occur when the surface is depleted of carriers, which is not the case for metallic-like material. Thus $Ru(NH_3)_6^{3+/2+}$ reduction should be sensitive to the electrical properties of pBDD. Previous studies have shown close to reversible behaviour for $Ru(NH_3)_6^{3+/2+}$ at hydrogen-terminated diamond with boron dopant levels thought to be below the metallic threshold, i.e. low 10^{19} atoms cm^{-3}.[10,11] This response was attributed to additional surface carriers due to the presence of sp^2 carbon or from hydrogen-termination of the surface.[56]

As discussed in section 3.1, the diamond used in this work is free from surface sp^2 carbon impurities, is oxygen-terminated and has an average boron level above the metallic threshold. Hence, it is not unexpected that close to reversible behaviour is observed. However, it must be noted that the results are an average response from the whole of the electrode surface. Due to the heterogeneous nature of pBDD,

certain individual grains on the surface may not be doped sufficiently to put them in the metal-like conductivity range, as shown in the graph if Figure 1.5.[34]

Figures 3.9 (a) and (b) show CVs for 0.1 mM and 10 mM $Ru(NH_3)_6^{3+/2+}$ in 0.1 M KNO_3 at various scan rates. An increase in ΔE_p can be seen for the redox couple at the higher concentration i.e. for a 100 mV s^{-1} scan, increasing the concentration by two orders of magnitude from 0.1 mM to 10 mM, increases the ΔE_p values from 66 mV to 80 mV. Similar affects are also observed for 10 mM $IrCl_6^{2-/3-}$. One possible explanation for this is that increasing concentrations of redox species challenge the pBDD to exchange more charge carriers per unit area. Even for metallic doped pBDD, compared with traditional metallic electrodes, there is a reduced density of states, thus at higher concentrations the ease of electron transfer may be greatly affected. Another possible rationale is that the pBDD has an intrinsic resistance which is governed by the number and mobility of charge carriers. The pBDD sample used in this work has a resistance of 150 mΩ as determined from four point probe measurements. When the electrode has to pass higher currents, ohmic drop (iR) across the diamond increases, which can affect ΔE_p. However, using Ohms' law, the iR drop at 500 mV s^{-1} for 10 mM solution is calculated as ca. 6 μV, showing this is unlikely.

Interestingly, previous studies on pBDD samples grown under the same conditions showed a dramatic increase in ΔE_p values with increasing concentration, the only difference being the area of electrode exposed to solution. For example, using an electrode of area 0.18 cm^2, compared to 7.83 x 10^{-3} cm^2 employed here, and a scan rate of 100 mV s^{-1}, increasing the concentration of $Ru(NH_3)_6^{3+/2+}$ from 0.1 mM to 10

mM, increased the ΔE_p values from 65 mV to 162 mV.[25] Even though the current densities are the same, the total current passed was larger in the latter case (hundreds of µA) compared with this work (tens of µA). *iR* drop across the pBDD for the larger electrode at a υ of 500 mV s^{-1} is ca. 90 µV, which can still be considered negligible and indicates that affects such as solution resistance is playing a role.

Figure 3.9 (c) shows CVs at the fabricated disc pBDD electrode for the oxidation of 0.1 mM $Fe(CN)_6^{3-/4-}$ in 0.1 M KNO_3 giving ΔE_p values close to reversible behaviour (Table 3.1). The wave shapes indicate fast electron kinetics (i.e. diffusion control) for the redox electrochemistry of $Fe(CN)_6^{3-/4-}$ at heavily doped pBDD which has been oxygen-terminated by boiling in acid. This suggests an electron transfer rate (k_r) >> 0.002 cm s^{-1} assuming k_t = 0.002 cm s^{-1}. Extensive studies of $Fe(CN)_6^{3-/4-}$ on traditional electrode materials have shown a complex electrochemical response dependent on the electrode material, as well as supporting electrolyte type, redox species concentration and surface chemical state/functionalities.[57,58] Several papers have presented voltammetry of $Fe(CN)_6^{3-/4-}$ at highly and heavily boron doped pBDD electrodes where it is suggested that electron transfer kinetics are slower at an oxygen-terminated pBDD surface in comparison with hydrogen-terminated samples.[10,16,59,60] In contrast, a number of studies have found that after anodic pretreatment of pBDD, an increase in charge transfer was achieved i.e. ΔE_p values decreased from 200 to 90 mV.[17,61] The effect of surface termination on electron transfer kinetics of $Fe(CN)_6^{3-/4-}$ has been attributed to several factors including the potential of the reaction plane[12], this is where the negative charge on the oxygen containing groups can repel negatively charged redox species. Site-blocking oxygen functional groups have also been suggested as inhibiting electron transfer.[10,61] As

such, it is beneficial to relate the electrochemical response to the chemical groups present on our fabricated electrode surface.

As discussed in section 3.2, the functional groups which reside on the diamond surface are dependent on crystal orientation and the method of termination. From the XPS spectra in Figure 3.4, for the acid treated, lapped pBDD used herein there was a relatively low O/C 1s ratio of 10 %, with 8.5 % forming hydroxyl or ether groups and 1.5 % involved in carbonyl and ester groups. A relatively large percentage of the C 1s peak i.e. 18 % was due to carbon bonded to hydrogen. The low amount of carbonyl and ester groups on the diamond surface may account for the almost reversible response of $Fe(CN)_6^{3-/4-}$, where more available sites for chemical-electrode interactions are available. Furthermore, the metallically-doped boron concentration ensures that the loss of some surface hydrogen does not affect the electron transfer capabilities. This corresponds with reports from Girard *et al.* who grew HFCVD pBDD with boron concentrations of 1×10^{20} atom cm^{-3} and showed that mild anodic oxidation (1.6 V vs. MSE for 5 s in 0.5 M H_2SO_4) gave a carbon bonded to hydrogen percentage of ca. 10 %, which interestingly increased to 37 % for more extreme anodic pretreatments (3.5 V vs. MSE for 5 s in 0.5 M H_2SO_4).[40] This coincided with a decrease in O/C 1s from 20 % to 10 %, and an improved reversible response (ΔE_p values decreased from 750 mV to 300 mV) for 5 mM $Fe(CN)_6^{3-/4-}$ in 0.5 M KOH. In fact, the two previously mentioned studies which showed improved reversibility after electrochemical pretreatments, both performed extreme anodic polarisation of the pBDD. The electrochemical response of the fabricated electrode was stable even after potential cycling between 3 and -3V.

Investigations of the classic inner-sphere redox couple $Fe^{3+/2+}$, at sp^2 carbon electrodes, have shown that electron transfer kinetics can be strongly affected by the electrode surface, most notably the presence of oxides.[62] Figure 3.10 shows a CV for 1 mM $Fe^{3+/2+}$ in 0.1 M $HClO_4$ at a scan rate of 100 mV s^{-1} at the 1 mm diameter pBDD disc electrode. The ΔE_p of 630 mV indicates a quasi-reversible system, falling between the values observed by others for as-deposited (ΔE_p of 837 mV) and oxygen-terminated (ΔE_p of 466 mV) semi-metallic pBDD with similar analyte concentrations.[11,12] However, severe anodic pretreatments have been shown to diminish the reversibility of $Fe^{3+/2+}$ in comparison to the hydrogen-terminated surface.[63] In a similar approach, as with $Fe(CN)_6^{3-/4-}$, it has been suggested that a specific oxygen containing functional group affects the electron transfer kinetics. In this case, carbonyls are responsible for facilitating $Fe^{3+/2+}$ electron transfer, as has been previously suggested for glassy carbon electrodes.[13,57] As shown in Figure 3.4 (b), the XPS shows that while extremely oxidised functional groups are present on the surface of the pBDD used in this study, only a relatively small amount (a maximum of 1.5 %) of the C 1s peak is due to carbonyl groups, which could explain the observed response.

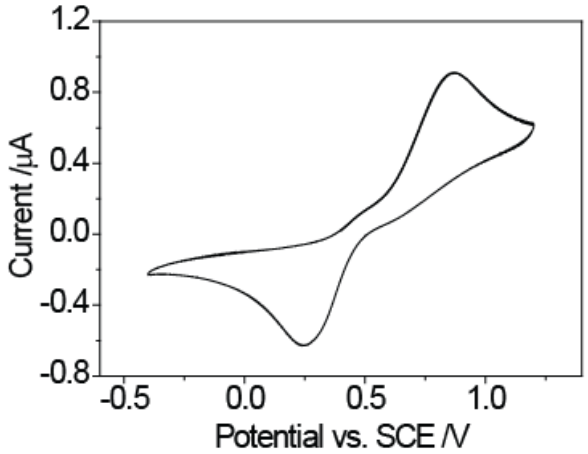

Figure 3.10: CV for the reduction of 1 mM $Fe^{3+/2+}$ in 0.1 M $HClO_4$ at a scan rate of 100 mV s^{-1}.

Longevity testing was also performed using the fabricated electrodes in order to assess the stability of the electrochemical signal. Figure 3.11 shows consecutive CVs for the electrolysis of 0.1 mM $FcTMA^+$ in 0.1 M KCl run every 2 hours over a 12 hour period, leaving the electrode submerged in the solution. All voltammograms show consistent peak currents and separations with no evidence of blocking of the electrode.

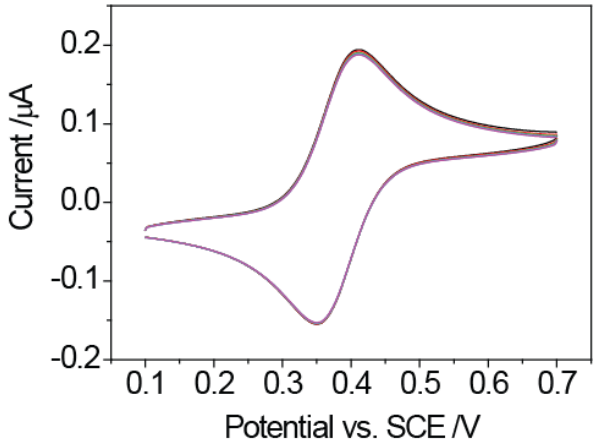

Figure 3.11: CVs for the oxidation of 0.1 mM $FcTMA^+$ in 0.1 M KCl over a 12 hour period at 100 mV s^{-1}.

In order to investigate the stability of the pBDD surface in more challenging conditions, the electrode was used to electrochemically oxidise chlorophenols which have been reported to produce oligomers and polymers which can foul the electrode surface during the oxidation process.[64,65] Holding the electrode at anodic potentials has been suggested to generate $OH^{\cdot}$ which can oxidatively remove the fouling polymer layer.[64,66] For example, it has been shown that by holding the pBDD at 2.64 V for 4 mins the electrode can be effectively reactivated after cycling in 5 mM 2,4-dichlorophenol.[67]

Figure 3.12 (a) presents 10 consecutively recorded CVs for the oxidation of 0.1 mM 2-chlorophenol in phosphate buffer, pH 7 at a scan rate of 100 mV s^{-1}. After the first cycle, new peaks appear at ca. 0.27 V vs. SCE and have been attributed to the oxidation and reduction of benzoquinone, a product of chlorophenol oxidation. A decrease in the oxidation current of 2-chlorophenol at 0.65 V can be observed with each cycle, indicating fouling of the electrode by this benzoquinone layer. In order to obtain reproducible CVs, it was necessary to return the pBDD surface to its original state. Figure 3.12 (b) shows the first CV for the oxidation of 2-chlorophenol at a newly fabricated electrode in solid black, the purple line shows a CV using the same electrode which had become fouled after 10 cycles in 2-chorophenol, then held at -4 V for 3 min. These cleaning parameters were necessary to clean the electrode at such high phenol concentrations. At this potential an acidic environment is created at the electrode surface, also bubbling due to hydrogen gas evolution occurs. The voltammograms show that by holding the electrode at -4 V, removal of the fouling layer occurs. It is important to note that the oxygen-terminated surface is stable even after experiencing these extreme potentials, in comparison to the changing nature of a hydrogen-terminated surface.

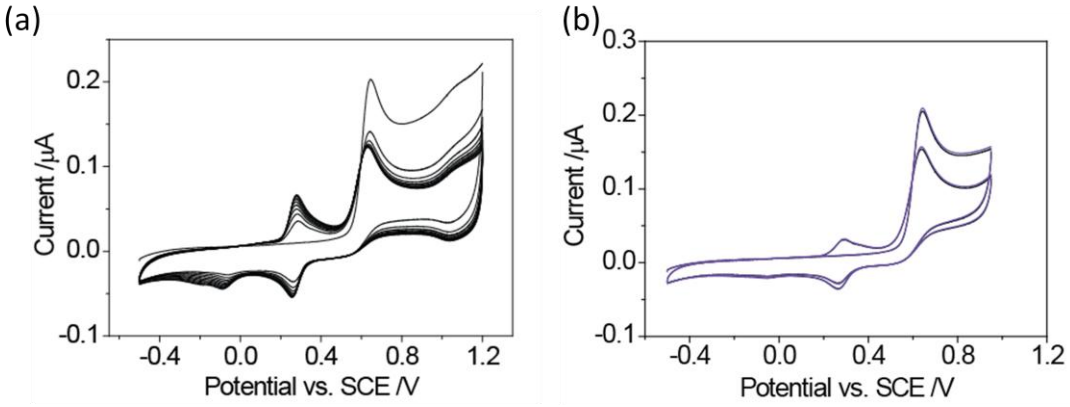

Figure 3.12: CVs for the oxidation of 0.1 mM 2-chlorophenol in phosphate buffer, pH 7 at a scan rate of 100 mV s^{-1} (a) showing fouling of pBDD during cycling without a cleaning step and (b) at a fresh pBDD electrode (black) and after subsequent cleaning step of -4 V for 3 min (purple).

3.5. CONCLUSION

The pBDD material used in this work was characterised with various techniques. AFM showed that after lapping the pBDD had grain sizes ranging from 2 – 20 µm. The average roughness of the surface within a grain was shown to be 1 – 2 nm, with step heights between grains ranging from 4 to 7 nm. AFM and FE-SEM were correlated to show that the larger, less doped grains were higher in topography. Micro-Raman showed that the diamond surface was heterogeneous, where larger grains have lower levels of boron than the smaller grains present. However, overall it is shown by SIMs, that the pBDD had an average boron concentration greater than the metallic threshold of > 3 x 10^{20} boron atoms cm^{-3}. A Fano resonance was observed in all areas of the pBDD using micro-Raman, even in the lower doped regions indicating that boron concentration was ≥ 1 x 10^{20} atoms cm^{-3}. Raman also indicated that no non-diamond carbon was present, even at grain boundaries. The chemical nature of the diamond surface was investigated using XPS and was found to be oxygen-terminated after acid treatments. A variety of oxygen containing functional groups were found to be present on the diamond surface, with 8.5 % of the C 1s peak due to hydroxyl and ether groups, and 1.5 % due to ester and carbonyl groups.

A robust 1 mm diameter disc pBDD electrode was fabricated. Glass sealing was found to give good insulation around the diamond electrode and provided an electrode format which was very easy to use. These electrodes were tested using chemical standard inner- and outer-sphere redox mediators and were found to give current-voltage responses close to reversibility for $Ru(NH_3)_6^{3+/2+}$, $IrCl_6^{2-/3-}$ and

$Fe(CN)_6^{3-/4}$, even at high concentrations i.e. 10 mM. Due to hindered water electrolysis and oxygen reduction, the pBDD electrodes were found to give extended solvent windows with lower background currents in comparison to a commercial Pt electrode, both of which would provide a clear advantage in electroanalysis. The stability of the pBDD electrode was also investigated in the oxidation of chlorophenol, where the robustness and stability of diamond was used to advantage for *in-situ* cleaning.

3.6. REFERENCES

(1) Pleskov, Y. V. *Russ. J. Electrochem.* **2002**, *38*, 1275.
(2) Xu, J. S.; Granger, M. C.; Chen, Q. Y.; Strojek, J. W.; Lister, T. E.; Swain, G. M. *Anal. Chem.* **1997**, *69*, A591.
(3) Compton, R. G.; Foord, J. S.; Marken, F. *Electroanalysis* **2003**, *15*, 1349.
(4) Ramesham, R.; Rose, M. F. *Diamond Relat. Mater.* **1997**, *6*, 17.
(5) Kraft, A. *Int. J. Electrochem. Sci.* **2007**, *2*, 355.
(6) Luong, J. H. T.; Male, K. B.; Glennon, J. D. *Analyst* **2010**, *135*, 3008.
(7) Toghill, K. E.; Compton, R. G. *Electroanalysis* **2010**, *22*, 1947.
(8) Alehashem, S.; Chambers, F.; Strojek, J. W.; Swain, G. M.; Ramesham, R. *Anal. Chem.* **1995**, *67*, 2812.
(9) Angus, J. C.; Martin, H. B.; Landau, U.; Evstefeeva, Y. E.; Miller, B.; Vinokur, N. *New Diamond Front. Carbon Technol.* **1999**, *9*, 175.
(10) Granger, M. C.; Swain, G. M. *J. Electrochem. Soc.* **1999**, *146*, 4551.
(11) Granger, M. C.; Witek, M.; Xu, J. S.; Wang, J.; Hupert, M.; Hanks, A.; Koppang, M. D.; Butler, J. E.; Lucazeau, G.; Mermoux, M.; Strojek, J. W.; Swain, G. M. *Anal. Chem.* **2000**, *72*, 3793.
(12) Yagi, I.; Notsu, H.; Kondo, T.; Tryk, D. A.; Fujishima, A. *J. Electroanal. Chem.* **1999**, *473*, 173.
(13) Fischer, A. E.; Show, Y.; Swain, G. M. *Anal. Chem.* **2004**, *76*, 2553.
(14) Nishimura, K.; Das, K.; Glass, J. T. *J. Appl. Phys.* **1991**, *69*, 3142.
(15) Werner, M.; Job, R.; Zaitzev, A.; Fahrner, W. R.; Seifert, W.; Johnston, C.; Chalker, P. R. *Phys. Status Solidi A* **1996**, *154*, 385.
(16) Actis, P.; Denoyelle, A.; Boukherroub, R.; Szunerits, S. *Electrochem. Commun.* **2008**, *10*, 402.
(17) Goeting, C. H.; Marken, F.; Gutierrez-Sosa, A.; Compton, R. G.; Foord, J. S. *New Diamond Front. Carbon Technol.* **1999**, *9*, 207.
(18) Wang, M.; Simon, N.; Decorse-Pascanut, C.; Bouttemy, M.; Etcheberry, A.; Li, M. S.; Boukherroub, R.; Szunerits, S. *Electrochim. Acta* **2009**, *54*, 5818.
(19) Latto, M. N.; Pastor-Moreno, G.; Riley, D. J. *Electroanalysis* **2004**, *16*, 434.
(20) Swain, G. M.; Ramesham, R. *Anal. Chem.* **1993**, *65*, 345.
(21) Nebel, C. E.; Ristein, J. *Thin-Film Diamond II*; Elsevier Academic Press, 2004; Vol. 77.
(22) Bennett, J. A.; Wang, J. A.; Show, Y.; Swain, G. M. *J. Electrochem. Soc.* **2004**, *151*, E306.
(23) Balmer, R. S.; Brandon, J. R.; Clewes, S. L.; Dhillon, H. K.; Dodson, J. M.; Friel, I.; Inglis, P. N.; Madgwick, T. D.; Markham, M. L.; Mollart, T. P.; Perkins, N.; Scarsbrook, G. A.; Twitchen, D. J.; Whitehead, A. J.; Wilman, J. J.; Woollard, S. M. *J. Phys.: Condens. Matter* **2009**, *21*.
(24) Martin, H. B.; Argoitia, A.; Landau, U.; Anderson, A. B.; Angus, J. C. *J. Electrochem. Soc.* **1996**, *143*, L133.
(25) Wilson, N. R.; Clewes, S. L.; Newton, M. E.; Unwin, P. R.; Macpherson, J. V. *J. Phys. Chem. B* **2006**, *110*, 5639.
(26) Zuo, S. S.; Yaran, M. K.; Grotjohn, T. A.; Reinhard, D. K.; Asmussen, J. *Diamond Relat. Mater.* **2008**, *17*, 300.
(27) Miller, J. B.; Brandes, G. R. *J. Appl. Phys.* **1997**, *82*, 4538.
(28) Janssen, G.; Vanenckevort, W. J. P.; Vollenberg, W.; Giling, L. J. *Diamond Relat. Mater.* **1992**, *1*, 789.
(29) Hird, J. R.; Field, J. E. *Proc. R. Soc. London, A* **2004**, *460*, 3547.
(30) Gheeraert, E.; Gonon, P.; Deneuville, A.; Abello, L.; Lucazeau, G. *Diamond Relat. Mater.* **1993**, *2*, 742.
(31) Pruvost, F.; Bustarret, E.; Deneuville, A. *Diamond Relat. Mater.* **2000**, *9*, 295.

(32) Bernard, M. *Diamond Relat. Mater.* **2004**, *13*, 282.
(33) Levy-Clement, C.; Ndao, N. A.; Katty, A.; Bernard, M.; Deneuville, A.; Comninellis, C.; Fujishima, A. *Diamond Relat. Mater.* **2003**, *12*, 606.
(34) Lagrange, J. P.; Deneuville, A.; Gheeraert, E. *Diamond Relat. Mater.* **1998**, *7*, 1390.
(35) Thomas, R. E.; Rudder, R. A.; Markunas, R. J. *J. Vac. Sci. Technol., A* **1992**, *10*, 2451.
(36) Goeting, C. H.; Marken, F.; Gutierrez-Sosa, A.; Compton, R. G.; Foord, J. S. *Diamond Relat. Mater.* **2000**, *9*, 390.
(37) Notsu, H.; Yagi, I.; Tatsuma, T.; Tryk, D. A.; Fujishima, A. *J. Electroanal. Chem.* **2000**, *492*, 31.
(38) Notsu, H.; Fukazawa, T.; Tatsuma, T.; Tryk, D. A.; Fujishima, A. *Electrochem. Solid-State Lett.* **2001**, *4*, H1.
(39) Rao, T. N.; Tryk, D. A.; Hashimoto, K.; Fujishima, A. *J. Electrochem. Soc.* **1999**, *146*, 680.
(40) Girard, H.; Simon, N.; Ballutaud, D.; Herlern, M.; Etcheberry, A. *Diamond Relat. Mater.* **2007**, *16*, 316.
(41) Ferro, S.; Dal Colle, M.; De Battisti, A. *Carbon* **2005**, *43*, 1191.
(42) Thoms, B. D.; Russell, J. N.; Pehrsson, P. E.; Butler, J. E. *J. Chem. Phys.* **1994**, *100*, 8425.
(43) Pehrsson, P. E.; Long, J. P.; Marchywka, M. J.; Butler, J. E. *Appl. Phys. Lett.* **1995**, *67*, 3414.
(44) Tachibana, T.; Williams, B. E.; Glass, J. T. *Phys. Rev. B* **1992**, *45*, 11975.
(45) Wightman, R. M.; Wipf, D. O. *Electroanal. Chem.* **1989**, *15*, 267.
(46) Correia, A. N.; Machado, S. A. S. *Electrochim. Acta* **1998**, *43*, 367.
(47) Damjanovic, A.; Dey, A.; Bockris, J. O. M. *Electrochim. Acta* **1966**, *11*, 791.
(48) Yeager, E. *Electrochim. Acta* **1984**, *29*, 1527.
(49) Yeager, E. *J. Mol. Catal.* **1986**, *38*, 5.
(50) Rillema, D. P.; Allen, G.; Meyer, T. J.; Conrad, D. *Inorg. Chem.* **1983**, *22*, 1617.
(51) Bard, A. J.; Faulkner, L. R. *Electrochemical methods: Fundamentals and Applications*; John Wiley & Sons, INC., 2001.
(52) Macpherson, J. V.; Ohare, D.; Unwin, P. R.; Winlove, C. P. *Biophys. J.* **1997**, *73*, 2771.
(53) Rice, R. J.; McCreery, R. L. *Anal. Chem.* **1989**, *61*, 1637.
(54) Conyers, J. L.; White, H. S. *Anal. Chem.* **2000**, *72*, 4441.
(55) Girard, H. A.; Simon, N.; Ballutaud, D.; Etcheberry, A. *C. R. Chim.* **2008**, *11*, 1010.
(56) Liu, F. B.; Wang, J. D.; Liu, B.; Li, X. M.; Chen, D. R. *Diamond Relat. Mater.* **2007**, *16*, 454.
(57) Chen, P. H.; Fryling, M. A.; McCreery, R. L. *Anal. Chem.* **1995**, *67*, 3115.
(58) Ranganathan, S.; Kuo, T. C.; McCreery, R. L. *Anal. Chem.* **1999**, *71*, 3574.
(59) Marken, F.; Paddon, C. A.; Asogan, D. *Electrochem. Commun.* **2002**, *4*, 62.
(60) Boukherroub, R.; Wallart, X.; Szunerits, S.; Marcus, B.; Bouvier, P.; Mermoux, M. *Electrochem. Commun.* **2005**, *7*, 937.
(61) McEvoy, J. P.; Foord, J. S. *Electrochim. Acta* **2005**, *50*, 2933.
(62) Hu, I. F.; Karweik, D. H.; Kuwana, T. *J. Electroanal. Chem.* **1985**, *188*, 59.
(63) Ferro, S.; De Battisti, A. *Electrochim. Acta* **2002**, *47*, 1641.
(64) Gattrell, M.; Kirk, D. W. *J. Electrochem. Soc.* **1993**, *140*, 903.
(65) Tahar, N. B.; Savall, A. *J. Electrochem. Soc.* **1998**, *145*, 3427.
(66) Rodgers, J. D.; Jedral, W.; Bunce, N. I. *Environ. Sci. Technol.* **1999**, *33*, 1453.
(67) Terashima, C.; Rao, T. N.; Sarada, B. V.; Tryk, D. A.; Fujishima, A. *Anal. Chem.* **2002**, *74*, 895.

CHAPTER 4

Amperometric Oxygen Sensor Based on a Platinum Nanoparticle-Modified pBDD Disc Electrode

Pt nanoparticle (NP)-modified pBDD disc electrodes have been fabricated and employed as amperometric sensors for the determination of dissolved oxygen concentration in aqueous solution. Electrodeposition of Pt onto the diamond electrodes was optimized so as to give the maximum oxygen reduction peak current with the lowest background signal. Pt NPs, >0−10 nm diameter, were found to deposit randomly across the pBDD electrode, with no preference for grain boundaries. The more conductive grains were found to promote the formation of smaller nanoparticles at higher density. With the use of potential step chronoamperometry, in which the potential was stepped to a diffusion-limited value, a four electron oxygen reduction process was found to occur at the Pt NP-modified pBDD electrode. Furthermore the chronoamperometric response scaled linearly with dissolved oxygen concentration, varied by changing the oxygen/nitrogen ratio of gas flowed into solution. The sensor was used to detect dissolved oxygen concentrations with high precision over the pH range 4−10.

4.1. INTRODUCTION

The detection of dissolved oxygen, particularly in aqueous solutions, has been of great interest and study over the last fifty years due to its importance in environmental monitoring, industrial safety, fuel cell technology and the automotive industry.[1] Various dissolved oxygen sensors are available commercially including, for example, optical, polarographic and galvanic-based sensors.[2] The most common dissolved oxygen sensor is based on the Clark-type polarographic probe,[3] in which a permselective membrane (most commonly poly-(tetrafluoroethylene)), separating an internal filling solution and the exterior solution, is used to detect oxygen amperometrically at a platinum (Pt) electrode. A potential is applied to the electrode to reduce oxygen, often under diffusion-controlled conditions and the current that flows is proportional to the concentration of oxygen present.[4] These sensors have good detection limits and accuracy, but the use of a permselective membrane severely limits the response time. Furthermore, if the electrode becomes blocked, the reliability is compromised and so routine conditioning or membrane replacement is common. [5]

The mechanism for the electrochemical reduction of oxygen has been widely investigated for various electrode materials over a wide range of solution conditions. The mechanism is complicated and has been found to be dependent on solution pH, electrode material and size (mass transport rate).[6] Two limiting reaction pathways have been identified: reduction of oxygen to hydrogen peroxide via a two-electron pathway[7,8] and reduction of oxygen to water by a four-electron pathway.[9]

The reduction of oxygen at Pt is generally considered to occur via a four-electron process, as shown in equations (4.1) and (4.2), for alkaline and acidic solutions, respectively.[10] However, it has also been demonstrated that high rates of mass transport can lower the apparent number of electrons involved.[11-13]

$$O_2 + 2H_2O + 4e^- \rightarrow 4OH^- \qquad (4.1)$$

$$O_2 + 4H^+ + 4e^- \rightarrow 2H_2O \qquad (4.2)$$

pBDD is presently the subject of considerable interest as an electrode material. The very wide potential window in aqueous solution, low background currents, and resistance to fouling[14-16] make it particularly attractive for use in electroanalysis. BDD is also resistant to corrosion under both acidic and alkaline conditions, as well as at extreme positive and negative applied potentials,[17] and is stable at high temperatures and pressures.[16]

The electrochemical reduction of oxygen has been shown to be kinetically retarded at impurity-free pBDD compared to other electrode materials. For example, previous work by Yano *et al.*[18,19] demonstrated that after cycling to + 1.8 V vs. Ag/AgCl, in alkaline solution to remove/deactivate sp^2-type carbon impurities, pBDD was insensitive to oxygen reduction, in both acidic and basic media. There has thus been interest in the functionalisation of pBDD surfaces in order to enhance the sensitivity to amperometric oxygen detection, whilst retaining as many of the useful properties of the BDD as possible.

Various approaches have been investigated, ranging from functionalisation with metal nanoparticles, such as gold[20,21] to the use of quinone[22] and bismuth films.[23] In

the case of gold functionalisation, it was found that gold nanoparticles on pBDD had an oxygen catalytic efficiency in both acid[21] and alkaline[24] solutions. On vacuum-evaporated Au nanoclusters on pBDD films, Yagi *et al.*[25] deduced that oxygen reduction occurred via a four-electron pathway in acidic solution. This was also the case for alkaline solution in the work of Szunerits *et al.*[24] for Au NPs electrochemically reduced onto the surface of pBDD. Wang *et al.* carried out oxygen reduction studies on Pt NPs (10- 300 nm in diameter) electrodeposited on hydrophobic hydrogen-terminated pBDD films. Due to a weak attachment to the hydrophobic surface it was necessary to anchor the particles in position using a secondary intrinsic diamond layer, grown onto the surface after Pt deposition.[26] These Pt-pBDD electrodes were shown to have a very similar oxygen reduction response, in oxygen saturated solution conditions, to clean Pt foil.

Despite the growing body of work on the electrocatalytic reduction of oxygen at functionalized diamond surfaces, there has hitherto been little or no work exploring the capabilities of functionalized pBDD as a quantitative amperometric oxygen sensor. Thus, given the exemplary electrocatalytic properties of Pt towards oxygen reduction,[10] in this paper we investigate the electrodeposition conditions which produce the most favourable stable Pt-pBDD composite structure for the amperometric detection of oxygen, over a wide range of oxygen concentrations and pH (4-10) values. Hydrophilic oxygen terminated surfaces are employed to maximise attachment strengths of the Pt NP to the pBDD surface. Specifically, we demonstrate how to optimise the current signal arising from oxygen reduction at electrically-contacted Pt particles on pBDD while simultaneously minimising the overall background current. Consistent with previous work we show that pBDD is an

attractive conducting support material for this work as it exhibits low background signals.[27]

4.2. RESULTS AND DISCUSSION

4.2.1 **pBDD Disc Electrode Characterisation**

The 1 mm diameter disc pBDD electrodes described and characterised in Chapter 3, were used in the work. Figure 4.1 shows CVs recorded at 100 mV s^{-1} with a (a) 1 mm diameter pBDD disc electrode and (b) 3 mm Pt disc electrode in deaerated (nitrogen saturated: black line) and aerated (red line) 0.1 M KNO_3 solutions. The currents have been normalized by electrode area and are presented as current density to enable comparison between the two electrodes. Figure 4.1 (black trace) clearly shows the greatly minimized background current for pBDD compared with Pt and the extended solvent window. In this instance, background currents are due to several factors including surface oxidation/reduction processes, hydrogen adsorption/desorption, double layer charging, solvent decomposition *etc*,[28] which are relatively small at the pBDD surface over the potential range shown. The inset to Figure 4.1 (a) shows that similar data are recorded with pBDD not subjected to a laser cutting process. This result thus confirms that the laser cutting process had no detrimental effect on the quality of the diamond electrode surface, for example through the introduction of graphitic impurities, which would act to narrow the solvent window.

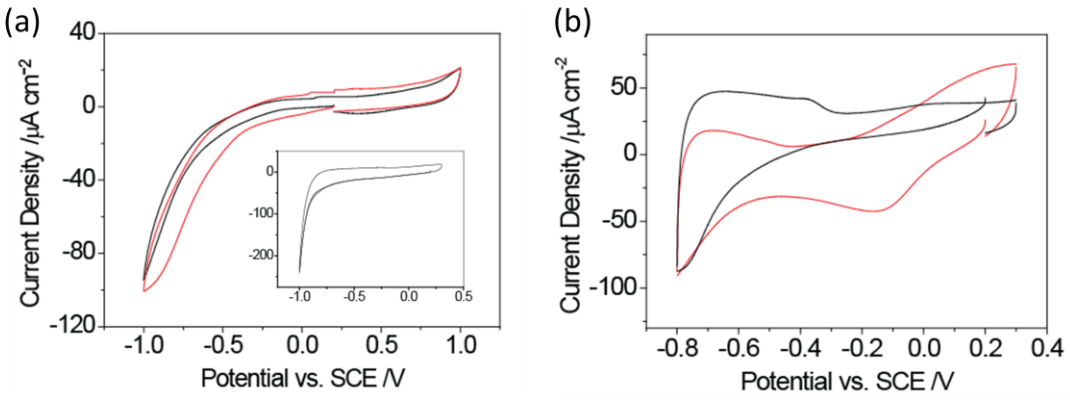

Figure 4.1: CVs recorded at a (a) 1 mm diameter pBDD disc electrode and (b) 3 mm diameter platinum disc electrode, in nitrogen-saturated (black) and aerated (red) 0.1 M KNO_3 at a scan rate of 100 mV s^{-1}. The inset to part (a) shows the background response of pBDD not subject to a laser cutting procedure.

In aerated solution (red trace), a reduction peak can be clearly identified at the platinum electrode occurring ~ -0.175 V vs. SCE. This is in the potential range for oxygen reduction on Pt[11] and is of the magnitude expected. A particularly interesting aspect of the CV for aerated solution with pBDD is that the response appears almost featureless, and there is no clearly discernable wave for oxygen reduction, in the potential range investigated, consistent with previous work.[29]

4.2.2 **Pt NP Electrodeposition and Optimisation**

To improve the sensitivity of pBDD towards amperometric oxygen detection, while retaining the low background currents inherent with pBDD electrodes (to aid in low concentration detection), decoration of the surface with electrodeposited Pt particles of different size and density was explored. The main aim was to achieve minimal background current from processes at the Pt particles, which scale with surface area, whilst obtaining a well-defined and quantitative signal for oxygen reduction. Pt was electrodeposited onto the pBDD electrode surface using chronoamperometry in a

quiescent solution containing 1 mM K_2PtCl_6 in 0.1 M HCl solution. As discussed below, a high driving force was used to ensure a high nucleation rate and thus a high density of small particles. Different deposition times were investigated, to elucidate the effect of platinum particle size and density on subsequent measurements of oxygen reduction.

Electrodeposition potentials more negative than -1.0 V gave noisy chronoamperometric signals due to concomitant H_2 evolution at the deposited Pt.[30] A potential of -1.0 V was therefore the most negative driving potential that could be applied without the detrimental interfering effects of H_2 evolution. Figure 4.2 shows a series of CVs of oxygen reduction in aerated solution for pBDD electrodes subjected to Pt electrodeposition times in the range 0.1 to 60 s. Comparing the CV for a 0.1 s Pt electrodeposition time (curve (ii)) with the background signal (curve (i)), it can be seen that a significant broad voltammetric feature appears, once Pt is on the surface, although the reduction process is highly irreversible. Indeed, the inflexion in the current-voltage characteristic at ca. -0.5 V tentatively suggests that reduction may occur as two, two electron transfer processes due to high mass transport to ultra-small particles at low density.[31]

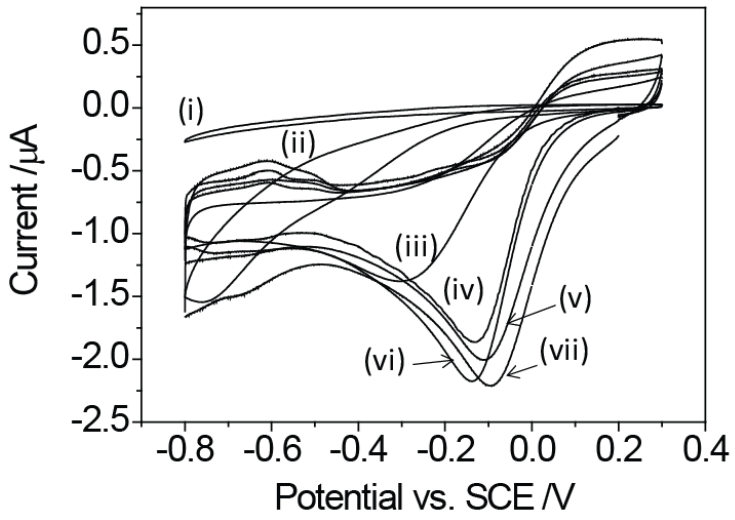

Figure 4.2: CVs for the reduction of oxygen in aerated 0.1 M KNO_3 at a scan rate of 50 mV s^{-1}, at (i) a pBDD unmodified electrode and ((ii)−(vii)) Pt NP-modified pBDD electrodes where the Pt NPs were deposited at −1.0 V for (ii) 0.1, (iii) 0.25, (iv) 0.50, (v) 1, (vi) 5, and (vii) 30 s.

As the Pt electrodeposition time was increased, a well-defined peak current developed for oxygen reduction, such that the voltammetric response is characteristic of planar diffusion. With increased Pt electrodeposition times the peak current moves to increasingly anodic potentials, indicating that the oxygen reduction reaction generally becomes increasingly more favourable as the quantity of Pt on the surface increases. Figure 4.2 indicates that the reduction current gradually increases with increasing Pt electrodeposition time up to 5 s. The same peak current (ca. 2.15 μA; background subtracted) is seen for times ≥ 5 s. Optimum deposition parameters of -1.0 V for 5 s (curve (vi)) were chosen for subsequent studies as these conditions gave low background currents, due to the reduced amount of Pt on the surface, with good oxygen amperometric detection sensitivity, which could be quantitatively described (*vide infra*).

4.2.3 **Pt NP Characterisation**

FE-SEM and AFM were used to characterize the surface of Pt NP-modified pBDD electrodes for the deposition parameters defined above. Figures 4.3 (a) and (b) show typical images at different magnifications of a Pt NP-modified pBDD electrode (Pt electrodeposited at -1.0 V for 5 s) using FE-SEM. Using the In-lens detector it is possible to resolve both the underlying grain structure of the pBDD and the Pt particle distribution.[32] In Figure 4.3 (b) the Pt NPs can be seen to be deposited randomly over the pBDD surface with no evidence of preferential deposition at grain boundaries. Grain boundaries have been suggested as the main electrochemically active sites on other pBDD samples,[33] however, the data in Figure 4.3 is consistent with our previous conducting-AFM studies[34] and metal deposition data[32] and work by others.[35]

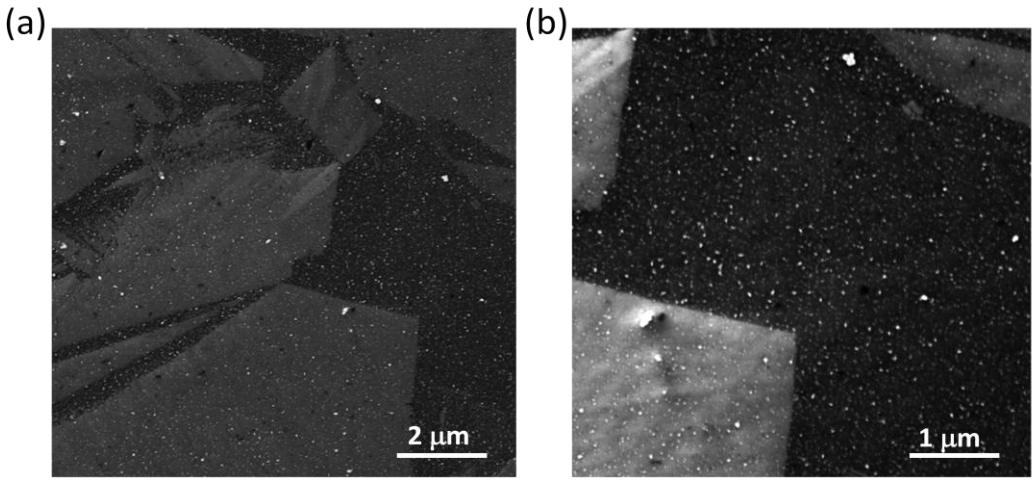

Figure 4.3: FE-SEM images of a Pt NP-modified pBDD electrode, with Pt deposition parameters of -1.0 V for 5 s at two magnifications (see scale bars).

From Figure 4.3 (b) FE-SEM appears to indicate a difference in particle density between grains of varying conductance.[32] The less conducting grains appear lighter in FE-SEM images, because there is more associated charging during imaging.[28] In

these regions, the Pt NP density appears lower than the neighbouring higher conductance regions. Due to static charging effects it is not possible to obtain quantitative information on particle size with FE-SEM, thus the morphology of the Pt NPs was further investigated with tapping-mode AFM.

Figure 4.4 (a) shows a 1 μm x 1 μm tapping mode AFM image of electrochemically deposited Pt NPs (-1.0 V for 5 s) in an area where there are two different grains. The grain boundary is indicated by the dashed line. As can be seen from the line profile, there is only a slight change in height at the boundary of the grains of ca. 2 nm, as the sample has been polished to yield a surface roughness of ca. 1 - 2 nm. The small step height is due to differently orientated grains polishing at slightly different rates.[36] There is evidently no preferential particle deposition at the boundary between the two different grains in the images shown, but there is a clear difference in the density of particles on a grain, with the grain at the left hand side of the image showing a much higher particle density.

Figure 4.4 (b) was recorded at higher resolution (0.5 μm x 0.5 μm) in the area just to the right of the grain boundary in Figure 4.4 (a) and shows a particle surface density of ca. 130 Pt NPs μm^{-2} with the associated size distribution shown (mean NP size of ca. 3 nm ± 2.5 nm). Figure 4.4 (c) shows a 1 μm x 1 μm scan in the area to the left of the grain boundary in Figure 4.4 (a). Here, the particle distribution is ca. 340 Pt NPs μm^{-2}, with the size distribution shown in the inset (mean NP size of 1 nm ± 2 nm).

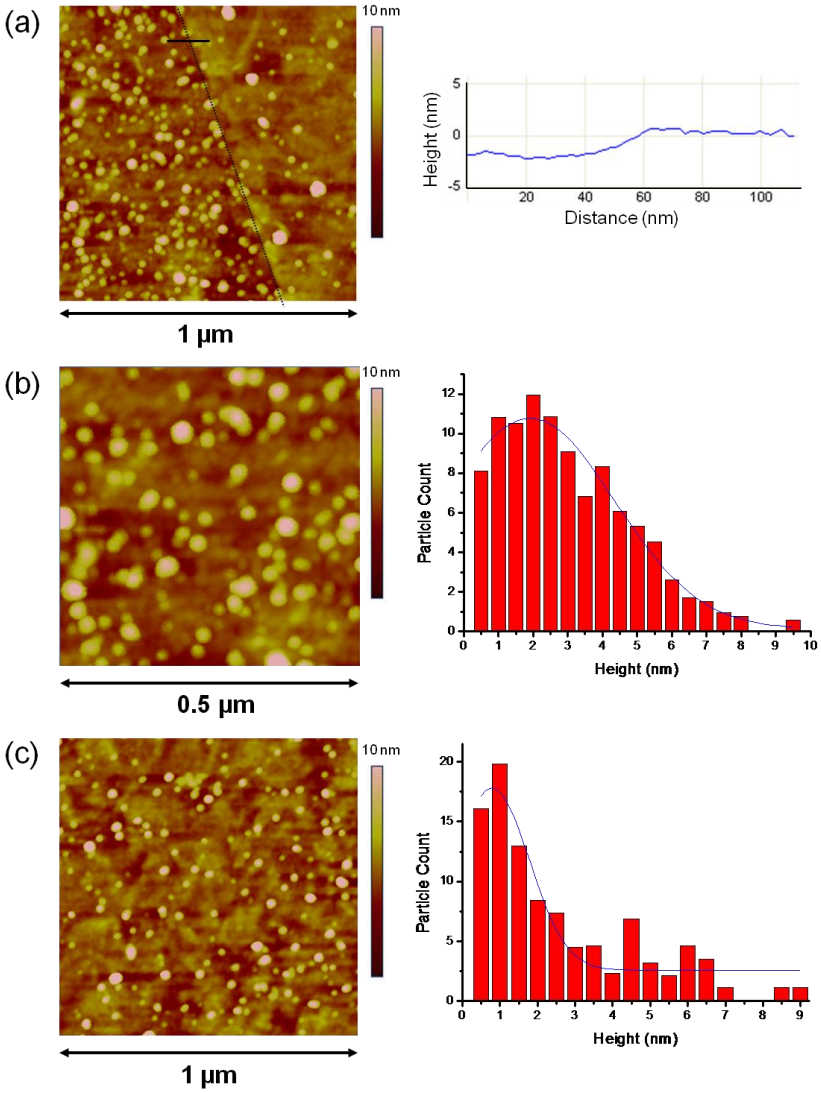

Figure 4.4: AFM (tapping mode) height images of Pt NPs electrodeposited onto a pBDD electrode at -1.0 V for 5 s. (a) Image of the boundary between two different grains, with the black line indicating the location of the cross section shown. (b) The Pt NP size distribution in an area on the right of the grain boundary with a histogram showing particle height distribution. (c) Particles to the left of the grain boundary with a histogram showing particle height distribution.

The AFM and FE-SEM data are consistent with our previous studies of electrodeposited metals on pBDD;[32] smaller particles at high density are found at higher conductivity grains. Given the variation in boron uptake, ~5×10^{19} to >5×10^{20} cm^{-3} over the sample,[34,35] changes in conductivity of over 2 orders of magnitude are expected over different grains. This is also in accordance with our previous studies where we highlighted in detail that typically two types of characteristic

conductivities are observed on Element Six-prepared pBDD surfaces.[38] It is, however, important to note that although electrodeposition is non-uniform across the surface, the close spacing of the Pt particles means that on the timescale of typical amperometric or voltammetric measurements there will be considerable diffusional overlap between neighbouring particles, so that the electrode behaves as a conventional planar electrode as evident from Figure 4.2 and further work reported herein.

4.2.4 **Dissolved Oxygen Detection**

The sensitivity of the composite electrode to varying dissolved oxygen concentrations, denoted as % oxygen in an oxygen/nitrogen ratio, for different pH conditions (pH 4, 5.5, 7.5 and 10) was investigated. Figure 4.5 (a) shows CVs for the reduction of oxygen in 0.1 M KNO_3 and 0.1 mM H_2SO_4 unbuffered solution (pH 4) at a Pt NP-modified pBDD electrode over the range 0 – 100 % oxygenated solution. A clear oxygen reduction peak was observed at ca. -0.195 V, which showed a strong response to the dissolved oxygen concentration. A plot of peak currents (background corrected by the response with 0 % oxygen) versus dissolved oxygen concentration is shown in Figure 4.5 (b). The dissolved oxygen concentrations, were calculated using Henry's law assuming an ideal dilute solution and a Henry's law constant for oxygen of 769.2 atom/(mol dm^{-3}).[37] There is a strong correlation of peak current on dissolved oxygen concentration.

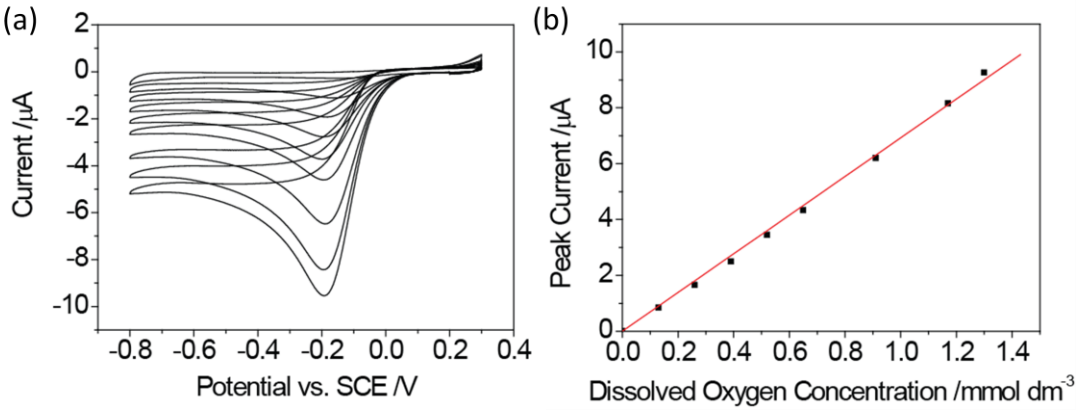

Figure 4.5: (a) CVs for the reduction of oxygen in 0.1M KNO_3 and H_2SO_4 (pH 4) at a Pt NP-modified pBDD electrode, at percentages of oxygen of 0 (smallest current), 10, 20, 30, 40, 50, 70, 90, and 100% (largest current). (b) Plot of background corrected peak current against dissolved oxygen concentration; error bars lie within the data point symbols. Replicate experiments were performed with new solutions and new electrodes.

Chronoamperometry was employed to determine the apparent number of electrons in the oxygen reduction process at the Pt NP-modified BDD electrodes over the pH range 4 – 10, and to provide an alternative means of quantitative oxygen concentration analysis. Figure 4.6(a) shows typical chronoamperometric curves for the reduction of oxygen in 0.1 M KNO_3 and H_2SO_4 (pH 4), at various oxygen concentrations (in the range 0 – 100 %). The curves were obtained by stepping the potential from 0.2 V (where no redox processes occured) to -0.5 V (where oxygen reduction was transport-limited). The current scale was chosen to emphasize medium to long time data. The inset to Figure 4.6(a) shows the full scale data.

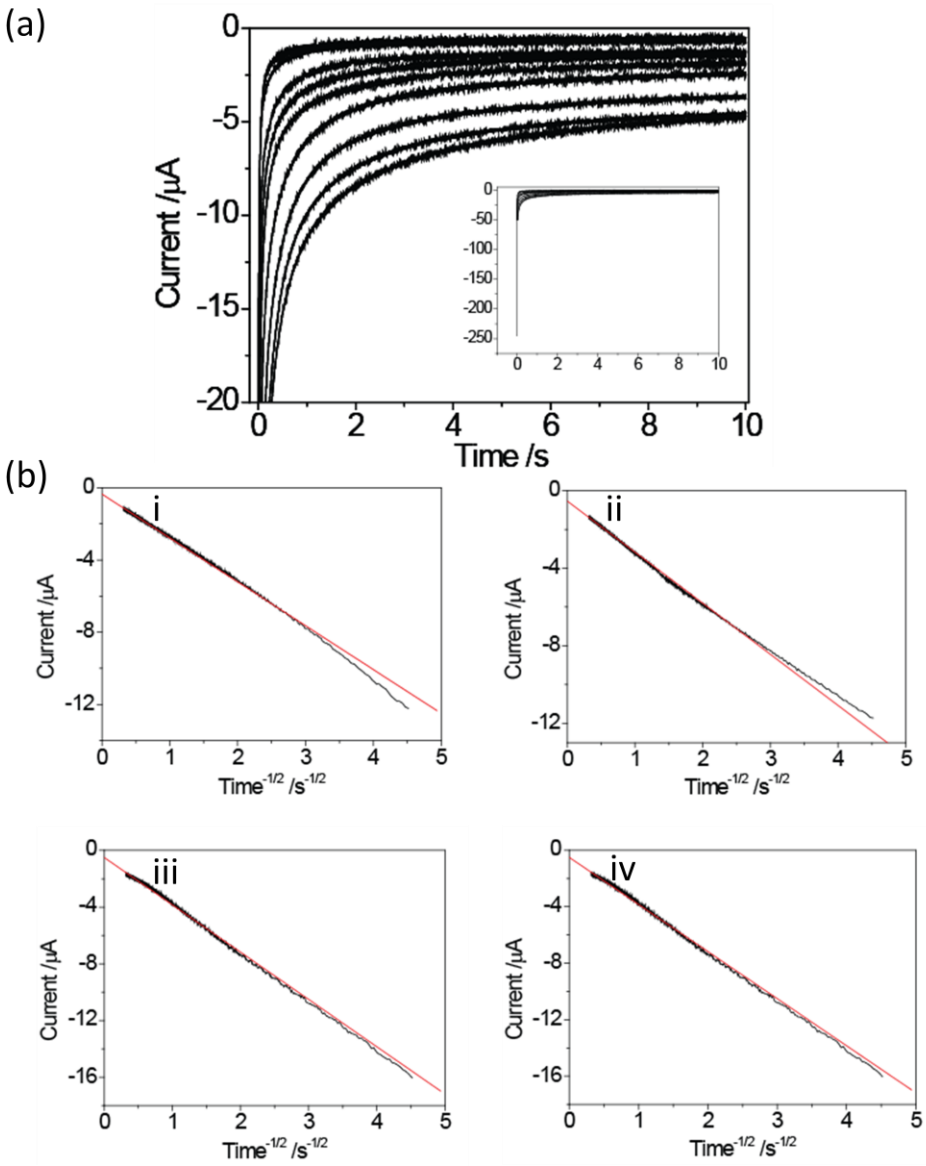

Figure 4.6: (a) Chronoamperometric curves for reduction of oxygen in 0.1M KNO_3 and H_2SO_4 (pH 4) at a Pt NP-modified pBDD electrode, at percentages of oxygen of 0 (smallest current), 10, 20, 30, 40, 50, 70, 90, and 100% (largest current). The insert shows the full data set. (b) Chronoamperometric i plotted against $t^{-1/2}$ for 0.1 M KNO_3 solution with 30% oxygen at (i) pH 4, (ii) pH 5.5, (iii) pH 7.5, and (iv) pH 10.

Over a reasonable timescale, *i* plotted against time$^{-1/2}$ ($t^{-1/2}$), for all oxygen concentrations investigated and all pH solution conditions yielded a straight line as predicted by the Cottrell equation (4.3):

$$i(t) = \frac{n\mathrm{F}AD^{1/2}c^*}{\pi^{1/2}t^{1/2}} \qquad (4.3)$$

Figure 4.6 (b) illustrates this aspect of the analysis for a 30 % oxygen concentration in solutions of (i) pH 4; (ii) 5.5; (iii) 7.5 and (iv) 10. The gradients of the Cottrell plots give the apparent number of electrons transferred as 3.6 ± 0.1, 4.2 ± 0.1, 3.8 ± 0.1and 3.7 ± 0.1 for pH 4, 5.5, 7.5 and 10 respectively. The analysis assumes a *D* for oxygen of 2.28 x 10^{-5} cm^2 s^{-1}.[11] The observation of a four-electron transfer process in the pH range 4 – 10, is consistent with studies carried out on Pt NPs in aerated acidic solution[26] and Au NPs on BDD in aerated acidic[24] and alkaline[25] solutions. Cottrellian analysis assumes linear diffusion to the geometric area of the pBDD electrodes. This provides further evidence that on the timescale identified the diffusion fields of the individual Pt nanoparticles overlap during the amperometric detection of oxygen.

Figure 4.7 shows a plot of the gradients from the Cottrellian analyses (background corrected), as well as the current at 3 s, versus the oxygen concentration, for pH 4 (□), 5.5 (○), 7.5 (Δ) and 10 (∇). A linear relationship between the chronoamperometric gradient and concentration of oxygen at the Pt NP-modified pBDD electrode is observed at all pH in the range 4 – 10. The long time current (~ > 5 s) flowing at the electrode in nitrogen-saturated solution (i.e. 0 % oxygen) is ca. 0.1 μA as can be seen from Figure 4.6 (a) giving a background gradient of – 0.4 μA $s^{1/2}$ (representing a limit of detection). Thus it follows it should be possible to detect dissolved oxygen concentrations as low as ca. 1 ppb under a wide range of pH conditions.

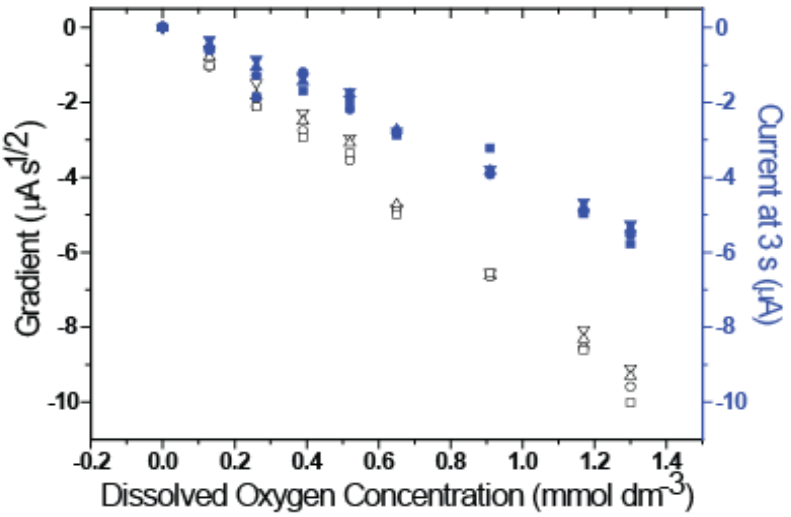

Figure 4.7: Cottrell gradient (black) and the current taken at 3 s (blue) plotted against the dissolved oxygen concentration in 0.1 M KNO_3 solution for (□) pH 4, (○) pH 5.5, (Δ) pH 7.5, and (▽) pH 10.

The reproducibility of the response of the pBDD electrodes over a 12 h time period was also examined. Chronoamperometric measurements were taken every hour for 12 h in a 0.1 M KNO_3 solution of pH 5.5 with oxygen at 40%. Figure 4.8 (a) shows the chronoamperometric gradient, as well as the current at 3 s. For all 12 measurements the chronoamperometric gradient was in the range 3.59−3.79 μA $s^{1/2}$, which according to the data in Figure 4.7 represented a variation of 30 μM of oxygen in solution. This data also supports the high stability and electroactivity of Pt NPs deposited on hydrophilic (oxygen-terminated) pBDD. Longer time testing with an aerated solution over a 2 week period, with a chronoamperometric transient recorded every day, is shown in the Figure 4.8(b). For these 14 measurements, the gradient was in the range −1.47 to −1.75 μA $s^{1/2}$ (representing a variation of 42 μM). Thus the results presented show significant promise for the use of Pt-NP modified pBDD electrodes over extensive time periods.

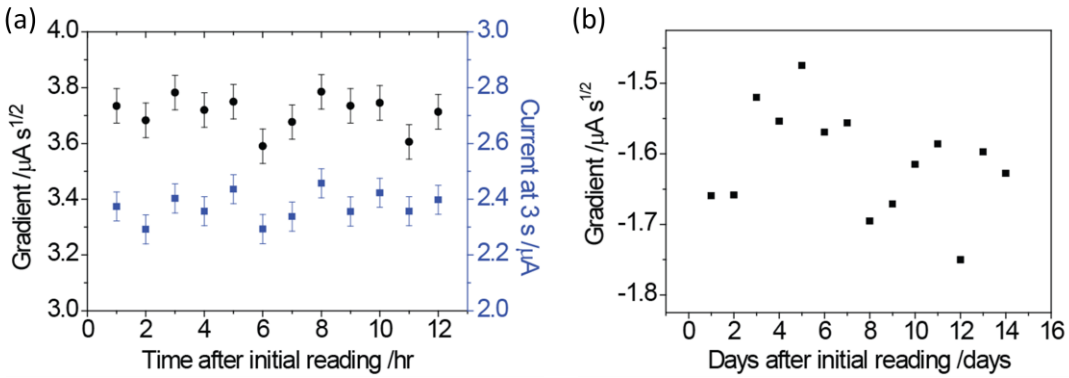

Figure 4.8: (a) Cottrell gradient (black) and the current taken at 3 s (blue) recorded every hour for 12 h in 0.1 M KNO_3 (pH 5.5) at a Pt NP-modified pBDD electrode at 40% oxygen. Error bars show standard deviation of five repeat experiment; (b) Cottrell gradients recorded every day for two weeks in 0.1 M KNO_3 (pH 5.5) under aerated conditions.

To address the issue of electrode use in a more challenging media, e.g., halide containing solutions, many of the experiments detailed in Figures 4.5-4.8 were repeated but with a 0.1 M KCl solution (pH 5.6). The sensitivity of the composite electrode to varying dissolved oxygen concentrations in the presence of chloride ions was investigated. Different ratios of oxygen to nitrogen were flowed into 0.1 M KCl for ca. 30 mins, removing the electrode in between readings. Chronoamperometric curves were recorded by stepping the potential from 0.0 V to -0.7 V and holding for 10 s. Figure 4.9 (a) shows the Cottrell gradient plotted against the dissolved oxygen concentration. As can be seen, a linear relationship is again observed as with KNO_3, indicating that the electrode can be calibrated and that chloride does not impede the use of the electrode for analysis. The reproducibility of the response of the electrode in 0.1 M KCl was also investigated. Chronoamperometric measurements were taken every hour over a twelve hour period where the electrode was left immersed in the solution, with oxygen at 40 %. As can be seen from Figure 4.9 (b), all the Cottrell gradients over the twelve hours were in the range -2.51 to -2.64 μA $s^{1/2}$.

Interestingly these results show better stability of the electrode under chloride conditions than in the presence of nitrate.

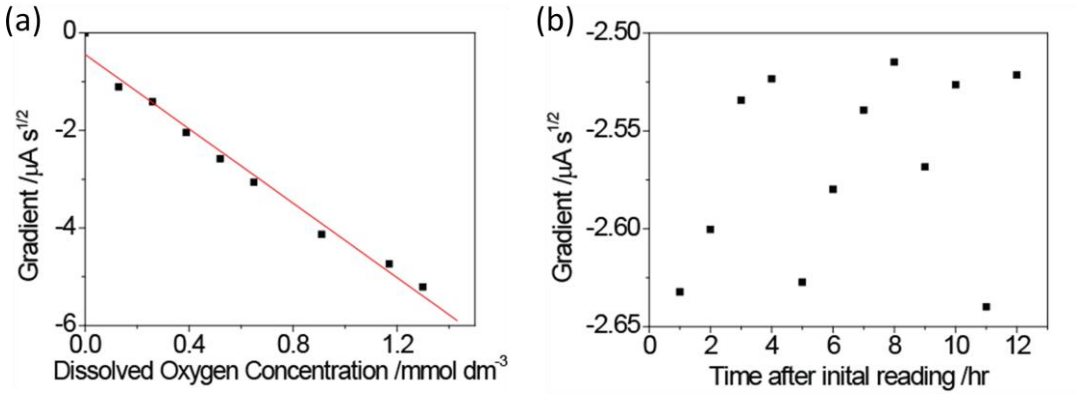

Figure 4.9: (a) Cottrell gradient from chronoamperometric curves plotted against the dissolved oxygen concentration in 0.1 M KCl solution; (b) Cottrell gradients recorded every hour for twelve hours in 0.1 M KCl (pH 5.5) with oxygen at 40 %.

4.3. CONCLUSION

Pt NPs electrodeposited on hydrophilic oxygen-terminated pBDD (surface roughness 1−2 nm) provide an electrode which gives an excellent response for both the cyclic voltammetric and amperometric detection of oxygen, 0−100% in solution. By careful choice of electrodeposition conditions, composite electrodes can be readily produced capable of oxygen monitoring with a limit of detection at the ~parts per billion level over the pH range 4−10 and stability over at least a 2 week period (daily use). Thus we envisage that one possible use of this electrode could be as an oxygen sensor in aquatic environments.

The use of Pt electrodeposition conditions of −1.0 V vs. SCE and 5 s resulted in the formation of Pt NPs with sizes of ~3 nm ± 2.5 nm (s.d.) (surface density ~130 NPs μm^{-2}) and ~1 nm ± 2 nm (s.d.) (surface density ~340 NPs μm^{-2}) in the low and high

conductivity grains, respectively. As a result of the low background currents associated with pBDD and the low surface area of Pt NPs (compared with a continuous film of Pt), the corresponding voltammetric response for oxygen reduction at the pBDD-Pt composite showed significantly lower background signals compared to Pt electrodes. Pt particle size and density was found to vary between grains of differing conductivity, in line with previous results; smallest particles, highest density on more conducting grains.[32] The nanoparticle spacing was sufficiently close so that on the time scale of the voltammetric and chronoamperometric measurements there was interaction of oxygen diffusion fields to neighboring particles resulting in a planar diffusion field to the geometric area of the composite. With the use of chronoamperometry, the oxygen reduction current response was found to follow a four-electron transfer process in the pH range 4−10, for the full range of oxygen concentrations.

4.4. REFERENCES

(1) Stetter, J. R.; Li, J. *Chem. Rev. (Washington, DC, U. S.)* **2008**, *108*, 352.
(2) Ramamoorthy, R.; Dutta, P. K.; Akbar, S. A. *J. Mater. Sci.* **2003**, *38*, 4271.
(3) Hickman, M. L. *The measurement of dissolved oxygen.*; John Wiley, New York,, 1978.
(4) Knake, R.; Jacquinot, P.; Hodgson, A. W. E.; Hauser, P. C. *Anal. Chim. Acta* **2005**, *549*, 1.
(5) Sosna, M.; Denuault, G.; Pascal, R. W.; Prien, R. D.; Mowlem, M. *Sens. Actuators, B* **2007**, *123*, 344.
(6) Yeager, E. *J. Mol. Catal.* **1986**, *38*, 5.
(7) Wroblowa, H. S.; Pan, Y. C.; Razumney, G. *J. Electroanal. Chem.* **1976**, *69*, 195.
(8) Zurilla, R. W.; Sen, R. K.; Yeager, E. *J. Electrochem. Soc.* **1978**, *125*, 1103.
(9) Damjanovic, A.; Genshaw, M. A.; Bockris, J. O. M. *J. Electrochem. Soc.* **1967**, *114*, 1107.
(10) Yeager, E. *Electrochim. Acta* **1984**, *29*, 1527.
(11) Pletcher, D.; Sotiropoulos, S. *J. Electroanal. Chem.* **1993**, *356*, 109.
(12) Birkin, P. R.; Elliott, J. M.; Watson, Y. E. *Chem. Commun. (Cambridge, U. K.)* **2000**, 1693.
(13) Pletcher, D.; Sotiropoulos, S. *J. Chem. Soc., Faraday Trans.* **1995**, *91*, 457.
(14) Pleskov, Y. V. *Russ. J. Electrochem.* **2002**, *38*, 1275.
(15) Xu, J. S.; Granger, M. C.; Chen, Q. Y.; Strojek, J. W.; Lister, T. E.; Swain, G. M. *Anal. Chem.* **1997**, *69*, A591.
(16) Compton, R. G.; Foord, J. S.; Marken, F. *Electroanalysis* **2003**, *15*, 1349.
(17) Ramesham, R.; Rose, M. F. *Diamond Relat. Mater.* **1997**, *6*, 17.
(18) Yano, T.; Tryk, D. A.; Hashimoto, K.; Fujishima, A. *J. Electrochem. Soc.* **1998**, *145*, 1870.
(19) Yano, T.; Popa, E.; Tryk, D. A.; Hashimoto, K.; Fujishima, A. *J. Electrochem. Soc.* **1999**, *146*, 1081.
(20) Tian, R.-h.; Zhi, J.-f. *Electrochem. Commun.* **2007**, *9*, 1120.
(21) Zhang, Y. R.; Asahina, S.; Yoshihara, S.; Shirakashi, T. *Electrochim. Acta* **2003**, *48*, 741.
(22) Sarapuu, A.; Helstein, K.; Schiffrin, D. J.; Tammeveski, K. *Electrochem. Solid-State Lett.* **2005**, *8*, E30.
(23) Kruusma, J.; Banks, C. E.; Compton, R. G. *Anal. Bioanal. Chem.* **2004**, *379*, 700.
(24) Szunerits, S.; Manesse, M.; Actis, P.; Marcus, B.; Denuault, G.; Jama, C.; Boukherroub, R. *Electrochem. Solid-State Lett.* **2007**, *10*, G43.
(25) Yagi, I.; Ishida, T.; Uosaki, K. *Electrochem. Commun.* **2004**, *6*, 773.
(26) Wang, J.; Swain, G. M. *J. Electrochem. Soc.* **2003**, *150*, E24.
(27) Jolley, S.; Koppang, M.; Jackson, T.; Swain, G. M. *Anal. Chem.* **1997**, *69*, 4099.
(28) Bard, A. J.; Faulkner, L. R. *Electrochemical methods: Fundamentals and Applications*; John Wiley & Sons, INC., 2001.
(29) Szunerits, S.; Boukherroub, R. *C. R. Chim.* **2008**, *11*, 1004.
(30) Pletcher, D.; Sotiropoulos, S. *J. Chem. Soc., Faraday Trans.* **1994**, *90*, 3663.
(31) Colley, A. L.; Macpherson, J. V.; Unwin, P. R. *Electrochem. Commun.* **2008**, *10*, 1334.
(32) Colley, A. L.; Williams, C. G.; Johansson, U. D.; Newton, M. E.; Unwin, P. R.; Wilson, N. R.; Macpherson, J. V. *Anal. Chem.* **2006**, *78*, 2539.
(33) Holt, K. B.; Bard, A. J.; Show, Y.; Swain, G. M. *J. Phys. Chem. B* **2004**, *108*, 15117.
(34) Wilson, N. R.; Clewes, S. L.; Newton, M. E.; Unwin, P. R.; Macpherson, J. V. *J. Phys. Chem. B* **2006**, *110*, 5639.

(35) Szunerits, S.; Mermoux, M.; Crisci, A.; Marcus, B.; Bouvier, P.; Delabouglise, D.; Petit, J.-P.; Janel, S.; Boukherroub, R.; Tay, L. *J. Phys. Chem. B* **2006**, *110*, 23888.
(36) El-Dasher, B. S.; Gray, J. J.; Tringe, J. W.; Biener, J.; Hamza, A. V.; Wild, C.; Worner, E.; Koidl, P. *Appl. Phys. Lett.* **2006**, *88*.
(37) Manahan, S. E. *Environmental Chemistry*; CRC Press: Florida, 2004.

CHAPTER 5

Electrodeposition of Nickel Hydroxide Nanoparticles on pBDD Electrodes for Oxidative Electrocatalysis

The electrosynthesis of uniformly dispersed nickel hydroxide ($Ni(OH)_2$) NPs on pBDD is demonstrated for the first time. This has been achieved by electrogenerating OH^- at the pBDD surface in the presence of Ni^{2+} to create local conditions near the electrode where highly supersaturated (relative saturation ratio > 10^5) nickel hydroxide solutions are generated for short periods of time (approximately seconds). This results in the deposition of nickel hydroxide NPs directly on the electrode surface, as confirmed by XPS. We show that by simply increasing the electrogeneration time and, hence, increasing both the local concentration of OH^- and extent of the precipitation reaction, it is possible to increase the size of the NPs. The effect of nickel hydroxide NP size on electrocatalytic activity was investigated by measuring the steady-state current for the oxidation of glucose in alkaline media. For NPs ≥ 25 nm in size, glucose oxidation is close to diffusion-controlled. However, for the smallest NPs produced (~12 nm) the currents passed suggest kinetic limitations. For glucose at an effective surface coverage of nickel hydroxide of ~20 nmol cm^{-2}, equivalent to 15 ng of nickel hydroxide, this functionalized electrode showed a sensitivity of 330 μA mM^{-1} cm^{-2} and a limit of detection of 400 nM. The latter represents one of the lowest limits of detection for glucose for nickel hydroxide-based electrodes. The electrocatalytic oxidation properties of this electrode toward methanol and ethanol was also found to be very efficient, yielding very high density currents of ~1010 A g^{-1} for 0.5 M ethanol and 990 A g^{-1} for 0.47 M methanol.

5.1. INTRODUCTION

The search for electrocatalytic materials is the focus of intense study in a variety of research areas, such as for fuel cell catalysts, energy storage, chemical synthesis, and electrochemical-based sensors.[1-4] Among many possible electrocatalytic materials, $Ni(OH)_2$ has been the subject of much investigation, particularly as a fuel cell catalyst, for secondary batteries,[5-7] and as an electrocatalyst for organic synthesis.[8,9] The electrocatalytic effect is considered to arise from unpaired d electrons or empty d orbitals associated with the oxidized form of Ni (NiOOH; i.e., Ni^{3+}), which are available for bond formation with adsorbed species or redox intermediates.[10-12]

For electrocatalytic applications, it has often been found that by moving from bulk materials to nanosized structures, catalytic activity can be significantly increased.[13] Thus, decorating supporting substrates with isolated NPs or nanostructures is a popular strategy to create efficient electrocatalysts.[13-15] Although many chemical routes, such as sonochemistry, sol gel, and solvothermal methods, among others,[16-20] have been described for the formation of $Ni(OH)_2$ on surfaces, these methods typically result in thin film structures.[21-23]

The direct formation of particles *in-situ* on the electrode support of interest represents a simpler alternative to the techniques described above. Furthermore, as amply demonstrated for the formation of immobilized metal nanostructures, judicious choice of electrode potential and time opens up the possibility of controlling the size and coverage of electrodeposited nanostructures.[24] The choice of substrate electrode material, which provides electrical connection to the NPs, is also an important consideration.[13] The properties of the surface must be such that a strong

NP−electrode interaction is favored. The background (parasitic) current contribution from the substrate electrode should also, ideally, be negligible in the potential region of interest. A substrate electrode with a wide potential window also enables depositions to be carried out free from complications from the evolution of gaseous products from direct solvent/electrolyte electrolysis. Finally, the support electrode should also be stable and inert in the solution of interest, particularly to ensure the physical integrity of the electrode and to avoid the production of chemical species that might poison the electrode and electrocatalyst.

pBDD meets many of the requirements cited above. It has generated considerable interest as an electrode material, particularly as a consequence of its very wide potential window in aqueous solution compared with traditional electrodes.[25] Moreover, pBDD is characterized by a very low sensitivity to dissolved oxygen, very low background currents, reduced susceptibility to passivation, and corrosion stability in aggressive media and at elevated temperatures and pressures.[26,27] As such, pBDD represents an extremely interesting electrode platform for the electrochemically driven deposition of $Ni(OH)_2$ NPs.

To date, previous studies of $Ni(OH)_2$ electrodeposition have focused on two approaches: either (i) the electrochemical generation of a base in the presence of Ni^{2+} to form nickel hydroxide directly,[28-30]

$$Ni^{2+}_{(aq)} + 2OH^-_{(aq)} \rightarrow Ni(OH)_{2\,(s)} \qquad (5.1)$$

or (ii) an indirect approach in which nickel is first electrodeposited,

$$Ni^{2+}_{(aq)} + 2e^- \rightarrow Ni_{(s)} \qquad (5.2)$$

or a nickel metal electrode is employed[31,32] and the nickel is fully oxidized by potential cycling in base.[33-35] In some cases, it is also possible to form mixtures of $Ni(OH)_2$ and metallic nickel due to both processes described in equations 5.1 and 5.2, occurring during electrodeposition.[36]

To the best of our knowledge, there are no reports in the literature that show the production of isolated NPs on an electrode surface via the direct approach; rather, thin film structures tend to be produced. For the indirect approach, there are only limited reports of the formation of predominantly approximately micrometer-sized $Ni(OH)_2$ particles.[34,35] Furthermore, because this methodology requires electrodeposition of nickel first (equation 5.2), heterogeneities in the electroactivity of the electrode surfaces employed result in a heterogeneous surface distribution of particles.[34,37] Thus, the ability to tightly control the surface coverage and particle size, which is particularly problematic for fundamental studies, is lost.

In this chapter, the formation of randomly isolated $Ni(OH)_2$ NPs on a hydrophilic oxygen-terminated pBDD surface is demonstrated. Herein, the direct method is used where the electrode is biased at an appropriate potential to potentiostatically increase the local pH of the solution, in the presence of Ni^{2+}, to create very high ($>10^5$) relative saturation ratios[38] for a short period of time (approximately seconds). Under these conditions, we show that it is possible to precipitate $Ni(OH)_2$ particles as small as ~10 nm in height randomly over the heterogeneously electroactive pBDD surface. Longer deposition times (>30 s) lead to aggregated structures. By simply controlling the electrodeposition time, it is possible to change the size of the structures formed. In this way, we are able to create electrocatalytic surfaces to investigate, for the first

time, the effect of NP size on the electrocatalytic activity of nickel hydroxide toward methanol, ethanol, and glucose oxidation.

5.2. RESULTS AND DISCUSSION

5.2.1 **Electrodeposition of Nickel Hydroxide**

$Ni(OH)_2$ NPs were synthesized *in- situ* on the fabricated 1 mm disc pBDD electrode (Chapter 1) surface from a 10 mM nickel nitrate solution (pH = 6). The precipitation of $Ni(OH)_2$ is considered to occur due to the electroreduction of nitrate ions (from the nickel salt) in solution,[39,40]

$$NO_3^- + 7H_2O + 8e^- \rightarrow NH_4^+ + 10OH^- \qquad (5.3)$$

resulting in an increase in the local pH. This, in turn, drives the precipitation of $Ni(OH)_2$ on the pBDD surface (solubility product, K_{sp}, of $Ni(OH)_2$ is 5.48×10^{-16} at 25 °C[41]) according to equation 5.1. To drive the homogeneous nucleation of NPs in solution it is important to (i) produce a high concentration of OH^- to form a highly supersaturated solution[38] and (ii) keep the time scales of production short to avoid NP aggregation. This was achieved by exploring different combinations of applied electrode potential and time. Applying a potential of −1.1 V vs Ag/AgCl for different times (from 1 to 100 s) was found to be the most effective strategy for producing different sized $Ni(OH)_2$ NPs on the surface.

5.2.2 **Surface Characterization of Nickel Hydroxide-Modified Electrodes**

We first consider simple CV measurements of the modified electrodes, which allow an estimation of the amount of electroactive $Ni(OH)_2$ on the electrode surface.

Figure 5.1 shows a typical CV recorded in 0.1 M KOH at 5 mV s^{-1} for a $Ni(OH)_2$ - modified pBDD electrode produced using a deposition time of 5 s (procedure outlined above). As the potential is scanned more positive, the current increases due to oxidation of Ni^{2+} ($Ni(OH)_2$) to Ni^{3+} (NiOOH).

$$Ni(OH)_2 + OH^- \rightarrow NiOOH + H_2O + e^- \qquad (5.4)$$

Calculation of the charge associated with oxidation (Q_{ox}) of $Ni(OH)_2$ and subsequent reduction (Q_{red}) of the electrogenerated NiOOH gives a value for Q_{ox}/Q_{red} of ~1. The amount of deposited $Ni(OH)_2$ can be calculated as an effective surface concentration (Γ), on the electrode surface,

$$\Gamma = Q_{ox} / nFA \qquad (5.5)$$

In this potential window, background contributions from the pBDD electrode are negligible.

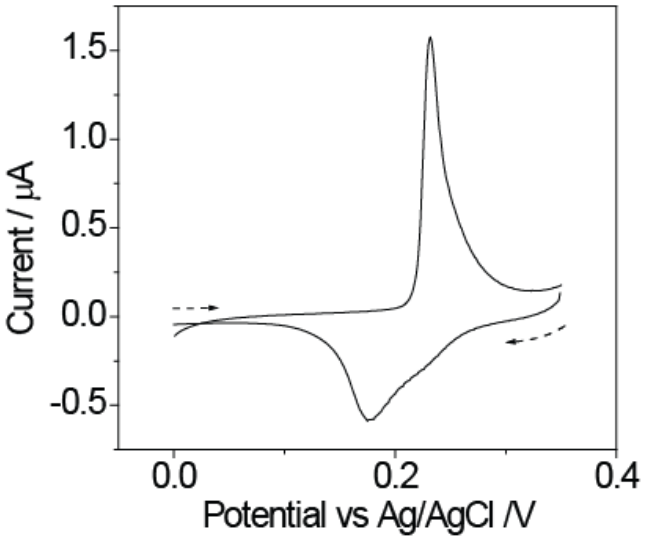

Figure 5.1: Typical CV recorded in 0.1 M KOH only for a $Ni(OH)_2$*-modified (*Γ *~20 nmol* cm^{-2}*) pBDD. The scan rate is 5 mV* s^{-1}.

5.2.3 Morphological Characterization of the Nickel Hydroxide Modified Electrodes

FE-SEM and AFM were used to characterize the surface of the $Ni(OH)_2$-modified pBDD electrodes. Figure 5.2 shows typical FE-SEM images for the modified electrodes for Γ values of (a) ~20 ± 4 nmol cm^{-2}, (b) ~140 ± 20 nmol cm^{-2} and (c) ~420 ± 70 nmol cm^{-2} (determined from CV measurements), produced by depositing for times of (a) 5, (b) 30, and (c) 100 s, respectively, for a constant potential of −1.1 V. Note the linearity of the amount of $Ni(OH)_2$ deposited with the deposition time.

At the shortest deposition times (Figure 5.2 (ai)), the FE-SEM images show isolated NPs that are distributed uniformly over the pBDD surface, even though pBDD is a heterogeneous surface comprising grains (crystal faces) of varying conductivity (due to differential boron uptake).[42] Two grains are evident in Figure 5.2 (a); the grain boundary is indicated by the black arrow. Figure 5.2 (aii) shows that NP deposition is random over larger surface areas comprising many grains. Significantly, this contrasts with the direct metal deposition approach on pBDD, where typically the resulting approximately micrometer-sized metal nucleation structures are observed to be grain-dependent.[15,34,37,43]

Clearly, the direct route, described here, is thus much better for the production of uniformly dispersed $Ni(OH)_2$ NPs on a pBDD surface. At 30 s (Figure 5.2 (b)), isolated NP deposition is still favoured, but there is evidence of some aggregation, as shown in the inset. After 100 s, these aggregates appear to be larger and more numerous, although again with no preference for particular grains on the surface.

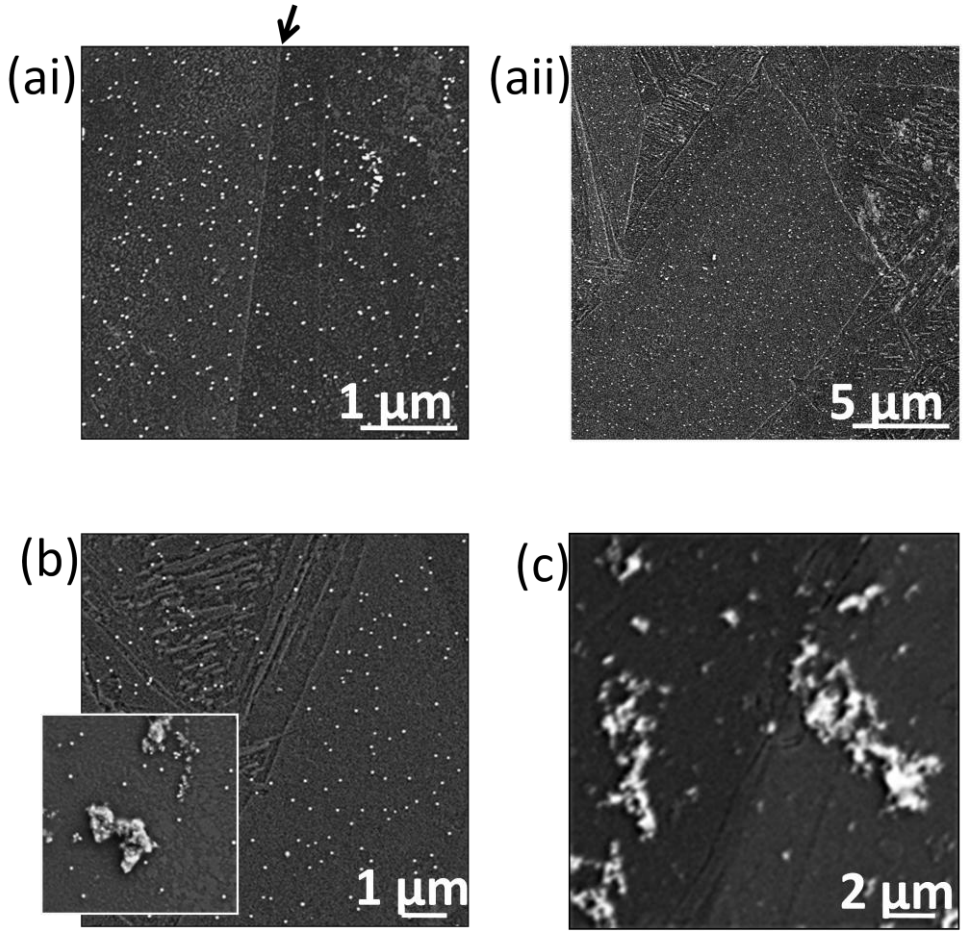

Figure 5.2: Typical FE-SEM images obtained from $Ni(OH)_2$ deposited pBDD electrodes for (a) Γ ~ 20 nmol cm^{-2} (images i and ii are obtained at higher and lower resolution, respectively) (b) Γ ~140 nmol cm^{-2}, and (c) Γ ~ 420 nmol cm^{-2}. Deposition times (at −1.1 V versus Ag/AgCl) were 5, 30, and 100 s, respectively. The inset to panel (b) is 2.5 µm x 2.5 µm.

AFM was used to provide quantitative information on NP size. Figure 5.3 shows typical 1 µm × 1 µm AFM images for Γ ($Ni(OH)_2$) ~20 nmol cm^{-2} (deposition time 5 s) recorded on different pBDD grains. These were identified topographically using AFM (from larger scans) from differences in surface height. Different BDD crystallographic orientations polish at different rates, resulting in 2−6 nm steps on the surface separating differently orientated grains.[42] The associated histograms show no significant differences in NP size or number density between different grains in agreement with the FE-SEM images (Figure 5.2). The average NP number density from Figure 5.3 (a) and (b) is ~87 ± 12 and 85 ± 12 NPs μm^{-2}, respectively,

and the corresponding mean NP size (taken from the AFM height data) is ~25 ± 6 and 24 ± 6 nm, with the associated size distribution shown in the histograms. It is important to note that the close spacing of the $Ni(OH)_2$ NPs means that on the time scale of typical amperometric or voltammetric electrocatalytic measurements, with these electrodes, there will be considerable or essentially total diffusional overlap between neighboring particles.

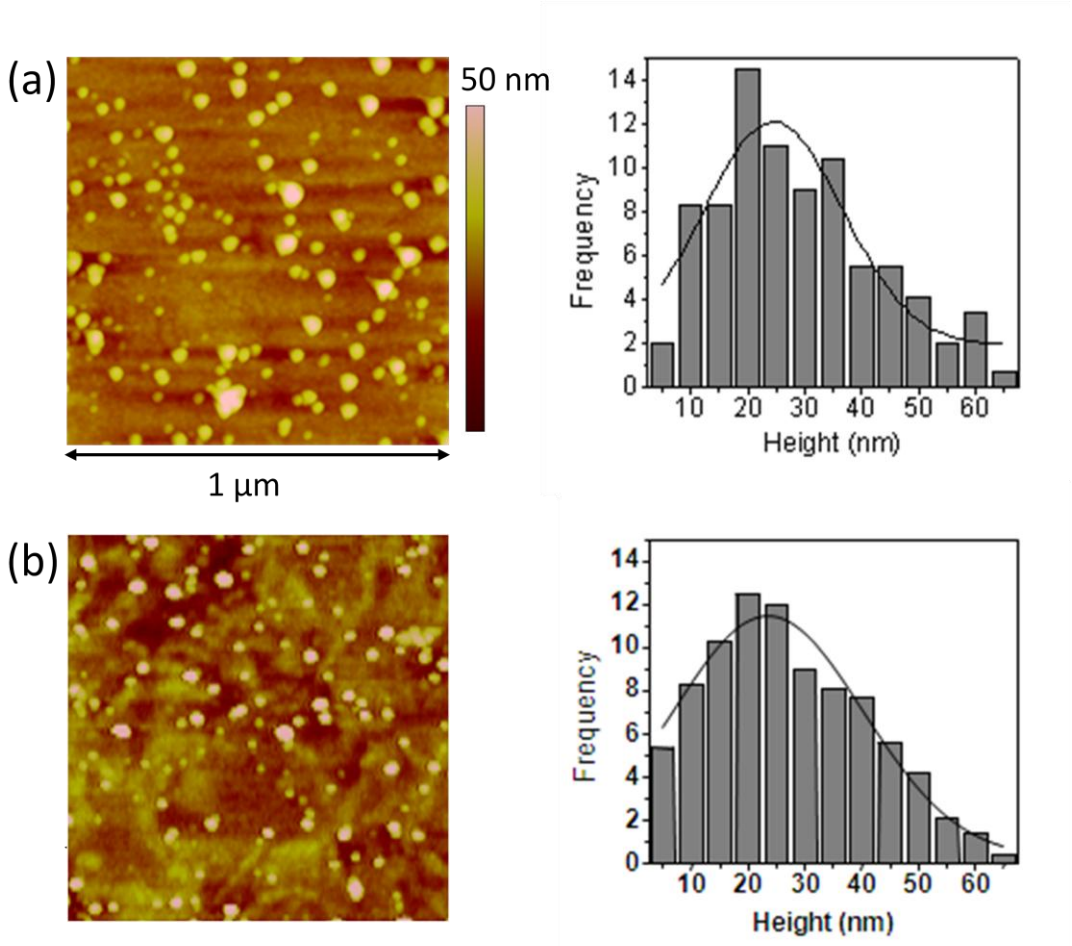

Figure 5.3: AFM (tapping mode) 1 µm × 1 µm height images of $Ni(OH)_2$ deposited onto a pBDD electrode on two differing conductivity grains (distinguished by height differences from differential polishing) for Γ ~20 nmol cm^{-2} (5 s deposition). Opposite each is a histogram showing NP height distribution.

Figure 5.4 shows AFM images for different $Ni(OH)_2$ deposition times of (a) 1; (b) 15; (c) 30, and (d, e) 100 s. NPs of 12 ± 3, 39 ± 9, and 43 ± 8 nm in height were found for 1, 15, and 30 s, respectively, clearly showing that the mean size of

particles increases with deposition time. For 1 and 15 s, the surface coverage of NPs on the surface was 25 ± 5 NPs μm^{-2} and 87 ± 15 NPs μm^{-2}. For times of 30 s and longer, the images show signs of particle aggregation, making it difficult to quantify number densities accurately. For example, in the insert to Figure 5.4 (c), it is possible to observe discrete aggregates, although at 30 s, these are sparsely deposited over the surface, consistent with the FE-SEM data shown in Figure 5.2 (b).

After 100 s, AFM images (Figure 5.4 (d) and (e)) show that areas of the surface have become covered with aggregated $Ni(OH)_2$ structures that are micrometers in length, similar to those seen in Figure 5.2 (c). Figure 5.4 (d) is recorded on the surface of an aggregate, whereas Figure 5.4 (e), imaged over a larger length scale, shows the typical size of an aggregate, the dimensions of which are clearly shown in the cross section data (Figure 5.4 (f)).

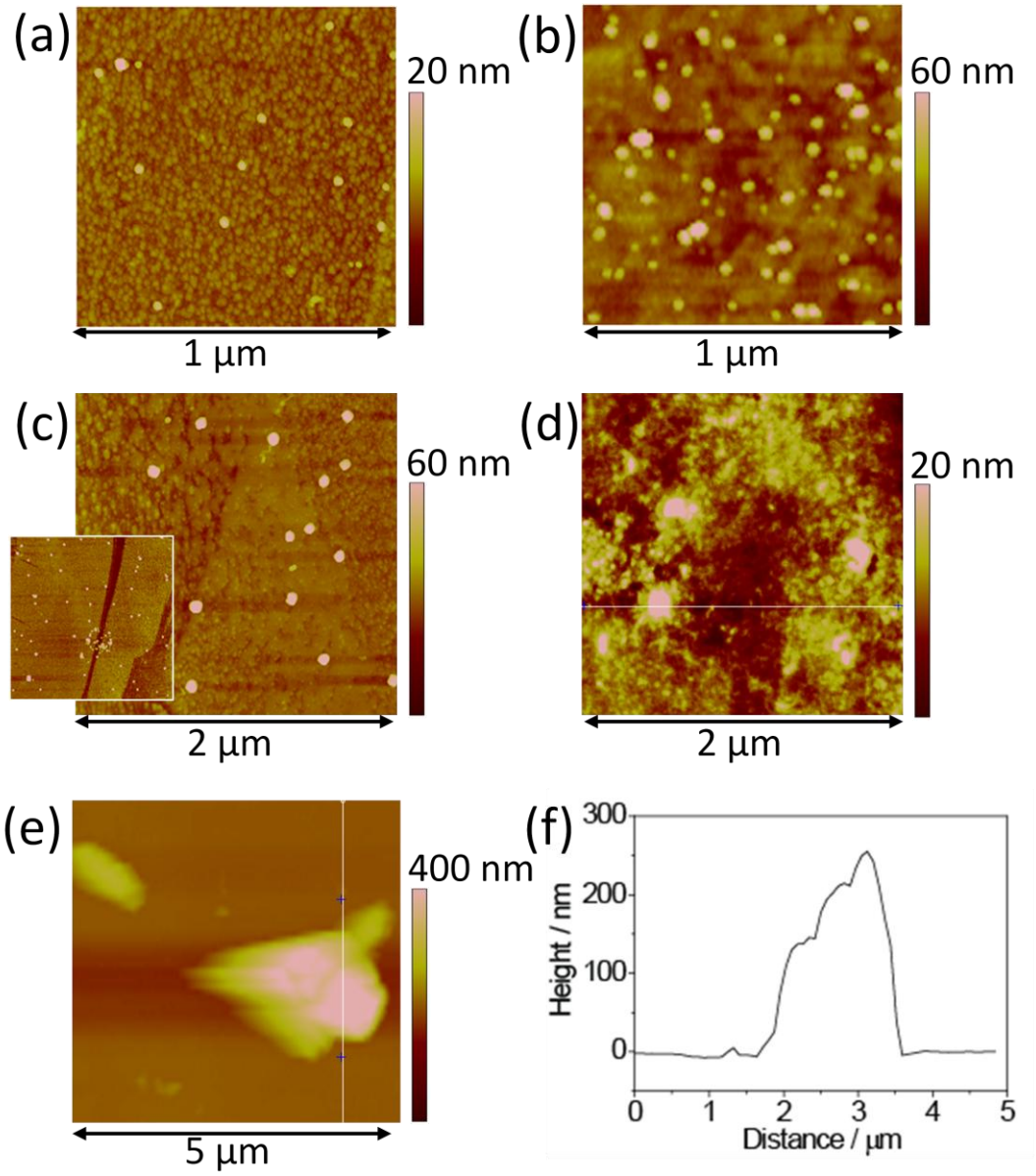

Figure 5.4: AFM (tapping mode) height images of $Ni(OH)_2$ deposited onto a pBDD electrode for (a) 1, (b) 15, (c) 30, and (d, e) 100 s. The insert to panel c is a 5 µm × 5 µm image. For d, the image was recorded in the area of an aggregated structure, and e was recorded with a larger scan size to emphasize the height of a typical aggregate. Part f shows a height cross section of the aggregate.

Assuming the NPs are spherical, which is likely, given their formation route (described in equation 5.1), AFM images (e.g., Figures 5.3 and 5.4) also enable a charge, Q_{AFM}, to be calculated associated with NP surface coverage. For example, for Γ ~20 nmol cm^{-2} (5 s deposition), assuming a NP surface coverage of ~86 NP μm^{-2}, Q_{AFM} is given by

$$Q_{AFM} = \frac{4\pi r^3 N_d A \rho n F}{3M} \qquad (5.6)$$

where r is the radius of a spherical NP; N_d is the number density of NPs (surface coverage); and M and ρ are the molar mass and density of the $Ni(OH)_2$ NP particle: 92.7 g mol^{-1} and 4.15 g cm^{-3}, respectively, and $n = 1$.[44] The calculated value of Q_{AFM} = 19 ± 6 μC (from eq 5.5) agrees well with 15.9 μC ± 4 μC obtained from consideration of Q_{ox} and Q_{red}, indicating that all NPs on the surface are electrochemically active and that the redox process involves essentially complete conversion of $Ni(OH)_2$ to Ni(OOH) in the NP.

5.2.4 **XPS Studies**

The chemical identity of the surface of the modified electrode was investigated using XPS. Figure 5.5 shows the XPS spectrum for a pBDD $Ni(OH)_2$-modified electrode for a deposition time of 30 s. A main peak at 855.7 eV is observed for Ni $2p_{3/2}$, with satellite peaks due to plasmon losses and final state effects at 861.5 eV.[45] By comparing the data with previous XPS studies on Ni, NiO, NiOOH, and $Ni(OH)_2$, the main peak can be assigned to Ni^{2+} in $Ni(OH)_2$.[46-48] The presence of Ni metal, NiOOH, or NiO would be indicated by peaks and satellite peaks at lower binding energies, which are not observed. Hence, under the experimental conditions employed here, it is clear that $Ni(OH)_2$ is formed predominantly via the pathway described in equation 5.1, resulting in NP formation in solution, followed by deposition on the electrode surface.

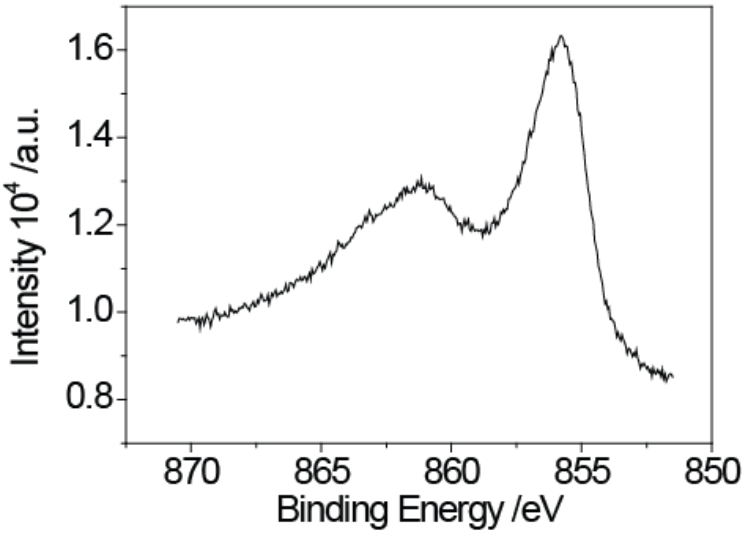

Figure 5.5: XPS Ni $2p_{3/2}$ spectra of $Ni(OH)_2$ modified pBDD electrode with deposition parameters of −1.1 V for 30 s.

5.2.5 **Electrogenerated Hydroxide Concentration Profiles**

Given the proposition of homogeneous $Ni(OH)_2$ NP formation in solution, it is informative to calculate the $Ni(OH)_2$ supersaturations, defined here as a relative saturation ratio (S),

$$S = [Ni^{2+}]\,[OH^-]^2 / K_{sp} \qquad (5.7)$$

that are generated using the protocol outlined. $[Ni^{2+}]$ = 10 mM, and K_{sp} is known; hence, by calculating $[OH^-]$, it is possible to calculate S, using equation 5.7. To provide an estimate, we assume that the current that flows during electrodeposition is due to OH^- production and not Ni deposition. This is reasonable, given the results presented above. A typical current−time curve recorded during a 5 s deposition is shown in Figure 5.6 (a). It can be seen that after a short time, a relatively constant current prevails, which corresponds to a constant flux of $[OH^-]$ at the electrode surface. Under these constant flux conditions, $[OH^-]$ profiles can be calculated using the analytical expression;[49]

$$C - C_o = \frac{j_o l}{D}\left\{\frac{Dt}{l^2} + \frac{3x^2 - l^2}{6l^2} - \frac{2}{\pi^2}\sum_m^{\infty}\frac{(-1)^m}{m^2}\exp(-Dm^2\pi^2 t/l^2)\cos\frac{m\pi x}{l}\right\} \quad (5.8)$$

where C is the concentration, C_0 is the initial concentration; j_0 is the flux obtained from $j_0 = i^- /(nF)$, where i^- is the experimental current density measured during deposition; D is the diffusion coefficient of hydroxide ions (= 5.6×10^{-5} cm^2 s^{-1}),[50] l is the separation between the electrode surface and a parallel boundary (here, we use l = 0.22 cm so that diffusion from or to the electrode surface is unrestricted), t is time, x is the distance from electrode, and m is the number of points used (= 100) in the numerical simulation.

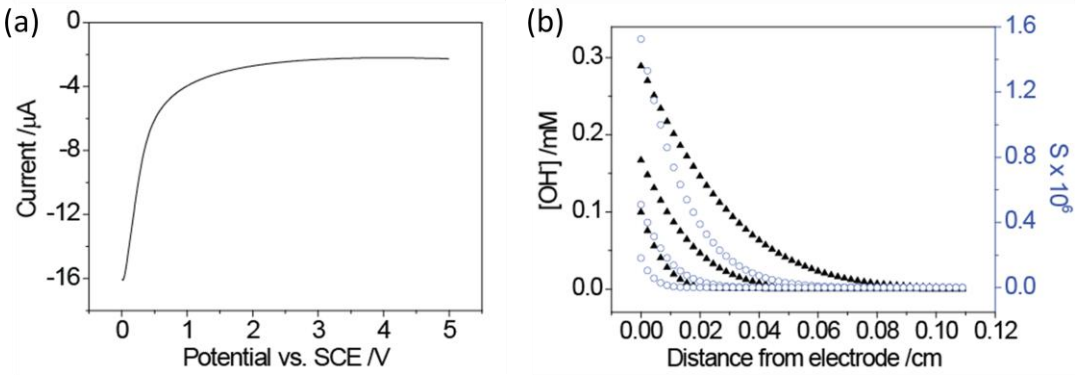

Figure 5.6: (a) Typical current−time curve recorded by holding the pBDD electrode at −1.1 V for 5 s in a solution containing 10 mM $Ni(NO_3)_2$. (b) Numerical simulation for generation of OH^- (▲) as a function of distance from the electrode surface for times of 1 s (lower curve), 5 s (middle curve), and 15 s (upper curve). Also shown are the corresponding plots of S (○), calculated using equation 5.8 versus distance from electrode surface.

Concentration profiles have been simulated for three different times: t = 1, 5, and 15 s (lower, middle, and upper ▲ data points, respectively), indicative of the time scales employed herein. It can be seen that >10^{-4} M concentrations of hydroxide are generated close to the electrode, which when converted using equation 5.7 into S values (○ in Figure 5.6), produce very high values, on the order of 10^5−10^6. Thus, it

is no surprise that using this precipitation approach,[38] homogeneous NPs of $Ni(OH)_2$ are produced.

Although the electrogeneration of [OH^-] may occur differently at the different electrically conducting grains in pBDD, the small grain size compared with the hydroxide concentration boundary layer thickness (Figure 5.6) means that these grain heterogeneities will be largely unimportant. This is evidenced by the lack of grain-dependent $Ni(OH)_2$ deposition morphology, as seen in Figures 5.2−5.4.

In summary, the XPS, AFM, and FE-SEM data demonstrate that simply by changing the time scale of the deposition process, it is possible to tune and control the type of $Ni(OH)_2$ nanostructure formed on the pBDD surface, from isolated NPs of height ~10 nm (at short times) toward larger isolated NPs and, finally, to a surface dominated by aggregated NP structures. Importantly, in these studies, we create extremely high supersaturations to favour NP formation via precipitation.[38] Furthermore, and in contrast to all other studies, we use much shorter times for [OH^-] electrogeneration to prevent significant NP aggregation in solution and on the surface. This ability to readily control the size of nanostructures on a surface is valuable in the context of understanding optimal structures for electroanalysis or electrocatalysis, which we focus on in the remainder of this paper.

5.2.6 **Nickel Hydroxide Electrocatalyzed Glucose Oxidation**

Although research on the electrochemical detection of glucose is widely reported, most studies deal with the use of the enzyme glucose oxidase to indirectly determine the concentration of glucose.[51-53] Modification of the electrode surface with a

suitable electrocatalytic system to enable direct oxidation of glucose represents an interesting alternative to conventional enzymatic sensing. Recently, the use of the Ni^{2+}/Ni^{3+} redox couple to electrocatalyze glucose oxidation[54,55] has been recognized, stimulating research into the use of nickel and nickel hydroxide-/oxide[32]-modified electrodes in strongly alkaline solutions as electrodes for glucose oxidation.

Figure 5.7 shows CVs of $Ni(OH)_2$-modified pBDD electrodes (—), Γ ~20 nmol cm^{-2}, for the oxidation of 100 μM glucose in 0.1 M KOH. The surface was uniformly covered with $Ni(OH)_2$ NPs (Figures 5.2 (a) and 5.3). Also shown is the voltammetric response (- - -) of the surface in the absence of glucose; that is, 0.1 M KOH only. Finally, the inset gives the CV response in the presence of 1 mM glucose at *bare* pBDD. All CVs were recorded at 5 mV s^{-1}. At the bare pBDD surface, no signal was detected for the direct oxidation of glucose, even when the concentration was increased to 1 mM. This indicates that pBDD is an excellent electrochemically inert support for the $Ni(OH)_2$ NPs in alkaline glucose solutions. Other support electrodes employed previously (e.g., Au) have been shown to contribute to glucose oxidation, complicating the interpretation of the CV response.[56,57]

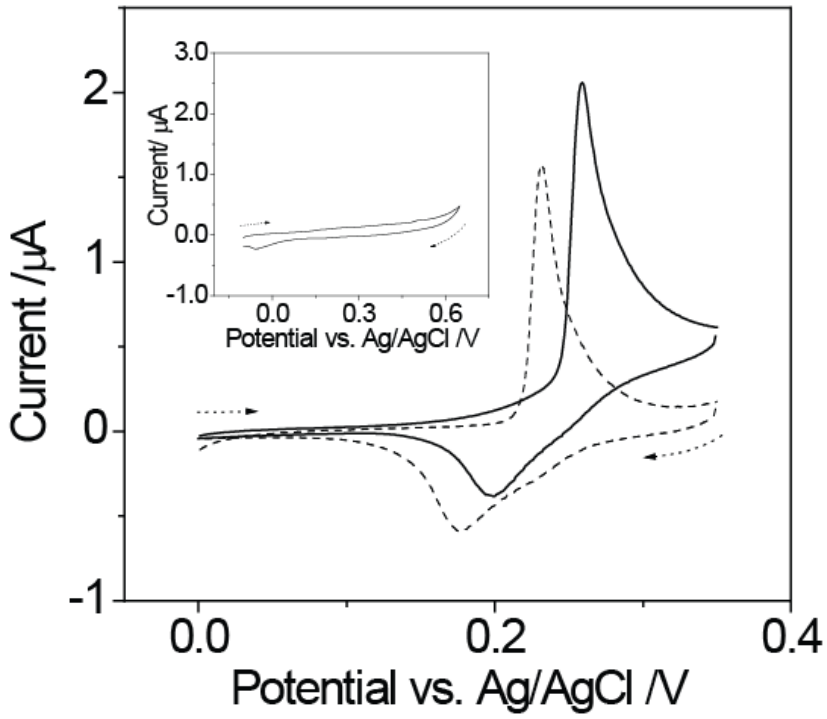

Figure 5.7: Cyclic voltammetry recorded in the absence (- - -) and presence (──) of 100 μM glucose, in 0.1 M KOH, for a $Ni(OH)_2$ *-modified (Γ ~20 nmol cm^{-2}) pBDD. The scan rate is 5 mV s^{-1}. Inset: CV of the bare pBDD in 0.1 M KOH solution containing 1 mM of glucose*

In the absence of glucose, as the potential is scanned more positive, the current increases due to oxidation of Ni^{2+} to Ni^{3+}. Figure 5.7 shows that in the presence of glucose, there is a clear increase in the anodic current and a decrease in the cathodic current compared with the response without glucose, as expected for an electrocatalytic process. In the potential region 0.15−0.25 V, there appears to be a small prewave that is likely to be due to the oxidation of $Ni(OH)_2$ to Ni(OOH). Beyond this potential, the current rises steeply due to the increased turnover of glucose driving the oxidation of $Ni(OH)_2$ to Ni(OOH), which is reconverted to $Ni(OH)_2$ in the process.

To verify how the amount of $Ni(OH)_2$ on the surface affects the electrocatalytic response, five electrodes were prepared with differing Γ values: (a) ~4 nmol cm^{-2} (1 s deposition; Figure 5.4 (a)), (b) ~20 nmol cm^{-2} (5 s deposition; Figures 5.2 (a) and 5.3), (c) ~75 nmol cm^{-2} (15 s deposition; Figure 5.4 (b)), (d) ~140 nmol cm^{-2} (30 s deposition; Figures 5.2 (b) and 5.4 (c)), and (e) ~420 nmol cm^{-2} (100 s deposition; Figures 5.2 (b) and 5.4 (d), (e), (f)). For all electrodes, the current−time response for the oxidation of 100 μM glucose was recorded at 0.35 V for a period of 90 s. Although the current after this period of time approaches steady-state behavior, the true steady-state current (i_{ss}), was determined on a reciprocal time plot ($t^{-1/2}$) by extrapolating the current value to the steady-state value.

Figure 5.8 shows i_{ss} (●) and i_{ss}/Γ (○) as a function of Γ. Increasing Γ leads to an increase in i_{ss}, until it approaches an almost steady value for Γ > 140 nmol cm^{-2}. When i_{ss} is normalized by Γ, there is, rather strikingly, an interesting size dependence of the NP current density, which indicates that the smallest NPs (~12 nm) are less active than those which are larger (~25 nm). Thereafter, as the NP size increases, the effective efficiency decreases because the reaction becomes increasing mass-transport-controlled and the flux to increasingly large NPs decreases (vide infra).

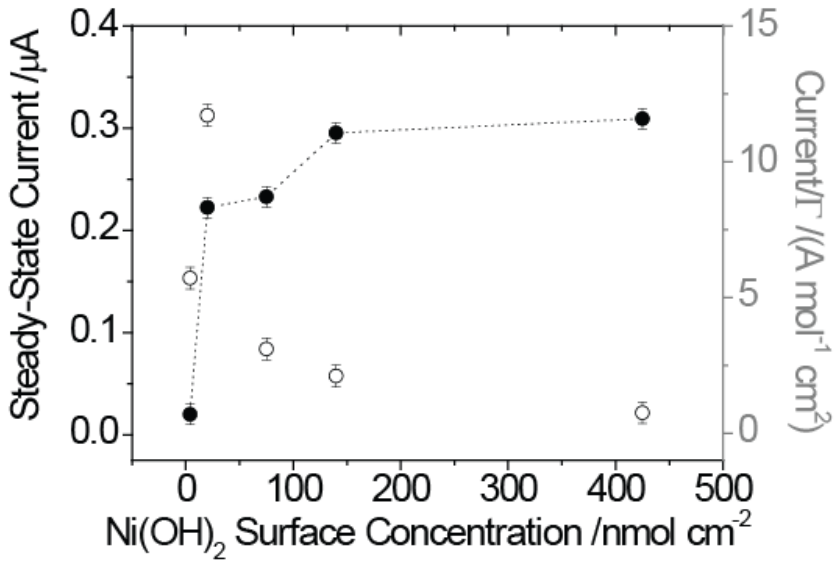

Figure 5.8: Electrocatalytic steady-state current for the oxidation of 100 μM glucose at $Ni(OH)_2$*-functionalized pBDD electrodes in 0.1 M KOH for Γ values (−●−) of ~ 4, 20, 75, 140, and 420 nmol cm*$^{-2}$*. Normalized steady-state currents as a function of Γ, (− ○ −), for the same surface coverages as above.*

For the limiting currents measured, it is useful to estimate, using equation 5.9, the thickness of the established diffusion layer to determine whether the reaction is under kinetic or mass transfer control.

$$i_{ss} = nFADc^*/\delta \qquad (5.9)$$

D, *c**, and δ are the diffusion coefficient of glucose (6.7×10^{-6} cm^2 s^{-1});[38] concentration of glucose (100 μM); and diffusion layer thickness, respectively. This equation treats the electrode as being uniformly active, which is reasonable, given the close NP spacing (see Figures 5.2−5.4). δ is calculated to be 3050 (Γ ~4 nmol cm^{-2}), 274 (Γ ~20 nmol cm^{-2}), 262 (Γ ~75 nmol cm^{-2}), 206 (Γ ~140 nmol cm^{-2}), and 197 μm (Γ ~420 nmol cm^{-2}). Except for the smallest Γ value, the δ values are similar to those measured experimentally for diffusion-controlled reactions at a macroelectrode under steady-state conditions, for which the time scale is sufficient such that natural convection operates.[58]

This simple analysis suggests that for Γ values in the range 20−140 nmol cm^{-2}, the Ni^{3+} electrocatalysed oxidation of glucose tends toward diffusion-control;[59,60] however, the δ value calculated for Γ = 4 nmol cm^{-2} strongly suggests that other factors control the current. At this surface coverage, the NPs are the smallest, and thus, the flux to each particle is at its highest for all of the morphologies considered. Thus, the process is now likely to be under kinetic control; we are presently exploring this observation in more detail.

When considering the normalized (i_{ss}/Γ) values, (○ in Figure 5.8), it is clear that the isolated $Ni(OH)_2$ NP-pBDD structures formed at Γ ~20 nmol cm^{-2} are the most effective in terms of amount of material utilized. This highlights a key advantage of working with isolated NPs, as opposed to aggregates or thin film structures, which have been predominantly employed in previous $Ni(OH)_2$ studies.[21,23,39,40,59]

Figure 5.9 (a) shows the *i*−*t* behavior of the $Ni(OH)_2$ -modified pBDD electrode at the optimal (for material usage) $Ni(OH)_2$ surface concentration (Γ ~20 nM cm^{-2}) of those investigated, in 0.1 M KOH containing different glucose concentrations in the range 50 μM−1 mM. For all experiments, the potential was held at 0.35 V for a period of 90 s, although the data is shown only for times of 30−90 s to emphasize the long time behaviour. As the glucose concentration was increased, the chronoamperometric current increased monotonically. Figure 5.9 (b) shows the resulting calibration curve of i_{ss} (evaluated as described above) against glucose concentration. The plot is linear, and using eq 5.9, the gradient yields a δ value of 230 μm, consistent with a diffusion-controlled process. From the calibration data, a

sensitivity of 330 ± 10 μA mM^{-1} cm^{-2} was determined, with a limit of detection (S/N = 3) of 400 nM.

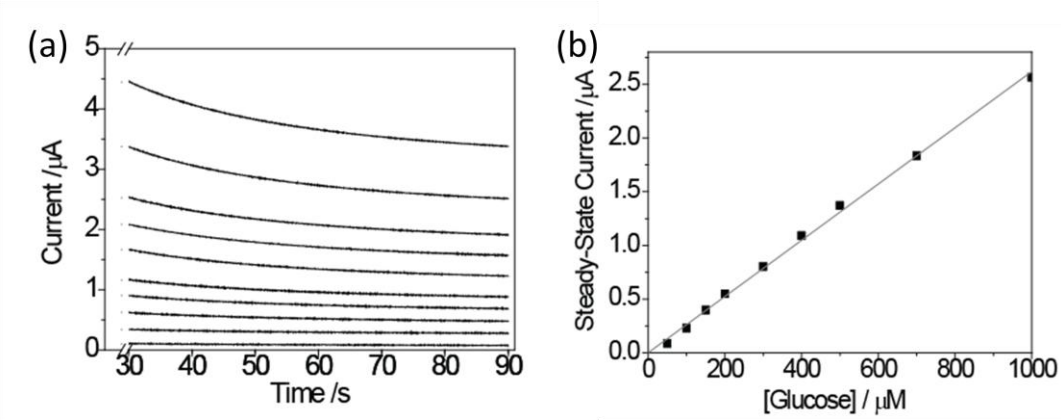

Figure 5.9: (a) Current−time curves recorded by holding the potential of the $Ni(OH)_2$ NP modified pBDD electrode at 0.35 V for 90 s (for Γ = 20 nmol cm^{-2}) for glucose concentrations of 0 (smallest), 50, 100, 150, 200, 300, 400, 500, 700, and 1000 μM (highest) in 0.1 M KOH. (B) Calibration curve of the steady-state current versus glucose concentration for Γ = 20 nmol cm^{-2}.

This data (especially the limit of detection) compares extremely favourably with the most sensitive $Ni(OH)_2$ modified electrode glucose sensors currently described in the literature. Reference 37 summarizes all previous studies to the year 2010. This result is particularly impressive when considering the small amount of $Ni(OH)_2$ employed on the surface (~2 μg cm^{-2}) resulting in a sensitivity based on catalyst mass of 115 ± 5 μA mM^{-1} $μg^{-1}$.

5.2.7 **Catalytic Oxidation of Alcohols by Nickel Hydroxide NPs**

Given the results above for glucose, $Ni(OH)_2$ NP-modified pBDD electrodes were employed to investigate the electrocatalytic oxidation of methanol and ethanol, of importance for the development of fuel cell catalysts. Alcohol electrooxidation under alkaline conditions can be achieved with higher efficiencies, making $Ni(OH)_2$ particles particularly interesting, given their stability under these conditions.[61-63] CVs

recorded in 0.1 M KOH in the absence (- - -) and presence (—) of (a) 0.5 M ethanol and (b) 0.47 M methanol, at a scan rate of 5 mV s^{-1}, are shown in Figure 5.10. The currents have been normalized by the mass of $Ni(OH)_2$ deposited on the electrode surface. For comparison, the inset to Figure 5.10(a) shows the response of a bare pBDD electrode in 0.1 M KOH electrolyte in the presence of both 1 M ethanol and 1 M methanol. The CV is featureless, indicating that a pBDD electrode is incapable of electrochemically oxidizing either alcohol in this potential region.

The characteristic signal of $Ni(OH)_2$ oxidation and subsequent reduction of NiOOH for the $Ni(OH)_2$ -modified pBDD is clearly evident in the CVs in Figure 5.10, recorded in the absence of the alcohols. In the presence of the alcohols, the current signal rises dramatically as the electrochemically generated NiOOH is able to oxidatively catalyze the ethanol (a) and methanol (b), present in solution. Interestingly, the current that flows in the presence of the alcohol occurs at less positive potentials than many reported studies,[64-67] likely indicating that α-phase $Ni(OH)_2$ dominates.[68,69] This is particularly significant because it means complications from the catalytic oxidation of hydroxide ions are avoided.

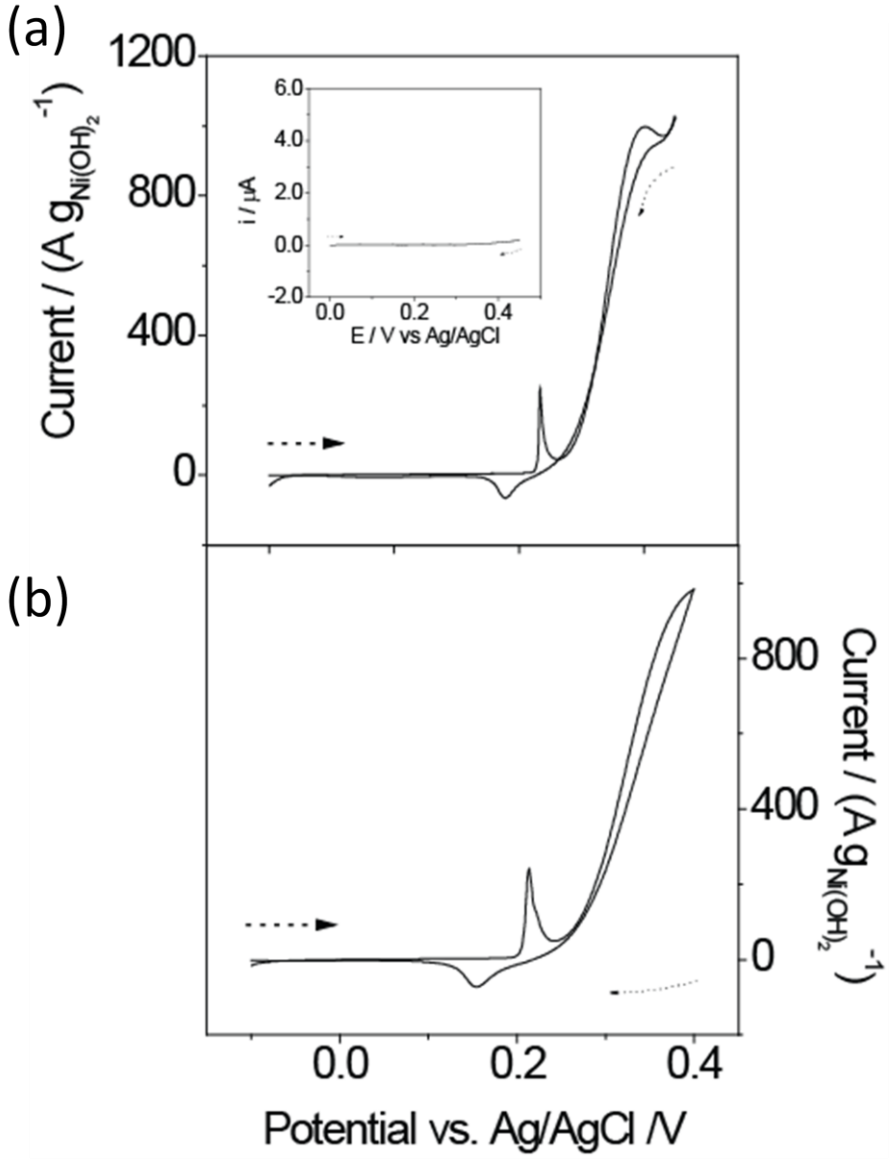

Figure 5.10: CVs performed at 5 mV s^{-1} at a $Ni(OH)_2$ NP modified pBDD electrode (Γ = 20 nmol cm^{-2}) in 0.1 M KOH and (a) 0.5 M ethanol and (b) 0.47 M methanol. Inset: CV of bare pBDD in a 0.1 M KOH solution containing both 1 M ethanol and 1 M methanol.

Maximum normalized currents of ~1010 A g^{-1} for ethanol (0.5 M) and ~990 A g^{-1} for methanol (0.47 M) oxidation were found. These values are much higher than very recent reports using other nanostructured catalysts.[65,70] For example, CVs employing electrodes modified by Pt/MnO_2/carbon nanotubes (CNTs) showed a maximum catalytic current of ~450 A g^{-1} in an electrolyte solution containing 1 M methanol in 1 M $HClO_4$.[16-20,65] Replacement of the Pt component of the composite

by RuPt resulted in maximum currents of ~900 A g^{-1} for the same electrolyte conditions.[15,65] In other work, CNT-modified electrodes functionalized with Pt and PtRu NPs produced normalized currents up to 300 A g^{-1} using 0.5 M H_2SO_4 as electrolyte and 1 M methanol.[70]

Although there are other reports in the literature of the use of $Ni(OH)_2$ and $Ni(OH)_2$ composite electrodes for the oxidation of methanol and ethanol,[10,64,66,67,71] it is not possible to extract mass-normalized catalytic current from such data for comparison with ours. The electrodes were typically prepared by electrodepositing nickel for hundreds of seconds and then oxidizing in alkaline solution to produce nickel hydroxide; the amount of $Ni(OH)_2$ on the electrodes is not typically known.

However, by noting parameters presented in these papers[10,64,66,67,71] (such as the anodic peak current (charge) of the $Ni(OH)_2$ modified electrodes in the absence of alcohol (provides an estimation of the amount of nickel hydroxide), the maximum electrocatalytic current obtained in a region where there are no complications from hydroxide catalyzed oxidation, and the alcohol concentration and the electrolyte employed), it is possible to draw the following qualitative conclusions: (1) The nanostructured $Ni(OH)_2$ pBDD electrode presented herein appears to show the largest electrocatalytic current based on mass usage. This re-emphasizes again one of the advantages of using $Ni(OH)_2$ isolated NP structures. (2) The larger electrocatalytic currents are achieved at lower alcohol concentrations and at less positive potentials than many of the reported studies.[64] (3) The deposition method employed in this work has the advantage of ease of use and is inexpensive.

5.3. CONCLUSION

The electrosynthesis of uniformly dispersed $Ni(OH)_2$ NPs with narrow size distributions on pBDD electrodes has been demonstrated for the first time. This was achieved by electrogenerating OH^- in the presence of Ni^{2+} to create highly supersaturated ($S > 10^5$) $Ni(OH)_2$ solutions close to the electrode for short periods of time (approximately seconds). This resulted in the electrodeposition of $Ni(OH)_2$ NPs via precipitation directly on the electrode surface, as confirmed by XPS, FE-SEM, and AFM. The size of the NPs could be tuned by controlling the reaction conditions, particularly the [OH^-] electrogeneration time. After 1 s, NPs with dimensions of 12 ± 3 nm were produced with a surface coverage of 25 ± 5 NPs μm^{-1}, increasing in size and surface coverage to ~39 ± 9 nm and 87 ± 15 NPs μm^{-2}, respectively, after 15 s. Longer times resulted in larger particles, which ultimately formed aggregates. After 100 s, the surface was dominated by such structures which were a few micrometers in height.

The $Ni(OH)_2$ surface coverage was calculated by considering the charge passed during direct oxidation of $Ni(OH)_2$. This value was in good agreement with that calculated on the basis of AFM images of the surface coverage, assuming spherical NPs. The close correlation of the two results suggests that during this solid-state electrooxidation process, the entire volume of $Ni(OH)_2$ was oxidized, not just the surface of the NP.

The effect of NP size on electrocatalytic activity was investigated by measuring the steady-state current for the oxidation of glucose in alkaline media. It was found that for NPs ≥ 25 nm in size, glucose oxidation was predominantly diffusion-controlled.

However, for the smallest NPs produced (~12 nm) the currents passed were much smaller than expected on the basis of diffusion control; this was attributed to kinetic limitations. For glucose, the optimal surface coverage was Γ ~20 nmol cm^{-2}, which corresponded to isolated NPs of size ~25 ± 6 nm and a surface coverage of 85 ± 12 NPs μm^{-2}. For the size of the electrode employed (1 mm diameter disc), this corresponded to 15 ng of $Ni(OH)_2$ on the surface. For glucose oxidation, this electrode showed a sensitivity of 330 μA mM^{-1} cm^{-2} and a limit of detection of 400 nM. The latter represents one of the lowest limits of detection for glucose for $Ni(OH)_2$ -based electrodes.

The electrocatalytic oxidation of this electrode toward methanol and ethanol was also found to be very efficient, achieving very high density currents of ~1010 A g^{-1} for 0.5 M ethanol and 990 A g^{-1} for 0.47 M methanol.

5.4. REFERENCES

(1) Li, H.; Li, H.; Deng, J.-F. *Catal. Today* **2002**, *74*, 53.
(2) Bond, G. C.; Thompson, D. T. *Catal. Rev. - Sci. Eng.* **1999**, *41*, 319
(3) Daniel, M.-C.; Astruc, D. *Chem. Rev. (Washington, DC, U. S.)* **2003**, *104*, 293.
(4) Burda, C.; Chen, X.; Narayanan, R.; El-Sayed, M. A. *Chem. Rev. (Washington, DC, U. S.)* **2005**, *105*, 1025.
(5) Vassal, N.; Salmon, E.; Fauvarque, J. F. *J. Electrochem. Soc.* **1999**, *146*, 20.
(6) Sac-Epee, N.; Palacin, M. R.; Beaudoin, B.; Delahaye-Vidal, A.; Jamin, T.; Chabre, Y.; Tarascon, J. M. *J. Electrochem. Soc.* **1997**, *144*, 3896.
(7) Chen, J.; Bradhurst, D. H.; Dou, S. X.; Liu, H. K. *J. Electrochem. Soc.* **1999**, *146*, 3606.
(8) Schäfer, H. J.; Schneider, R. *Tetrahedron* **1991**, *47*, 715.
(9) Berger, R. J.; Doesburg, E. B. M.; van Ommen, J. G.; Ross, J. R. H. *Appl. Catal., A* **1996**, *143*, 343.
(10) Cox, P.; Pletcher, D. *J. Appl. Electrochem.* **1990**, *20*, 549.
(11) Lo, Y. L.; Hwang, B. J. *J. Electrochem. Soc.* **1995**, *142*, 445.
(12) Pletcher, D. *J. Appl. Electrochem.* **1984**, *14*, 403.
(13) Welch, C.; Compton, R. *Anal. Bioanal. Chem.* **2006**, *384*, 601.
(14) Polsky, R.; Gill, R.; Kaganovsky, L.; Willner, I. *Anal. Chem.* **2006**, *78*, 2268.
(15) Hutton, L.; Newton, M. E.; Unwin, P. R.; Macpherson, J. V. *Anal. Chem.* **2009**, *81*, 1023.
(16) Jeevanandam, P.; Koltypin, Y.; Gedanken, A. *Nano Lett.* **2001**, *1*, 263.
(17) Pejova, B.; Kocareva, T.; Najdoski, M.; Grozdanov, I. *Appl. Surf. Sci.* **2000**, *165*, 271.
(18) Vidotti, M.; Salvador, R. P.; Córdoba de Torresi, S. I. *Ultrason. Sonochem.* **2009**, *16*, 35.
(19) Wang, Y.; Zhu, Q.; Zhang, H. *Chem. Commun. (Cambridge, U. K.)* **2005**, 5231.
(20) Duan, G.; Cai, W.; Luo, Y.; Li, Z.; Lei, Y. *The Journal of Physical Chemistry B* **2006**, *110*, 15729.
(21) Vidotti, M.; Córdoba de Torresi, S. I. *Electrochim. Acta* **2009**, *54*, 2800.
(22) Wu, M.-S.; Hsieh, H.-H. *Electrochim. Acta* **2008**, *53*, 3427.
(23) Sawaby, A.; Selim, M. S.; Marzouk, S. Y.; Mostafa, M. A.; Hosny, A. *Physica B (Amsterdam, Neth.)* **2010**, *405*, 3412.
(24) Walter, E. C.; Murray, B. J.; Favier, F.; Kaltenpoth, G.; Grunze, M.; Penner, R. M. *J. Phys. Chem. B* **2002**, *106*, 11407.
(25) Compton, R. G.; Foord, J. S.; Marken, F. *Electroanalysis* **2003**, *15*, 1349.
(26) Xu, J. S.; Granger, M. C.; Chen, Q. Y.; Strojek, J. W.; Lister, T. E.; Swain, G. M. *Anal. Chem.* **1997**, *69*, A591.
(27) Shin, D.; Tryk, D. A.; Fujishima, A.; Merkoci, A.; Wang, J. *Electroanalysis* **2005**, *17*, 305.
(28) Therese, G. H. A.; Kamath, P. V. *Chem. Mater.* **2000**, *12*, 1195.
(29) Tan, Y.; Srinivasan, S.; Choi, K.-S. *J. Am. Chem. Soc.* **2005**, *127*, 3596.
(30) Streinz, C. C.; Hartman, A. P.; Motupally, S.; Weidner, J. W. *J. Electrochem. Soc.* **1995**, *142*, 1084.
(31) Giovanelli, D.; Lawrence, N. S.; Jiang, L.; Jones, T. G. J.; Compton, R. G. *Sens. Actuators, B* **2003**, *88*, 320.
(32) Reim, R. E.; Van Effen, R. M. *Anal. Chem.* **1986**, *58*, 3203.
(33) Deo, R. P.; Lawrence, N. S.; Wang, J. *Analyst* **2004**, *129*, 1076.
(34) Stradiotto, N. R.; Toghill, K. E.; Xiao, L.; Moshar, A.; Compton, R. G. *Electroanalysis* **2009**, *21*, 2627.
(35) Chang, Y.; Qiao, J.; Liu, Q.; Shangguan, L.; Ma, X.; Shuang, S.; Dong, C. *Anal. Lett.* **2008**, *41*, 3147

(36) Toghill, K. E.; Xiao, L.; Stradiotto, N. R.; Compton, R. G. *Electroanalysis* **2010**, *22*, 491.
(37) Toghill, K. E.; Xiao, L.; Phillips, M. A.; Compton, R. G. *Sens. Actuators, B* **2010**, *147*, 642.
(38) Sangwal, K. *Additives and Crystallisation Processes: From Fundamentals to Applications*; John Wiley & Sons Ltd, West Sussex, 2007.
(39) Corrigan, D. A. *J. Electrochem. Soc.* **1987**, *134*, 377.
(40) Portemer, F.; Delahaye-Vidal, A.; Figlarz, M. *J. Electrochem. Soc.* **1992**, *139*, 671.
(41) Lide, D. R., Ed. *Handbook of Chemistry and Physics, 90th ed.*; CRC Press: Boca Raton 2009.
(42) Wilson, N. R.; Clewes, S. L.; Newton, M. E.; Unwin, P. R.; Macpherson, J. V. *J. Phys. Chem. B* **2006**, *110*, 5639.
(43) Colley, A. L.; Williams, C. G.; Johansson, U. D.; Newton, M. E.; Unwin, P. R.; Wilson, N. R.; Macpherson, J. V. *Anal. Chem.* **2006**, *78*, 2539.
(44) Torto, N.; Ruzgas, T.; Gorton, L. *J. Electroanal. Chem.* **1999**, *464*, 252.
(45) Grosvenor, A. P.; Biesinger, M. C.; Smart, R. S. C.; McIntyre, N. S. *Surf. Sci.* **2006**, *600*, 1771.
(46) Deki, S.; Hosokawa, A.; Béléké, A. B.; Mizuhata, M. *Thin Solid Films* **2009**, *517*, 1546.
(47) Chigane, M.; Ishikawa, M. *J. Chem. Soc., Faraday Trans.* **1998**, *94*, 3665.
(48) McIntyre, N. S.; Cook, M. G. *Anal. Chem.* **1975**, *47*, 2208.
(49) Crank, J. *The Mathematics of Diffusion, 2nd ed.*; Clarendon Press: Oxford, 1975.
(50) Breiter, M. H., K. Z. *Elektrochem.* **1960**, *64*, 462.
(51) Wang, J. *Electroanalysis* **2001**, *13*, 983.
(52) Newman, J. D.; Turner, A. P. F. *Biosens. Bioelectron.* **2005**, *20*, 2435.
(53) Burt, D. P.; Unwin, P. R. *Electrochem. Commun.* **2008**, *10*, 934.
(54) Cheung, K.-C.; Wong, W.-L.; Ma, D.-L.; Lai, T.-S.; Wong, K.-Y. *Coord. Chem. Rev.* **2007**, *251*, 2367.
(55) Quintino, M. d. S. M.; Winnischofer, H.; Nakamura, M.; Araki, K.; Toma, H. E.; Angnes, L. *Anal. Chim. Acta* **2005**, *539*, 215.
(56) Casella, I. G.; Guascito, M. R.; Sannazzaro, M. G. *J. Electroanal. Chem.* **1999**, *462*, 202.
(57) Xiang, C.; Xie, Q.; Yao, S. *Electroanalysis* **2003**, *15*, 987.
(58) Amatore, C.; Szunerits, S.; Thouin, L.; Warkocz, J.-S. *Electroanalysis* **2001**, *13*, 646.
(59) Jafarian, M.; Forouzandeh, F.; Danaee, I.; Gobal, F.; Mahjani, M. *J. Solid State Electrochem.* **2009**, *13*, 1171.
(60) Shamsipur, M.; Najafi, M.; Hosseini, M.-R. M. *Bioelectrochemistry* **2010**, *77*, 120.
(61) Wasmus, S.; Küver, A. *J. Electroanal. Chem.* **1999**, *461*, 14.
(62) Villullas, H. M.; Mattos-Costa, F. I.; Bulhões, L. O. S. *J. Phys. Chem. B* **2004**, *108*, 12898.
(63) Huang, S.-y.; Chang, C.-m.; Wang, K.-w.; Yeh, C.-t. *ChemPhysChem* **2007**, *8*, 1774.
(64) El-Shafei, A. A. *J. Electroanal. Chem.* **1999**, *471*, 89.
(65) Zhou, C.; Wang, H.; Peng, F.; Liang, J.; Yu, H.; Yang, J. *Langmuir* **2009**, *25*, 7711.
(66) Yi, Q.; Huang, W.; Zhang, J.; Liu, X.; Li, L. *Catal. Commun.* **2008**, *9*, 2053.
(67) Danaee, I.; Jafarian, M.; Forouzandeh, F.; Gobal, F.; Mahjani, M. G. *Int. J. Hydrogen Energy* **2008**, *33*, 4367.
(68) Kim, M.-S.; Kim, K.-B. *J. Electrochem. Soc.* **1998**, *145*, 507.
(69) Wehrens-Dijksma, M.; Notten, P. H. L. *Electrochim. Acta* **2006**, *51*, 3609.
(70) Wu, B.; Hu, D.; Kuang, Y.; Liu, B.; Zhang, X.; Chen, J. *Angew. Chem., Int. Ed.* **2009**, *48*, 4751.
(71) Weng, Y.-C.; Chou, T.-C. *J. Electrochem. Soc.* **2006**, *153*, H127.

CHAPTER 6

Factors Controlling Stripping Voltammetry of Pb at pBDD Electrodes: New Insights from High-Resolution Microscopy

We report wide-ranging studies to elucidate the factors and issues controlling stripping voltammetry of metal ions on solid electrodes using the well-known Pb/Pb^{2+} couple on pBDD as an exemplar system. Notably, high-resolution microscopy techniques have revealed new insights into the features observed in DP−ASV which provide a deeper understanding of how best to utilize this technique. DP−ASV was employed in an impinging wall-jet configuration to detect Pb^{2+} at a pBDD macrodisc electrode. The deposition process was driven to produce a grain-independent homogeneous distribution of Pb NPs on the electrode surface; this resulted in the observation of narrow stripping peaks. Lower calibration gradients of current or charge versus concentration were found for the low concentrations, correlating with a lower than expected amount of Pb deposited on the surface. This was attributed to the complex nature of nucleation and growth at solid surfaces in this concentration regime, complicating mass transport. At high concentrations a nonlinear response was observed, with less Pb detected than expected, in addition to the observation of a second stripping peak. AFM and FE-SEM revealed the second peak to be due to a change in deposition morphology from isolated NPs to grain-independent heterogeneous structures comprising both thin films and NPs; the second peak is associated with stripping from the thin-film structures. AFM also revealed a substantial amount of Pb remaining on the surface after stripping at high concentration, explaining the nonlinear relationship between stripping peak current (or charge) and concentration. The studies herein highlight important and complex physicochemical processes involved in the electroanalysis of heavy metals at solid electrodes, such as pBDD, that need to be accounted for when using stripping voltammetry methods.

6.1. INTRODUCTION

ASV is well-established for the detection of heavy metals.[1] The analyte of interest is reduced at the electrode surface in a preconcentration step, followed by anodic sweeping of the electrode potential to oxidatively strip reduced analyte from the surface in a quantifiable way.[1] Until recently, Hg films[2,3] and drops[4-6] have been the electrodes of choice for trace-level metal detection, offering sub parts per billion detection limits.[7] Hg is particularly attractive as an electrode material, as it has a wide cathodic potential window, enabling metal deposition via reduction without hydrogen evolution at the electrode. Furthermore, because it is liquid at room temperature, Hg−metal amalgams result, following reduction of the metal of interest. Thus, during stripping, symmetrical voltammetric peaks are typically obtained, characterized with defined widths at half-height, due to the "homogeneous" nature of the Hg electrode. However, the toxicity of Hg is now of great concern, and alternative nontoxic electrode materials for heavy-metal detection are highly sought.[8,9]

One of the most important considerations for a Hg replacement electrode is the need for a wide cathodic potential window. pBDD is currently attracting much attention due to its very wide potential window in aqueous solution, low background currents, and resistance to fouling.[10-12] pBDD is also resistant to corrosion under both acidic and alkaline conditions, as well as at extreme potentials,[13] and is stable at high temperatures and pressures. pBDD has been used with different ASV techniques, including linear sweep voltammetry (LSV),[14] differential pulse voltammetry (DPV),[15,16] and square-wave voltammetry (SWV),[17] to detect a wide range of heavy metals. These include, for example, Zn, Cd, Pb, and Cu, down to parts per billion

levels in electrolyte solutions, lake and tap water, river sediment, and wastewater sludge.[17-19]

In contrast to those obtained on Hg electrodes, the stripping peaks obtained on pBDD electrodes are often broad and largely asymmetric.[15,16,19] This has been attributed to the use of (i) a heterogeneously active solid electrode where the different crystallographically orientated grains are characterized by different electrical conductivity and surface structure[20] and (ii) a heterogeneous size distribution of electrodeposited structures.[18,21] In general, dependent on the solution conditions, applied potential, time, and structure of the pBDD surface (e.g., grain size, surface roughness, and surface termination),[20,22-24] a wide variation in electrodeposited metal particle size and surface morphology has been reported using electron microscopy and AFM. However, to date, there have been no high-resolution microscopy studies of the effect of anodic stripping on the electrodeposited metal structures that form during stripping voltammetry. Speculation on stripping-induced changes in the metal surface morphology is often inferred from indirect analysis of the current−voltage (or time) response.

Double stripping peaks have been observed for anodic metal dissolution at relatively high metal ion concentrations (e.g., >100 ppb for the case of Pb[18]), attributed loosely to the "nature" of the metal deposit on the surface (no microscopic evidence was presented).[18] The majority of previous studies also report an excess charge associated with deposition compared to stripping.[16,25-27] This has been attributed to several factors: (i) incomplete metal stripping, (ii) detachment of metal particles from the electrode surface,[26,28,29] and (iii) hydrogen evolution during deposition,[15] catalyzed

by the deposited metallic nanostructures. Again, however, a lack of complementary microscopic investigation means that these suggestions remain conjectures.

Given the current level of understanding of ASV on pBDD, the goal of this study is to develop new insights into the deposition and stripping process, particularly through the use of AFM. Herein, we investigate the electrodeposition and stripping behaviour of Pb^{2+}/Pb at pBDD electrodes for Pb^{2+} concentrations in the nanomolar to micromolar range. This system was selected for detailed investigation as it is among the most studied, but as highlighted, there are many questions regarding DP−ASV analysis that are yet to be answered. The aim is to correlate the observed current response with metal nucleation/growth and dissolution mechanisms. To increase mass transport during the deposition step[30-34] (and reduce deposition times), we use an impinging jet setup,[35-38] which has well-characterized hydrodynamics,[39] to deliver solution to the pBDD electrode.

6.2. Results and Discussion

6.2.1 *In-Situ* Cleaning of the pBDD Electrode

The electrochemical measurements carried-out in this chapter were performed using two types of electrode. The 1 mm diameter disc electrodes sealed in glass capillaries as detailed in section 3.3, were used for electrochemical analysis. The electrodes fabricated as described in section 2.2.2.were used for the microscopy studies. To carry out multiple (repetitive) stripping voltammetry measurements on the same electrode, without needing to mechanically clean between each measurement, an *in-situ* electrochemical cleaning process was developed. The aim was to provide a clean

and reproducible surface for the start of each measurement, ensuring that no Pb remained on the surface from a previous voltammetric analysis.[14] We selected a convenient cleaning time of 10 min and then determined the potential required to achieve a clean, Pb-free surface.

Figure 6.1 shows typical 3 μm × 3 μm *ex-situ* AFM height images of the pBDD electrode surface recorded *in air* for the following situations: (a) prior to electrodeposition, (b) after deposition of 1 μM Pb^{2+} (−1.5 V for 400 s) using the impinging jet arrangement, and (c) after application of a potential of +1.2 V to the electrode surface for 600 s to remove electrodeposited Pb by oxidation. At this potential (+1.2 V), protons are also generated and bubbles of oxygen evolved (to further aid Pb dissolution). A high concentration of Pb was deliberately employed for the deposition step to demonstrate the effectiveness of the *in-situ* electrochemical cleaning process. Figure 6.1 (d) shows an XPS spectrum of the pBDD electrode after cleaning using the *in-situ* protocol. The inset shows the binding energy region which is most sensitive to the presence of Pb.

It is evident from Figure 6.1 (b) that electrodeposition of Pb results in extensive coverage of the pBDD surface in Pb NPs, here with an average height of 19 ± 7 nm (SD) and coverage of 160 ± 12 NPs μm^{-2}. Importantly, comparison of parts (a) and (c) of Figure 6.1 highlights that pBDD is returned to a pristine state after the *in-situ* electrochemical cleaning process, proving that the deposited Pb NPs can be removed effectively.

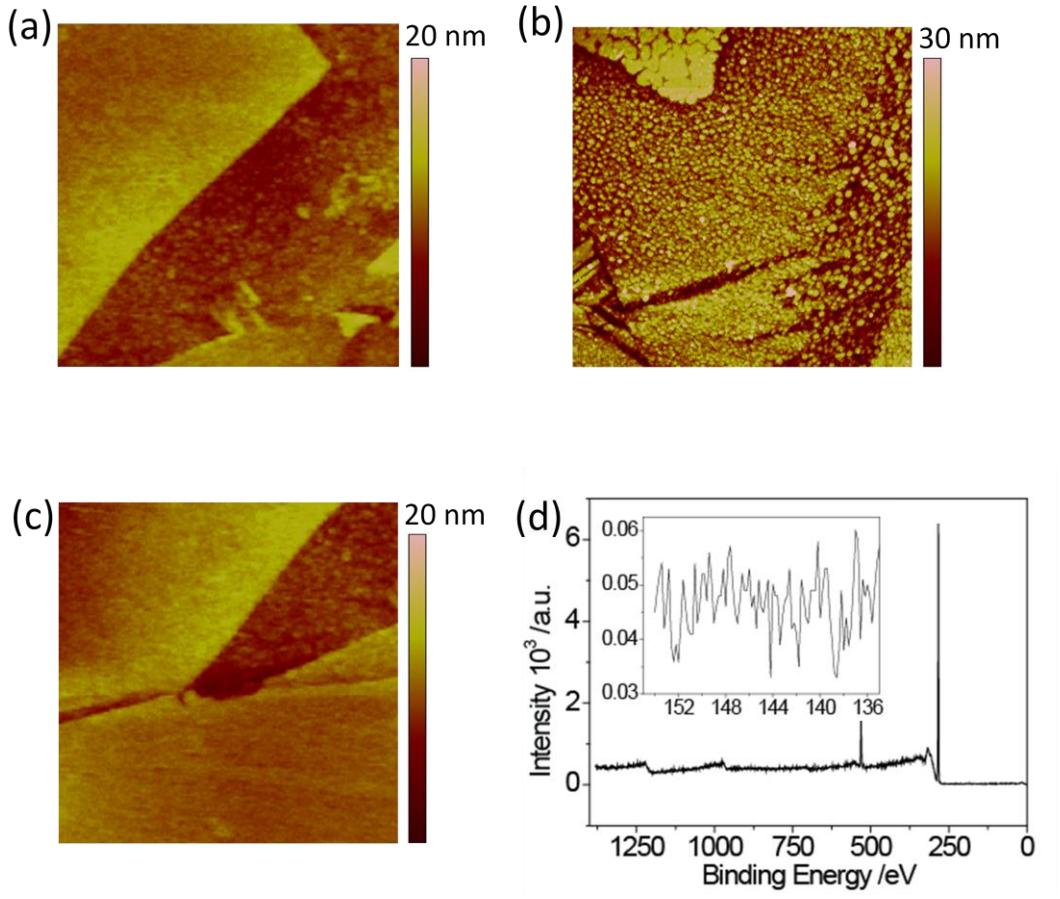

Figure 6.1: Typical ex-situ AFM 3 μm × 3 μm height images of a pBDD surface (a) prior to electrodeposition, (b) after deposition of 1 μM Pb^{2+} (deposition parameters were 400 s deposition at −1.5 V (vs. SCE) with a volume flow rate of 0.1 mL s^{-1}), and (c) after in-situ cleaning of the surface (+1.2 V for 600 s). (d) XPS survey spectra of the electrode after in-situ cleaning of the surface, with the inset showing the Pb 4f signature region.

This is further confirmed by the XPS spectrum of the electrode after the *in-situ* cleaning process. The Pb 4f spectral region (inset to Figure 6.1 (d)) shows no detectable signal for Pb; only XPS signatures for carbon and oxygen are present at ~ 284 and ~532 eV corresponding to the C 1s and O 1s orbitals, respectively. This is as expected for a clean oxygen-terminated sp^3 carbon surface.[40]

Finally, the cleaning procedure could be used repeatedly on the pBDD electrode with no deterioration in the performance of the electrode. Furthermore, the DPV signal (in

background electrolyte), after cleaning in this way, was essentially analogous to that for a freshly polished electrode.

6.2.2 **Impinging Jet-Differential Pulse Stripping Voltammetry**

An impinging flow wall-jet was set-up as described in section 2.4.4. Experiments were performed to characterize the hydrodynamics of the system prior to Pb stripping analysis. The capillary nozzle diameter and nozzle-pBDD electrode separation were 50 µm and 500 µm respectively. Figure 6.2 (a) shows CVs recorded for the reduction of 0.1 mM $Ru(NH_3)_6^{3+}$ in 0.1 M KNO_3, at a scan rate of 100 mV s^{-1}, for V_f of 0.025 (lowest curve) ml s^{-1}, 0.04 ml s^{-1}, 0.05 ml s^{-1}, 0.1 ml s^{-1}, 0.25 ml s^{-1}, 0.4 ml s^{-1}, 0.5 (highest curve) ml s^{-1}. A steady-state diffusion-limited response in all cases is observed as expected for convection-diffusive controlled systems. Equation 6.1 describes the i_{lim} at a wall jet electrode.[41]

$$i_{lim} = 1.59\, nFc^{*}D^{2/3}\upsilon^{-5/12}a^{-1/2}R^{3/4}V_f^{3/4} \qquad (6.1)$$

where υ is the viscosity of the solution, a is the diameter of the circular nozzle, and R is the radius of the electrode. Figure 6.2 (b) shows a plot of i_{lim} (taken from Figure 6.2 (a)), plotted against $V_f^{3/4}$ which in accordance with equation 6.1 is linear and intercepts the origin. The gradient of the line reveals D=6.1 x 10^{-6} cm^2 s^{-1} for $Ru(NH_3)_6^{3+}$ which is in close agreement with theory.[42]

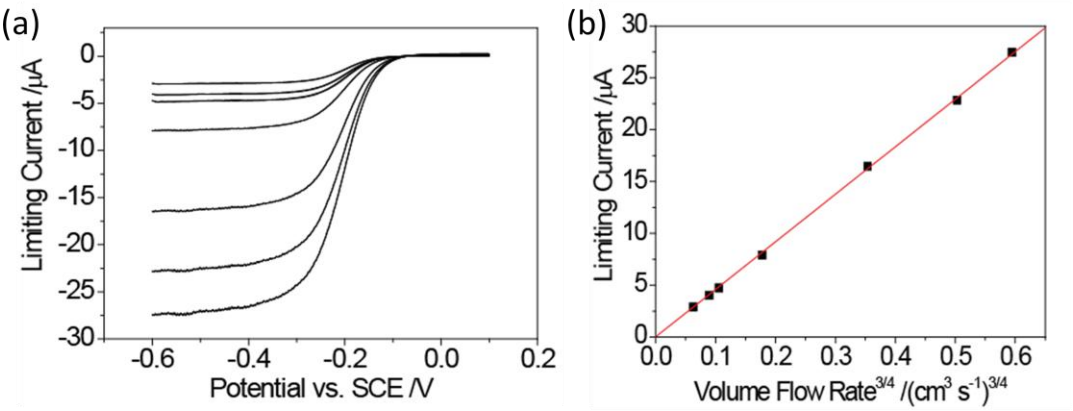

Figure 6.2: (a) CVs for the reduction of 0.1 mM $Ru(NH_3)_6^{3+}$ in 0.1 M KNO_3 at a 1 mm diameter pBDD disc electrode in the impinging wall-jet configuration with a scan rate of 100 mV s^{-1} at volume flow rates of 0.025, 0.04, 0.05, 0.1, 0.25, 0.4, 0.5 ml s^{-1}. (b) Plot of i_{lim} versus $V_f^{3/4}$.

Figure 6.3 (a) shows a selection of typical DPV curves for Pb stripping analysis in 0.1 M KNO_3 for [Pb^{2+}] in the range from 40 nM to 1 μM. For each concentration, deposition occurred for a period of 400 s at a potential of −1.5 V vs. SCE, sufficient to cause the diffusion-limited reduction of Pb^{2+} to Pb at the pBDD electrode. During deposition, solution was flowed onto the electrode using the parameters described in Chapter 2.

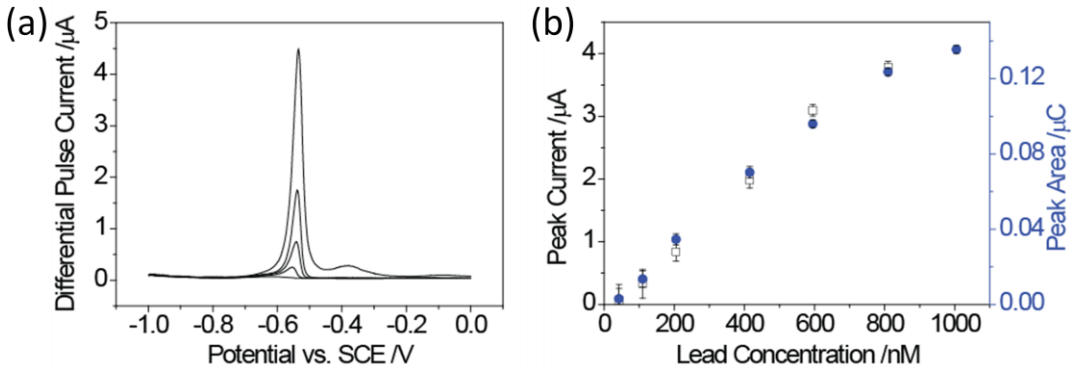

Figure 6.3 (a) DPV (pulse width, 50 mV; pulse amplitude, 50 mV; step size, 2 mV) in 0.1 M KNO_3 for 42 (lowest curve), 110, 205, 415, and 1005 (highest curve) nM Pb^{2+}. Deposition parameters were 400 s at −1.5 V (vs. SCE) with a volume flow rate of 0.1 mL s^{-1}. Between each measurement, the pBDD electrode was cleaned in-situ. (b) Calibration plot of the peak current (□) and peak area (●) versus Pb^{2+} concentration for the Pb^{2+} concentrations shown in (a). All curves have been background corrected.

Figure 6.3 (b) shows a corresponding plot of the DPV peak current (black) and area under the peak (blue) versus [Pb^{2+}]. The charge data (i.e., area under the DPV peak or peaks) takes into account all areas above the background baseline. For Pb^{2+} concentrations in the range of 40−800 nM, a single DPV stripping peak was observed, occurring at similar potentials (between −0.53 and −0.55 V) at all but the lowest concentration. At the highest concentration of 1 μM, a second stripping peak appeared at −0.38 V. As the concentration was increased further, the magnitude of this second peak was also found to increase as shown in Figure 6.4, where DPV was used to strip Pb for [Pb^{2+}] of 1 μM (smallest curve), 2.5 μM, 4 μM and 5 μM (largest curve) Pb^{2+}. At all [Pb^{2+}] two peaks are observed. Both peaks increase with increasing [Pb^{2+}]. The plot in Figure 6.3 (b) shows a linear relationship between either peak current or peak area and [Pb^{2+}], within a defined concentration range of ~100 to ~700 nM. For the two-peak DPV behaviour (1 μM Pb^{2+}), only the peak area data have been included in Figure 6.3 (b). In the linear concentration region, gradients of 4.6 nA nM^{-1} (peak current) and 16.3 nC nM^{-1} (peak area) were obtained.

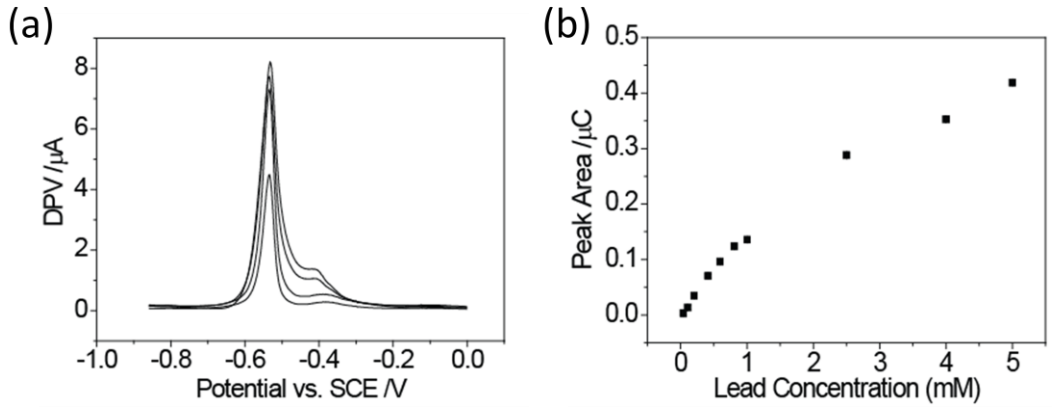

Figure 6.4: (a) DPV response (pulse width: 50 mV; pulse amplitude: 50 mV; step size: 2 mV) in 0.1 M KNO_3 for 1 (lowest curve), 2.5, 4 and 5 μM (highest curve) Pb^{2+}.Deposition parameters are 400 s at -1.5 V (vs. SCE) with a flow rate of 0.1 ml s^{-1}. (b) Calibration plot of peak area (■) versus [Pb^{2+}] for concentrations of 42 nM, 110 nM, 205 nM, 415 nM, 1 μM, 2.51 μM, 4 μM and 5 μM.

To detect lower [Pb^{2+}] accurately, longer preconcentration times were necessary. Figure 6.5 (a) shows a selection of typical DPV curves for [Pb^{2+}] in the range of 4−100 nM. Deposition occurred with the impinging jet arrangement with the electrode held at −1.5 V vs. SCE for 800 s. Within this concentration range, only one stripping peak was observed, which was seen to shift slightly to more negative potentials with decreasing concentration. For example, the peak DPV potentials for 100, 40, and 4 nM Pb were −0.54, −0.58, and −0.62 V, respectively.

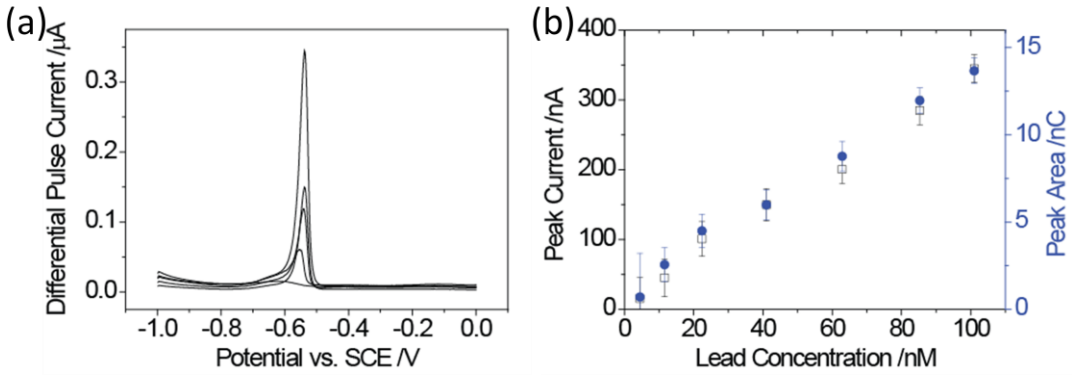

Figure 6.5 (a) DPV (pulse width, 50 mV; pulse amplitude, 50 mV; step size, 2 mV) in 0.1 M KNO_3 for 4.5 (lowest curve), 11.6, 22.4, 41, and 101 (highest curve) nM Pb^{2+}. Deposition parameters were 800 s at −1.5 V (vs. SCE) with a volume flow rate of 0.1 mL s^{-1}. Between each measurement, the pBDD electrode was cleaned in-situ. (b) Calibration plot of the peak current (□) and peak area (●) versus Pb^{2+} concentration for the Pb^{2+} concentrations shown in (a).

Figure 6.5 (b) summarizes the data as plots of both the peak current (black) and area under the peak (blue) versus [Pb^{2+}] for concentrations as low as 4 nM (1 ppb), which are linear, with gradients of 3.4 nA nM^{-1} and 12.4 nC nM^{-1}. Taking into account the proportionality between the stripping peak charge/current and deposition time,[1,7] the calibration slopes from Figure 6.5 (b) (lower concentration range) are smaller than expected on the basis of those obtained from the linear region in Figure 6.3 (b) (higher concentration range). The reasons for this are considered further below.

6.2.3 *Ex-Situ* Electrochemical AFM

Ex-situ AFM was employed to image the pBDD surface after both Pb deposition and stripping to explore further (i) the nonlinearity of the relationship between the charge (or peak current) and concentration at high [Pb^{2+}] (Figure 6.3 (b) and 6.4 (b)), (ii) the double stripping peak behaviour, observed at high [Pb^{2+}] in Figure 6.3 (a) and 6.4 (a), (iii) the negative shift in peak potential with decreasing [Pb^{2+}] at low concentrations (Figure 6.5 (a)), and (iv) the lower calibration gradient obtained for lower [Pb^{2+}]. Figure 6.6 shows typical 1 μm × 1 μm AFM height images of the pBDD electrode after (a) deposition of Pb and (b) subsequent DPV stripping. For deposition, the impinging jet arrangement was employed using the same conditions as for Figure 6.3 (a) for [Pb^{2+}] = (i) 1 μM (ii) 100 nM, and (iii) 10 nM.

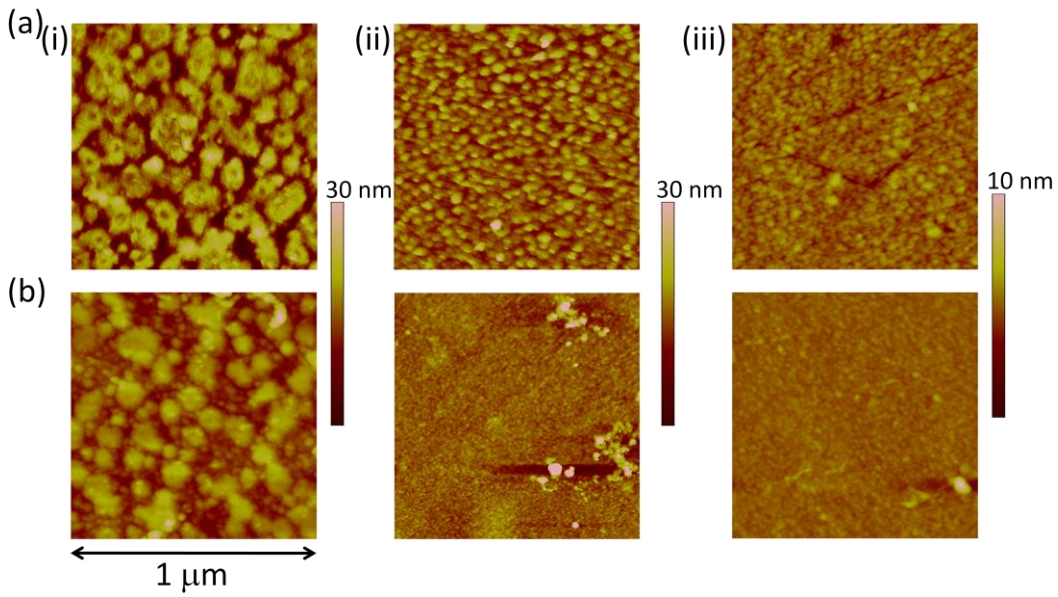

Figure 6.6: Typical 1 μm × 1 μm ex-situ AFM height images of the surface of a pBDD electrode after (a) Pb deposition for 400 s at −1.5 V (vs. SCE) with a volume flow rate of 0.1 mL s^{-1} and (b) Pb stripping using DPV at 200 mV s^{-1} (pulse width, 50 mV; pulse amplitude, 50 mV) in 0.1 M KNO_3 at (i) 1 μM Pb^{2+}, (ii) 100 nM Pb^{2+}, and (iii) 10 nM Pb^{2+}.

The effect of [Pb^{2+}] on the morphology of electrodeposited Pb can clearly be seen by comparing the images in Figure 6.6 (ai,ii,iii). In Figure 6.6 (ai) for [Pb^{2+}] = 1 μM, extensive film-like islands of Pb are observed on the surface. In contrast, for lower [Pb^{2+}], i.e., 100 nM (aii) and 10 nM (aiii), Pb NPs with heights of 18 ± 5.2 nm (SD) and 5 ± 1.3 nm (SD) and NP densities of 165 and 142 μm^{-2}, respectively, are homogeneously dispersed across the pBDD surface. The relatively homogeneous distribution of NP sizes is also reflected in the narrow stripping peak widths of the DPV signature.[18,21,43] We achieve this here for the case of [Pb^{2+}] = 10 nM and 100 nM through the use of a high driving force (large overpotential) to ensure a high nucleation rate and thus a high density of small particles.[23] Others have advocated the use of pulsed galvanostatic deposition to achieve NPs with a narrow size distribution.[18]

It is thus clear that, as [Pb^{2+}] decreases, for the deposition potential and time considered, smaller isolated NPs form. This is consistent with work using other metals on highly oriented pyrolytic graphite electrode surfaces.[44] The AFM images in Figure 6.6 (a) also provide evidence that the shift in the stripping peak potential with decreasing [Pb^{2+}] (Figures 6.3 (a) and 6.5 (a)) is most likely related to an NP size-dependent redox potential[45] for the Pb/Pb^{2+} couple. Similar shifts were seen for the Cd/Cd^{2+} couple on BDD with decreasing [Cd^{2+}],[17] but no explanation was provided as to why this occurred.

It is informative to calculate the quantity of Pb deposited on the pBDD surface during the deposition step and compare this value to the amount estimated by AFM analysis. This can be done readily for [Pb^{2+}] = 100 and 10 nM, where isolated NPs

are evident. The charge associated with Pb deposited on the pBDD electrode was estimated from the average of several AFM images of NP deposition. As it was not possible to unambiguously determine the true geometry of the NPs from the AFM images, the particles were assumed to be both hemispherical (upper charge limit) and spherical (lower charge limit). Note there was no significant pBDD grain dependence of the Pb NP size and surface coverage (*vide infra*).

Values of 16.7 ± 0.8 μC (hemisphere), 4.2 ± 1.9 μC (sphere) and 0.5 ± 0.02 μC (hemisphere), 0.09 ± 0.04 μC (sphere) were estimated from the AFM images for the 100 and 10 nM solutions, respectively. Values of 22.5 μC (100 nM) and 2.3 μC (10 nM) were calculated from consideration of the limiting current at the pBDD (equation 6.1) for Pb deposition in a wall-jet configuration,[41] assuming diffusion-limited deposition[46] and that D for Pb^{2+} is 1.34×10^{-5} cm^2 s^{-1}.[47]

The experimental and theoretical charge comparisons are much closer for $[Pb^{2+}]$ = 100 nM than for $[Pb^{2+}]$ = 10 nM. Moreover, the data obtained at 100 nM are more consistent with hemispherical-shaped NPs. One reason for the higher estimate of Pb on the surface, as predicted from the diffusion-limited current, compared to that measured by AFM could be particle instability for smaller NPs on the pBDD surface under the hydrodynamic conditions of the impinging jet. Additionally, or alternatively, at very low concentrations, there is likely to be a more significant induction time for the nucleation of NPs on pBDD which is not taken into account when using equation 6.1 calculate the charge passed for deposition. Such effects are unimportant for ASV at Hg or Hg film electrodes but are clearly an issue for heterogeneous nucleation and growth on any solid electrode. This issue does not,

hitherto, appear to have been adequately considered, and the studies herein highlight the general need for further fundamental studies of metal nucleation and growth from very low concentration solutions.

Typical 1 μm × 1 μm AFM height images of the surface after DPV at [Pb^{2+}] of (i) 1 μM, (ii) 100 nM, and (iii) 10 nM are shown in Figure 6.6 (b). After dissolution, the size of the islands in Figure 6.6 (bi) has clearly decreased, with smaller particles now evident in the background. However, the striking feature is that a substantial amount of Pb remains on the surface which is not detected in the DPV. In contrast, for both panels ii and iii of Figures 6.6 (b), the resulting surface morphology, after DPV, shows more complete removal of Pb.

The change in the amount of Pb on the surface, expressed as a volume, was calculated from 1 μm × 1 μm AFM images obtained prior to and after stripping. Cross-sectional height analysis of the Pb film was used for volume calculations at high concentrations (1 μM), whereas hemispherical NPs (*vide supra*) were assumed at the lower concentrations (100 and 10 nM). For 1 μM Pb (parts (ai) and (bi) of Figure 6.6), a 60 ± 5% reduction in volume, after stripping, was determined. The percentage removal increased to 91 ± 5% and 92 ± 5% for [Pb^{2+}] = 100 and 10 nM, respectively.

The significantly higher proportion of Pb left on the surface during the stripping step for 1 μM Pb^{2+} compared to the lower concentrations helps to explain the nonlinear calibration plot of charge (or peak current) versus [Pb^{2+}] at high [Pb^{2+}] (Figure 6.3 (b) and 6.4 (b)). Incomplete anodic dissolution of electrodeposited Pb from pBDD

electrode surfaces has previously been inferred in the literature, typically by considering the charges associated with deposition and stripping,[16,24,25,27] although this approach has also been disputed.[18] In contrast, the AFM images in Figure 6.6 provide direct visual evidence that the amount of Pb deposited on the surface and the resultant surface morphology are significant factors in determining the extent to which Pb is subsequently removed and detected during DPV stripping.

Previous electrodeposition studies of Pt[23] and Ag[48] on pBDD have evidenced grain-dependent nucleation behaviour, albeit at much lower driving forces.[43] Given the typical size of grains in pBDD,[20] larger scan size (5 μm × 5 μm) AFM images of the pBDD electrode surface were recorded after deposition using the impinging jet arrangement for [Pb^{2+}] = (a) 1 μM, (b) 100 nM, and (c) 10 nM (Figure 6.7) to elucidate if this was the case for Pb at the concentrations and deposition conditions pertinent to stripping voltammetry.

For 1 μM [Pb^{2+}], Figure 6.7 (a) shows a central structure, 25 nm in height, which is similar to the film-like topology observed in Figure 6.6 (ai). Areas outside this region show the deposition of Pb NPs, with heights of 19 ± 7 nm (SD) at a high density of ~160 μm^{-2}. At the lower [Pb^{2+}] of 100 nM (Figure 6.7 (b)), the NP surface coverages and heights are similar over the majority of the image. For example, the area outlined in white supports NPs of height 16 ± 5 nm at ~170 NPs μm^{-2}, with surrounding areas supporting NPs ~19 ± 6 nm in height at ~160 NPs μm^{-2}. Only in a few isolated regions is the coverage so high that thin-film formation is favoured. At [Pb^{2+}] = 10 nM (Figure 6. 7(c)), again there are no evident differences in deposit morphology for different pBDD grains.

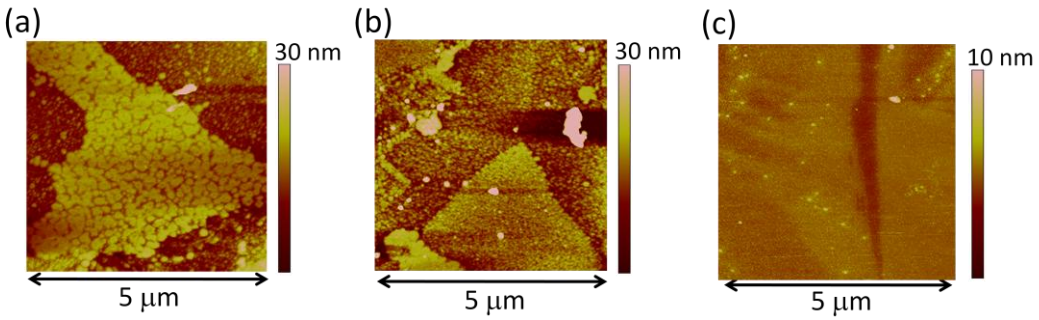

Figure 6.7: Typical 5 µm × 5 µm ex-situ AFM images of the surface of a pBDD electrode after electrodeposition of Pb for 400 s at −1.5 V (vs. SCE) with a volume flow rate of 0.1 mL s^{-1} for (a) 1 µM Pb^{2+}, (b) 100 nM Pb^{2+}, and (c) 10 nM Pb^{2+}. The dashed white line denotes the border of a grain.

Thus, in general, at [Pb^{2+}] < 1 µM, for the deposition times and potentials employed herein, there are no significant differences in metal deposition between different surface grains of pBDD. This contrasts with previous studies employing smaller deposition overpotentials and higher metal ion concentrations, where differences were seen,[48,49] as the more conductive grains were able to support higher interfacial fluxes of metal ions.

The origin of the island-like Pb structure observed in Figure 6.7 (a) is particularly interesting. To investigate this further, AFM studies were carried out under the same deposition conditions as for Figure 6.7(a), but with shorter deposition times to capture the earlier stages of film growth. Figure 6.8(a) shows typical (i, ii) 3 µm × 3 µm and (iii, iv) 5 µm × 5 µm AFM images recorded after 300 s of 1 µM Pb^{2+} deposition at −1.5 V and Figure 6.8 (b) a typical 5 µm × 5 µm AFM image recorded after 400 s of Pb^{2+} deposition at −1.5 V.

As Figure 6.8 (a) clearly shows, small circular-shaped islands have formed on the surface of an individual grain, which grow outward to merge with other islands,

ultimately forming the structures shown in Figure 6.7 (a). In Figure 6.8 (b), two grains of different boron dopant densities are clearly present, as indicated by the clear step in height between grains (*vide supra*). Interestingly, the Pb island actually grows across the grain boundary from one grain to the next, with no significant change in the growth morphology, a process which is independent of the underlying boron doping level. Our many AFM and FE-SEM images recorded, from which it is possible to qualitatively infer differences in boron dopant levels (*vide supra*), indicate no preference for particular pBDD grains during the initial stages of thin-film formation. Thus, we believe that, under the deposition conditions employed herein, differences in electrical characteristics associated with grains of different boron dopant levels do not play a significant role in Pb film formation.

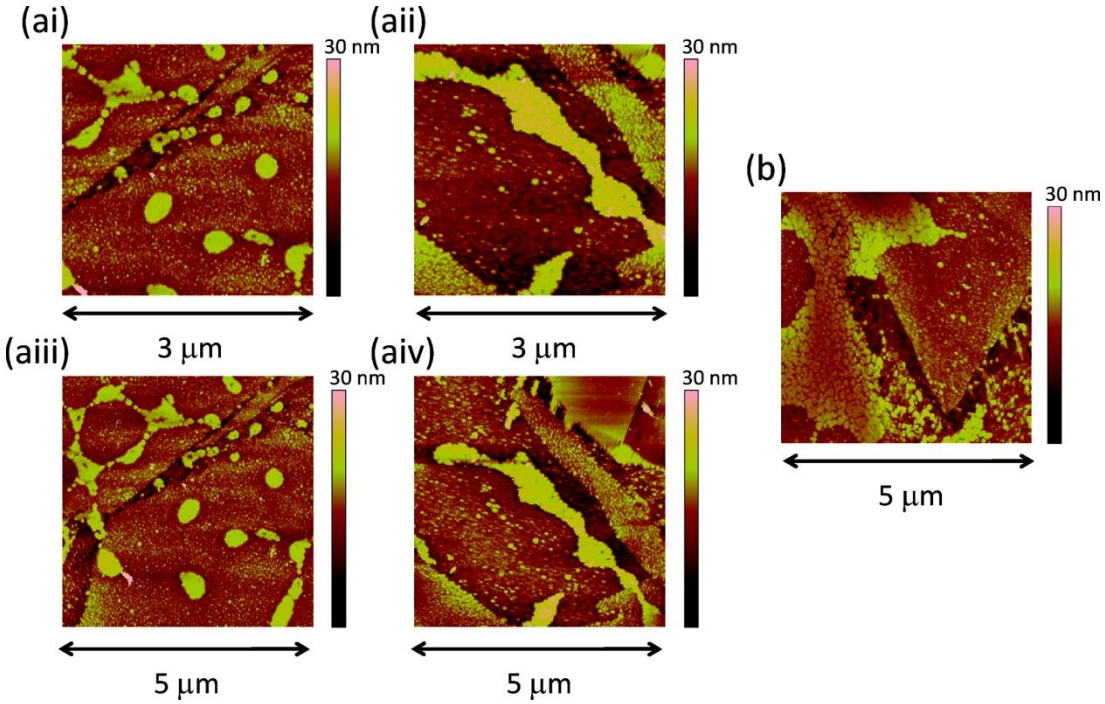

Figure 6.8: Typical ex-situ AFM images of the surface of the pBDD electrode after electrodeposition of 1 µM Pb^{2+} at −1.5 V (vs. SCE), with V_f = 0.1 mL s^{-1}, recorded after (a) 300 s and (b) 400 s.

The origin of the double stripping peak in previous DPV data on pBDD, seen here at higher [Pb^{2+}], e.g., Figure 6.3 (a), has been either ignored[16] or tentatively attributed to some aspect of the metal deposit on the electrode surface.[18] Recent numerical simulations have shown that the morphology/structure of a metal deposit on an electrode surface will affect the stripping characteristics. In particular, it was shown numerically that the stripping response from hemispherically shaped deposits should occur at less positive potentials than that of a thin uniform film of the same mass, provided the particles are small, as is the case here.[21]

Thus, to investigate this aspect further, Figure 6.9 shows typical FE-SEM images recorded after Pb deposition at a range of concentrations, (a) 0.5 μM, (b) 10 μM, and (c) 30 μM, and the associated DPV response after Pb stripping. For all experiments, deposition was carried out for 400 s with the electrode held at −1.5 V. Note that the crystal-like features seen in the FE-SEM images are crystals of potassium nitrate that result when the sample was removed from solution, rinsed gently so as to not perturb the metallic deposits, and then left to dry.

It is strikingly clear that, when only NPs are formed in the deposition step, i.e., at the lower [Pb^{2+}] (and/or deposition time), there is a single stripping peak in the DPV response. As [Pb^{2+}] is increased and both NPs and thin-film-like structures are formed during electrodeposition, a second peak emerges in the DPV response, as also seen in Figure 6.3 (a) and 6.4 (a). Indeed, at the highest concentration employed, where FE-SEM reveals the surface to be largely dominated by the film-like structures, the second stripping peak is significantly larger than the first peak. The

images in Figure 6.9 thus suggest that the two peaks are intimately related to the different metal morphologies on the pBDD surface.

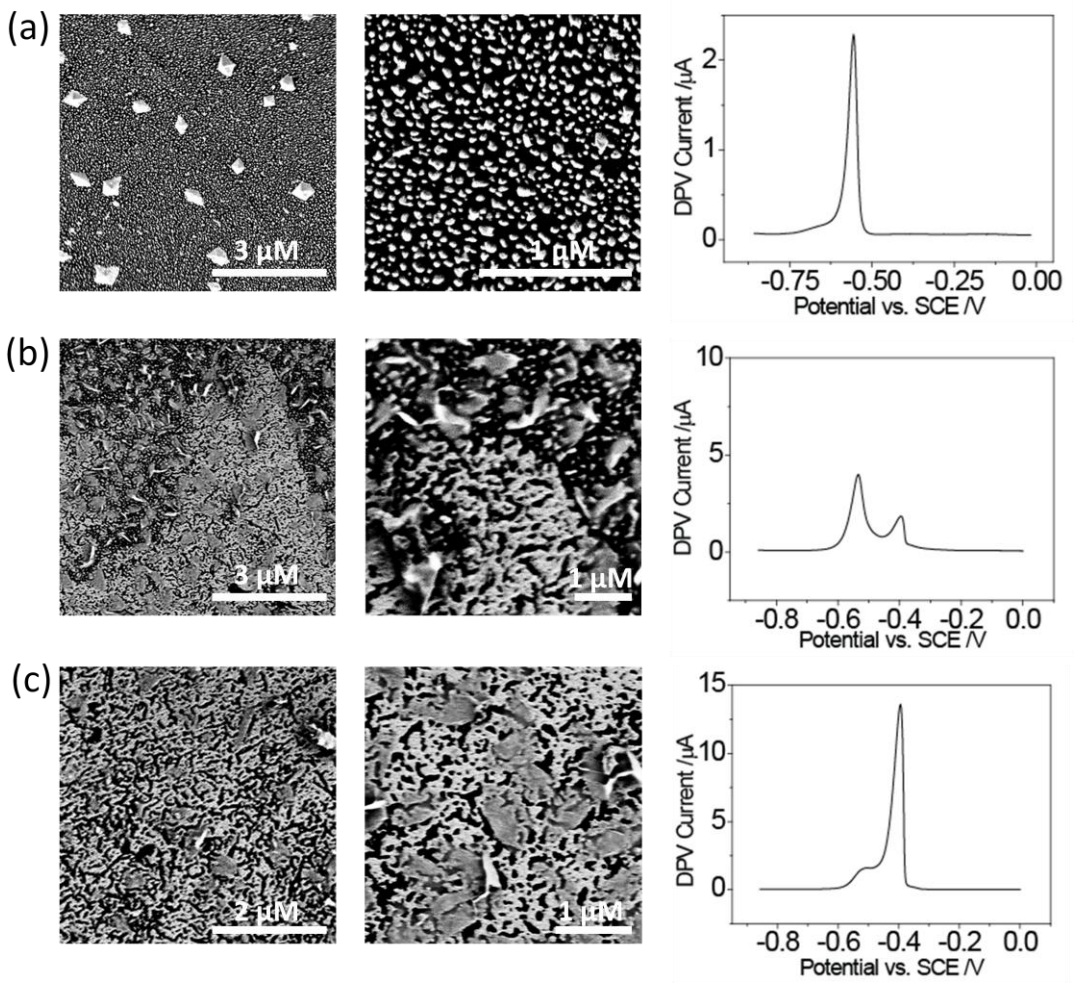

Figure 6.9: Typical FE-SEM images of the pBDD electrode after Pb deposition for 400 s at −1.5 V (vs. SCE), with V_f = 0.1 mL s^{-1}, with the associated DPV response (pulse width, 50 mV; pulse amplitude, 50 mV; step size, 2 mV) in 0.1 M KNO_3 for (a) 0.5 µM Pb^{2+}, (b) 10 µM Pb^{2+}, and (c) 30 µM Pb^{2+}.

6.2.4 *In-Situ* Electrochemical Atomic Force Microscopy

To provide further information on the deposition and stripping behaviour of Pb on pBDD, *in-situ* AFM was carried out so that the deposition morphology could be matched more closely with the resulting electrodissolution topography. However, as *in-situ* AFM is used in quiescent solution, the Pb^{2+} concentration was scaled up to

compensate for the decreased mass transport rates during deposition. The focus of these experiments was on NP deposition and stripping.

Figure 6.10 shows typical 1 × 1 μm *in-situ* AFM images for $[Pb^{2+}]$ = (i) 10 μM, (ii) 1 μM, and (iii) 100 nM after (a) deposition of Pb in quiescent solution (400 s at −1.5 V) and (b) DPV stripping of Pb from the surface. In each case, the deposition and stripping images were recorded in the same location. The deductions from the *in-situ* experiments are as for the ex situ experiments. First, as $[Pb^{2+}]$ decreases, and the overall deposition flux decreases, the average height of the NPs decreases, here from 26 ± 5.3 nm (10 μM) to 14 ± 4.6 nm (1 μM) and finally to 8 ± 2.3 nm (100 nM). Second, the volume of Pb removed from the pBDD surface after stripping increases as the concentration decreases, i.e., 63 ± 3% (10 μM), 93 ± 5% (1 μM), and 95 ± 5% (100 nM). This re-emphasizes that at high concentrations it is not always possible to remove all the deposited material in the stripping step, a point which needs to be carefully considered and addressed for heavy metal stripping voltammetry at solid electrodes. The *in-situ* cleaning step described is also crucial for obtaining a clean and reproducible surface prior to each measurement.

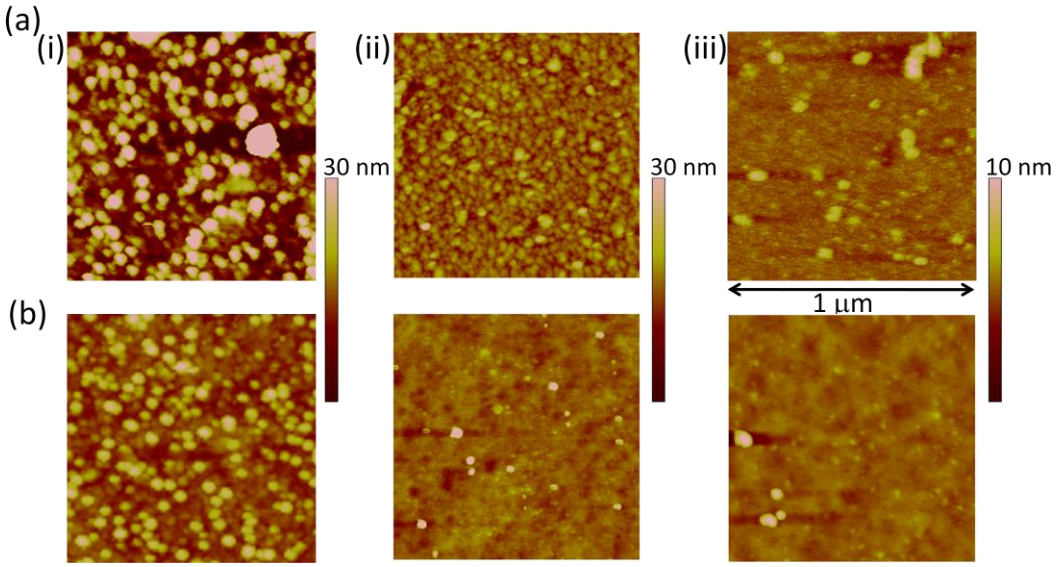

Figure 6.10: Typical 1 µm × 1 µm in-situ AFM height images of the surface of a pBDD electrode after (a) Pb deposition for 400 s at −1.5 V (vs. SCE) in stationary solution and (b) Pb stripping using DPV (pulse width, 50 mV; pulse amplitude, 50 mV; step size, 2 mV) in 0.1 M KNO_3 for (i) 10 µM Pb^{2+}, (ii) 1 µM Pb^{2+}, and (iii) 100 nM Pb^{2+}. Images of deposition and stripping were recorded in the same location for the same concentration.

6.3. CONCLUSION

High-resolution microscopy techniques, including AFM and FE-SEM, have been utilized successfully to provide a greater understanding of the features observed by us and others in DP-ASV of the popular Pb^{2+}/Pb system at pBDD, an example of a heterogeneous solid electrode. Significantly, the studies presented have allowed a comprehensive assessment of several long-standing questions in the literature, including the origin of the lower calibration gradients at low concentration, the observation of a second peak in the DPV response at higher concentrations, the nonlinear calibration gradient at high concentrations, and finally the effect, if any, of the varying electrical conductivity of the pBDD surface on the Pb deposition and stripping process.

DPV was implemented with hydrodynamic control using an impinging wall jet (during deposition) to deposit and detect Pb^{2+} (as Pb) quantitatively in the nanomolar (sub parts per billion) to micromolar concentration range. High driving potentials were employed to produce relatively homogeneous distributions of NPs on the surface, reflected in the narrow DPV stripping peaks observed.

In the low concentration regime, AFM revealed that the amount of Pb deposited on the surface, as estimated by AFM analysis, was lower than expected for simple convective-diffusive control of the deposition process. This was reflected in the reduced gradients of the calibration plots of the peak DPV current and/or DPV charge versus [Pb^{2+}] in the lower concentration range. This highlights an important factor in stripping analysis at low concentration; i.e., complications are likely to arise from the nucleation and growth of NPs in this concentration regime, particularly finite induction kinetics which lead to complex variations in mass transport during the deposition step. This aspect of metal stripping analysis at solid electrodes requires further attention in general. As the concentration of Pb^{2+} was increased, AFM clearly showed that the size of the NPs deposited on the surface also increased. This correlated with a positive shift in the stripping peak potential which could thus be ascribed to an NP size-dependent redox potential for the Pb/Pb^{2+} couple.

FE-SEM and AFM revealed that the emergence of a second peak in the DPV, at higher [Pb^{2+}], correlated with a change in the deposition morphology from small isolated NPs to heterogeneous structures comprising both thin films and NPs. The second peak was associated with stripping from the thin-film structures. This peak

became larger the greater the extent of thin-film coverage and could even dominate the response.

AFM further revealed that increasing the amount of Pb on the pBDD surface made it more difficult to completely remove it all in one DPV sweep. Thus, a substantial amount of Pb could remain on the electrode surface, undetected by DPV. This was especially evident for extensive metal deposition, which produced the thin-film island morphologies and also explained the nonlinear calibration gradient at higher [Pb^{2+}].

By comparing AFM and FE-SEM images, it was possible to qualitatively determine how the boron dopant levels varied across the surface of the pBDD due to differential boron uptake of different grains. In general, variations in the electrical conductivity of the pBDD surface played no role in the nucleation and growth morphologies observed.

Finally, for all of the studies described, an *in-situ* electrochemical cleaning process was developed in which Pb could be completely removed from the electrode surface. Initial studies focused on a cleaning period of 10 min, and it was shown that an electrode potential of +1.2 V after a stripping measurement was sufficient to create a clean surface for subsequent, repeat electroanalysis. AFM and XPS analysis confirmed that this procedure worked effectively at all concentrations to remove all electrodeposited Pb from the surface.

6.4. REFERENCES

(1) Wang, J. *Stripping Analysis: Principles, Instrumentation and Applications*; VCH: Deerfield Beach, FL, 1985.
(2) Daniele, S.; Mazzocchin, G. A. *Anal. Chim. Acta* **1993**, *273*, 3.
(3) Wang, J.; Lu, J.; Chen, L. *Anal. Chim. Acta* **1992**, *259*, 123.
(4) Florence, T. M. *Journal of Electroanalytical Chemistry and Interfacial Electrochemistry* **1970**, *27*, 273.
(5) Batley, G. E. *Anal. Chim. Acta* **1981**, *124*, 121.
(6) Acebal, S. A.; De Luca Rebello, A. *Anal. Chim. Acta* **1983**, *148*, 71.
(7) Wang, J. *Controlled-Potential Techniques*; John Wiley & Sons, Inc., 2002.
(8) Agra-Gutierrez, C.; L. Hardcastle, J.; C. Ball, J.; G. Compton, R. *Analyst* **1999**, *124*, 1053.
(9) Brainina, K. Z.; Kubysheva, I. V.; Miroshnikova, E. G.; Parshakov, S. I.; Maksimov, Y. G.; Volkonsky, A. E. *Field. Anal. Chem. Tech.* **2001**, *5*, 260.
(10) Pleskov, Y. V. *Russ. J. Electrochem.* **2002**, *38*, 1275.
(11) Xu, J. S.; Granger, M. C.; Chen, Q. Y.; Strojek, J. W.; Lister, T. E.; Swain, G. M. *Anal. Chem.* **1997**, *69*, A591.
(12) Compton, R. G.; Foord, J. S.; Marken, F. *Electroanalysis* **2003**, *15*, 1349.
(13) Ramesham, R.; Rose, M. F. *Diamond Relat. Mater.* **1997**, *6*, 17.
(14) Dragoe, D.; Spataru, N.; Kawasaki, R.; Manivannan, A.; Spataru, T.; Tryk, D. A.; Fujishima, A. *Electrochim. Acta* **2006**, *51*, 2437.
(15) McGaw, E. A.; Swain, G. M. *Anal. Chim. Acta* **2006**, *575*, 180.
(16) Manivannan, A.; Tryk, D. A.; Fujishima, A. *Electrochem. Solid-State Lett.* **1999**, *2*, 455.
(17) Babyak, C.; Smart, R. R. *Electroanalysis* **2004**, *16*, 175.
(18) Sonthalia, P.; McGaw, E.; Show, Y.; Swain, G. M. *Anal. Chim. Acta* **2004**, *522*, 35.
(19) Tsai, Y. C.; Coles, B. A.; Holt, K.; Foord, J. S.; Marken, F.; Compton, R. G. *Electroanalysis* **2001**, *13*, 831.
(20) Wilson, N. R.; Clewes, S. L.; Newton, M. E.; Unwin, P. R.; Macpherson, J. V. *J. Phys. Chem. B* **2006**, *110*, 5639.
(21) Jones, S. E. W.; Toghill, K. E.; Zheng, S. H.; Morin, S.; Compton, R. G. *J. Phys. Chem. C* **2009**, *113*, 2846.
(22) Batchelor-McAuley, C.; Banks, C. E.; Simm, A. O.; Jones, T. G. J.; Compton, R. G. *Analyst* **2006**, *131*, 106.
(23) Hutton, L.; Newton, M. E.; Unwin, P. R.; Macpherson, J. V. *Anal. Chem.* **2009**, *81*, 1023.
(24) Hyde, M. E.; Jacobs, R.; Compton, R. G. *J. Phys. Chem. B* **2002**, *106*, 11075.
(25) Goeting, C. H.; Jones, F.; Foord, J. S.; Eklund, J. C.; Marken, F.; Compton, R. G.; Chalker, P. R.; Johnston, C. *J. Electroanal. Chem.* **1998**, *442*, 207.
(26) Zhu, P.; Zhu, J.; Yang, S.; Zhang, X.; Zhang, G. *Fresenius. J. Anal. Chem.* **1995**, *353*, 171.
(27) Awada, M.; Strojek, J. W.; Swain, G. M. *J. Electrochem. Soc.* **1995**, *142*, L42.
(28) Vinokur, N.; Miller, B.; Avyigal, Y.; Kalish, R. *J. Electrochem. Soc.* **1999**, *146*, 125.
(29) Nakabayashi, S.; Tryk, D. A.; Fujishima, A.; Ohta, N. *Chem. Phys. Lett.* **1999**, *300*, 409.
(30) Omanović, D.; Peharec, Ž.; Magjer, T.; Lovrić, M.; Branica, M. *Electroanalysis* **1994**, *6*, 1029.
(31) Saterlay, A. J.; Agra-Gutiérrez, C.; Taylor, M. P.; Marken, F.; Compton, R. G. *Electroanalysis* **1999**, *11*, 1083.
(32) Saterlay, A. J.; Foord, J. S.; Compton, R. G. *Analyst* **1999**, *124*, 1791.
(33) Saterlay, A. J.; Marken, F.; Foord, J. S.; Compton, R. G. *Talanta* **2000**, *53*, 403.

(34) Banks, C. E.; Hyde, M. E.; Tomcik, P.; Jacobs, R.; Compton, R. G. *Talanta* **2004**, *62*, 279.
(35) Macpherson, J. V.; Marcar, S.; Unwin, P. R. *Anal. Chem.* **1994**, *66*, 2175.
(36) Macpherson, J. V.; Beeston, M. A.; Unwin, P. R. *J. Chem. Soc., Faraday Trans.* **1995**, *91*, 899.
(37) Martin, R. D.; Unwin, P. R. *J. Electroanal. Chem.* **1995**, *397*, 325.
(38) Melville, J. L.; Coles, B. A.; Compton, R. G.; Simjee, N.; Macpherson, J. V.; Unwin, P. R. *J. Phys. Chem. B* **2002**, *107*, 379.
(39) Bitziou, E.; Rudd, N. C.; Edwards, M. A.; Unwin, P. R. *Anal. Chem.* **2006**, *78*, 1435.
(40) Liu, F. B.; Wang, J. D.; Liu, B.; Li, X. M.; Chen, D. R. *Diamond Relat. Mater.* **2007**, *16*, 454.
(41) Albery, W. J.; Brett, C. M. A. *Journal of Electroanalytical Chemistry and Interfacial Electrochemistry* **1983**, *148*, 201.
(42) Wehmeyer, K. R.; Wightman, R. M. *Anal. Chem.* **1985**, *57*, 1989.
(43) Song, Y.; Swain, G. M. *Anal. Chem.* **2007**, *79*, 2412.
(44) Fransaer, J. L.; Penner, R. M. *J. Phys. Chem. B* **1999**, *103*, 7643.
(45) Henglein, A. *J. Phys. Chem.* **1993**, *97*, 5457.
(46) Oldham, H. B. M., J.C. *Fundamentals of Electrochemical Science*; Academic Press: New York, 1994.
(47) Lide, D. R., Ed. *Handbook of Chemistry and Physics, 90th ed.*; CRC Press: Boca Raton 2009.
(48) Colley, A. L.; Williams, C. G.; Johansson, U. D.; Newton, M. E.; Unwin, P. R.; Wilson, N. R.; Macpherson, J. V. *Anal. Chem.* **2006**, *78*, 2539.
(49) Simm, A. O.; Ji, X.; Banks, C. E.; Hyde, M. E.; Compton, R. G. *ChemPhysChem* **2006**, *7*, 704.

CHAPTER 7

Fabrication and Characterisation of All-Diamond Electrodes for Electroanalysis

In this chapter, the fabrication and characterisation of the first all-diamond hydrodynamic electrodes are described. Two formats are discussed, the tubular flow ring electrode, TFRE, and the dual band electrode, DBE, comprising pBDD ring and band electrodes insulated with intrinsic diamond. Laser machining was used to define the electrode geometry either by cutting a hole through sandwiched intrinsic-pBDD-intrinsic layers or by patterning insulating diamond and then overgrowing with pBDD. After polishing, these all-diamond structures were found to be co-planar with ultra-smooth surfaces.

For the TFRE with a 500 μm diameter tube, electrode length of ca. 90 μm, the steady-state current response for the oxidation of $FcTMA^+$ was found to obey that predicted by Levich for a tubular electrode operating under laminar flow conditions. The flow device was also applied to the detection of the neurotransmitter dopamine. At relatively high concentrations of the analyte, the combination of pBDD in this geometry flow system resulted in the eradication of electrode fouling.

For the DBE under hydrodynamic flow conditions, with bands 200 μm wide and 6 mm long, the steady-state limiting current response at one of the band electrodes for the reduction of $Ru(NH_3)_6^{3+/2+}$ was also found to obey that predicted by Levich for a channel flow band electrode operating under laminar flow conditions. The DBE was applied to solution conductivity measurements and calibrated in varying concentrations of KCl, with a linear response over the concentration range 7 mM to 0.12 M. The cell constant was experimentally determined as 6.8 cm^{-1} agreeing well with the theoretical prediction of 7 cm^{-1}.

7.1. INTRODUCTION

pBDD attracts much interest as an electrode material for electroanalysis,[1,2] due to its unique properties as discussed in Chapters 1 and 3. Typically, macro-sized pBDD electrodes (≥ 1 mm) are employed in voltammetric electroanalytical measurements,[3,4] although in order to improve sensitivity there has been a push towards the development and application of pBDD-based microelectrodes[5,6-9] and microarrays.[10-13] An alternative strategy is the use of hydrodynamic techniques which serve to increase the steady-state current signal, due to an increased flux of material to the electrode surface. However, to-date there have only been a limited number of hydrodynamic studies employing pBDD electrodes. For example, electroanalysis of dopamine[14] and nicotinamide adenine dinucleotide[15] using pBDD rotating disc electrodes and the detection of chlorophenols,[16] employing BDD channel flow electrodes.[17] pBDD disc microelectrodes have also been used as detectors in capillary electrophoresis and flow injection analysis.[18-20]

Conductometric measurements are also used as a form of non specific electroanalysis in both laboratories and industrial processes, applications include monitoring of demineralization and leak detection. Traditional conductivity measurements use two metal electrodes in contact with the solution aligned parallel to each other as shown in Figure 7.1. An ac current (or voltage) is applied to the electrodes and the resulting ac voltage (or current) is used to determine the solution conductivity.

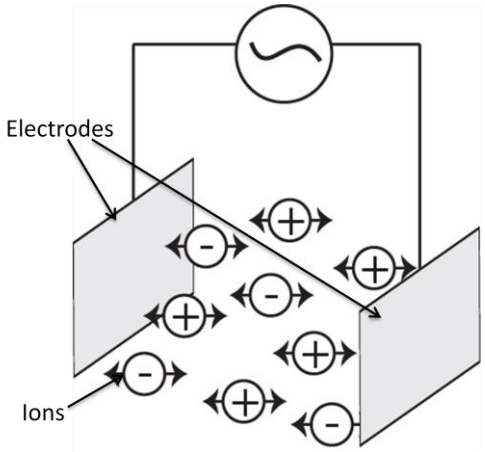

Figure 7.1: Schematic of a traditional parallel plate conductivity meter, with ions moving in solution between the electrodes.

The measured potential is not only determined by the solution conductivity, but also depends on the geometry of the electrodes. The cell constant, k (cm^{-1}) is the proportionality factor between the actual solution conductivity and the potential response of the sensor. For the set-up shown in Figure 7.1, the cell constant is defined as;

$$k = d/A \qquad (7.1)$$

where d (cm) is the perpendicular distance between the electrodes. This assumes that the electric field lines are perpendicular to the electrodes and fringing effects are negligible. Solution conductivity measurements can be made more ion specific, for example in conjunction with capillary electrophoresis which separates out ions prior to conductivity sensing.[21] Ion specificity can also be achieved in conjunction with membranes immobilised on the electrode surface which react with specific biomolecules thus changing the conductivity of the membrane,[22] or through ion specific temperature dependency, where algorithms analyse data over a range of temperatures and provide ion concentrations due to their temperature dependent limiting molar conductivities.[23] During industrial use, the electrode can experience fouling due to continuous employment and should therefore be fabricated from a

fouling resistant material, or one which will be able to withstand the required extreme procedures for both *ex-situ* and *in-situ* use. The electrode material must be able to withstand a wide range of solution conditions, including extreme pH, different temperatures and solvent systems without deterioration.

Recently, miniaturisation and integrated lab-on-chip devices of chemical analysis systems has seen movement away from traditional parallel plate conductivity designs, as shown in Figure 7.1, towards planar geometries.[24,25] Thus only small volumes of the electrode material are now required. Experimental and mathematical optimization of the design for both two and multiple planar electrode structures has been reported.[26,27] The majority of work carried-out in this area has employed patterned Au electrodes with thin film coatings of insulating Ta_2O_5 in order to provide low electrode/solution impedance and to stabilise the electrode by reducing any redox processes that may take place.[28]

One of the major problems associated with the use of pBDD as an electrode material, especially when employed in non-traditional geometrical arrangements is how to process the starting material to obtain the desired geometry, and, of particular importance in hydrodynamic studies, the use of a suitable insulating material which results in a co-planar structure.[9,11,29,30] Recessing or protrusion of the electrode surface from the surrounding insulator can significantly affect the flow hydrodynamics.[31] It is also desirable that the insulating material employed does not limit the wide range of applications made possible through use of BDD as an electrode material, *e.g.* chemical stability in all environments, and at elevated temperatures and pressure *etc*.

An elegant solution to this problem has been to fabricate all-diamond electrodes, where the pBDD is insulated with intrinsic diamond. Although work in this area has been limited, the concept was demonstrated with the development of all-diamond pBDD disc UMEs. Here a layer of pBDD was grown and patterned to reveal cylindrical-type structures. Subsequent overgrowth with intrinsic diamond and polishing to reveal the tops of the cylinders, resulted in intrinsic diamond insulated co-planar BDD disk UMEs, 10 to 50 μm in diameter as shown in Figure 7.2.[32,33] In a slightly different approach, pBDD band structures were patterned onto an insulating diamond substrate, however this geometry is no longer co-planar as the bands, 30 μm in width, protrude ~ 2.5 μm above the surface.[34]

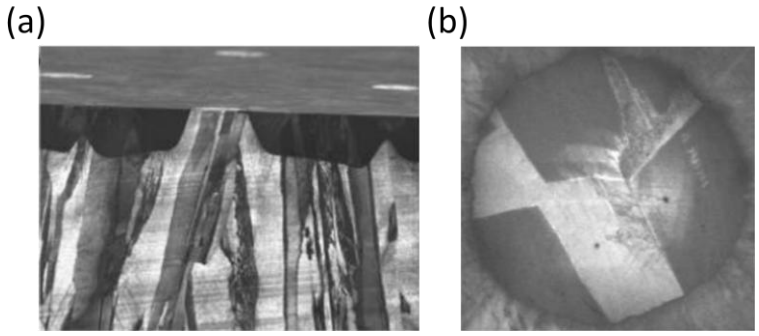

Figure 7.2: SEM images of a pBDD electrode in an all-diamond array (a) side and (b) top views.[32]

In this chapter we show that all-diamond electrodes of two different geometries can be fabricated using layered diamond structures and laser micromachining techniques. The first of these is the TFRE, for hydrodynamic flow electroanalytical applications. A three-layered diamond structure comprising (1) 455 μm thick insulating, (2) ca. 90 μm thick conducting, and finally (3) 170 μm thick insulating layers of polycrystalline diamond is grown, then laser machined (to define the flow through hole) and further polished to smooth the inside of the cut surface, resulting in the

formation of a TFRE. The second all-diamond electrode geometry is the DBE. Freestanding ca. 500 μm thick intrinsic diamond is patterned using laser machining. pBDD overgrowth and subsequent lapping reveals co-planar individually addressable bands electrodes.

7.2. TUBULAR FLOW MICROELECTRODE

7.2.1 **Electrode Fabrication**

Layered polycrystalline diamond samples were prepared by Element Six Ltd. (E6 Ltd., Ascot, U.K.) using a commercial microwave plasma CVD process. The diamond wafer consisted of a ca. 455 μm thick layer of mechanical grade CVD intrinsic diamond, which was lapped on both sides. Mechanical grade CVD diamond is optically opaque and electrically insulating. A ca. 90 μm thick layer of pBDD was first grown on the nucleation face (boron dopant density ca. 3×10^{20} B atoms cm^{-3}, as estimated from electrical resistivity measurements) followed by a ca. 170 μm layer of intrinsic mechanical grade diamond to fully insulate the pBDD layer. A 355 nm laser micromachining system (E-355H-3-ATHI-O system, Oxford Lasers) was used to cut a 10 mm diameter disk from the diamond wafer and then a hole, 500 μm in diameter, in the centre to create the tube (duct) through which solution flows. To enable electrical connection to the conducting pBDD layer, a "*top hat*" structure (top diameter 6 mm, bottom diameter 10 mm) was created by laser milling through the diamond to expose the pBDD layer, as shown schematically in Figure 7.3 (a).

In order to achieve a smooth inner surface, and to remove any amorphous carbon deposited during laser cutting, a precision vertical diamond wire saw (Well Diamond Wire Saws Inc) with a modified sample stage was used to polish the inside of the tube. A 280 µm diameter diamond impregnated wire (MTI Corporation) on a tensional pulley was pulled up and down through the lasered hole, slightly offset so the wire was forced against the inner wall. At the same time, the diamond was rotated on a stage at 60 rpm so that an even polish was obtained on all parts of the inner wall of the tube. Figure 7.3 (b) shows a magnified image of the wire passing through the all-diamond TFRE.

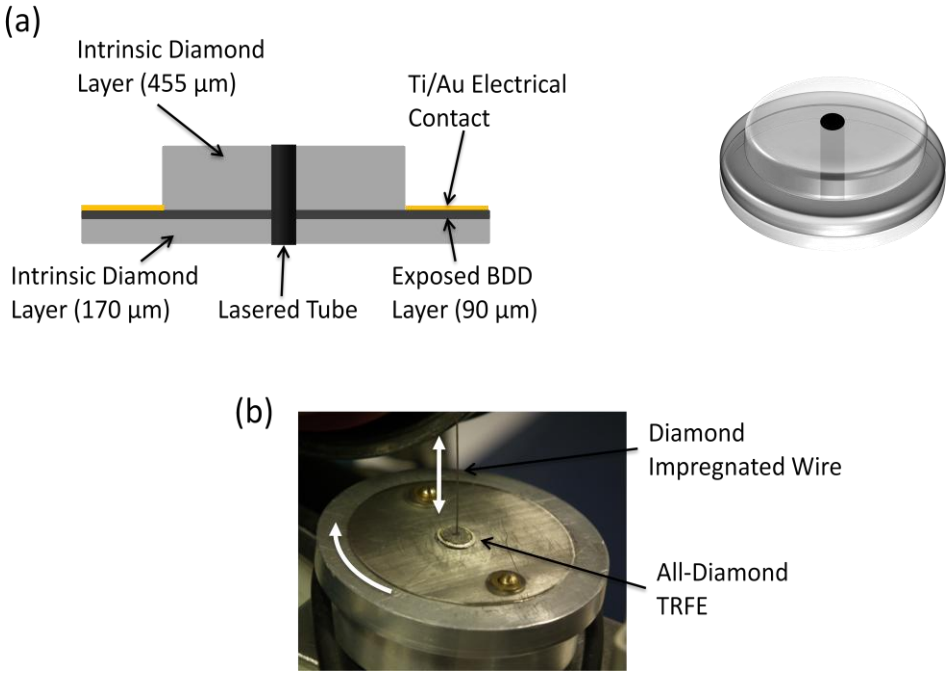

Figure 7.3: (a) Schematic of all-diamond TFRE where the BDD layer is between two intrinsic diamond layers with a hole lasered vertically through the middle for tubular flow. (b) Photo of the all-diamond TFRE polishing set-up with the diamond impregnated wire.

The TFRE was acid-cleaned, as described previously,[35] giving an oxygen-terminated surface. Layers of Ti (10 nm) and Au (400 nm) were sputtered (Moorfield Minibox) onto the outer exposed planar pBDD surface (Figure 7.3 (a)) and annealed at 475 ^{o}C

for 4 hrs. The dissembled and assembled device is shown in Figures 7.4 (a) and (b) respectively. The diamond (labelled i, in Figure 7.4 (a)) was placed in the flow device set-up and a copper ring connector (Cu foil, 300 μm thick, Goodfellows) with arms either side (labelled ii) was used to make contact with the Ti/Au layer, to provide the external electrical contact to the TFRE. A thin polyimide spacer (200 μm thick, Goodfellows, labelled iii) was employed to separate the diamond from a circular Ag/AgCl reference electrode (labelled iv).

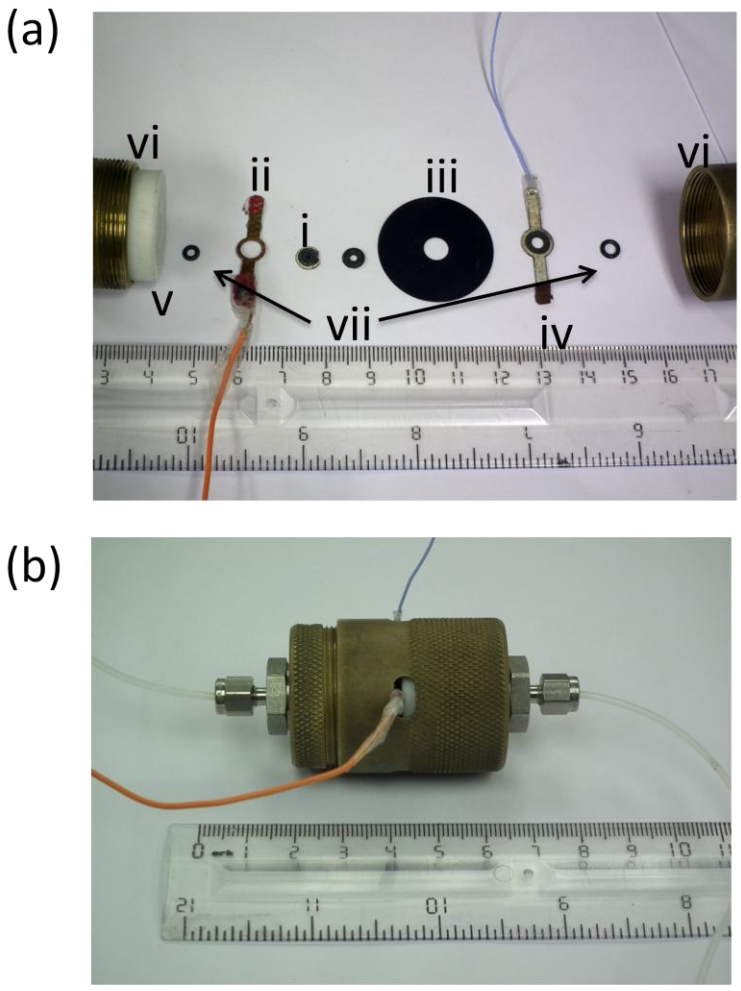

Figure 7.4: Photographs of an all-diamond TFRE flow set-up; (a) showing the individual components and (b) the completed device, ready to use.

The copper connector, the polyimide spacer and the Ag/AgCl electrode were all cut to shape using the laser micromachining system and cleaned, before use, in 0.1 M HCl. The Ag/AgCl electrode was produced by chloridising Ag foil (500 μm thick, Goodfellows). The electrodes were compressed between two PTFE blocks (labelled v) and held in place with brass housing (labelled vi) which was screwed together (Figure 7.4 (b)). Stainless steel swagelok tubing fittings (tube o.d. $1/6^{th}$ inch) with an O-ring seal were mounted into the PTFE blocks to make the inlet and outlet connectors. The device was made water tight with rubber o-rings (labelled vii).

7.2.2 **Electrode Characterisation**

The structure and surface finish of the all-diamond TFRE were characterised using FE-SEM, WLI and micro-Raman. This was achieved by cross sectioning the TFRE, through the centre, using the laser cutter. Figures 7.5 (a) and (b) show low and high resolution FE-SEM images of the inside of the TFRE. At low resolution the inner curved structure of the entire TFRE is visible. The conducting BDD region is clearly seen as a dark band, sandwiched between the lighter insulating intrinsic diamond. Note that the contrast on the FE-SEM image has been reversed to aid identification.[36] At higher resolution more detailed structure on the intrinsic-doped diamond interface is revealed (no inversion of contrast necessary). The interface between the nucleation face of the pBDD layer and the intrinsic diamond is sharp; a consequence of growing the pBDD on a lapped diamond surface. In contrast, the interface between the growth face of pBDD and the intrinsic diamond is less sharp, as the pBDD face was not lapped before regrowth of the intrinsic layer. This polishing step did not occur to avoid any possible damage to the layered structure, resulting from e.g. cracking of the disc. However, at both interfaces, growth between the intrinsic / pBDD and

pBDD / intrinsic surfaces appears continuous, which is essential to guarantee a good seal for subsequent voltammetry.

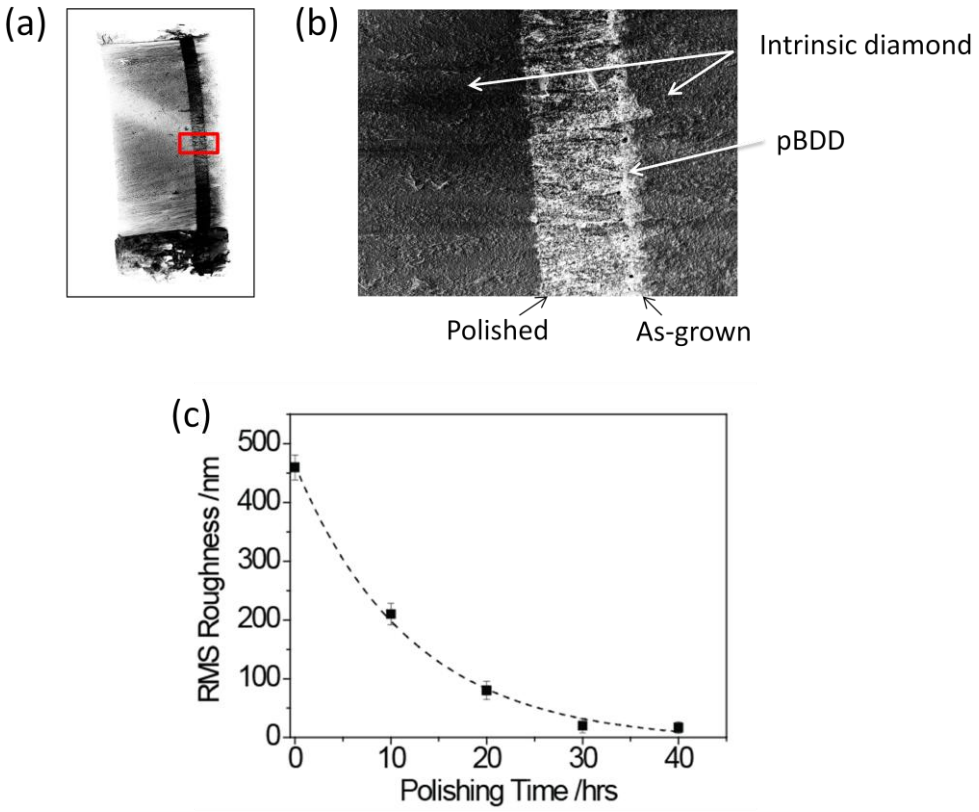

Figure 7.5: FE-SEM images of an all-diamond TFRE at (a) low (note contrast inversion) and (b) high resolution. (c) Plot of rms surface roughness, obtained using WLI as a function of polishing time.

The surface roughness inside the hole was investigated using WLI on five electrodes, which were each subject to a different polishing time. After polishing, the electrode was cut in half in order to determine surface roughness. Figure 7.5 (c) shows a plot of polishing time versus root mean square (rms) surface roughness. Prior to polishing, the inner surface of the laser cut hole revealed a rms surface roughness of 460 nm. After 10 hours, the surface roughness decreased significantly to a value of 210 nm rms. Continued polishing showed a decrease in the surface roughness to 20 nm rms (30 hours of polishing). After 30 hrs the rate of polishing seemed to

significantly decrease so that after a further 10 hours (40 hours in total) the surface finish inside the tube had not improved. All further experiments were thus performed using TFRE's which had been polished for ≥ 30 hrs. It is also interesting to note that there are no major features on the WLI cross sections that would indicate that the different layers of diamond (intrinsic and conducting) polish at significantly different rates, in this configuration.

Raman spectra were recorded to analyse the quality and boron content of the polished all-diamond TFRE. In the intrinsic diamond regions either side of the BDD layer, Figures 7.6 (a) and (c), a large diamond (sp^3) peak at 1332 cm^{-1}, as well as a small broad non-diamond carbon (sp^2) signal at 1560 cm^{-1} are seen. The latter is not unexpected given that opaque mechanical grade intrinsic diamond contains defects and inter-granular non-diamond carbon. In the region of the boron-doped layer, Figure 7.6 (b) again shows a diamond (sp^3) peak centred at 1332 cm^{-1}, but the large attenuation of the peak (Fano resonance) and the boron related peak at ca. 500 cm^{-1} indicates a high boron content (≥ 3 x 10^{20} atoms cm^{-3}), in agreement with the electrical resistivity measurements, therefore the electrode should exhibit metallic-like conductivity.[37] The conducting BDD layer is evidently of high quality with negligible amounts of sp^2 carbon impurities. Importantly, the Raman spectrum also indicates any amorphous carbon left from the laser cutting process has been removed after ≥ 30 hrs polishing.

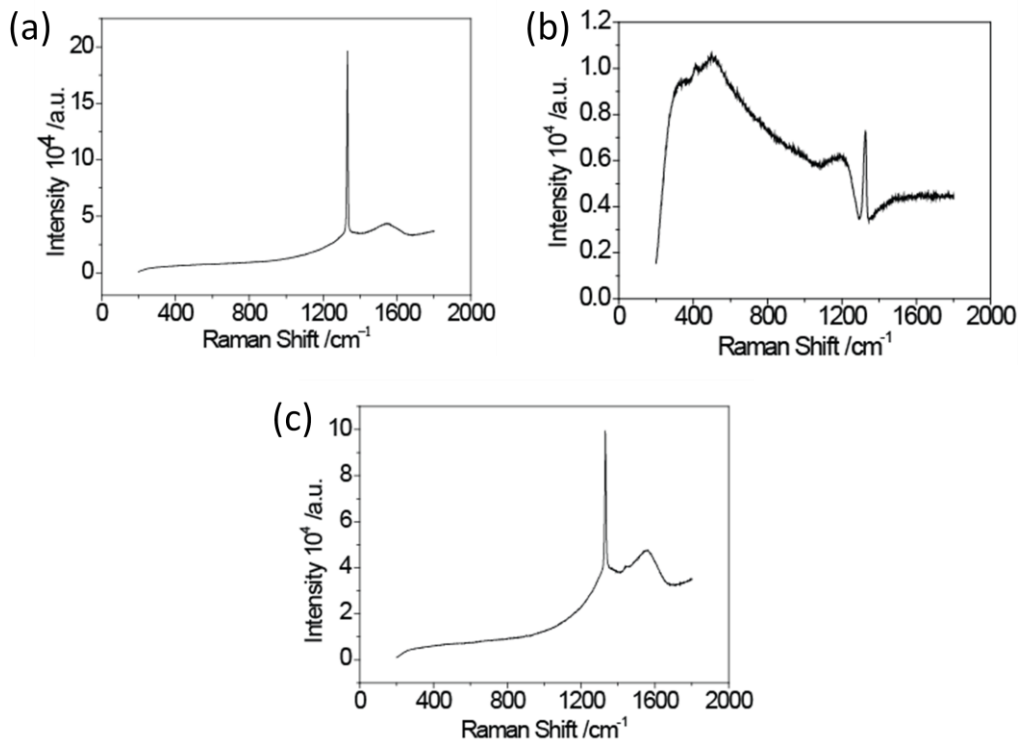

Figure 7.6: Typical raman spectra for the TFRE taken at room temperature with a 514.5 nm laser in the vicinity of (a) entry layer of mechanical grade intrinsic diamond; (b) BDD electrode layer; and (c) the exit layer of mechanical grade intrinsic diamond.

7.2.3 **Hydrodynamic Electrochemistry**

To assess the hydrodynamics of the TFRE, CVs were recorded for 0.1 mM $FcTMA^+$ in 0.1 M KCl at a scan rate of 50 mV s^{-1} under stationary conditions (lowest current) and for various V_f, in the range 0.028 - 0.167 (highest current) cm^3 s^{-1} as shown in Figure 7.7 (ai). The TFRE was orientated such that solution flow encountered the diamond channel in the 455 µm thick layer of intrinsic diamond first. Laminar tubular flow was treated first by Levich[38] and then later by Blaedel and Klatt,[39] who determined that the i_{lim} response as a function of V_f, for well-developed laminar flow in the axial direction is:

$$i_{lim} = 5.43nFc^* D^{2/3} X^{2/3} V_f^{1/3} \qquad (7.2)$$

where X is the length of the tubular electrode (= 90 ± 5 µm).

In Figure 7.7 (a) a steady-state sigmoidal current response is observed which increases with increasing V_f. A plot of i_{lim} versus $V_f^{1/3}$ (red solid squares) gives a straight line response which agrees very well with theory (black line), as shown in Figure 7.7 (b), for D of $FcTMA^+$ = 6 x 10^{-6} cm^2 s^{-1} and n = 1. This demonstrates that (i) the entrance length of the TFRE is sufficient for laminar Poiseulle flow to be established; and (ii) the pBDD electrode is not significantly recessed or protruding from the insulating diamond surface to affect the laminar flow profile, consistent with the data shown in Figure 7.3. The mass transport coefficient (k_t) can be calculated from:

$$k_t = \frac{0.865 D^{2/3} V_f^{1/3}}{X^{1/3} r_t} \qquad (7.3)$$

where r_t is the radius of the tube. For the highest V_f employed here (= 0.167 cm^3 s^{-1}), with r_t = 250 μm, k_t = 0.03 cm s^{-1}, which is a reasonable value for electron transfer kinetic studies. However, to access faster electron transfer rate constant coefficients there is considerable scope for achieving higher k_t values with this flow design through the use of ultra-thin conducting layers of pBDD coupled with smaller tube diameters in the layered structure. Work in this area is currently in progress.

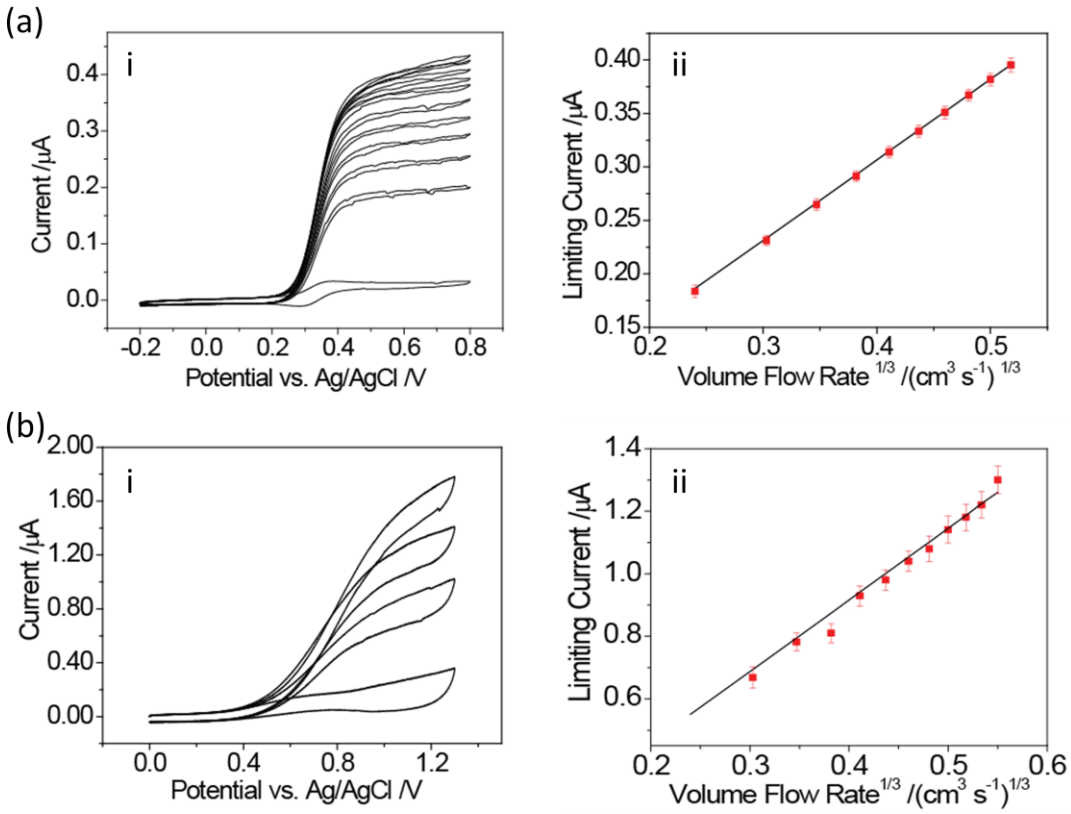

Figure 7.7: (ai) CVs for the oxidation of 0.1 mM $FcTMA^+$ in 0.1 M KCl with V_f of 0 (lowest current), 0.028, 0.056, 0.069, 0.083, 0.097, 0.111, 0.125, 0.139, 0.153 and 0.167 (highest current) $cm^3\ s^{-1}$ at a scan rate of 50 mV s^{-1} (aii) Plot of experimental (■) and theoretical (—) steady state current against $V_f^{1/3}$ for 0.1 mM $FcTMA^+$ in 0.1 M KCl. Error bars show standard deviation of 5 experiments. (bi) CVs for the oxidation of 0.15 mM dopamine in 0.1 M PBS with V_f of 0 (lowest current), 0.028, 0.083 and 0.167 (highest current) $cm^3\ s^{-1}$ and a scan rate of 50 mV s^{-1}. (bii) Plot of experimental (■) and theoretical (—) pseudo steady-state current against $V_f^{1/3}$ for 0.15 mM dopamine in 0.1 M PBS. Error bars show standard deviation of 5 experiments.

After initial characterisation studies, the TFRE was employed to detect the neurotransmitter dopamine. Dopamine oxidation is well known to result in fouling of the electrode surface resulting in a significant decrease in the expected electrochemical signal, especially after repeated use of the electrode.[40-42] Although, pBDD has been shown to reduce fouling, it does not eradicate the problem in quiescent solution. Figure 7.7 (bi) shows typical CVs recorded at the all-diamond TFRE for the oxidation of 0.15 mM dopamine in 0.1 M PBS at 0 (lowest current), 0.028, 0.083 and 0.167 (highest current) $cm^3\ s^{-1}$ flow rates. The electrode was not

cleaned in between measurements. As shown in Figure 7.7 (bi) the CVs approach a pseudo steady-state plateau. Figure 7.7 (bii) shows a plot of i_{lim} versus $V_f^{1/3}$ and the corresponding fit to theory (black line) assuming n=2 and D=6 x 10^{-6} cm^2 s^{-1}.[43] Importantly, a linear response is seen, with experimental results agreeing well with theory. Thus, in this flow geometry, where the products of electrolysis can be washed away downstream from the electrode, coupled with the deployment of a pBDD electrode, eradication of electrode fouling, even at this relatively high dopamine concentration, is achieved. Hence, the use of an all-diamond TFRE for the on-line detection of dopamine from *in vivo* analysis[44,45] and digested tissue samples may be realisable. These results also show that the TFRE can be used repeatedly to detect various analytes without any deterioration in the electrochemical response of the pBDD electrode.

7.3. DUAL BAND ELECTRODE

7.3.1 **Electrode Fabrication**

A 500 µm thick optical grade intrinsic (insulating) polycrystalline diamond, grown via MWCVD by Element Six Ltd., was used as the starting material for electrode fabrication. Several pairs of trenches were lasered into the diamond using a laser micromachining system (E-355H-3-ATHI-O system, Oxford Lasers) with a view to fabricating a number of DBEs with different dimensions. However, due to problems with diamond growth and processing, only one DBE was completed. Figure 7.8 (a) shows side-on and top view images of typical trenches lasered into the diamond to depths of ca. 25 µm. As described in section 3.3, laser kerfing is a technique used to make a V-shaped cut to enable the laser to cleanly cut thicker material.

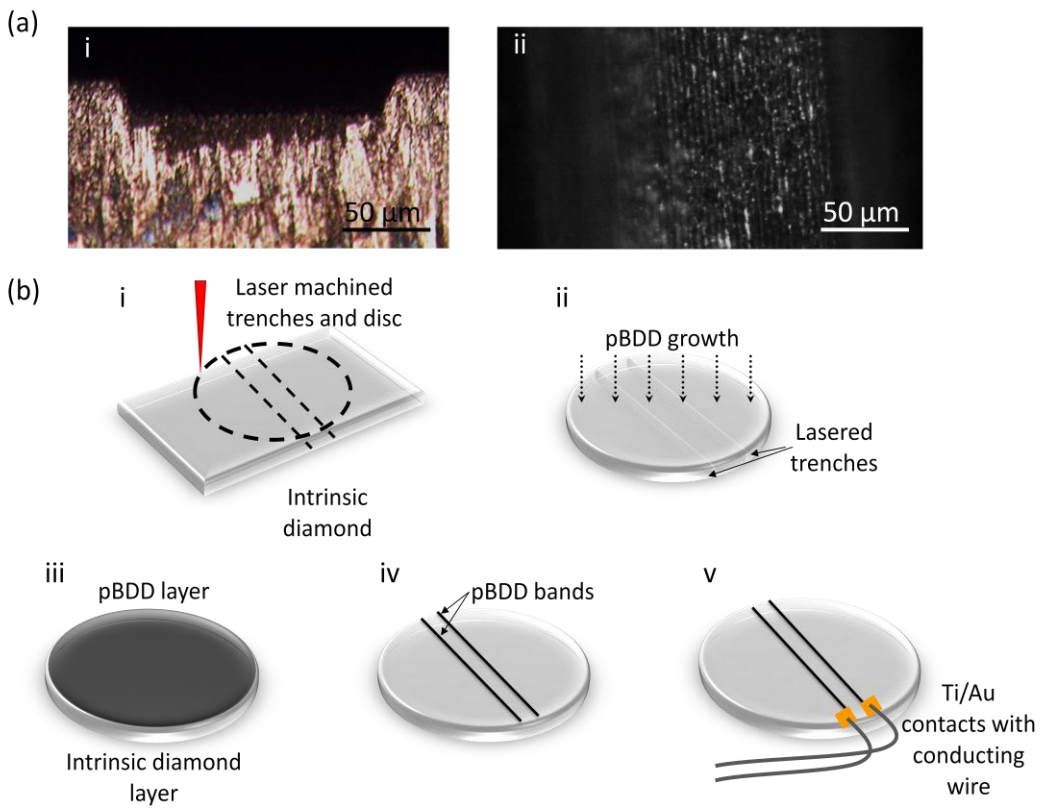

Figure 7.8: (a) Images of laser machined trench in intrinsic diamond (i) side view and (ii) top view. (b) Schematic of the DBE fabrication process.

In this case it was also used to create angled sides to the trenches, in order to facilitate the nucleation and growth of a pBDD layer in the recess. A 6 mm diameter disc was lasered out with the trenches bisecting the sample as shown in Figure 7.8 (bi). The next step was the overgrowth of a conducting pBDD layer which was carried out by the group of Dr. Ken Haenen at the University of Hasselt, Department of Materials (Figure 7.8 (bii)). The heavily doped pBDD was deposited in the trenches and on the top face of the intrinsic diamond (Figure 7.8 (biii)). The sample was subsequently lapped in-house at the University of Warwick to give individually addressable dual band electrodes with a width of 6 mm, length of 200 µm and separation of 300 µm (Figure 7.8 (biv)). The diamond was then acid cleaned and Ti/Au top contacts were made to the pBDD as previously discussed in section 3.3

(Figure 7.8 (bv)). A schematic of the overall electrode fabrication process is shown in Figure 7.8(b).

7.3.2 **Electrode Characterisation**

The quality of the diamond and electrode surface polish was studied using Raman and AFM. Figures 7.9 (a) and (b) show micro-Raman taken at the top surface for the intrinsic and pBDD sections of the DBE respectively. For the intrinsic diamond only a large diamond (sp^3) peak at 1332 cm^{-1} is observed, and no sp^2 Raman features (i.e. no non-diamond carbon) as expected for the high optical grade, in contrast to the mechanical grade intrinsic diamond used for the TFRE. It also verifies that all the pBDD grown over this surface has been removed via lapping. Figure 7.9 (b) is taken on the lapped pBDD surface which will function as the electrode. Again a diamond (sp^3) peak centred at 1332 cm^{-1} is seen however, due to a Fano effect this peak is asymmetric and attenuated.[46] A high boron concentration is responsible for the peaks at ca. 1220 cm^{-1} and 500 cm^{-1}.[37] Thus the dopant density of the pBDD is at least ≥ 3 x 10^{20} atoms cm^{-3} suggesting metal-like conductivity.[37,46] No evidence of sp^2 carbon is observed.

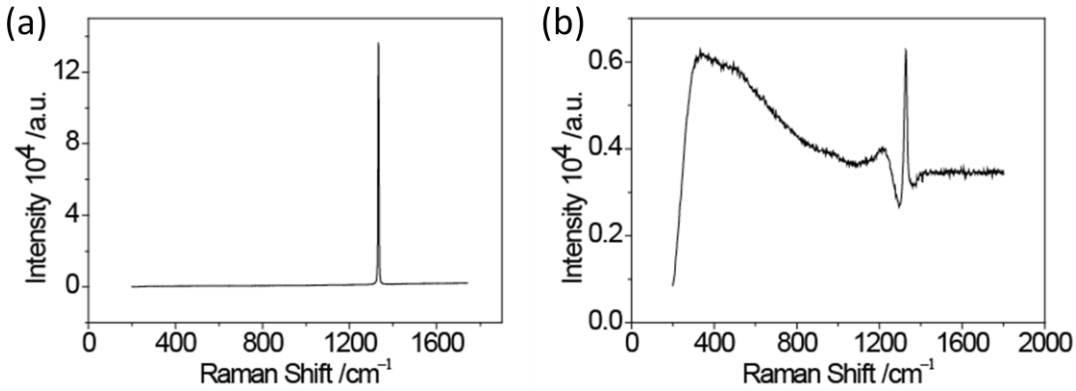

Figure 7.9: Typical raman spectra for the DBE taken at room temperature with a 514.5 nm laser in the vicinity of (a) intrinsic diamond and (b) pBDD electrode.

AFM was employed to study the topography of the electrode surface. Both the quality of the lapping i.e. average surface roughness over an area of tens of microns and the interface between the different types of diamond were imaged. Figure 7.10 (a) is the optical image from the AFM that was used to locate the band edges. Figure 7.10 (b) shows a 10 µm x 10 µm height image and a cross sectional height plot corresponding to the white line. The band edge bisects the AFM image with a height difference between the intrinsic and pBDD of ca. 5 nm. Interestingly, this height difference is comparable to the height differences seen between differently doped grains on Element Six polished pBDD, as discussed in Chapter 3 and shown in Figure 3.1. Due to the polycrystalline nature of the sample, height differences on this scale coincide with previously seen samples in Chapter 3 and would not be expected to interfere with the flow hydrodynamics. Parallel lines at a 45^{o} angle can also be seen in the AFM image in Figure 7.10 (b). These are most likely polishing lines and at less than 1 nm in height are of negligible concern.

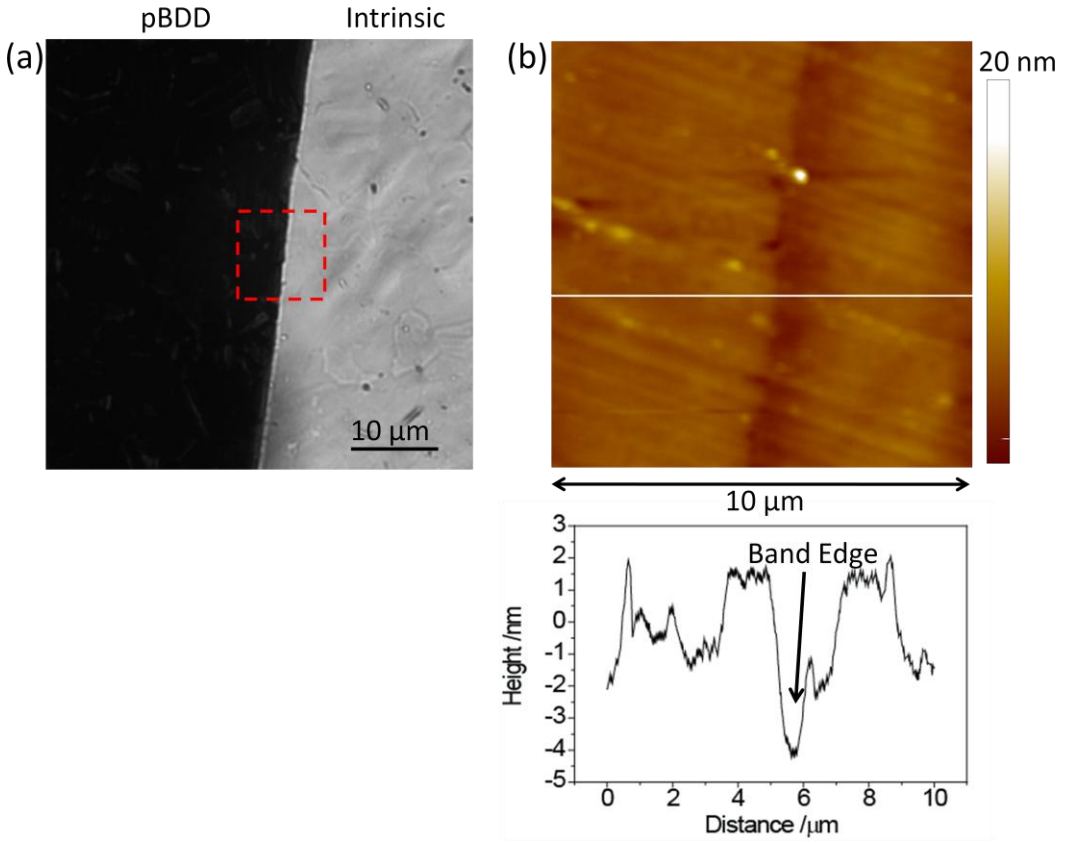

Figure 7.10: (a) Optical microscope image of band edge. (b) 10 µm x 10 µm tapping mode height image of pBDD/intrinsic diamond interface with typical cross section.

7.3.3 **Hydrodynamic Electrochemistry**

The electrochemical response of an individual band electrode was studied under hydrodynamic conditions. This was achieved by employing a channel flow cell which had been fabricated using microstereolithography.[17] Figures 7.11 (a) and (b) show the channel flow cell and experimental set-up, where the flow cell sits on top of the DBE (fastened with cotton string) with the bands extending out either side of the cell allowing electrical connection. The height of the channel ($2h$) was 260 µm with a channel length (l_{chan}) and width (w_{chan}) of 3.5 mm and 3 mm respectively. The first band electrode was used as the working electrode and was positioned 1.5 mm into the length of the channel.

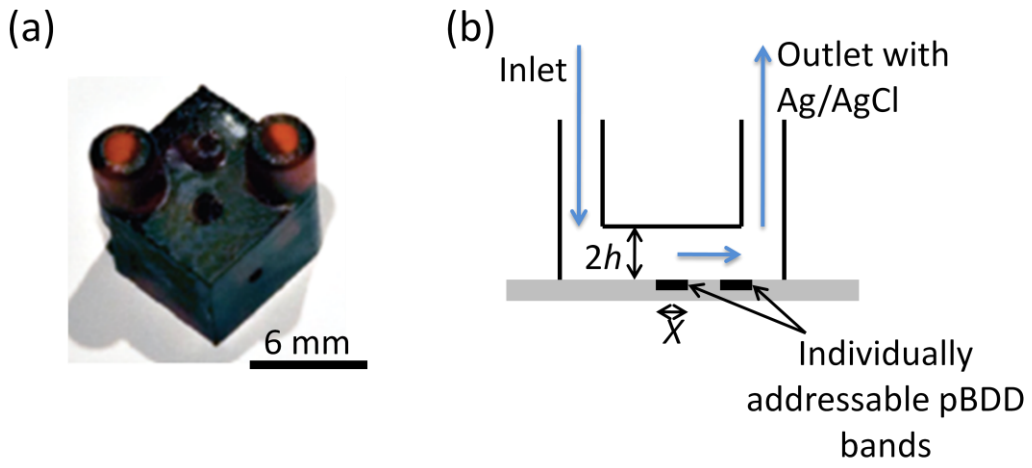

Figure 7.11: (a) Image of flow cell fabricated via microstereolithography and (b) schematic of the experimental set-up for flow over the DBE.

Under laminar flow conditions it is expected that i_{lim} should vary with V_f in accordance with the Levich equation;[17,47]

$$i_{\text{lim}} = 1.165nFC_b D^{2/3} \bar{U}^{1/3} h^{-1/3} wX^{2/3} \qquad (7.4)$$

where w is the width of the band electrode exposed to solution, X is the length of the band electrode and $\bar{U}$ is defined in terms of V_f, by

$$\bar{U} = V_f / (2hw_{chan}) \qquad (7.5)$$

Figure 7.12 (a) shows typical LSVs for the reduction of 0.4 mM $Ru(NH_3)_6^{3+/2+}$ in 0.1 M KNO_3 at a scan rate of 10 mV s^{-1} for various volume flow rates of 1, 5, 10, 15, 20 and 25 cm^3 min^{-1}. A sigmoidal steady state response is observed with i_{lim} increasing with increasing volume flow rate. A plot of experimental i_{lim} against $V_f^{1/3}$ is given in Figure 7.12 (b) and compared to theoretical values calculated from equation 7.3, assuming h = 130 µm, D = 8 x 10^{-6} cm^2 s^{-1}, w = 3 mm and X = 200 µm. The i_{lim} increases linearly with $V_f^{1/3}$ in accordance with the Levich equation and the steady state current magnitudes are in good agreement with those predicted.

The absence of any significant background currents at these negative potentials also suggests that the pBDD is of high quality with no sp^2 carbon present. The results show great potential for the use of all diamond bands for hydrodynamic electrochemical applications such as on-line analysis, as well as multiple electrode experiments such as generation-collection analysis.

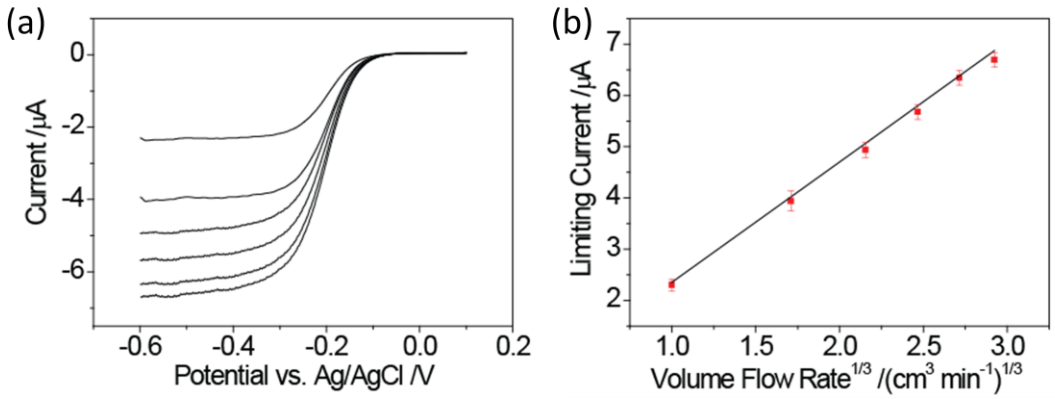

Figure 7.12: (a) LSVs for the reduction of 0.4 mM $Ru(NH_3)_6^{3+/2+}$ in 0.1 M KNO_3 at a scan rate of 10 mV s^{-1} for various volume flow rates of 1 (least negative curve), 5, 10, 15, 20 and 25 (most negative curve) cm^3 min^{-1}. (b) Plot of experimental (■) and theoretical (—) steady state current against $V_f^{1/3}$ for 0.4 mM $Ru(NH_3)_6^{3+/2+}$ in 0.1 M KNO_3. Error bars show standard deviation of 5 experiments.

7.3.4 **Solution Conductivity Measurements**

Traditional conductivity sensors are fabricated from supposedly 'inert' metal electrodes e.g. Pt, where a constant alternating current, ac, is applied between the electrodes to avoid electrolysis and the resulting potential measured. For a planar, two electrode conductivity sensor an electric field is set-up as shown in Figure 7.13. The resulting potential is established due to the solution resistance, but also through non ideal components including double layer capacitance at the electrode/solution interface and faradic impedance i.e. electrolysis.[48]

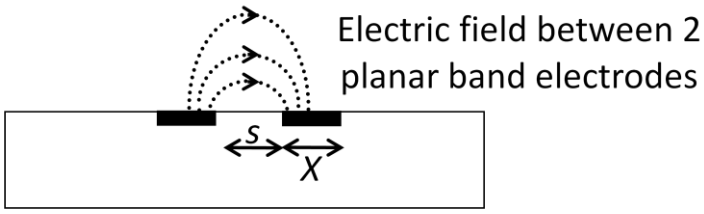

Figure 7.13: Cross section of the DBE showing electric field between the planar electrodes.

In order to minimise these non ideal components, electrodes with both low capacitance and faradic interferences are needed. As pBDD has been shown to have low double layer capacitance[49] and resistance to fouling,[50] the use of the DBE as a solution conductivity sensor was investigated. A constant ac current of 5 µA was applied between the two bands at a frequency of 10 kHz and the resulting potential was measured, this was performed using an ac power supply and voltmeter built in-house. A relatively high frequency was chosen in order to reduce electrode/solution capacitive effects, and was limited by the instrumentation employed in this experiment. Figure 7.14 (a) shows the calibration plot of output potential vs. solution conductivity. The conductivity was varied using varying concentrations of KCl in solution ranging from 0.9 mM to 0.12 M for the DBE defined by *w* of 3 mm, *X* of 200 µm and electrode separation (*s*) of 300 µm. The measurements were carried out at room temperature (23 ^{o}C) and solution conductivities were obtained from standard tables.[51]

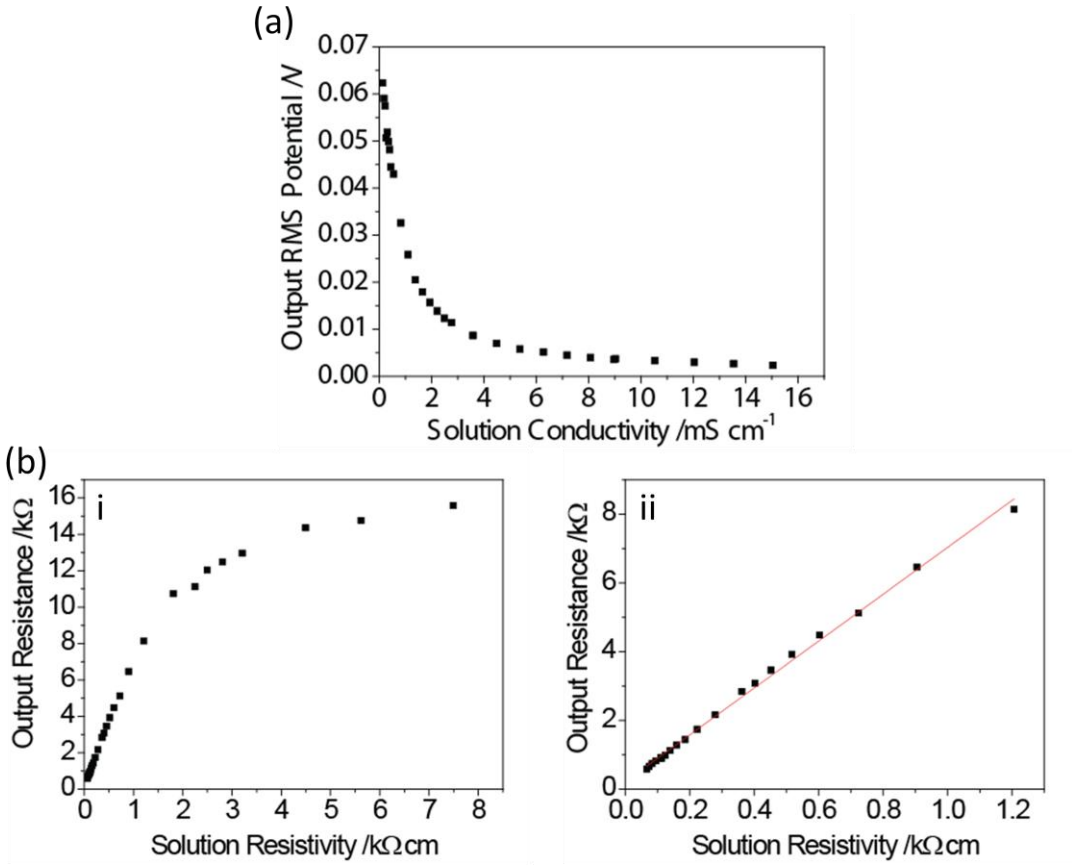

Figure 7.14: (a) Calibration curve of output potential against solution conductivity; (b) plot of experimental output resistance against solution resistivity (i) over the whole solution conductivity range and (ii) from 0.8 mS cm^{-1} and above (■) with a linear fit (----), for varying concentrations of KCl, recorded with an ac of 5 µA at 10 kHz.

The resulting curve shows that as solution conductivity increases, there is a decrease in output potential. Figure 7.14 (b) presents these results as solution resistivity (1/solution conductivity) versus output resistance (output potential/applied current). Solution resistivities in the range 0.066 kΩ cm to 7.5 kΩ cm are shown in Figure 7.14 (bi) whilst those in the range 0.066 kΩ cm to 1.2 kΩ cm are presented in Figure 7.14 (bii) and yield a linear fit ($R \geq 0.998$). Above 1.2 kΩ cm a curve in the calibration can be seen. The deviation from linearity at higher solution resistivities can be explained by considering the impedance (Z), of the system. For a simplified electrical equivalent model, the solution resistance and the capacitance between the

electrodes, can be considered as a resistor and capacitor in parallel (ignoring double layer capacitance which would be in series with the solution resistance). As such, the magnitude of *Z* is given by equation 7.6;

$$|Z|^{-1} = \sqrt{\left(\frac{1}{Rs}\right)^2 + \omega^2 C^2} \qquad (7.6)$$

where R_s is the resistance of the solution, ω is the frequency of the ac and *C* is the capacitance between the electrodes, both being constant for a given experimental set-up. When the solution resistance is small, the first term in equation 7.6 is large and the second term is negligible. However, as the solution resistance increases, the first term becomes smaller and the capacitative component starts to have an effect. As *C* is related to the electrode geometry, as discussed below, the concentration at which non-linearity starts to occur can be varied.

As mentioned in section 7.1, the cell constant, k (cm^{-1}) for a conductivity meter is defined as the proportionality factor between solution resistivity, ρ (Ω cm) and the measured resistance, R_t (Ω) and is given by the equation:

$$R_t = k\,\rho \qquad (7.7)$$

For traditional parallel electrode formats, k is equal to equation 7.1. However, for planar electrodes, the fringing of the electric field as shown in Figure 7.13, complicates the calculation of k. As such, equation 7.7 can be used to determine k for the all-diamond conductivity meter from the linear KCl calibration data, where capacitative effects are negligible. Analysis of Figure 7.14 (bii) yields a linear fit giving a cell constant of 6.8 ± 0.1 cm^{-1}.

Using Gauss's law, assuming a homogeneous medium between the electrodes, *C* can be related to k via equation 7.8;[27]

$$C = \varepsilon_o \varepsilon_r / \ k \qquad (7.8)$$

where ε_o is the permittivity of free space and ε_r is the relative dielectric constant of water. Olthuis *et al.* have previously shown that the capacitance per unit width of the planar electrodes, C_w, can be calculated using the mathematic method of conformal transformation, given by equation 7.9;[52]

$$C_w = \frac{\varepsilon o \ \varepsilon r}{2} \frac{K\left[(1-k^2)^{1/2}\right]}{K(k)} \frac{1}{w} \qquad (7.9)$$

K(k) is the complete elliptic integral of the first kind;

$$K(k) = \int_{t=o}^{1} \frac{dt}{\left[(1-t^2)\,(1-k^2t^2)\right]^{1/2}} \qquad (7.10)$$

and *k* is the variable of function *K* and is equal to the sensor dimensions *s*/(*s*+*X*). For the given dimensions of the DBE, assuming ε_o = 8.85 x 10^{-12} Fm^{-1} and ε_r = 80.22, *C* was calculated as 1.7 µF, giving a cell constant of 7 cm^{-1}, in good agreement with that determined experimentally, showing that for solution conductivities of 0.8 mS cm^{-1} and greater, the sensor functions as predicted. Using the equations above, it is possible to design a DBE with optimised *w*, *X* and *s* to produce a smaller cell constant, enabling lower solution conductivities to be measured. For example, increasing *w* to 4 mm, *X* to 250 µm and decreasing *s* to 50 µm, a cell constant of 2.5 is theoretically achievable.

7.4. CONCLUSIONS

Described above is the fabrication and characterisation of the first all-diamond hydrodynamic electrodes in two formats, the TFRE and the DBE, comprising pBDD ring and band electrodes insulated with intrinsic diamond. Laser machining was used to define the electrode geometry either by cutting a hole through sandwiched intrinsic-pBDD-intrinsic layers or by patterning insulating diamond and then

overgrowing with pBDD. After polishing procedures, these all-diamond structures were found to be co-planar with ultra-smooth surfaces.

For a TFRE with a 500 μm diameter tube, electrode length of ca. 90 μm, and an intrinsic diamond entrance length of ca. 455 μm, the steady-state limiting current – volume flow rate characteristics for the oxidation of $FcTMA^+$ were found to obey that predicted by Levich for a tubular electrode operating under laminar flow conditions. Application of this flow device to the detection of the neurotransmitter dopamine was shown. Importantly, it was demonstrated that even at relatively high concentrations of the analyte, the combination of pBDD in this geometry flow system resulted in the eradication of electrode fouling. As this is a common problem with the voltammetric detection of dopamine, this paves the way for use of this flow system in on-line detection systems.

For an all-diamond dual band electrode, 200 μm long and 6 mm wide, the steady-state limiting current – volume flow rate characteristics at one of the band electrodes for the reduction of $Ru(NH_3)_6^{3+/2+}$ were also found to obey that predicted by Levich for a channel flow band electrode operating under laminar flow conditions. The DBE was applied to solution conductivity measurements. The cell constant was experimentally determined as 6.8 cm^{-1} agreeing well with the theoretical prediction of 7 cm^{-1}, with a linear calibration over the concentration range from 7 mM to 0.12 M. A major advantage of all-diamond electrodes is that they can be used extensively, withstanding aggressive media and strong cleaning procedures without any deterioration of geometry or response.

These all-diamond platforms are extremely promising for significant further work, which will consider: (1) TFRE with significantly increased mass transport coefficients by employing ultra-thin conducting films coupled with smaller diameter holes; (2) TFRE with multiple apertures, it will be possible to increase the limiting current signal for detection of low concentrations of analytes in solution, in a similar manner to UME planar arrays developing multiple; and for both designs (3) the development of individually addressable conducting layer electrodes in both DBE and TFRE formats. The latter will facilitate time of flight, generation-collection type experiments aimed at for example, characterising the lifetime of transient species, indirect electrochemical determination of the concentration of electroinactive species *etc*.

7.5. REFERENCES

(1) Compton, R. G.; Foord, J. S.; Marken, F. *Electroanalysis* **2003**, *15*, 1349.
(2) Kraft, A. *Int. J. Electrochem. Sci.* **2007**, *2*, 355.
(3) Granger, M. C.; Witek, M.; Xu, J. S.; Wang, J.; Hupert, M.; Hanks, A.; Koppang, M. D.; Butler, J. E.; Lucazeau, G.; Mermoux, M.; Strojek, J. W.; Swain, G. M. *Anal. Chem.* **2000**, *72*, 3793.
(4) Spataru, N.; Sarada, B. V.; Popa, E.; Tryk, D. A.; Fujishima, A. *Anal. Chem.* **2001**, *73*, 514.
(5) Martin, H. B.; Argoitia, A.; Landau, U.; Anderson, A. B.; Angus, J. C. *J. Electrochem. Soc.* **1996**, *143*, L133.
(6) Chiku, M.; Watanabe, T.; Einaga, Y. *Diamond Relat. Mater.* **2010**, *19*, 673.
(7) Sarada, B. V.; Rao, T. N.; Tryk, D. A.; Fujishima, A. *J. Electrochem. Soc.* **1999**, *146*, 1469.
(8) Cooper, J. B.; Pang, S.; Albin, S.; Zheng, J. L.; Johnson, R. M. *Anal. Chem.* **1998**, *70*, 464.
(9) Hu, J. P.; Holt, K. B.; Foord, J. S. *Anal. Chem.* **2009**, *81*, 5663.
(10) Tsunozaki, K.; Einaga, Y.; Rao, T. N.; Fujishima, A. *Chem. Lett.* **2002**, 502.
(11) Provent, C.; Haenni, W.; Santoli, E.; Rychen, P. *Electrochim. Acta* **2004**, *49*, 3737.
(12) Soh, K. L.; Kang, W. P.; Davidson, J. L.; Basu, S.; Wong, Y. M.; Cliffel, D. E.; Bonds, A. B.; Swain, G. M. *Diamond Relat. Mater.* **2004**, *13*, 2009.
(13) Kang, W. P.; Davidson, J. L.; Wong, Y. M.; Soh, K. L.; Gurbuz, Y. *Carbon-derived micro- and nanostructures for chemical sensing*; IEEE Sensors: New York, 2004.
(14) Sopchak, D.; Miller, B.; Kalish, R.; Avyigal, Y.; Shi, X. *Electroanalysis* **2002**, *14*, 473.
(15) Rao, T. N.; Yagi, I.; Miwa, T.; Tryk, D. A.; Fujishima, A. *Anal. Chem.* **1999**, *71*, 2506.
(16) Prado, C.; Murcott, G. G.; Marken, F.; Foord, J. S.; Compton, R. G. *Electroanalysis* **2002**, *14*, 975.
(17) Snowden, M. E.; King, P. H.; Covington, J. A.; Macpherson, J. V.; Unwin, P. R. *Anal. Chem.* **2010**, *82*, 3124.
(18) Shin, D. C.; Sarada, B. V.; Tryk, D. A.; Fujishima, A. *Anal. Chem.* **2003**, *75*, 530.
(19) Cvacka, J.; Quaiserova, V.; Park, J.; Show, Y.; Muck, A.; Swain, G. M. *Anal. Chem.* **2003**, *75*, 2678.
(20) Preechaworapun, A.; Chuanuwatanakul, S.; Einaga, Y.; Grudpan, K.; Motomizu, S.; Chailapakul, O. *Talanta* **2006**, *68*, 1726.
(21) Mayrhofer, K.; Zemann, A. J.; Schnell, E.; Bonn, G. K. *Anal. Chem.* **1999**, *71*, 3828.
(22) Kruise, J.; Rispens, J. G.; Bergveld, P.; Kremer, F. J. B.; Starmans, D.; Haak, J. R.; Feijen, J.; Reinhoudt, D. N. *Sens. Actuators, B* **1992**, *6*, 101.
(23) Langereis, G. R.; Olthuis, W.; Bergveld, P. *Chemom. Intell. Lab. Syst.* **2000**, *50*, 211.
(24) Liu, Y.; Wipf, D. O.; Henry, C. S. *Analyst* **2001**, *126*, 1248.
(25) Guijt, R. M.; Baltussen, E.; van der Steen, G.; Frank, H.; Billiet, H.; Schalkhammer, T.; Laugere, F.; Vellekoop, M.; Berthold, A.; Sarro, L.; van Dedem, G. W. K. *Electrophoresis* **2001**, *22*, 2537.
(26) Jacobs, P.; Varlan, A.; Sansen, W. *Med. Biol. Eng. Comput.* **1995**, *33*, 802.
(27) Timmer, B.; Sparreboom, W.; Olthuis, W.; Bergveld, P.; van den Berg, A. *Lab Chip* **2002**, *2*, 121.
(28) Olthuis, W.; Sprenkels, A. J.; Bomer, J. G.; Bergveld, P. *Sens. Actuators, B* **1997**, *43*, 211.
(29) Holt, K. B.; Hu, J. P.; Foord, J. S. *Anal. Chem.* **2007**, *79*, 2556.
(30) Soh, K. L.; Kang, W. P.; Davidson, J. L.; Wong, Y. M.; Cliffel, D. E.; Swain, G. M. *Diamond Relat. Mater.* **2008**, *17*, 900.

(31) Bitziou, E.; Rudd, N. C.; Unwin, P. R. *J. Electroanal. Chem.* **2007**, *602*, 263.
(32) Pagels, M.; Hall, C. E.; Lawrence, N. S.; Meredith, A.; Jones, T. G. J.; Godfried, H. P.; Pickles, C. S. J.; Wilman, J.; Banks, C. E.; Compton, R. G.; Jiang, L. *Anal. Chem.* **2005**, *77*, 3705.
(33) Colley, A. L.; Williams, C. G.; Johansson, U. D.; Newton, M. E.; Unwin, P. R.; Wilson, N. R.; Macpherson, J. V. *Anal. Chem.* **2006**, *78*, 2539.
(34) Zhong, D. J.; Tao, F. M.; Xu, Y. L.; Jia, J. P. *Proc. Inst. Mech. Eng., IMechE Conf.* **2007**, *221*, 201.
(35) Hutton, L.; Newton, M. E.; Unwin, P. R.; Macpherson, J. V. *Anal. Chem.* **2009**, *81*, 1023.
(36) Wilson, N. R.; Clewes, S. L.; Newton, M. E.; Unwin, P. R.; Macpherson, J. V. *J. Phys. Chem. B* **2006**, *110*, 5639.
(37) Bernard, M. *Diamond Relat. Mater.* **2004**, *13*, 282.
(38) Levich, V. G. *Physiochemical Hydrodynamics*; Prentice Hall, Englewood Cliffs, NJ, 1962.
(39) Blaedel, W. J.; Klatt, L. N. *Anal. Chem.* **1966**, *38*, 879.
(40) Shakkthivel, P.; Chen, S.-M. *Biosens. Bioelectron.* **2007**, *22*, 1680.
(41) Pihel, K.; Walker, Q. D.; Wightman, R. M. *Anal. Chem.* **1996**, *68*, 2084.
(42) Chuekachang, S.; Kruefu, V.; Chaiyasit, S.; Phanichphant, S. In *5th IEEE International Conference on Nano/Micro Engineered and Molecular Systems (NEMS)* **2010**, 133.
(43) DuVall, S. H.; McCreery, R. L. *J. Am. Chem. Soc.* **2000**, *122*, 6759.
(44) Murai, S.; Saito, H.; Abe, E.; Nagahama, H.; Miyate, H.; Masuda, Y.; Itoh, T. *Eur. J. Pharmacol.* **1990**, *183*, 417.
(45) Thomas, D. H.; Taylor, J. D.; Barnaby, O. S.; Hage, D. S. *Clin. Chim. Acta* **2008**, *398*, 63.
(46) Locher, R.; Wagner, J.; Fuchs, F.; Maier, M.; Gonon, P.; Koidl, P. *Diamond Relat. Mater.* **1995**, *4*, 678.
(47) Compton, R. G.; Unwin, P. R. *J. Electroanal. Chem.* **1986**, *206*, 57.
(48) Olthuis, W.; Volanschi, A.; Bomer, J. G.; Bergveld, P. *Sens. Actuators, B* **1993**, *13*, 230.
(49) Xu, J. S.; Granger, M. C.; Chen, Q. Y.; Strojek, J. W.; Lister, T. E.; Swain, G. M. *Anal. Chem.* **1997**, *69*, A591.
(50) Sarada, B. V.; Rao, T. N.; Tryk, D. A.; Fujishima, A. *Anal. Chem.* **2000**, *72*, 1632.
(51) Owen, H. S. H. a. B. B. *The Physical Chemistry of Electrolytic Solutions*; Reinhold, New York, 1958.
(52) Olthuis, W.; Streekstra, W.; Bergveld, P. *Sens. Actuators, B* **1995**, *24*, 252.

Conclusions

CVD grown diamond is an exciting material whose properties can be tuned for specific applications. The diamond samples used in this thesis were grown by Element Six Ltd. and The University of Hasselt via MWCVD. As discussed in Chapter 1, investigations into the use of CVD grown BDD in electrochemistry have found a number of advantages when being utilised as a working electrode. pBDD provides a wide solvent window, allowing access to a wider potential range in comparison to traditional electrodes e.g. Pt. Lower background currents are also achieved with pBDD electrodes due to low capacitance and the absence of any redox active surface species. The lack of a dissolved oxygen reduction signal, also aids in clear analytical responses. The morphological stability of diamond has positive implications for use under harsh conditions i.e. extreme positive and negative potentials, high temperatures and pressures etc. While diamond is initially hydrogen-terminated after growth, oxygen-terminating the surface prior to electrochemical experimentals ensures a stable terminated from the outset.

This thesis aimed to take advantage of the properties of pBDD in electroanalysis of various redox active species using new experimental procedures to produce a wide range of pBDD electrode geometries. In order to effectively and efficiently employ pBDD in electroanalysis, ohmically contacted 1 mm diameter disc pBDD electrodes sealed in glass were fabricated as detailed in Chapter 3. This electrode format was easy to use and, due to ohmic contacts and smaller area exposed to solution, enabled the interpretation of results where the experimental set-up had negligible impact.

The pBDD material used was extensively characterised using AFM, FE-SEM, micro-Raman and XPS to determine the quality of the material.

Using the In-lens secondary electron detector on the FE-SEM, images showed a polycrystalline grain morphology, where the larger grains tended to have brighter contrast, indicating a lower boron content, previously verified using C-AFM.[1] The topography of the surface was studied using AFM and for the 500 μm thick samples employed, were found to have grain sizes ranging from 2 – 20 μm, with an average surface roughness of 1 – 2 nm within a grain and 6 nm over the whole of the surface. The AFM was correlated to FE-SEM to show that the larger grains with a lower boron content, were higher in topography. Consequently, information gathered via AFM could be related back to grain type. Micro-Raman was obtained for the different grains present, where a Fano-type resonance was observed for both grain types to varying degrees. For the brighter (larger) grains a small asymmetry of the 1332 cm^{-1} peak indicated a boron concentration of $\geq 1 \times 10^{20}$ atoms cm^{-3}. For the darker (smaller) grains, a larger Fano effect and a peak at ca. 500 cm^{-1} indicated a higher boron concentration of $\geq 3 \times 10^{20}$ atoms cm^{-3}. Importantly, the Raman showed that all areas of the pBDD surface were expected to be within at least the hopping conduction regime, with the higher doped regions in the metallic conduction region.[2-4]

XPS of the acid cleaned diamond confirmed that an oxygen-terminated surface was present with an O/C 1s ratio of 10 %. A variety of carbon-containing functional groups were found to be present including hydroxyl, ether, ester and carbonyl groups. The current-voltage response of the oxygen-terminated pBDD was

investigated using a range of outer- and inner-sphere redox mediators. Close to reversible behaviour was observed for $Ru(NH_3)_6^{3+/2+}$, $IrCl_6^{2-/3-}$ and $Fe(CN)_6^{3-/4}$ with a slight increase in ΔE_p when increasing the concentration from 1 mM to 10 mM. The electrochemical response of the pBDD was also shown to be stable even after applying relatively harsh cleaning conditions i.e. -4 V vs. SCE for 3 min to aid in the oxidation of 2-chlorophenol.

The 1 mm disc pBDD electrodes were used in conjunction with electrodeposited Pt NPs for the detection of oxygen, as described in Chapter 4. The CV signal for oxygen detection was found to be optimal when electrodepositing Pt at -1.0 V vs. SCE over 5 s. Pt NPs with sizes of ~3 nm ± 2.5 nm (s.d.) (surface density ~130 NPs μm^{-2}) and ~1 nm ± 2 nm (s.d.) (surface density ~340 NPs μm^{-2}) in the low and high conductivity grains, respectively were formed. As a result of the low background currents associated with pBDD and the low surface area of Pt NPs (compared with a continuous film of Pt), the corresponding voltammetric response for oxygen reduction at the pBDD-Pt composite showed significantly lower background signals compared to Pt electrodes. Therefore an excellent response from 0 to 100 % oxygen saturation and a limit of detection at the ~parts per billion level over the pH range 4−10 and stability over at least a 2 week period (daily use).

Chapter 5 also utilised composite electrodes for the electroanalysis of glucose, methanol and ethanol. In this case, $Ni(OH)_2$ was electrodeposited onto the pBDD surface by electrogenerating OH^- in the presence of Ni^{2+} to create highly supersaturated ($S > 10^5$) nickel hydroxide solutions close to the electrode surface resulting in the precipitation of nickel hydroxide NPs. The effect of NP size on

electrocatalytic activity was investigated by measuring the steady-state current for the oxidation of glucose in alkaline media. It was found that for NPs ≥ 25 nm in size, glucose oxidation was predominantly diffusion-controlled. However, for the smallest NPs produced (~12 nm) the currents passed were much smaller than expected on the basis of diffusion control; this was attributed to kinetic limitations. For glucose oxidation, this electrode showed a sensitivity of 330 μA mM^{-1} cm^{-2} and a limit of detection of 400 nM. The electrocatalytic oxidation of this electrode toward methanol and ethanol was also found to be very efficient, achieving very high density currents of ~1010 A g^{-1} for 0.5 M ethanol and 990 A g^{-1} for 0.47 M methanol. The next step for these composite electrodes is to trial them in real-world situations. For example, dissolved oxygen sensing in streams and wastewater as well as glucose detection in biological samples.

Chapter 6 involved the use of high-resolution microscopy techniques, such as AFM and FE-SEM, to provide a greater understanding of the features observed by us and others in DPV-ASV of the popular Pb^{2+}/Pb system at pBDD, an example of a heterogeneous solid electrode. AFM revealed that the amount of Pb deposited onto the diamond surface using an impinging jet delivery system was less than expected over the concentration range 4−100 nM given the diffusion-convection set-up. This in turn, produced lower calibration gradients at low Pb^{2+} concentration. AFM and FE-SEM imaging showed that as the Pb^{2+} concentration was increased, a change in the deposition morphology occurred from small isolated NPs (100 nM) to heterogeneous structures comprising both thin films and NPs (1 μM). A second peak in the DPV response at these high concentrations was associated with stripping from the thin-film structures. AFM further revealed that increasing the amount of Pb

on the pBDD surface made it more difficult to completely remove in one DPV sweep. Thus, a substantial amount of Pb could remain on the electrode surface, undetected by DPV thus producing nonlinear calibration plots. Multi-metal detection is the next big challenge in this field. Investigations into how different metals will deposit and strip on the pBDD surface in the presence of each other, will be essential in understanding the electrochemical response and may aid in determining experimental protocols.

While laser micromachining of pBDD was shown in Chapter 1 to be an ideal procedure to process diamond and determine electrode geometry, in order to maximise the advantages of pBDD electrodes and not compromise any of the properties previously mentioned, all-diamond electrodes were fabricated and characterised in Chapter 7. TFRE and DBE were made with pBDD ring and dual band electrodes which were insulated with intrinsic diamond. Laser machining was again used to define the electrode geometry and polishing procedures provided co-planar all-diamond structures with ultra-smooth surfaces

The $i_{lim} - V_f$ response for the oxidation of $FcTMA^+$ at the TFRE was found to obey that predicted by Levich for a tubular electrode operating under laminar flow conditions. It was also demonstrated that at relatively high concentrations of dopamine, the combination of pBDD in this geometry flow system resulted in the eradication of electrode fouling. The steady-state limiting current – volume flow rate response for the reduction of $Ru(NH_3)_6^{3+/2+}$ was found to obey that predicted by Levich for a channel flow band electrode operating under laminar flow conditions. This suggests that both electrode formats could be used for on-line analysis. The

DBE was also used for solution conductivity measurements where a cell constant was experimentally determined as 6.8 cm^{-1} with a linear calibration over the concentration range from 7 mM to 0.12 M.

A major advantage of all-diamond electrodes is that even when used in aggressive media or subject to strong cleaning procedures, there is no deterioration of the geometry or response. Significant further work is proposed for these all-diamond electrodes including multiple apertures in the TFRE to increase analytical signal and multiple individually addressable electrodes for both the TFRE and DBE format for use in generation-collection experiments. Other forms of all-diamond electrode could also be beneficial, for example all-diamond UMEs.

8.1. REFERENCES

(1) Wilson, N. R.; Clewes, S. L.; Newton, M. E.; Unwin, P. R.; Macpherson, J. V. *J. Phys. Chem. B* **2006**, *110*, 5639.

(2) Lagrange, J. P.; Deneuville, A.; Gheeraert, E. *Diamond Relat. Mater.* **1998**, *7*, 1390.

(3) Deneuville, A.; Baron, C.; Ghodbane, S.; Agnès, C. *Diamond Relat. Mater.* **2007**, *16*, 915.

(4) Levy-Clement, C.; Ndao, N. A.; Katty, A.; Bernard, M.; Deneuville, A.; Comninellis, C.; Fujishima, A. *Diamond Relat. Mater.* **2003**, *12*, 606.